

Titre: Capillary Modelling for Flow Control and Accurate Mass Transport in
Title: Microfluidics

Auteur: Samuel Castonguay
Author:

Date: 2022

Type: Mémoire ou thèse / Dissertation or Thesis

Référence: Castonguay, S. (2022). Capillary Modelling for Flow Control and Accurate Mass
Citation: Transport in Microfluidics [Ph.D. thesis, Polytechnique Montréal]. PolyPublie.
<https://publications.polymtl.ca/10527/>

 **Document en libre accès dans PolyPublie**
Open Access document in PolyPublie

URL de PolyPublie: <https://publications.polymtl.ca/10527/>
PolyPublie URL:

**Directeurs de
recherche:** Thomas Gervais, & Emmanuel Delamarche
Advisors:

Programme: Génie physique
Program:

POLYTECHNIQUE MONTRÉAL
affiliée à l'Université de Montréal

Capillary Modelling for Flow Control and Accurate Mass Transport in Microfluidics

SAMUEL CASTONGUAY
Département de génie physique

Thèse présentée en vue de l'obtention du diplôme de *Philosophiæ Doctor*
Génie physique

Août 2022

POLYTECHNIQUE MONTRÉAL
affiliée à l'Université de Montréal

Cette thèse intitulée :

Capillary Modelling for Flow Control and Accurate Mass Transport in Microfluidics

présentée par **Samuel CASTONGUAY**
en vue de l'obtention du diplôme de *Philosophiæ Doctor*
a été dûment acceptée par le jury d'examen constitué de :

Oussama MOUTANABBIR, président

Thomas GERVAIS, membre et directeur de recherche

Emmanuel DELAMARCHE, membre et codirecteur de recherche

Bruno BLAIS, membre

Liviu CLIME, membre externe

DEDICATION

To my family...

À ma famille...

ACKNOWLEDGEMENTS

I am grateful to my supervisor and co-supervisor, Thomas Gervais and Emmanuel Delamarche, for their timely support, immense knowledge, and constant source of motivation. I consider myself very fortunate to have had the opportunity of working with both of you. I would like to give special thanks to my supervisor Thomas, world-class communicator in science, who has been a great mentor and led me in the world of research in fluid dynamics and applied physics. I also want to thank Onur Gökçe and Yuksel Temiz, with whom I had the pleasure to discuss and collaborate with, both in person in Zürich and remotely from Montreal and Sweden. I also had the pleasure of collaborating remotely with Marco Rocca and Marie Laetitia Salva.

Acknowledging everyone I will remember fondly from those five PhD years at Polytechnique is simply impossible, but I want to name a few nonetheless. I would like to thank all members, past and present, of the μ FO lab at Polytechnique with whom I had the pleasure to collaborate, discuss and share experiences. I had the chance to work alongside Amélie St-Georges-Robillard, Dina Dorri, Elena Refet, Rodin Chermat, Pierre Clapperton-Richard, Lucas Aubé, Oscar Boyadjian-Braize, Maeva Bavoux, Étienne Laurent, Robin Guay-Lord, Alexandre R. Brunet, and Nassim Rousset to name a few. I would like to give special thanks to Pierre-Alexandre Goyette and Étienne Boulais, two friends and colleagues I had the pleasure to work with as part of the "PhD trio" at μ FO lab. I would also like to thank François Daoust, Frédéric Monet, Sébastien Loranger, Victor Lambin Iezzi, Pierre Plym, Anthony Roberge, Yannick Cuerno, Arthur Poiffaut, and Gabriel Taillon, past and present graduate members of other laboratories and institutions I had the pleasure to hang out with during my PhD. I want to give a special thank to my close friend Jean-Sébastien Boisvert, with whom I had the pleasure of sharing most of my years at Polytechnique. Our numerous discussions were always interesting and fun, and made those years flow by in an instant.

I am grateful to our IBM collaborators for this opportunity to be working at the frontline of contemporary issues, for which I had the privilege of using my passion for physics to participate in building roads towards solving those challenges. I want to acknowledge financing support from Polytechnique Montreal's graduate Ph.D. fellowship, as well as computational resources from Compute Canada and Calcul Québec. Compute Canada and Calcul Québec are funded by the Canada Foundation for Innovation, the Natural Sciences and Engineering Research Council of Canada, the Department of National Defence, the Ministère de l'Économie, de la Science et de l'Innovation du Québec and the Fonds de Recherche du Québec - Nature et Technologies. Finally, I want to thank all my friends and family for their constant support and encouragements throughout all these years. You made this journey agreeable and forever memorable.

RÉSUMÉ

Les dispositifs microfluidiques et les laboratoires sur puce reposent sur des effets d'échelle dominant dans les dimensions submillimétriques à micrométriques. Par exemple, les forces de surface (e.g., la tension superficielle) dominent par rapport aux forces de volume (e.g., la gravité) à l'échelle submillimétrique. Il s'agit d'un effet souhaitable lors de la conception de microsystèmes capillaires, car les forces de surface sont critiques pour le pompage, l'obtention d'un contrôle supérieur sur le débit et tous les effets capillaires en général. D'autre part, les pertes visqueuses augmentent considérablement plus les systèmes sont miniaturisés, ce qui augmente la pression capillaire requise pour entraîner les fluides. La microfluidique capillaire repose sur cette plage optimale où les forces capillaires dominent sur les forces volumiques et la résistance hydraulique.

L'objectif de cette thèse est de développer des outils analytiques et numériques pour une meilleure conception et optimisation d'éléments microfluidiques capillaires dans le cadre de diagnostics de précision et de sécurité embarquées sur puce. Pour atteindre cet objectif, des cadres théoriques pour de nouveaux phénomènes d'écoulement capillaire sont établis et des outils numériques sont développés pour aider à comprendre et à prédire le comportement des écoulements capillaires dans des microstructures complexes, fournissant ainsi de nouveaux paradigmes pour le fonctionnement et l'optimisation des dispositifs. Ces nouveaux écoulements capillaires comprennent les écoulements auto-coalescents et les écoulements inverses de Washburn, deux types d'écoulement capillaire offrant un contrôle supérieur sur le déplacement des fluides dans les microstructures permettant un transport d'espèces dispersives et réactives plus précis.

Les écoulements auto-coalescents améliorent la résolution spatio-temporelle des réactifs reconstitués sur puce, facilitant les cinétiques biochimiques complexes nécessitant un contrôle précis des distributions de concentration d'un ou plusieurs réactifs. L'auto-coalescence se produit lorsqu'une goutte d'eau est confinée dans une microstructure, étirée le long d'une barrière capillaire, puis se rétracte sur elle-même. L'écoulement à surface libre résultant peut être simplifié en utilisant la propriété d'invariance des équations de Navier-Stokes sous des transformations galiléennes pour régulariser les conditions aux frontières qui sont dynamiques et en montrant que les modules d'auto-coalescence peuvent être approximés par des cellules de Hele-Shaw dans lesquelles les équations de Navier-Stokes sont réduites à un simple écoulement potentiel 2D. Puisque l'équation de Laplace est invariante de sous transformations conformes, c'est-à-dire que les solutions sont équivalentes sous des transformations préservant les angles locaux, des outils de distorsion spatiale conforme sont utilisés pour fournir une solution implicite générale aux écoulements auto-coalescents. Des solutions asymptotiques explicites sont fournies au voisinage de l'interface capillaire mobile, mon-

trant une augmentation linéaire de la vitesse semblable aux écoulements potentiels sur un cylindre infini, et infiniment loin du ménisque, montrant une diminution exponentielle de la vitesse, mathématiquement analogue au phénomène de digitation visqueuse de Saffman-Taylor. La diminution exponentielle de la vitesse est une caractéristique clé de l'auto-coalescence et est fondamentale pour minimiser les effets dispersifs dans les microcanaux.

Les écoulements inverses de Washburn ont été découverts pour la première fois numériquement à l'aide de méthodes de suivi d'interface pour les écoulements multiphasiques, soit la méthode du volume de fluide (VOF pour « Volume Of Fluid ») pour l'évolution de l'interface avec la méthode des volumes finis (FVM pour « Finite Volume Method ») pour la discrétisation spatiale et le modèle de force de surface continue (CSF pour « Continuous Surface Force ») pour la tension superficielle. La modélisation des écoulements capillaires est laborieuse en raison des approximations de la mécanique des milieux continus qui sont erronés à l'échelle moléculaire où se produit le phénomène de mouillage. C'est-à-dire que les interfaces capillaires se déplacent sur les parois solides en raison de la dynamique moléculaire, soit que les molécules se fixent, se détachent et entrent constamment en collision avec le solide, et cela n'est pas pris en compte par la formulation continue de la dynamique des fluides. La solution analytique des équations de Navier-Stokes pour les écoulements dans un coin montre un comportement singulier pour la pression conduisant à des contraintes singulières à l'interface capillaire. Cet effet non physique est également capturé par des méthodes numériques et doit être corrigé correctement lorsque des simulations d'écoulement capillaire sont effectuées.

ABSTRACT

Microfluidic devices and lab-on-chip systems rely on scaling effects dominating in the sub-millimetre to micro-metre range. For instance, surface forces (e.g. surface tension) dominate over volume forces (e.g. gravity) at the sub-millimetre scale. This is a desirable effect when designing capillary-driven microsystems, as surface forces serve as the driving mechanism for pumping, obtaining superior control over the flow, and all capillary effects in general. On the other hand, viscous losses increase significantly the more systems are miniaturized which increases required capillary pressures to drive the flow. Capillary-driven microfluidics relies on this optimal range where capillary forces dominate over volume forces and hydraulic resistance.

The objective of this thesis is to develop analytical and numerical tools for better design and optimization of capillary-driven microfluidic elements in the framework of precision diagnostics and embedded security features on chip. To achieve this objective, theoretical frameworks for novel capillary flow phenomena are established, and numerical tools are developed to help understand and predict capillary flow behaviour in complex microstructures, thereby providing new paradigms for device operation and optimization. Novel capillary flows include self-coalescing and reverse-Washburn flows, two types of flow providing superior control over the flow in microstructures allowing for more accurate mass transport of dispersive and reactive species.

Self-coalescing flows in microstructures enhances the spatiotemporal resolution of reconstituted reagents on chip, facilitating complex bio-chemical kinetics requiring a precise control over the concentration distributions of one or multiple reagents. Self-coalescence occurs when a droplet of water is confined in a microstructure, stretched along a capillary pinning line, and subsequently retracts on itself. This resulting free-surface flow can be simplified by using the invariance property of the Navier-Stokes equations under Galilean transformations to regularize the dynamic boundary conditions and showing that self-coalescence modules can be approximated by Hele-Shaw cells in which the Navier-Stokes equation is reduced to a simple 2D potential flow. Because the Laplace equation is conformally invariant, i.e. solutions are equivalent under transformations preserving local angles, conformal mapping tools are used to provide a general implicit solution to self-coalescing flows. Explicit asymptotic solutions are provided in the vicinity of the moving capillary interface, showing a linear increase in velocity akin to potential flows over an infinite cylinder, and infinitely far from the meniscus, showing an exponential decrease of the velocity mathematically akin to the Saffman–Taylor instability and potential flows over back steps. The exponential decrease in velocity is a key feature of self-coalescence and fundamental in minimizing dispersive effects in microchannels.

Reverse-Washburn flows were first discovered numerically using interface tracking methods for multiphase flows, i.e. the Volume Of Fluid (VOF) method for interface evolution with the Finite Volume Method (FVM) for discretization and the Continuous Surface Force (CSF) model for surface tension modelling. Modelling capillary flows is challenging due to continuum mechanics breaking down at the molecular scale where the phenomenon of wetting occurs. That is, capillary interfaces can move on solid walls because molecules constantly attach, detach, and collide with the solid, and this is not captured by the continuum formulation of fluid dynamics. The analytical solution to the Navier-Stokes equations for corner flows displays a singular behaviour for the pressure in the corner leading to singular stresses at the capillary interface. This non-physical effect is also captured by numerical methods and must be taken correct when capillary flow simulations are conducted.

TABLE OF CONTENTS

DEDICATION	iii
ACKNOWLEDGEMENTS	iv
RÉSUMÉ	v
ABSTRACT	vii
TABLE OF CONTENTS	ix
LIST OF TABLES	xii
LIST OF FIGURES	xiii
LIST OF SYMBOLS AND ACRONYMS	xviii
LIST OF APPENDICES	xxii
CHAPTER 1 INTRODUCTION	1
1.1 Motivation and problems	3
1.1.1 The natural challenges: infectious diseases	3
1.1.2 The human challenge: falsified medicines and diagnostic products	4
1.2 Objectives & thesis outline	4
CHAPTER 2 LITERATURE REVIEW	7
2.1 Modelling in microfluidics	7
2.1.1 Constitutive equations of fluid dynamics	8
2.1.2 Application of conformal mapping to potential flows	11
2.1.3 Taylor-Aris dispersion	16
2.1.4 Capillary effects	17
2.1.5 Calculating the Young-Laplace pressure in complex geometries	18
2.1.6 Washburn flows	20
2.1.7 Concus-Finn criterion	21
2.1.8 Saffman-Taylor viscous fingering	21
2.2 Numerical modelling of capillary flows	22
2.2.1 Modelling interface evolution	24

2.2.2	Modelling surface tension	26
2.2.3	Numerical modelling of capillary flows in this thesis	28
2.3	Thesis Structure	30
CHAPTER 3 SELF-COALESCING FLOWS IN MICROFLUIDICS FOR PULSE-SHAPED DELIVERY OF REAGENTS		
		32
3.1	Introduction	32
3.2	Background : Hele-Shaw approximation in self-coalescence	34
3.3	SC free boundary problem formulation	35
3.4	Numerical solution of the flow inside a SCM	36
3.5	Solving the Schwarz-Christoffel mapping	40
3.6	Asymptotic solutions and self-coalescing flow modes	41
3.6.1	Flow profile far from the meniscus	41
3.6.2	Flow profile far from the meniscus: link with Saffman-Taylor viscous fin- gering	44
3.6.3	Entrance region flow profile	46
3.6.4	Physical interpretation of Self-Coalescence	49
3.7	Additional details regarding the conformal mapping methodology	51
3.7.1	Schwarz-Christoffel mapping numerical solution	51
3.7.2	Defining velocity numerically in the physical frame of reference	52
3.7.3	Solving the parameter problem <i>a posteriori</i>	53
3.7.4	Exact mapping of the SCM with the Schwarzian operator (open problem)	54
3.8	Rapid quantitative assays using SCMs	56
3.8.1	Reactive flows in SCMs	57
3.8.2	Resorufin production from two coupled enzyme reaction cascades	58
3.8.3	Model implementation using finite differences	60
3.9	Conclusion	64
CHAPTER 4 ARTICLE 1: A SIMPLE STATIC CONTACT ANGLE-BASED MESH-DEPENDENCY CORRECTION FOR 3D CAPILLARY FLOW SIMULATIONS		
		67
4.1	Introduction	67
4.2	Numerical methodology	69
4.3	Benchmark case and the mesh-dependency problem	71
4.4	The dynamics of capillary flow	71
4.5	Boundary conditions and mesh-dependent results	72
4.6	Contact angle-based correction and mesh optimization	77
4.7	3D simulation results	78

4.8	Conclusion	80
4.9	Supplementary videos	84
CHAPTER 5 ARTICLE 2: DYNAMICS OF ACCELERATING CAPILLARY FLOW . . .		85
5.1	Introduction	85
5.2	The Dynamics of Capillary Flow	86
5.3	Methodology	88
5.4	Results & Discussion	89
5.5	Conclusion	90
5.6	Appendix	91
5.6.1	Derivation of the Bosanquet and Reverse-Bosanquet equations	91
5.6.2	Digital twins and numerical methodology	92
5.6.3	Derivation of the Washburn and reverse-Washburn equations for a self-coalescence module	93
5.7	Supplementary Material	96
CHAPTER 6 GENERAL DISCUSSION		99
6.1	Self-coalescing flows in microfluidics for pulse-shaped delivery of reagents	99
6.2	A simple static contact angle-based mesh-dependency correction for 3D capillary flow simulations	100
6.3	The dynamics of accelerating capillary flow	100
6.4	Limitations	101
CHAPTER 7 CONCLUSION		105
7.1	Thesis contributions	105
7.2	Future research	105
7.2.1	Towards a complete SC solution	105
7.2.2	Washburn-Reverse-Washburn cycles	106
7.2.3	Customizable flows with electrocapillary-driven microfluidics	106
7.2.4	SCM-based benchmark tests	106
7.2.5	A comparative study between different CFD software packages	107
7.2.6	Full coupling of capillary dynamics with mass transport	107
7.3	Final words	108
REFERENCES		109
APPENDICES		136

LIST OF TABLES

Table 1.1	Scaling laws of typical physical quantities and dimensionless groups in microfluidics with respect to space (length, size, distance, etc.) and time.	2
Table 2.1	Scaling laws of typical dimensionless groups in microfluidics with respect to the length, L_0 , and height, H_0 , of a 2D channel and the physical macroscopic variables of the filling liquid.	10
Table 3.1	Parameter description and values used in COMSOL simulations.	41
Table 3.2	Definition of species and example of initial values.	60
Table 3.3	Diffusion coefficient for the coupled enzymatic reactions from Eq. 3.61-3.71.	61
Table 3.4	Reaction coefficients for the coupled enzymatic reactions from Eq. 3.61-3.71.	61
Table 4.1	Physical parameters for the simulations.	72
Table 4.2	Mesh details for the capillary pump case.	81
Table 5.1	Definition of parameters and variables for a SCM as shown in Fig. 5.2.	94
Table F.1	Vitesses du réseau D2Q9	185
Table F.2	Poids pour le réseau D2Q9	186
Table F.3	Erreur sur le rayon final de deux gouttes qui coalescent et de l'auto-coalescence d'un carré.	188

LIST OF FIGURES

Figure 1.1	Hydrophobic leaf from the Butchart garden on the Island of Vancouver. . .	1
Figure 1.2	Plage à Heist (pointillism) depicting a Kelvin–Helmholtz instability in the clouds.	3
Figure 1.3	Organization of the thesis work.	6
Figure 2.1	Capillary modelling flow chart.	7
Figure 2.2	Flow in a Hele-Shaw cell ($W \gg H$ and $H \rightarrow 0$).	11
Figure 2.3	S-C mapping of the upper half-plane to the semi-infinite strip.	13
Figure 2.4	Z map of a back step.	14
Figure 2.5	The School of Athens (rectangle) mapped into a back step.	15
Figure 2.6	Z map of an inclined back step.	15
Figure 2.7	Contact angles arising from a tri-phase equilibrium point.	18
Figure 2.8	Washburn flow between two parallel plates.	20
Figure 2.9	Liquid pinning on a CPL of edge steepness $\pi - \delta$ and contact angle θ . . .	21
Figure 2.10	Saffman-Taylor viscous fingering resulting from air displacing a spin coated thin film (a Hele-Shaw cell).	22
Figure 2.11	Simulation of a water droplet at equilibrium using VOF-FVM, CSF and interface compression in OpenFOAM.	29
Figure 3.1	Resuspension of printed amaranth dye in a microchannel.	33
Figure 3.2	Experimental resuspension of amaranth dye deposited by inkjet printing in the SCM.	33
Figure 3.3	Fluorescent microspheres (4.8 μm diameter) revealing stagnancy of the flow far from the receding meniscus. (See Video A.15)	34
Figure 3.4	Reference frame change $Z \rightarrow Z^*$ and Schwarz-Christoffel mapping $Z^* \rightarrow \Omega$	37
Figure 3.5	Geometry of the curved meniscus in a SCM.	38
Figure 3.6	Comparison of a uPIV experiment with a 3D Navier-Stokes finite element model and the simplified case of a Hele-Shaw cell using conformal mapping for different number of vertices N	42
Figure 3.7	Comparison of the asymptotic exponential velocity decay when far from the meniscus with the conformal mapping solution and experimental uPIV.	44
Figure 3.8	Numerical (dash-dot) and asymptotic (dot) solutions of the orthogonal velocity in the SCM as a function of position along the CPL for various contact angles θ_w and $\lambda = 0.5$	45

Figure 3.9	Filling of a SCM observed in fluorescence with a mirror symmetry at the lower boundary (left) and oil STVF in glycerin.	46
Figure 3.10	Different analytical maps providing an exponential velocity decay far from the inlet with characteristic decay lengths proportional to W/π	47
Figure 3.11	Self-similarity of the velocity near the origin with respect to λ with constant r	48
Figure 3.12	Comparison between the orthogonal flow profile within the SCM (blue solid line) and the flow over a cylinder (black dashed line) with identical radii.	49
Figure 3.13	Linear asymptote near the origin and exponential asymptote far from the meniscus. Comparison with the quasi-analytic S-C solution and experimental uPIV.	50
Figure 3.14	Numerical domain of the SCM.	52
Figure 3.15	Convergence of α and \tilde{A} with respect to the domain length L and number of vertices N	54
Figure 3.16	Schematic of resorufin production from two coupled enzyme reaction cascades.	59
Figure 3.17	Time step throughout a simulation.	62
Figure 3.18	Spatial and temporal evolution of species from initially spotted region.	65
Figure 4.1	Benchmark case of spontaneous imbibition in a 2D rectangular microchannel.	71
Figure 4.2	Volume fraction as a function of time for the benchmark case with $\theta = 60^\circ$	74
Figure 4.3	Evaluated Washburn characteristic time as a function of mesh size for the benchmark case with $\theta = 60^\circ$	74
Figure 4.4	Normalized stress on the walls $\ \tau_{xy}\ $ with respect to the mesh size Δ near the contact line.	75
Figure 4.5	Evaluated Washburn characteristic time normalized with respect to $\cos \theta$ as a function of the mesh size Δ and the contact angle θ	75
Figure 4.6	Evaluated Washburn characteristic time normalized with respect to $\cos \theta$ as a function of the mesh size Δ for different partial slip values f	76
Figure 4.7	Correction procedure for the 2D rectangular microchannel benchmark case with $\theta = 60^\circ$	79
Figure 4.8	Corrected contact angle $\theta_{\text{corr}}(i = 2)$ with respect to the mesh size Δ for different physical contact angles θ	80

Figure 4.9	Top view of a self-coalescence module schematic (a) in the initialization stage (t_1) and self-coalescence stage (t_2), cross-sectional view of the schematic (b) and simulation snapshots (c) taken at $t = 35$ ms, 85 ms and 122 ms.	81
Figure 4.10	Capillary filling of the self-coalescence module (a) without correction, and (b) with correction.	82
Figure 4.11	Top view of a capillary pump schematic (a) and simulation snapshots (b) taken at $t = 21$ ms (left) and 64 ms (right).	82
Figure 4.12	Capillary filling of a capillary pump (a) without correction, and (b) with correction.	83
Figure 4.13	Water volume fraction of a filling SCM. (Flash Player required)	84
Figure 4.14	Water volume fraction of a filling capillary pump. (Flash Player required)	84
Figure 5.1	Schematic of a filling capillary of arbitrary cross-sectional shape, cross-sectional area \mathcal{A} and length L	88
Figure 5.2	Brightfield image of the self-coalescence module (a) using the microscope at an angle of 45° , self-coalescence module schematic in the Washburn and R-W regimes ((b) at t_1 and t_2 respectively) and cross-section of the device along the capillary pinning line (c).	89
Figure 5.3	Side-by-side comparison of experiments (a) and simulations (b).	91
Figure 5.4	Superposition of the experimental (red), numerical (blue) and theoretical (black) results for a Washburn- Reverse-Washburn cycle in a capillary structure.	95
Figure 5.5	Brightfield image of the chip with a focus on the chip's inlet (top) and outlet valve (bottom).	96
Figure 5.6	Brightfield image of the entire chip with control channels (high inlet hydraulic resistance on the right side).	97
Figure 5.7	Chip placed on the loading pad.	97
Figure 5.8	Experimental setup for pipetting under a microscope.	97
Figure 5.9	Experimental data sets for DI water (a) and the glucose solution (b).	98
Figure 6.1	Spurious currents as a fonction of cell size for different contact angles with interFoam (VOF-FVM) and compressive CSF.	102
Figure 6.2	Schematic of the formation of a bubble in SCMs (a), and numerical results of the width of the bubble with respect to time (b) using VOF-FVM with the compressive CSF model.	103

Figure 6.3	Simulation snapshots of (a) a SCM without diversion barrier, and (b) design of a SCM in the shape of an Archimedean spiral with the "bubble" shape made evident when self-coalescence occurs.	104
Figure A.1	Description and modelling of self-coalescence in a microchannel.	138
Figure A.2	SCM for reagent reconstitution.	141
Figure A.3	Scalability of SCMs.	142
Figure A.4	Reagent pulse shaping and generation of complex concentration profiles.	143
Figure A.5	Biochemical reactions in SCMs.	145
Figure A.6	Characterization of reagent dissolution in SCMs and control experiments.	154
Figure A.7	Fabrication steps for SCMs with depressed barriers, and scanning electron microscopy images of representative SCMs.	155
Figure A.8	SCM volume scaling experiments.	156
Figure A.9	Assessment of the stability of the leading barrier.	157
Figure A.10	Predicted complex concentration profiles from diffusion–dispersion models.	158
Figure A.11	Release of reconstituted reagents from a SCM with time delays.	159
Figure A.12	Optimization and calibration of RPA reactions in SCMs.	159
Figure A.13	Characterization of dissolution of multiple reagents in SCMs.	160
Figure A.14	Experimental setup.	161
Figure A.15	Fluorescent microspheres revealing the streamlines of a self-coalescing flow.	162
Figure A.16	Reagent reconstitution in a SCM.	162
Figure A.17	Self-coalescence and Saffman–Taylor viscous fingering.	163
Figure A.18	Reagent transport inside a SCM.	166
Figure D.1	Validation of the EMS code by comparing results to simplified models.	176
Figure F.1	Coalescence de deux gouttes avec la LBM (fonction de couleur).	189
Figure F.2	Fonction de couleur d'un carré auto-coalescent.	190
Figure F.3	Erreur en fonction de la taille du maillage pour la simulation de deux gouttes qui coalescent.	191
Figure F.4	Erreur en fonction de la taille du maillage pour la simulation de l'auto-coalescence d'un carré.	191
Figure G.1	Schéma	195
Figure G.2	Fraction de volume dépendante en fonction du maillage.	196
Figure G.3	Augmentation de la constante de temps de Washburn en fonction du maillage.	196
Figure G.4	Quasi-invariance des résultats en fonction de la discrétisation en temps limitée par le nombre de Courant.	197

Figure G.5	Mesure de la pression pour différents maillages en un point fixe dans l'espace.	198
Figure G.6	Schéma du choix d'un intervalle δt pour calculer le temps moyen et la pression moyenne (\bar{t}, \bar{p})	198
Figure G.7	Profil de pression moyenné sur différents intervalles temporels.	199
Figure G.8	Pression au ménisque en fonction du moyennage temporel pour différents maillages.	200
Figure G.9	Schéma du choix d'un intervalle δt centré sur p_m pour calculer le temps moyen et la pression moyenne (\bar{t}, \bar{p})	200
Figure G.10	Profil de pression moyenné sur différents intervalles temporels centrés sur p_m	201
Figure G.11	Pression au ménisque en fonction du moyennage temporel avec la méthode centrée sur p_m pour différents maillages.	201
Figure G.12	Pression de Laplace calculée avec les deux méthodes et comparaison avec la valeur théorique.	203
Figure G.13	Vitesse moyennée à l'entrée du canal microfluidique.	203
Figure G.14	Résistance hydraulique en fonction du maillage comparée à la valeur théorique.	204
Figure G.15	Constante de temps de Washburn simulée comparée aux erreurs de discrétisation et de modélisation (résistance hydraulique et pression de Laplace).	205
Figure G.16	Substitution des valeurs calculés dans l'équation de Washburn et comparaison entre la constante de Washburn calculée et simulée.	205
Figure H.1	Spurious currents for a droplet of water. (Flash Player required)	207
Figure H.2	Execution time with respect to the physical simulation time t_{end}	208
Figure H.3	Execution time with respect to surface tension γ with $\gamma_0 = 0.072 \text{ N m}^{-1}$	208
Figure H.4	Execution time with respect to density ρ with $\rho_0 = 1000 \text{ kg m}^{-3}$	209
Figure H.5	Execution time with respect to viscosity $\nu = \mu/\rho$ with $\mu_0 = 0.001 \text{ Pa} \cdot \text{s}$	209

LIST OF SYMBOLS AND ACRONYMS

ALE	Arbitrary Lagrangian-Eulerian
BioMEMS	Biomedical Microelectromechanical Systems
CAD	Computer-Aided Design
CF	Concus-Finn
CFD	Computational Fluid Dynamics
CPL	Capillary Pinning Line
CSF	Continuum Surface Force
CSS	Continuum Surface Stress
DI	Deionized (water)
E-E	Euler-Euler
E-L	Euler-Lagrange
FD	Finite Difference
FDM	Finite Difference Method
FE	Finite Element
FEM	Finite Element Method
FT	Front Tracking
FTCS	Forward Time Centered Space
FV	Finite Volume
FVM	Finite Volume Method
LB	Lattice Boltzmann
LBM	Lattice Boltzmann Method
LOCD	Lab-On-Chip Devices
LS	Level-Set
MAC	Marker And Cell
MEMS	Microelectromechanical Systems
MLBM	Multiphase Lattice Boltzmann Method
MPLIC	Multicut PLIC
NS	Navier-Stokes
NTP	Normal Temperature and Pressure
OpenFOAM	open source Field Operation And Manipulation
PIMPLE	PISO-SIMPLE
PISO	Pressure-Implicit with Splitting of Operators
PIV	Particle Image Velocimetry

PLIC	Piecewise Linear Interface Calculation
POCD	Point-of-Care Diagnostics
PPIC	Piecewise Parabolic Interface Calculation
R-B	Reverse-Bosanquet
R-W	Reverse-Washburn
RDT	Rapid Diagnostic Test
S-C	Schwarz–Christoffel
SC	Self-Coalescence
SCM	Self-Coalescence Module
SIMPLE	Semi-Implicit Method for Pressure Linked Equations
SLIC	Simple Line Interface Calculation
SSF	Sharp Surface Force
STVF	Saffman-Taylor Viscous Fingering
TAD	Taylor-Aris Dispersion
UHP	Upper Half-Plane
VOF	Volume Of Fluid
WRW	Washburn-Reverse-Washburn (cycles)

δF	Variation in total Helmholtz free energy
δF_S	Variation in surface energy
δF_{pV}	Variation in pressure-volume energy
$\Delta p, \Delta p_S$	Young-Laplace pressure drop
δV	Variation in volume
Δ	Mesh size
ℓ	Arbitrary length
Γ	Domain boundary
γ, σ	Surface tension
κ	Curvature
λ	CPL position
\mathbb{C}	Complex numbers
\mathbb{N}	Natural numbers
\mathbb{N}^*	Natural numbers (excluding zero)
\mathbb{R}	Real numbers
μ, η	Viscosity
ω	Complex UHP coordinates
Ω	Complex UHP domain
Ω	Domain
ω_n	Complex UHP vertices
\bar{V}	Complex velocity
\bar{V}^*	Complex velocity in the Galilean reference frame
$\partial\Omega$	Domain bounds
ϕ_f	Flux across a given cell surface
Ψ	Complex potential
ρ	Density
τ	Time constant
τ_W	Washburn time constant
τ_{RW}	Reverse-Washburn time constant
\mathbf{F}_γ	Surface tension body force
\mathbf{n}_f	Unit vector of a given cell surface
\mathbf{u}	Velocity field
\mathbf{x}	Position vector
θ, θ_w	Contact angle
θ_{corr}	Corrected contact angle
θ_{num}	Numerical contact angle

θ_c	Critical contact angle
$\tilde{\xi}$	Dimensionless effective displacement
\tilde{t}	Dimensionless time
\tilde{x}	Dimensionless position, displacement
ξ	Effective displacement
$\ \tau_{xy}\ $	Wall stress module
C_γ	Compression factor
D	Diffusion coefficient
F	Helmholtz free energy
$G(\Delta)$	Correction function
H	Height
k, K	Reaction coefficients
L	Length
L_c	Characteristic length
p	Pressure
p_m, p_{cap}	Meniscus pressure, capillary pressure
Q	Flow rate
R_{hyd}	Hydraulic resistance
S_f	Surface area of a given cell surface
t	Complex bi-infinite strip coordinates
T	Complex bi-infinite strip domain
t	Time
t_n	Complex bi-infinite strip vertices
U	Velocity
U_m	Meniscus velocity
W	Width
x	Position, displacement
z	Complex Cartesian coordinates
z^*	Complex Cartesian coordinates in the Galilean reference frame
Ca	Capillary number
Co	Courant number (also known as CFL condition)
Kn	Knudsen number
La	Laplace number
Pé	Péclet number
Re	Reynolds number
We	Weber number

LIST OF APPENDICES

Appendix A	Self-Coalescing Flows in Microfluidics for Pulse-Shaped Delivery of Reagents	136
Appendix B	Saffman–Taylor instability	172
Appendix C	Conservation of mass and momentum for a continuum	174
Appendix D	EnzModSimulator code validation	176
Appendix E	EnzModSimulator input file example	180
Appendix F	Multiphase lattice Boltzmann method implementation (in French) / Implé- mentation de la méthode de Boltzmann sur réseau.	182
Appendix G	Heuristic proof and decoupling of modelling and discretization errors for capillary dynamic simulations with moving contact lines in microfluidic channels (in French) / Preuve heuristique et découplage des erreurs de mod- élisation et de discrétisation pour des simulations de dynamique capillaire avec ligne de contact en mouvement dans un canal microfluidique.	192
Appendix H	Parametric analysis of spurious currents in OpenFOAM (VOF-FVM with compressive CSF)	207

CHAPTER 1 INTRODUCTION

Capillary phenomena can be observed in everyday life such as dew drops on leaves observed after the rain or in the morning after a clear night (Fig. 1.1), or droplets of water coalescing and splitting on the window of a moving train. The formal study of liquid movement at submillimetre-scales has its origin tracing back to Pierre Simon de Laplace (1749-1827) and Thomas Young (1773-1829) [1, 2] with experiments dating back to the early 18th century [3, 4]. However, it took until the early 1990s, with the prior advent of micro and nanotechnology^{1,2}, for applied microfluidics to emerge. A key feature of microfluidics is the effects of scaling laws at the submillimetre scale (Tab. 1.1). Because surface forces scale as L^2 and volume forces scale as L^3 , surface forces generally dominate over volume forces at submillimetre scales. For instance, this is the case for gravity and surface tension. As a result, we can engineer capillary-driven systems impossible to design at larger scales. Limits at the other end of the scale also exist. Hydraulic resistance increases as L^{-4} which limits how small devices can be engineered from physical limits, e.g. increase in required driving pressures, or functional limits, e.g. cell damage due to high shear stresses in microchannels. Hence, “There’s Plenty of Room at the Bottom” should be rephrased for microfluidics as “There’s an Optimal Amount of Room at the Bottom”.



Figure 1.1 Hydrophobic leaf from the Butchart garden on the Island of Vancouver.³

From a first principle point of view, liquids can be represented as discrete particles, i.e. atoms and

¹Physicist and Nobel laureate Richard P. Feynman gave a seminal nanotechnology lecture entitled “There’s Plenty of Room at the Bottom” at an American Physical Society meeting at Caltech on December 29, 1959. This lecture is renowned by some to be the starting point that seeded the concept of nanotechnology.

²First termed as such by Norio Taniguchi in 1974.

³Courtesy of Thomas Gervais, 2022.

Table 1.1 Scaling laws of typical physical quantities and dimensionless groups in microfluidics with respect to space (length, size, distance, etc.) and time.

Time	L^0	T^1	Capillary displacement (Eq. 4.10)	$L^{1/2}$	$T^{1/2}$
Distance	L^1	T^0	Capillary velocity	$L^{1/2}$	$T^{-1/2}$
Area	L^2	T^0	Capillary acceleration	$L^{1/2}$	$T^{-3/2}$
Volume	L^3	T^0	Washburn time (Eq. 4.11)	L^1	T^0
Velocity	L^1	T^{-1}	SC velocity decay length (Eq. 3.29)	L^1	T^0
Acceleration	L^1	T^{-2}	Diffusion time (Eq. A.10)	L^2	T^0
Hydrostatic pressure (Eq. 5.2)	L^1	T^0	Young-Laplace pressure (Eq. 4.9)	L^{-1}	T^0
Critical contact angle (Eq. 4.13)	L^0	T^0	Hydraulic resistance (Eq. 5.2)	L^{-4}	T^0
Reynolds number (Eq. 4.12)	L^2	T^{-1}	Capillary number (Eq. 4.12)	L^1	T^{-1}
Webber number (Tab. 2.1)	L^3	T^{-2}	Péclet number (Tab. 2.1)	L^2	T^{-1}
Laplace number (Eq. 5.6)	L^1	T^0	Courant number (Eq. 2.73)	L^0	T^0

molecules, interacting through a given potential, e.g. Lennard-Jones potential [5, 6], varying as a function of distance between the particles. Assuming a large number of particles is modelled, a statistical representation of the system can be given using the Boltzmann equation [7]. This equation represents the temporal evolution of the entire 6-dimensional phase space, containing the set of all possible positions and momenta in 3 dimensions, of probability density functions describing the probability of finding particles in the phase space. Lastly, in the same way a pointillism painting turns into an image with non discernable dots when viewed from afar (Fig. 1.2), the behaviour of particles may be volume-averaged from which arise a continuum⁴ of macroscopic variables, e.g. velocity, density, and viscosity, evolving in time as described by the Navier-Stokes transport equations [8, 9]. Capillary dynamics can be modelled using all the previously mentioned levels of approximation [10], and different analytical and numerical methods to achieve this will be presented throughout this thesis.

Applications of microfluidics range from thermal and chemical process engineering [12–14], microreactors [15–17], lab-on-a-chip devices (LOCD) and BioMEMS [18–21], biology and medicine [19, 22, 23], and security features embedding on chip [24–27] to name a few. With advances in analytical, numerical, and manufacturing techniques in microtechnology, applied microfluidics for analysis has now reached enough maturity to be highly driven by applications and problem-oriented agendas [28, 29].

⁴If you are reading this on a screen, you are actively approximating discrete particles (pixels) as a continuum.

⁵Plage à Heist is a painting by the Belgian artist Georges Lemmen (1865–1916). (Georges Lemmen, Public domain, via Wikimedia Commons)

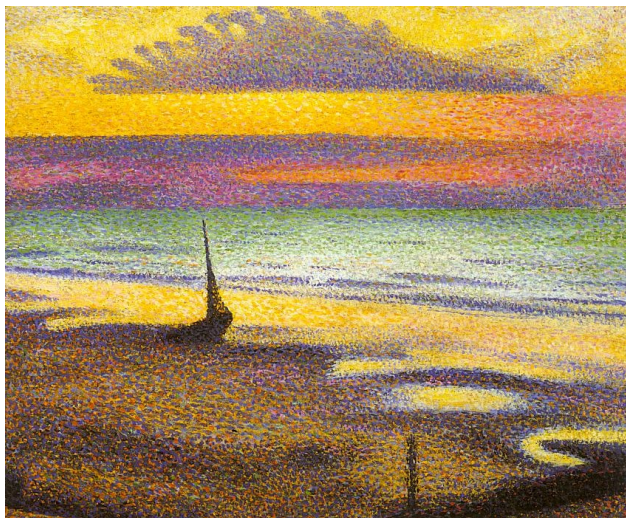


Figure 1.2 Plage à Heist⁵(pointillism) depicting a Kelvin–Helmholtz instability [11] in the clouds.

1.1 Motivation and problems

1.1.1 The natural challenges: infectious diseases

The 21st century has already seen several infectious disease outbreaks [30] including the 2003 severe acute respiratory syndrome (SARS) coronavirus, the 2009 swine flu pandemic caused by the H1N1 influenza virus, the 2012 Middle East respiratory syndrome (MERS) coronavirus outbreak, the 2013–2016 Western African Ebola virus epidemic, the 2015–2016 Zika virus epidemic, and not least the COVID-19 pandemic.

Globally, as of July 2022, there has been more than half a billion confirmed cases of COVID-19, including more than 6.4 million deaths, reported to the World Health Organization (WHO) [31]. Diagnostic testing for SARS-CoV-2 has been central in identifying COVID-19 cases as well as reducing transmission. Diagnostic testing methods now include at least 400 RDTs that are commercially available worldwide [32].

In 2010 and 2016, infectious diseases claimed 15 and 8.2 million lives worldwide, respectively, and two-thirds of them were caused by only 20 different diseases [33, 34]. Estimates suggest that we could save more than 1.2 million lives annually with the accessibility of point-of-care diagnostics (POCDs) in resource-limited regions for the screening of only 4 different infectious diseases [35]. Recent estimates show that precise and effective diagnosis could eradicate 90% of the current global malaria threat by 2030 [36]. This is one of several factors responsible for the increase in public and private awareness and funding of POCDs [37]. A 2022 report from Research and Markets projects that the global market for POCDs and RDTs will grow from USD 43.2 billion as of 2022 to USD

72.0 billion by 2027 [38]. This trend is also exacerbated by key factors such global increases in respiratory disease cases, e.g. COVID-19 and influenza, and improved access to POCDs through online platforms [39, 40].

1.1.2 The human challenge: falsified medicines and diagnostic products

Sadly, this growing market also attracts criminals producing counterfeited and defect goods for lucrative reasons. The World Health Association (WHO) estimated in 2010 that more than 8% of POCDs and rapid diagnostic tests (RDTs) were counterfeited with a rising trend as the market for POCDs and RDTs increases [41, 42]. In that same year, global healthcare fraud costs were estimated to USD 260 billion [43] including counterfeit drugs [44, 45]. This is worst in resource-limited regions such as Africa. For example, malaria RDTs were sold for syphilis screening tests in Mozambique, counterfeited malaria rapid tests were sold in the South African Republic and HIV RDTs with tempered expiry date were sold in the Democratic Republic of the Congo [46]. Furthermore, WHO estimated that up to 50% of consumed medicines in developing countries are counterfeited. Counterfeiting of tests for COVID-19 [47, 48], Ebola [49], malaria [41, 46], tuberculosis [46], HIV [50, 51], glucose control [46, 52] and pregnancy [46, 53] were observed to name a few.

Counterfeited products can cause serious health problems and even death. In response, there has been an increase in research and development in the past few years for new anti-counterfeit technologies for medical devices and pharmaceuticals [54–56]. Some examples are QR-codes written by lithography [24, 57], DNA-QR codes [58], moirés security features [59] and high-content optical codes embedded in microchannels [26].

In summary, motivation for this work is two-fold: capillary dynamics can help design 1) precise microfluidic-based POCD tests that are vital to detect and combat infectious diseases worldwide, and 2) novel security features on diagnostic tests to combat the recently observed proliferation of tests counterfeiting. Analytical and numerical analysis of free-surface flows using computational fluid dynamics (CFD) tools and analytical methods provides us with an understanding of the key features of capillary flows, a vital part for further optimization and technological innovation in those two areas.

1.2 Objectives & thesis outline

Capillary-driven microfluidic systems are paramount when optimizing, designing and developing autonomous microfluidic systems [60]. For instance, they are vital in implementing autonomous immunoassays with superior control over the flow signal sensing, and they allow easy splitting of

samples into smaller volumes for multiplexing [20]. Capillary dynamics can also be used for the implementation of crypto-anchors [61, 62], highly secure digital fingerprints embedded in products, for the security of POCDs and RDTs using high resolution resuspension of spotted dyes in microstructures [63]. Crypto-anchors can take many forms, such as optical codes, tiny computers or shade of magnetic inks that can authenticate products' originality, their content and if they have been used before.

Analytical and numerical modelling can be used to predict experimental results, reduce the need for costly and time-consuming experiments, develop proof of concepts and design rules, and understand the physical principles behind observed phenomena. Analytical modelling provides direct relationships between all variables of a given system based on underlying physics principles. However, it is challenging to predict exact experimental results with analytical methods. On the other hand, numerical methods can be used to solve complex systems more akin to experimental conditions. However, only one set of conditions may be analysed at a time and numerical methods do not provide a direct relationship between physical variables and physics.

With an approach from physics, we can develop new microfluidic elements that can be added to the vast microfluidics library. These devices can provide increased control over the flow and mass transport in microfluidic devices. In this thesis, I develop a framework for both analytical and numerical modelling of capillary processes, and describe how these methods can be used to discover and characterize new types of flows and engineer new generations of microfluidic elements. The outline of the thesis is presented in Fig. 1.3, and the main objectives are as follow:

- Understand and characterize newly discovered self-coalescing flows, which allows reagent reconstitution with minimal dispersion;
- Develop a numerical framework for modelling complex capillary driven flows in microstructures, which can be used as a tool to predict behavior of liquids in microsystems and optimize their design where analytical tools are limited;
- Predict, understand, and characterize Reverse-Washburn flows, a new capillary flow regime which provides enhanced control over passive flows in microchannels.

To achieve these objectives, the development of analytical and numerical tools is conducted to provide design rules and optimize devices operation with respect to flow control and mass transport of diffusive and reactive species in microstructures. More specifically, 1) self-coalescence is characterized and modelled, which can be used to increase spatiotemporal resolutions of reconstituted reagents deposited by inkjet printing in microstructures, 2) complex capillary flows can be modelled precisely using a numerical contact angle correction, which helps understand, predict, and

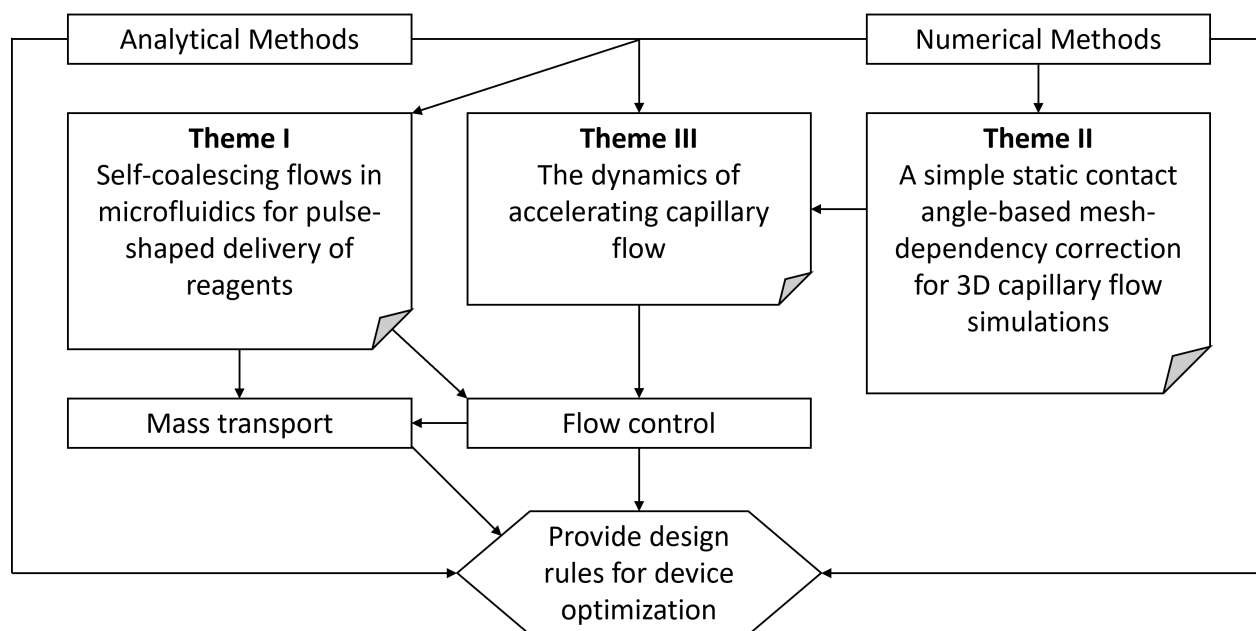


Figure 1.3 Organization of the thesis work. The central research objective of this thesis is to predict, characterize, and better understand capillary flows through modelling for optimization and design of devices providing enhanced control over the flow and accurate mass transport of diffusive and reactive species.

characterise capillary flows in cases where analytical tools cannot, and 3) numerical modelling is used to discover and characterise a new type of capillary flow, and the theoretical framework is developed.

CHAPTER 2 LITERATURE REVIEW

The following literature review is split in two main sections: 1) a review of important notions in microfluidics, capillary dynamics, and mass transport relevant for this work in Section 2.1, and 2) a review of capillary flow modelling using numerical methods in Section 2.2. A brief summary of the thesis structure is also provided in Section 2.3 with important acknowledgments for some of the work in this thesis.

2.1 Modelling in microfluidics

In this section, we describe important notions of theoretical microfluidics and methods for analytical and numerical analysis. Modelling in capillary dynamics can be summed up as presented in Fig. 2.1. Herein, we focus on applied numerical and analytical methods for continuum mechanics. Although, statistical and atomistic methods are briefly discussed in Section 2.2 and Appendix F. We first lay down the general constitutive equations of fluid dynamics and mass transport in Section 2.1.1 as well as relevant dimensional analyses (Section 2.1.1) that can be used to simplify these equation (Section 2.1.1). Applications of conformal mapping to potential flows, critical for the theoretical framework developed in Chapter 3, is introduced in Section 2.1.2, and important notions of capillary dynamics and capillary pinning on sharp edges are presented in Sections 2.1.4-2.1.7.

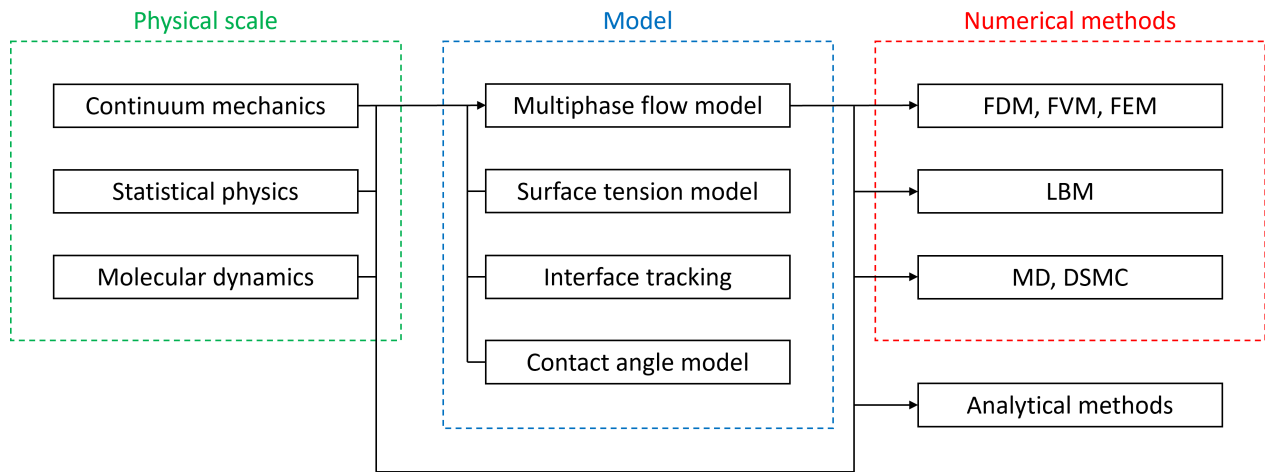


Figure 2.1 Capillary modelling flow chart.

2.1.1 Constitutive equations of fluid dynamics

In physics, the continuity equation is a mathematical expression that describes local conservation laws. In other words, it expresses how much of some physical quantity there is in a bounded region and how it is transported. Let us take for example an arbitrary extensive physical parameter Φ in a volume Ω bounded by a surface $\partial\Omega$. The total amount of Φ in Ω at a fixed time is the sum of the intensive parameter φ (units of Φ per unit of volume) all over the domain. Thus expressed as

$$\Phi = \int_{\Omega} \varphi d\Omega \quad (2.1)$$

This physical quantity is transported within a velocity field \mathbf{u} , and some of that quantity is created and annihilated at a rate s (units of φ per second) within Ω . Therefore, the variation of Φ through time is the rate at which it is transported in and out of Ω added to the rate at which the quantity is created and annihilated. Put in mathematical terms, the temporal variation of Φ is

$$\frac{\partial\Phi}{\partial t} = - \underbrace{\oint_{\partial\Omega} \varphi \mathbf{u} \cdot d\mathbf{S}}_{\text{transported}} - \underbrace{\int_{\Omega} s d\Omega}_{\text{created/annihilated}} \quad (2.2)$$

where $d\mathbf{S}$ is the infinitesimal surface vector. From the divergence theorem, this can be rewritten as

$$\frac{\partial\Phi}{\partial t} = - \int_{\Omega} \nabla \cdot (\varphi \mathbf{u}) d\Omega - \int_{\Omega} s d\Omega \quad (2.3)$$

and from Reynolds transport theorem

$$\int_{\Omega} \left(\frac{\partial\varphi}{\partial t} + \nabla \cdot (\varphi \mathbf{u}) + s \right) d\Omega = 0 \quad (2.4)$$

For the integral to be zero, the integrand has to be zero. Thus, the general continuity equation

$$\frac{\partial\varphi}{\partial t} + \nabla \cdot (\varphi \mathbf{u}) + s = 0 \quad (2.5)$$

Special cases of the continuity equation commonly used in fluid mechanics are the conservation of mass, momentum, and energy. Derivations of those the mass and momentum equations are provided in Appendix C.

For an incompressible isothermal Newtonian fluid with no mass source, the Navier-Stokes equation simplify to

$$\nabla \cdot \mathbf{u} = 0 \quad (2.6)$$

$$\rho \left(\frac{\partial \mathbf{u}}{\partial t} + \mathbf{u} \cdot \nabla \mathbf{u} \right) = -\nabla p + \mu \nabla^2 \mathbf{u} + \mathbf{f} \quad (2.7)$$

where p is the pressure, \mathbf{f} is an external momentum source term, e.g. gravity and surface tension, ρ is the density of the fluid and μ is its viscosity. The transport of reactive and diffusive species is described by

$$\frac{\partial C}{\partial t} = \nabla \cdot (D \nabla C) - \nabla \cdot (\mathbf{u} C) + R \quad (2.8)$$

where C is the concentration, D the diffusion coefficient, and R is a reaction term. Commonly encountered reaction terms in enzymatic reactions and lateral flow immunoassays are obtained from first and second order kinetics, and Michaelis-Menten kinetics [64].

Dimensionless forms of transport equations

It is useful to think of fluid dynamics in terms of dimensionless groups to understand and predict outcomes of complex systems with leading scaling laws. Introducing surface tension and gravity in the Navier-Stokes equation, we obtain

$$\rho \left(\frac{\partial \mathbf{u}}{\partial t} + \mathbf{u} \cdot \nabla \mathbf{u} \right) = -\nabla p + \mu \nabla^2 \mathbf{u} + \rho \mathbf{g} + \sigma \kappa (\nabla \alpha) \quad (2.9)$$

where \mathbf{g} is the gravitational acceleration vector, and $\sigma \kappa (\nabla \alpha)$ is a continuum formulation for modelling surface tension [65] with κ being the curvature of a multiphase field α , and σ is the surface tension¹.

Buckingham's theorem [66, 67] indicates that the system may be described by a combination of 3 dimensionless groups. Adimensionalizing the Navier-Stokes equation with the following dimensionless parameters:

$$\mathbf{x} = L_0 \tilde{\mathbf{x}}, \quad \mathbf{u} = U_0 \tilde{\mathbf{u}}, \quad t = \frac{L_0}{U_0} \tilde{t}, \quad p = \frac{\mu U_0}{L_0} \tilde{p}, \quad \nabla = \frac{\tilde{\nabla}}{L_0}, \quad \kappa = \frac{\tilde{\kappa}}{L_0}, \quad \mathbf{g} = g \tilde{\mathbf{g}} \quad (2.10)$$

we obtain the following equivalent dimensionless Navier-Stokes equation:

$$\text{Re} \left(\frac{\partial \tilde{\mathbf{u}}}{\partial \tilde{t}} + \tilde{\mathbf{u}} \cdot \tilde{\nabla} \tilde{\mathbf{u}} \right) = -\tilde{\nabla} \tilde{p} + \tilde{\nabla}^2 \tilde{\mathbf{u}} + \text{St}^{-1} \tilde{\mathbf{g}} + \text{Ca}^{-1} \tilde{\kappa} (\tilde{\nabla} \alpha) \quad (2.11)$$

$$\text{We} \left(\frac{\partial \tilde{\mathbf{u}}}{\partial \tilde{t}} + \tilde{\mathbf{u}} \cdot \tilde{\nabla} \tilde{\mathbf{u}} \right) = \text{Ca} (-\tilde{\nabla} \tilde{p} + \tilde{\nabla}^2 \tilde{\mathbf{u}}) + \text{Bo} \tilde{\mathbf{g}} + \tilde{\kappa} (\tilde{\nabla} \alpha) \quad (2.12)$$

where the dimensionless groups are defined in Tab. 2.1. Adding mass transport of diffusive and

¹Many other formulations exist to introduce surface tension effects, we selected this one specifically because of its relevance to the current work.

reactive species to the picture, an additional dimensionless group is needed. Introducing

$$C = C_0 \tilde{C}, \quad R = \frac{C_0 U_0}{L_0} \tilde{R} \quad (2.13)$$

we obtain the following dimensionless convection-diffusion-reaction equation:

$$\frac{\partial \tilde{C}}{\partial \tilde{t}} = \tilde{\nabla} \cdot (\text{Pé}^{-1} \tilde{\nabla} \tilde{C}) - \tilde{\nabla} \cdot (\tilde{\mathbf{u}} \tilde{C}) + \tilde{R} \quad (2.14)$$

Table 2.1 Scaling laws of typical dimensionless groups in microfluidics [68] with respect to the length, L_0 , and height, H_0 , of a 2D channel and the physical macroscopic variables of the filling liquid. Typical values for systems filling with water and small ions diffusing in water at normal temperature and pressure (NTP) in microfluidics: $L_0 = 1 \text{ cm}$, $H_0 = 50 \mu\text{m}$, $U_0 = 1 \text{ mm s}^{-1}$, $\rho = 1000 \text{ kg m}^{-3}$, $\mu = 1 \text{ mPas}$, $\sigma = 72.9 \times 10^{-3} \text{ J m}^{-2}$. $D = 2 \times 10^{-9} \text{ m}^2 \text{ s}^{-1}$.

Number	Symbol	Definition	Value	Relation
Reynolds	Re	$\frac{\rho U_0 H_0^2}{\mu L_0}$	2.5×10^{-4}	$\frac{\text{inertial force}}{\text{viscous force}}$
Capillary	Ca	$\frac{\mu U_0}{\sigma}$	1.4×10^{-5}	$\frac{\text{viscous force}}{\text{surface tension}}$
Webber	We	Re · Ca	3.4×10^{-9}	$\frac{\text{inertial force}}{\text{surface tension}}$
Laplace	La	$\frac{\text{Re}}{\text{Ca}}, \frac{\text{Re}^2}{\text{We}}$	1.8×10^1	$\frac{\text{inertia*surface tension}}{\text{momentum transport}}$
Bond	Bo	$\frac{\rho g H_0^2}{\sigma}$	3.4×10^{-4}	$\frac{\text{gravity}}{\text{surface tension}}$
Stokes	St	$\frac{\text{Ca}}{\text{Bo}}$	4.1×10^{-2}	$\frac{\text{viscous force}}{\text{gravity}}$
Schmidt	Sc	$\frac{\mu}{\rho D}$	5.0×10^2	$\frac{\text{momentum diffusion}}{\text{molecular diffusion}}$
Péclet	Pé	Re · Sc	1.3×10^{-1}	$\frac{\text{convection}}{\text{diffusion}}$

Simplification of the Navier-Stokes equations

Because of scaling effects in microfluidics, inertial and gravitational effects are negligible with respect to viscous in surface tension effects and the Reynolds and Bond numbers are generally very small. Furthermore, when looking for a single-phase flow solution where capillarity acts as a pressure boundary condition, we may also neglect capillary effects from the momentum equation (provided boundary conditions are treated accordingly). Thus, neglecting inertial, and gravitational,

and capillary effects in Eq. 2.11 and looking for a stationary flow solution, we obtain the (time-independent) Stokes flow equation:

$$\nabla p = \mu \nabla^2 \mathbf{u} \quad (2.15)$$

In cases where the flow is confined in a structure that is much thinner than it is wide, e.g. infinite parallel plates separated by an infinitesimally small gap $H \rightarrow 0$ along the z -axis, also known as a Hele-Shaw cell [69], we may assume that the pressure gradient along the same axis vanishes to zero, as per the lubrication theory [70]. This simplifies Eq. 2.15 to

$$\mathbf{u} = -\frac{z(H-z)}{2\mu} \nabla p \quad (2.16)$$

where $p \equiv p(x, y)$ and the flow profile along the z -axis is parabolic, i.e. Poiseuille flow [71], and velocity in the direction of the same axis is zero (Fig. 2.2). From the incompressibility condition, $\nabla \cdot \mathbf{u} = 0$, Eq. 2.16 may be rewritten as a simple potential flow obeying Laplace's equation on a 2D domain:

$$\nabla^2 p = 0 \quad (2.17)$$

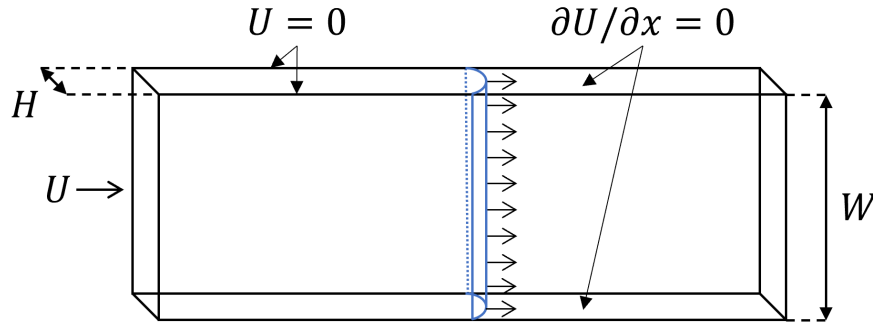


Figure 2.2 Flow in a Hele-Shaw cell ($W \gg H$ and $H \rightarrow 0$). Neumann boundary conditions on the side walls (top and bottom), and Dirichlet boundary conditions are set on the planes (in and out of the page).

Although significantly simpler than the Navier-Stokes equations, Eq. 2.17 may not be trivial to solve analytically on complex domains. In the following section, we introduce how potential flows may be solved using complex analysis and provide solutions to simple problems relevant for this work.

2.1.2 Application of conformal mapping to potential flows

Generalizing the pressure to a complex potential $\Psi(z)$ where $z = x + iy$, Laplace's equations becomes $\nabla_z^2 \Psi(z) = 0$ where $\nabla_z^2 = (d/dz)(d/d\bar{z})$. This equation is conformally invariant [72] and

can be solved using conformal mapping tools. A very useful map, critical for the work in Chapter 3 of this thesis, is obtained by the Schwarz-Christoffel (S-C) mapping. This convenient transformation discovered by two German mathematicians, Herman Amandus Schwarz (1843-1921) and Elwin Bruno Christoffel (1829-1900), consists in mapping the upper complex plane $\text{Im} > 0$ into the interior of a polygon [73, 74].

Let us first define a generic problem with its corresponding formalism. Consider Z , the interior of a polygon Γ formed by the z_1, \dots, z_n vertices and ϕ_1, \dots, ϕ_n exterior angles (see Fig. 2.3). The vertices are indexed in counterclockwise order from the inside of the polygon. The external angles of Γ must obey

$$\sum_{k=1}^n \phi_k = 2\pi \quad (2.18)$$

where $\phi_k \in [-\pi, \pi]$. The goal is to find a function $\zeta = f(\tau)$ which satisfies

$$z_k = f(t_k) \quad (2.19)$$

where

$$t_1 < t_2 < \dots < t_{n-1} < \infty \quad (2.20)$$

The S-C formula for a half-plane reads

$$f(\tau) = A + C \int \prod_{k=1}^{n-1} (\tau - t_k)^{-\frac{\phi_k}{\pi}} d\tau \quad (2.21)$$

where A and C are complex constants, $z_k = f(t_k)$ for $k \in \mathbb{N}^* \leq n-1$ and f is any map from the upper half-plane $\{T \in \mathbb{C} : \text{Im} > 0\}$ to $\{Z \in \mathbb{C}\}$. Examples of this transformation, of relative importance for the work in Chapter 3, follows.

Mapping the semi-infinite strip

We first give the example mapping of the upper half complex plane to the semi-infinite strip as shown in 2.3. The polygon Γ could be formed by the following coordinate-angle system:

$$z_1 = iW \quad \phi_1 = \pi/2 \quad (2.22)$$

$$z_2 = 0 \quad \phi_2 = \pi/2 \quad (2.23)$$

$$z_3 \rightarrow \infty \quad \phi_3 \rightarrow \pi \quad (2.24)$$

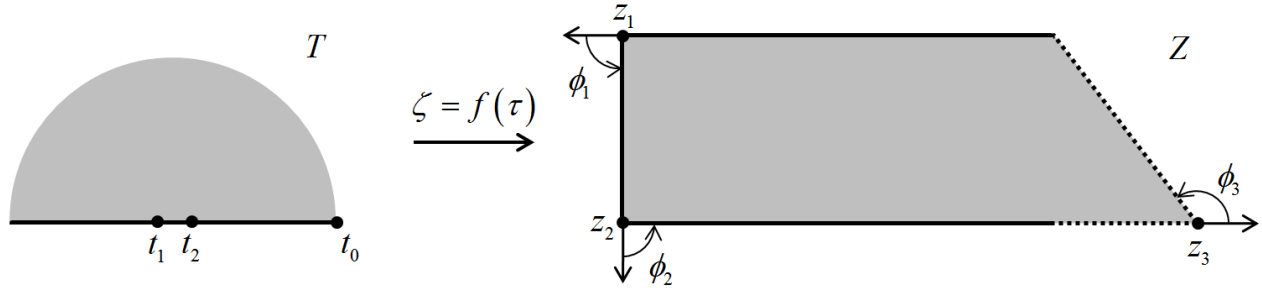


Figure 2.3 S-C mapping of the upper half-plane to the semi-infinite strip.

The next step is to define (in a semi-arbitrary manner²) the t_k values. Let us use $t_1 = -1$, $t_2 = 1$ and $t_3 \rightarrow \infty$. This translates into the S-C integral (Eq. 2.21)

$$f(\tau) = A + C \int^T \frac{1}{\sqrt{\tau+1}\sqrt{\tau-1}} d\tau \quad (2.25)$$

$$= A + C \operatorname{arccosh}(\tau) \quad (2.26)$$

where $f(-1) = z_1$, $f(1) = z_2$ and $f(\infty) = z_3$. From these conditions, the integration constants are calculated to be $A = 0$, and $C = W/\pi$, and the mapping solution from T to Z is

$$f(\tau) = \frac{W}{\pi} \operatorname{arccosh}(\tau) \quad (2.27)$$

Mapping a back step

The back step geometry (Fig. 2.4) is commonly encountered in fluid dynamics. Because inviscid flows can recapitulate flows at very large Reynolds numbers, this model may represent either an abrupt change in the width of a shallow ideal river from a bird's-eye view, or an abrupt step in depth as exemplified by an immersed concrete dam or flow over a riverbed [72]. For a back step domain, we define the following coordinate-angle system:

$$z_1 \rightarrow -\infty + iW/2 \quad \phi_1 \rightarrow \pi \quad (2.28)$$

$$z_2 = 0 \quad \phi_2 = -\pi/2 \quad (2.29)$$

$$z_3 = -iW/2 \quad \phi_3 = \pi/2 \quad (2.30)$$

$$z_4 \rightarrow \infty - iW/2 \quad \phi_4 \rightarrow \pi \quad (2.31)$$

Let us have $t_1 = 0$, $t_2 = t^* \in (0, 1)$, $t_3 = 1$ and $t_4 \rightarrow \infty$. This translates into the S-C integral (Eq.

²A specific definition of the t_k -values might be preferable in some circumstances for integration purposes. However, as long as the condition from Eq. 2.20 is respected the solution should be the same.

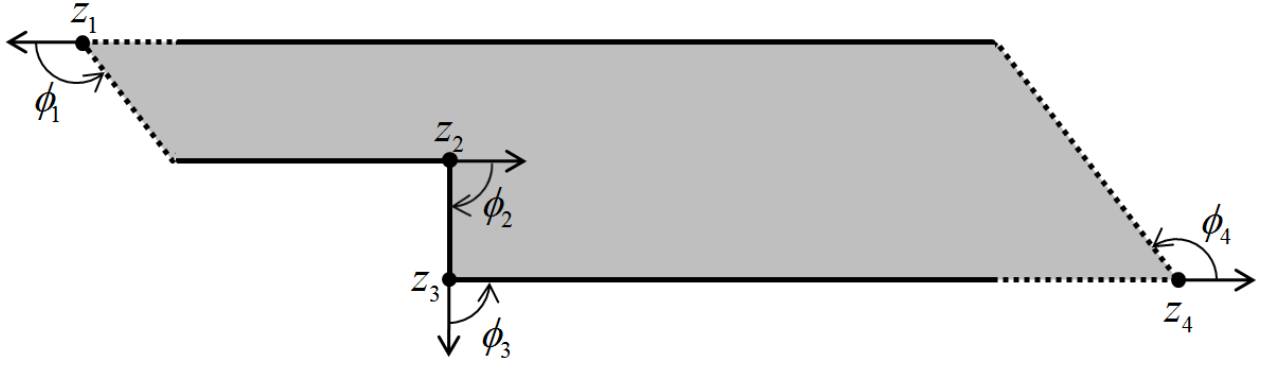


Figure 2.4 Z map of a back step.

2.21)

$$f(\tau) = A + C \int^T \frac{1}{\tau} \sqrt{\frac{\tau - t^*}{\tau - 1}} d\tau = A + CI \quad (2.32)$$

where $f(0) = z_1$, $f(t^*) = z_2$, $f(1) = z_3$ and $f(\infty) = z_4$. For integration convenience, let us define $t^* = 1/4$. The solution to this integral is

$$I = -\operatorname{arctanh} \left(2\sqrt{\frac{\tau - 1/4}{\tau - 1}} \right) - i4 \arctan \left(\frac{\frac{\sqrt{3}}{2} + i\sqrt{\tau - 1}}{\sqrt{\tau - 1/4}} \right) \quad (2.33)$$

From the two limits

$$\lim_{\tau \rightarrow t^*} I = 0 \quad \lim_{\tau \rightarrow t^*} (A + CI) = 0 \quad (2.34)$$

we find the first integration constant $A = 0$. Similarly, from

$$\lim_{\tau \rightarrow 1} I = -i\frac{\pi}{2} \quad \lim_{\tau \rightarrow 1} (CI) = -i\frac{W}{2} \quad (2.35)$$

we find the second integration constant $C = W/\pi$. The mapping solution from T to Z can then be given by

$$f(\tau) = -\frac{W}{\pi} \left[\operatorname{arctanh} \left(2\sqrt{\frac{\tau - 1/4}{\tau - 1}} \right) + i4 \arctan \left(\frac{\frac{\sqrt{3}}{2} + i\sqrt{\tau - 1}}{\sqrt{\tau - 1/4}} \right) \right] \quad (2.36)$$

A visual representation of the back step mapping from a rectangle is given in Fig. 2.5. The rectangle W is mapped in the upper half plane (UHP) T using the transformation [75]

$$t(w) = -i\frac{w+1}{w-1} \quad (2.37)$$

and the UHP T is mapped in the back step polygon Z using the transformation from Eq. 2.36 with

a width of 1.

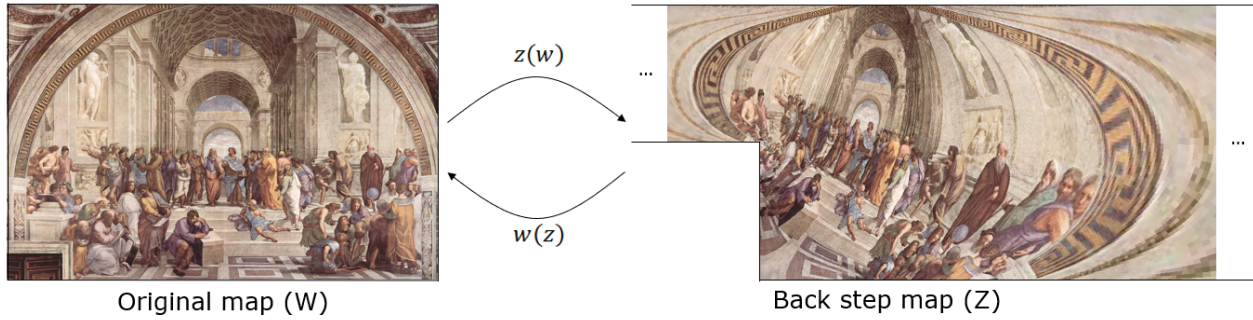


Figure 2.5 The School of Athens³(rectangle) mapped into a back step.

Mapping an inclined back step

A generalization of the back step geometry can be done by replacing the step with an inclined step of angle θ as shown in Fig. 2.6. The coordinate-angle system thus becomes

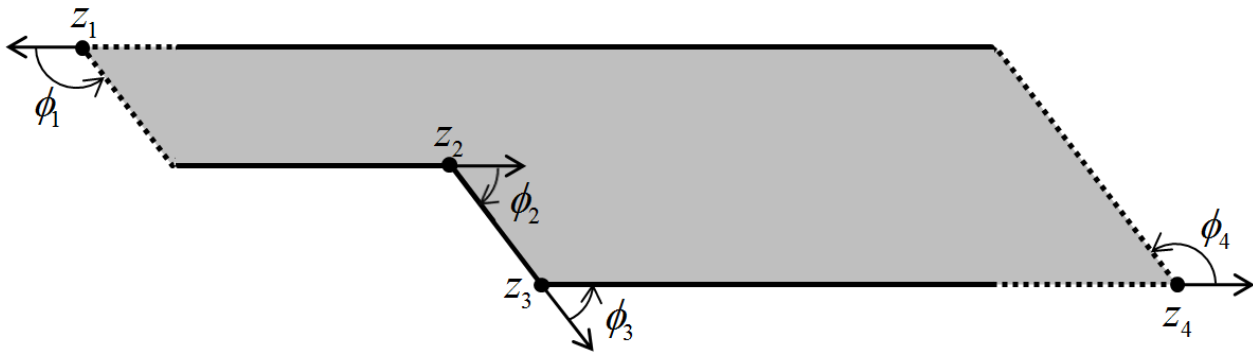


Figure 2.6 Z map of an inclined back step.

$$z_1 \rightarrow -\infty + iW/2 \quad \phi_1 \rightarrow \pi \quad (2.38)$$

$$z_2 = 0 \quad \phi_2 = -\theta \quad (2.39)$$

$$z_3 = \frac{W \cot \theta}{2} - i\frac{W}{2} \quad \phi_3 = \theta \quad (2.40)$$

$$z_4 \rightarrow \infty - iW/2 \quad \phi_4 \rightarrow \pi \quad (2.41)$$

Let us have $t_1 = 0$, $t_2 = t^* \in (0, 1)$, $t_3 = 1$ and $t_4 \rightarrow \infty$. This translates into the S-C integral (Eq.

³The School of Athens is a fresco by the Italian Renaissance artist Raffaello Sanzio da Urbino (1483-1520).

2.21)

$$f(\tau) = A + C \int^T \frac{1}{\tau} \left(\frac{\tau - t^*}{\tau - 1} \right)^{\theta/\pi} d\tau \quad (2.42)$$

where $f(0) = z_1$, $f(t^*) = z_2$, $f(1) = z_3$ and $f(\infty) = z_4$. For integration convenience, let us define $t^* = (1/2)^{\pi/\theta}$. The solution to this integral is

$$I = \int^T \frac{1}{\tau} \left(\frac{\tau - \left(\frac{1}{2}\right)^{\frac{\pi}{\theta}}}{\tau - 1} \right)^{\frac{\theta}{\pi}} d\tau = \frac{\pi(\tau - 1)}{\pi - \theta} \left(\frac{\tau - 2^{-\frac{\pi}{\theta}}}{\tau - 1} \right)^{\theta/\pi} \left(\frac{\tau - 1}{2^{\pi/\theta} - 1} + \tau \right)^{-\frac{\theta}{\pi}} F(\theta, \tau) \quad (2.43)$$

where

$$F(\theta, \tau) \equiv F_1 \left(1 - \frac{\theta}{\pi}; -\frac{\theta}{\pi}, 1; 2 - \frac{\theta}{\pi}; \frac{\tau - 1}{-1 + 2^{-\frac{\pi}{\theta}}}, 1 - \tau \right) \quad (2.44)$$

is the Appell hypergeometric function of two variables [76, 77]. From the two limits

$$\lim_{\tau \rightarrow 1} I = 0 \quad \lim_{\tau \rightarrow 1} (A + CI) = \frac{W \cot \theta}{2} - i \frac{W}{2} \quad (2.45)$$

we find the first integration constant $A = W(\cot \theta - i)/2$. Similarly, from the limits

$$\lim_{\tau \rightarrow t^*} I = -\frac{\pi \cot \theta}{2} - i \frac{\pi}{2} \quad \lim_{\tau \rightarrow t^*} \left(\frac{W \cot \theta}{2} - i \frac{W}{2} + CI \right) = 0 \quad (2.46)$$

we obtain the second integration constant $C = W(\cos(2\theta) - i \sin(2\theta))/\pi$. The mapping solution from T to Z is then given by

$$f(\tau) = \frac{1}{2} W \left(\frac{2e^{-2i\theta} (\tau - 1) \left(\frac{\tau - 1}{2^{\pi/\theta} - 1} + \tau \right)^{-\frac{\theta}{\pi}} \left(\frac{\tau - 2^{-\frac{\pi}{\theta}}}{\tau - 1} \right)^{\theta/\pi} F(\theta, \tau)}{\pi - \theta} + \cot(\theta) - i \right) \quad (2.47)$$

This map is suggesting that the general solution of self-coalescing flows in elongated structures, discussed at length in Chapter 3, follows a hypergeometric function behaviour. The natural progression from the semi-infinite strip to the back step and the inclined back step shows how the shape of the moving meniscus only impacts the flow in its vicinity. This is put in evidence in Fig. 3.10 and will be discussed in more details in Section 3.6 and Section 3.7.4.

2.1.3 Taylor-Aris dispersion

Taylor dispersion, or Taylor-Aris dispersion (TAD) and an effect of critical importance for Chapter 3, was first described by the British fluid dynamist G. I. Taylor [78], and was generalized for

arbitrary Péclet numbers a few years later by Rutherford Aris [79]. TAD is a convection-diffusion effect occurring when a steady-state Poiseuille flow (e.g. Eq. 2.16) is established in a channel with diffusion of a solute. Assuming an initially flat profile, the shear flow drives the solute forward faster in the middle of the channel than near the walls, where velocity is zero. This has for effect a stretching of the concentration profile, which then diffuses and homogenizes laterally. The effect may be generalized by an effective diffusion coefficient that increases in the direction of the flow. The effective diffusion coefficient in 1D can be written as [80]

$$K = D \left(1 + \frac{\text{Péc}^2}{k} \right) \quad (2.48)$$

where k is a parameter depending on the channel's geometry. For a rectangular channel of height H and width W ,

$$k = \frac{420}{17} \left(1 + 2.4 \frac{H}{W} + \left(\frac{H}{W} \right)^2 \right) \quad (2.49)$$

and for a cylindrical channel $k = 48$.

2.1.4 Capillary effects

Due to scaling effects in microfluidics, surface forces, e.g. surface tension, dominate over volume forces, e.g. gravity. This makes capillary effects vital in designing microfluidic devices. Capillary effects can be characterized by the Gibbs free energy [81] we define as

$$G(p, T) = U + pV - TS \quad (2.50)$$

where p is pressure, T is the temperature, U is the internal energy, V is volume, S is the entropy, and $H = U + pV$ is the enthalpy. Taking the total differential of Eq. 2.50, and assuming the system is at equilibrium or quasi-equilibrium, we obtain the variation in Gibbs free energy

$$\delta G = \delta U + p\delta V + V\delta p - T\delta S - S\delta T = 0 \quad (2.51)$$

In simple capillary systems without gravity or changes in temperature, variations in Gibbs free energy originate from variations in surface energy G_S and pressure-volume energy $G_{p,V}$, thus

$$\delta G = \delta G_S + \Delta p\delta V = 0 \quad (2.52)$$

where Δp is commonly referred to as the Young-Laplace pressure drop [1, 2]. In its most general form, the pressure drop is given by the product between the curvature of the interface, κ , and surface tension, σ , between the two liquids.

Using back of the envelope calculations we can calculate the surface tension of liquids from simple thermodynamics. The molecular weight of water at NTP is roughly $M = 18.015 \text{ g mol}^{-1}$, and the volume of one molecule of water is given by $V = MN_A/\rho$, where N_A is Avogadro's constant, and $\rho = 1000 \text{ kg m}^{-3}$ is water's density at NTP. The projected area of the molecule on a flat surface, i.e. the capillary interface, can be calculated as $A = CV^{2/3}$ where C is a geometric shape factor, e.g. $C = 1$ if we approximate the molecule's shape to be a cube, and $C = (9\pi/16)^{1/3} \approx 1.209$ for a sphere. Knowing that the average thermal energy carried by particles is $nk_B T/2$, where n is the number of degrees of freedom, we calculate the Gibbs free energy per area at equilibrium or quasi-equilibrium:

$$\sigma \equiv \left(\frac{\partial G}{\partial A} \right)_{p,V} = \frac{nk_B T}{2C} \left(\frac{\rho N_A}{M} \right)^{2/3} \quad (2.53)$$

Assuming a close packing of molecules with 6 neighbors and one neighbor missing due to the water/air interface, and knowing molecular bonds carry an energy of roughly $2k_B T$, we obtain for water at NTP $\sigma \in [71.1, 86.0] \text{ J m}^{-2}$ for a packing of spheres and cubes respectively. The measured value for water/air surface tension at NTP is 72.9 J m^{-2} [68].

For a capillary interface in contact with a solid surface, an equilibrium point between the solid-liquid, liquid-gas, and solid-gas surface tensions is reached (Fig. 2.7). The contact angle θ is given by the tri-phase (solid-liquid-gas) equilibrium point where the Gibbs energy is minimized. In mathematical terms,

$$\cos \theta = \frac{\sigma_{sg} - \sigma_{sl}}{\sigma_{lg}} \quad (2.54)$$

where for water and $\theta > 90^\circ$ we call the surface hydrophobic⁴, and for $\theta < 90^\circ$ hydrophilic⁵.

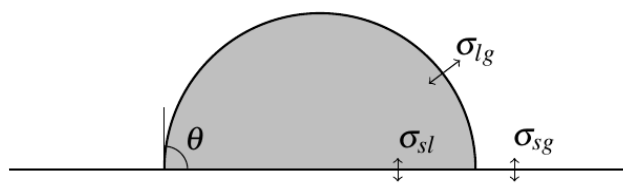


Figure 2.7 Contact angles arising from a tri-phase equilibrium point.

2.1.5 Calculating the Young-Laplace pressure in complex geometries

Calculating the capillary pressure drop resulting from an equilibrium of the total Gibbs free energy in systems composed of multiple walls with different contact angles can be simplified by calculating

⁴From the greek "phobos" meaning "fear".

⁵From the greek root "phil" meaning "love".

changes in surface energy for the solid-gas, solid-liquid, and liquid-gas phases. For a change of surface area $\delta\mathcal{S}$, the variation of the total Gibbs free energy, δG_S , at equilibrium is given by

$$\delta G_S = \sum_i \sigma_i \delta \mathcal{S}_i \quad (2.55)$$

where i denotes the different surface energy changes in the system, i.e. not limited to tri-phase systems. For a solid-liquid-gas system, the variation in surface energy is given by

$$\delta G_S = \sigma_{sg} \delta \mathcal{S}_{sg} + \sigma_{sl} \delta \mathcal{S}_{sl} + \sigma_{lg} \delta \mathcal{S}_{lg} \quad (2.56)$$

where $\delta \mathcal{S}_{sg}$, $\delta \mathcal{S}_{sl}$, and $\delta \mathcal{S}_{lg}$ correspond to a gain (or loss if negative) in solid-gas, solid-liquid, and liquid-gas surface area. From Eq. 2.52, we obtain the Young-Laplace pressure drop:

$$\Delta p = \frac{1}{\delta V} (\sigma_{sg} \delta \mathcal{S}_{sg} + \sigma_{sl} \delta \mathcal{S}_{sl} + \sigma_{lg} \delta \mathcal{S}_{lg}) \quad (2.57)$$

Variations in solid-gas and solid-liquid surface energy are generally equal and of opposite sign, for which we write $\delta \mathcal{S} = \delta \mathcal{S}_{sg} = -\delta \mathcal{S}_{sl}$. For a meniscus moving in a channel of cross-sectionnal area \mathcal{A} and a translational symmetry of the meniscus as it moves a distance δx , i.e. a straight or locally straight channel, we can write $\delta V = \delta x \delta \mathcal{A}$ and $\delta \mathcal{S}_i = \delta x \delta \ell_i$ where $\delta \ell_i$ is the peripheral length bounding the surface \mathcal{A} for the phase i . In this case, we can simplify the Young-Laplace pressure to

$$\Delta p = \frac{1}{\mathcal{A}} [\delta \ell (\sigma_{sg} - \sigma_{sl}) + \sigma_{lg} \delta \ell_{lg}] \quad (2.58)$$

From the contact angle's definition in Eq. 2.54, we can rewrite Eq. 2.58 as

$$\Delta p = \frac{\sigma}{\mathcal{A}} [\delta \ell \cos \theta + \delta \ell_{lg}] \quad (2.59)$$

where the liquid-gas surface tension is commonly referred to as "surface tension" alone, i.e. $\sigma \equiv \sigma_{lg}$. It is made evident from the previous equation that creation of an air-water interface is equivalent to wetting a superhydrophobic wall, and on the other hand retraction of an air-water interface is equivalent to wetting a superhydrophilic wall. For a channel of width W and height H , and one side of the channel being exposed to air, we obtain

$$\Delta p = \frac{\sigma}{HW} [(2W + H) \cos \theta - H] \quad (2.60)$$

where $[(2W + H) \cos \theta - H] / HW$ is the effective curvature of the capillary interface. This result is akin to the capillary pressure obtained at the moving front of menisci in self-coalescence modules

and will be discussed at length in this thesis (mostly Chapter 3 and 5). For a cylindrical tube of radius R , we simply recover $\Delta p = 2\sigma \cos \theta / R$.

2.1.6 Washburn flows

The underlying physics of capillary-driven flows can be described by the Washburn equation [82]. Washburn flows occur from a trade-off between capillary forces and viscous losses when filling microchannel. The Young-Laplace pressure drop is given by $\Delta p_{\text{surf}} = \sigma \kappa$ (Fig. 2.8), where $\kappa = \nabla_s \cdot \mathbf{n}$ is the curvature of the capillary interface calculated from the surface divergence of the normal surface vector \mathbf{n} . Assuming the pressure drop Δp between the meniscus' interface and the inlet is constant when filling a straight channel of arbitrary cross-sectional shape of surface \mathcal{A} , and that Poiseuille's flow is fully developed, the flow rate is described by the Hagen-Poiseuille law, hydrodynamic equivalent of Ohm's law, and can be written as

$$\Delta p_{\text{surf}} = x R_{\text{hyd},x} \mathcal{A} \frac{dx}{dt} \quad (2.61)$$

where $R_{\text{hyd},x}$ is the hydraulic resistance per unit length of the channel. Rearranging the terms, we obtain the following first-order nonlinear ordinary differential equation:

$$x \frac{dx}{dt} = \frac{\sigma \kappa}{\mathcal{A} R_{\text{hyd},x}} \quad (2.62)$$

Introducing the arbitrary length scale, ℓ , and the Washburn time, τ , the solution for $x(0) = 0$ can be rewritten as

$$x(t) = \ell \sqrt{\frac{t}{\tau}} \quad (2.63)$$

where $\tau = \mathcal{A} \ell^2 R_{\text{hyd},x} / 2\sigma \kappa$. For a capillary-driven flow confined between two identically hydrophilic parallel plates of height H , width W , and contact angle θ , we have $\mathcal{A} = HW$, $\kappa = 2 \cos \theta / H$, $R_{\text{hyd},x} = 12\eta / WH^3$, $\ell = H$, and $\tau = 3\eta H / \sigma \cos \theta$.

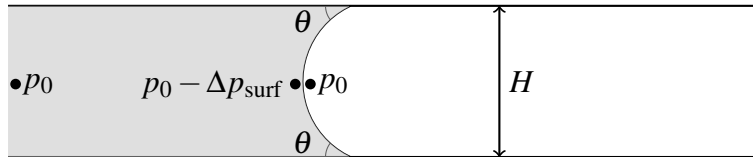


Figure 2.8 Washburn flow between two parallel plates.

2.1.7 Concus-Finn criterion

The pinning stability of a meniscus on a sharp corner of angle α is known as the Concus-Finn (CF) criterion [83–86], a phenomenon first investigated by Gibbs in 1961 [81]. Concus and Finn proposed that the shape of a surface pinned in a corner can be obtained by minimizing the energy of the system. An easy way to represent the minimization in the context of liquid pinning on a CPL, is presented in Fig. 2.9. Minimization of the energy occurs when the curvature is maximal, i.e. when the meniscus is a straight line. In other words, assuming no external pressure is applied on the system, the condition $\pi - \delta - \theta < \theta$ must be obeyed at equilibrium. Otherwise, the meniscus either hasn't reached equilibrium or is moving forward on the edge. We obtain from that condition the critical contact angle

$$\theta_c = \frac{\pi - \delta}{2} \quad (2.64)$$

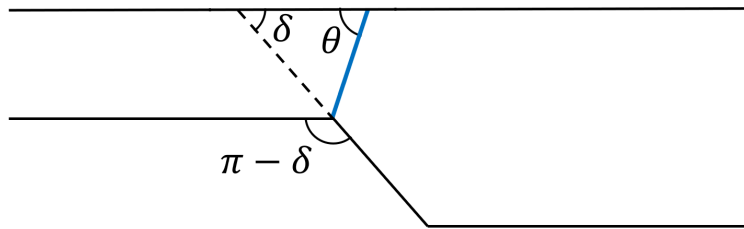


Figure 2.9 Liquid pinning on a CPL of edge steepness $\pi - \delta$ and contact angle θ .

Thus, if $\theta < \theta_c$ the criterion is not met and there exists no stable solution to the minimization of surface energy and the pinning fails. Otherwise, the interface is stable. A large body of literature exists on the theoretical, numerical, and experimental investigation of the CF criterion in pores, corners, and complex configurations [10, 87–97].

2.1.8 Saffman-Taylor viscous fingering

Saffman-Taylor viscous fingering (STVF), also known as Saffman-Taylor instability, occurs when a less viscous fluid is driven in a more viscous fluid in a media abiding by Darcy's law, e.g. porous media such as soils or Hele-Shaw cells (Fig. 2.10). This phenomenon of instability of liquid surfaces in porous media and Hele-Shaw cells was pointed out by Taylor [98] and verified experimentally by Lewis [99] in 1950 (Fig. 3.9). It was followed by a seminal paper by Saffman and Taylor in 1958 [100] describing the necessary criterion for stability. The stability of STVF was then further discussed by Bensimon [101] in a WKB approximation framework and complex analysis. A brief description of how STVF arises is presented in Appendix B.

⁷Attribution: Claire Trease, Kingston University, CC BY-SA 4.0, via Wikimedia Commons.



Figure 2.10 Saffman-Taylor viscous fingering resulting from the air displacing a spin coated thin film. The colours are resulting from thin-film interference.⁷

2.2 Numerical modelling of capillary flows

Theory and simulation of matter can be classified in time and length scales [102]. From the most fundamental scales up, we can classify them as: 1) ab initio (electronic) and semiempirical methods [103, 104], 2) atomistic methods [105, 106], 3) mesoscopic methods [107], and 4) continuum methods [108]. Because of the relatively large scale of systems in microfluidics and micro process engineering with respect to sub-atomistic scales, mesoscopic and continuum methods are preferred [109].

Modelling gas-fluid or immiscible fluid-fluid interfaces where surface tension plays an vital role is a common problem in computational fluid dynamics (CFD) known as the interface tracking problem. A large body of literature exists on solving this problem using multiple different approaches [109–113], from atomistic models with interacting potentials, to continuum mechanics with the Navier-Stokes equations [10, 114]. Once a scale class and a model is chosen, equations are discretized and solved using numerical methods (Fig. 2.1). We list some of the well-known properties of continuum CFD discretization methods (FDM, FVM, FEM) and LBM here below [108, 109]:

Finite Difference Method

- Simple one-for-one replacement of differential operators;
- Meshes must be structured, and curved meshes must be transformed so that discretized equations can be written on structured cartesian meshes (i.e. no complex geometries and structures);
- Neumann boundary conditions are approximated;
- Easy to implement.

Finite Volume Method

- Simple flux calculations through surfaces;
- Complex geometries and structures can be accommodated without coordinate transformations;
- Normal flux integration on surfaces guarantees conservation through the domain;
- Generally more strenuous to implement than FDM.

Finite Element Method

- Requires notions of functional analysis;
- Complex geometries and structures can be accommodated without coordinate transformations;
- Neumann boundary conditions are exact;
- Generally more strenuous to implement than FVM.

Lattice Boltzmann Method

- Originates from a mesoscopic description of fluid dynamics and can incorporate physical terms interacting at the sub-continuous scale;
- Complex geometries and structures can be accommodated, but issues may arise depending on the chosen LB formulation (e.g. in corners);
- Complex boundary effect occurring at the mesoscopic scale can be modelled using the bounce-back boundary condition;
- Easy to implement (similar structure as FDM).

Mesoscopic multiphase CFD models include the multiphase lattice Boltzmann method (MLBM) [113, 115]. The lattice Boltzmann method (LBM) originated from the lattice gas automata [116, 117] and derived from the minimal form of the Boltzmann kinetic equation. It consists in evolving discretized particle distribution functions on a grid. MLBM has been reported to be a powerful tool for the study of electrowetting [118, 119], self-priming of liquids [95], and powerful software packages have been developed based on this formulation [120, 121]. An example of implementation of the MLBM using colour functions is presented in Appendix F. Nevertheless, MLBM is still under a lot of development and standards (community consensus) have yet to be established. Furthermore, the intrinsic mesoscopic nature of MLBM does not provide any advantage, with respect to continuum methods, in solving main challenges (spurious currents, and contact line singularities) in capillary dynamics modelling [122–125]. These challenges will be addressed in more details in Section 2.2.2.

In microfluidics, the ratio between the mean free path of particles and the characteristic length scale of devices, characterized by the Knudsen number, is orders of magnitude smaller than unity and the

continuum interpretation of fluids applies [126]. Continuum-based methods for multiphase flows describing gas-liquid or immiscible liquid-liquid interface evolutions are numerous [109–112,127], and several open source and commercial softwares have been developed to model them [128–132]. A comparative study between different classification scales of fluids in a CF criterion validation framework shows promising results using FVM with the volume of fluid (VOF) method for finite interface modelling [10]. FVM is often preferred to FDM and FEM for its intrinsic conservation of physical quantities, including conservation of the phase field which is critical in calculating the interface location. Many open source and commercial software packages such as OpenFOAM [128], Ansys-Fluent [130], Gerris [129], and others use the VOF method with a FV discretization or variations thereof.

2.2.1 Modelling interface evolution

The fundamental idea behind sharp interface calculation methods originates from the Marker And Cell (MAC) formulation [133–135]. In this method, connected Lagrangian particles, or markers, are advected throughout the Eulerian domain. As the interface moves on the mesh, particles are deleted or added for proper resolution of the interface. These types of methods are generally known as Front Tracking (FT) methods [136, 137]. An other sharp interface calculation method akin to FT formulation are dynamic grid approaches where the interface is connected by grid nodes and moves with the mesh. Moving unstructured grid methods are generally based on the arbitrary Lagrangian–Eulerian (ALE) formulation [138]. FT methods are challenging to use for the study of capillarity as they generally can not deal with important interface topological deformations as observed in coalescence, breakup and pinning phenomena. And in cases where they can, they require complex algorithms [139]. On the other hand, topological changes are well captured by Eulerian methods.

The volume of fluid (VOF) method was first developed by Nichols and Hirt [140–142]. This method is based on the advection of a phase field, or volume fraction, by a simple first order transport equation we can write as

$$\frac{D\alpha}{Dt} \equiv \frac{\partial \alpha}{\partial t} + (\mathbf{u} \cdot \nabla) \alpha = 0 \quad (2.65)$$

where D/Dt is the material derivative operator, and α is the phase field taking values between 0 and 1, and a single set of Navier-Stokes equations is solved for the mixture. For an incompressible isothermal mixture, the Navier-Stokes equations are described by Eq. 2.6 and Eq. 2.7 with density and viscosity defined respectively as

$$\rho = \alpha \rho_1 + (1 - \alpha) \rho_2 \quad (2.66)$$

$$\mu = \alpha\mu_1 + (1 - \alpha)\mu_2 \quad (2.67)$$

where 1 and 2 denotes the two fluids. The interface is reconstructed from the phase field and can be either have a zero (sharp) or finite thickness. The advection of a phase field using Eulerian methods removes the difficulty MAC and ALE types of formulations have in modelling large topological deformations. However, the resolution of interfaces with Eulerian methods is dependent on the size of the local mesh. Examples of reconstruction methods for sharp interfaces with the VOF method are the Simple Line Interface Calculation (SLIC) method [143, 144], the Piecewise Linear Interface Calculation (PLIC) method, and the Piecewise Parabolic Interface Calculation (PPIC) method [145].

SLIC methods splits mixed-fluid cells ($0 < \alpha < 1$) in a piecewise constant manner in the direction of the cell. They are seldomly used nowadays, as gold standards gravitate towards the PLIC method and variations thereof [109]. In the PLIC method, the interface is reconstructed in the direction normal to the unit vector, reconstructed from neighboring cells, that points towards the positive phase. With the volume fraction known from α , and the unite vector, a surface can be reconstructed analytically and cut the cell where appropriate. Analytical reconstructions are only possible for single cuts on a given set of cell shapes, notably orthogonal hexahedral cells [146], triangular cells [147] and tetrahedral cells [148]. However, hybrid methods can be used where interfaces are reconstructed analytically where they can, and using other methods where they cannot, e.g. in OpenFOAM PLIC reverts back to interface compression [149] where it can't be applied [150]. Higher order methods such as the PPIC method reconstruct the interface using a similar approach, but with non-linear interface reconstruction schemes such as parabolic schemes [145], cubic splines [151, 152], and quadratic splines [153]. However, higher order schemes have not yet proven to be superior to more conventional methods such as the PLIC method.

A popular model for finite interface reconstruction using the VOF method, as implemented in the `interFoam` solver of OpenFOAM [128], us the following model [149]

$$\frac{\partial \alpha}{\partial t} + \nabla \cdot (\alpha \mathbf{u}) - \nabla \cdot [\alpha(1 - \alpha)\mathbf{u}_r] = 0 \quad (2.68)$$

where $\nabla \cdot [\alpha(1 - \alpha)\mathbf{u}_r]$ is an artificial compression term that has the advantage of being conservative, i.e. the total volume of phase is conserved after the operation. The compression velocity term is defined as

$$\mathbf{u}_r = \mathbf{n}_f \min \left[C_\gamma \frac{|\phi_f|}{|S_f|}, \max \frac{|\phi_f|}{|S_f|} \right] \quad (2.69)$$

where ϕ_f is the volume flux across the surface f , S_f is the surface area, \mathbf{n}_f is the unit vector of that surface, and $C_\gamma \in [0, 4]$ is a constant whereby $C_\gamma > 1$ enhances the compression, and $C_\gamma = 0$ removes compression.

Level Set (LS) method [154–157] is another technique used for interface tracking on Eulerian meshes. As opposed to FT methods, the LS method can model and capture interfaces with strong deformations. Similarly, as the VOF method, the LS method consists in advecting a LS function, ϕ , through the domain and reconstruct the interface at a given ϕ value, e.g. generally at $\phi = 0.5$. A popular LS model, e.g. as used in COMSOL Multiphysics [131], is to model the interface by solving the following equation:

$$\frac{D\phi}{Dt} = \gamma \nabla \cdot \left(\varepsilon \nabla \phi - \phi(1 - \phi) \frac{\nabla \phi}{\|\nabla \phi\|} \right) \quad (2.70)$$

where the parameter ε determines the thickness of the interface and should be equal to the largest value of the mesh size, and γ is a stabilization parameter. However, this parameter needs to be fine tuned for each specific problem and might result in strong diffusion of the interface or long computational times. Furthermore, signed distance-based LS methods are known to suffer from artificial mass losses, which is a critical flaw in modelling capillary interface as this directly affects the position of the meniscus in time. Several authors have assessed mass losses in LS methods and provide mass correction steps [158–161]. LS methods were successfully modified to be conservative [162, 163] and have been used in microfluidics [164], but this has yet to be implemented successfully in convenient open source or commercial CFD software packages.

The phase-field (PF) method [165] consists in solving the Cahn–Hilliard equation [166]:

$$\frac{\partial \alpha}{\partial t} = D \nabla^2 (\alpha^3 - \alpha - \beta \nabla^2 \alpha) \quad (2.71)$$

where D is a diffusion coefficient and α is the phase field taking values between -1 and 1 . To bound the phase field between 0 and 1 , as in the VOF method, the simple transformation $\alpha \rightarrow 2\alpha - 1$ can be applied. The diffusing quantity $\alpha^3 - \alpha - \beta \nabla^2 \alpha$ is a chemical potential, and $\sqrt{\beta}$ is the interface thickness. This method issues from a free energy formulation of nonuniform systems, making it the only model with a pure grounding in physics. However, high-order discretization schemes are required to capture the fourth-order term in Eq. 2.71, making it computationally intensive.

2.2.2 Modelling surface tension

With the reconstructed interface, surface tension forces are calculated and applied to the Eulerian grid. Line integrals are used to compute surface tension from sharp FT (Lagrangian) methods [136, 137, 167, 168] in conjunction with the immersed boundary, or immersed interface, method [169] to transpose the source term on the Eulerian grid.

The Continuous Surface Force (CSF) method [65] calculates the curvature of the interface, κ from

calculating the gradient of the phase field:

$$\kappa = \nabla \cdot \left(\frac{\nabla \alpha}{|\nabla \alpha|} \right) \quad (2.72)$$

The momentum source term $\kappa(\nabla \alpha)$ is then added in Eq. 5.10. The CSF method is explicit and requires a time step restriction to ensure numerical stability [65, 170]. However, methods have been implemented to reduce that restriction [171, 172]. On the other hand, the Continuous Surface Stress (CSS) and Sharp Surface Force (SSF) methods have the advantage of being intrinsically conservative and have been used by [145, 173].

A comparative study of the CSF, CSS, and SSF methods was conducted for a droplet and bubble relaxation benchmark [174, 175] and for droplets formation in T-junctions [176]. Droplets formation in T-junctions were also investigated using the PLIC method [177]. More recently, PLIC, CSF, SSF, and variations thereof, were also assessed for spontaneous imbibition in a microchannel [178]. CSF was also experimentally validated for capillary flows in SU8 and PDMS micropumps with pillars [179].

Transport problems with interface tracking and surface tension are challenging due to, in part, *spurious currents* (Fig. 2.11), also known as parasitic flow or artificial currents [180]. Spurious currents have the effect of increasing the flow velocity locally, increasing the simulation time by orders of magnitudes due to the Courant number limit on numerical time steps [181]. The Courant number is defined as

$$Co = U \frac{\Delta t}{\Delta x} \quad (2.73)$$

where U is the flow velocity, Δx is the cell size, and Δt is the numerical time step. Co is calculated in every directions, i.e. x, y, z in 3D, and the numerical time step is calculated from $\Delta t = Co_{\max} \max_{\Omega} \{\Delta x/U\}$ on the whole numerical domain Ω , with Co_{\max} being the maximal attributed Courant number (generally $Co_{\max} < 1$ for stability). Another important numerical time step limiter is the von Neumann stability criterion, also known as Fourier stability criterion, which limits time steps for the Forward Time Centered Space (FTCS) scheme in the following way:

$$D \frac{\Delta t}{\Delta x^2} \leq \frac{1}{2} \quad (2.74)$$

where D is the diffusion coefficient. However, convection is generally the highest limiter in CFD for laminar flows of water-like fluids. Numerical time steps might also be limited by reaction, e.g. Section 3.8, in which case Δt has to be small enough for the FTCS scheme to capture the physics of the problem or higher order temporal discretization schemes have to be used. Explicit-time integration schemes include, for example, the Lax–Wendroff method [182] and the Runge–Kutta

method [183, 184]. Implicit-time integration may also be preferred for unconditional stability; however, accuracy is not guaranteed. A large body of literature exists on how to reduce spurious currents using the CSF and CSS models [145, 167, 185–187]. There has been substantial work in the previous year to reduce spurious currents, and even completely eradicate them using accurate adaptive solver for surface-tension-driven interfacial flows [174, 188]. However, spurious currents are still a main issue for unstructured meshes, non-adaptive solvers, and most CFD codes whether commercial or open source. A parametric analysis of spurious currents in OpenFOAM (VOF-FVM with compressive CSF) for a droplet of water was done and details are provided in Appendix H.

An other challenge in modelling capillary flows is contact line dynamics on walls with Dirichlet boundary conditions using continuum (or mesoscopic) methods. Solving a moving capillary line on a wall is equivalent to a moving Neumann boundary condition (free-surface) on a static wall with a Dirichlet boundary condition of zero velocity. This corner flow problem is a classic problem of fluid dynamics and is known as Taylor’s scraping flow [189], named after the British physicist G. I. Taylor., and was generalized shortly after by Moffatt [190] for free-surface flows (Neumann boundary condition). The resulting pressure in cylindrical coordinates centered at $r = 0$ in the corner is given by

$$p(r, \theta) - p_\infty = \frac{2\mu U}{r} \frac{\theta \cos \theta \sin \beta - \beta \cos \beta \sin \theta}{\sin \beta \cos \beta - \beta} \quad (2.75)$$

where β is the angle of the corner, i.e. contact angle, and θ the angle coordinate. This result is obviously physically wrong as we approach $r \rightarrow 0$ since the pressure becomes singular⁸. More details on that effect and its characterization are given in Appendix G (in French).

Contact angles in OpenFOAM are imposed by updating the surface vector to the multiphase interface in the first cell layer using the dot product relation with the surface vector to the wall. Knowing the cosine of the angle between the two vectors (from the contact angle) and knowing the surface vector to the wall, we can find and fix the value of the surface vector to the multiphase interface.

Interface evolution and surface tension modelling are still under a lot of research. More recently, several methods were implemented in OpenFOAM, including the iso-advector method [192, 193], the PLIC method [194], and some variants thereof such as the Multicut PLIC (MPLIC) method [150].

2.2.3 Numerical modelling of capillary flows in this thesis

Chibbaro *et al.* compared the VOF method, LBM and MD in a CF criterion validation framework [10], i.e. a condition that is paramount in the operation and modelling of capillary-driven

⁸Huh and Scriven famously noted that "not even Herakles could sink a solid if the physical model were entirely valid, which they are not." [191]

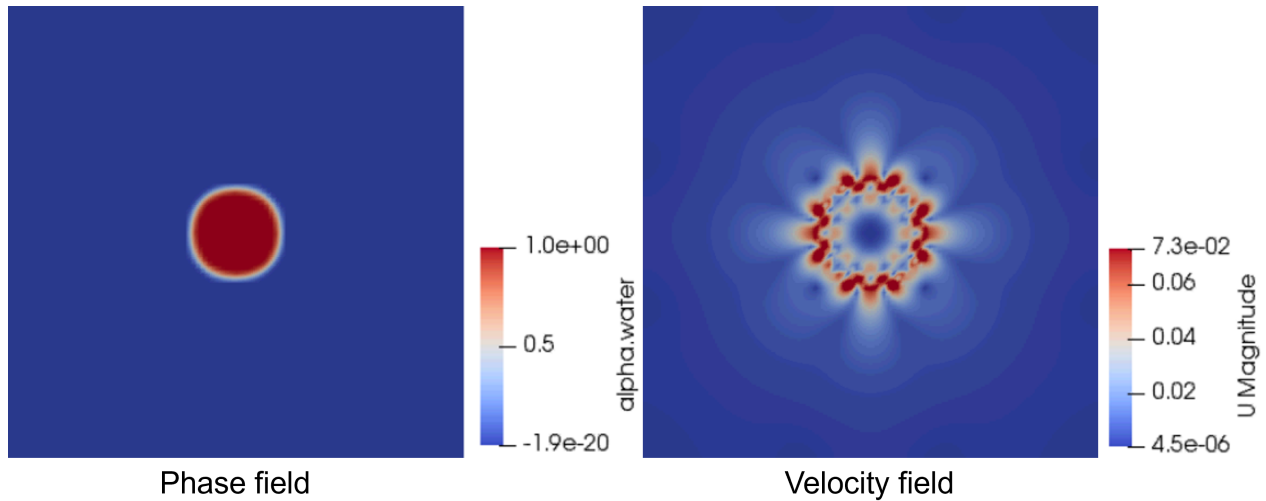


Figure 2.11 Simulation of a water droplet at equilibrium using VOF-FVM, CSF and interface compression in OpenFOAM. Although the droplet phase field (left) shows it is static in space, the velocity field (right) shows heavy spurious currents in the vicinity of the capillary interface. The domain size is 1 mm, and the water droplet radius is 100 μm .

microfluidics, such as phaseguides [195], valves [196] and self-coalescence modules [197]. MD failed in modelling the pinning of the meniscus for contact angles close to the critical CF criterion. Both LBM and VOF were successful in modelling the pinning. Furthermore, VOF was able to reproduce all the physical properties of the flow, as opposed to LBM and MD which had some discrepancies regarding surface tension and vapor density.

Because of the prevalence of VOF-FVM in the literature, comparative studies such as Chibbaro *et al.* [10], and available software packages [109], both commercial and open source, this method was selected for the multiphase computational work in this thesis (Chapter 4 and III), with OpenFOAM [128] as CFD solution. OpenFOAM is an open source C++ library that uses a tensorial approach to continuum-based CFD using object-oriented techniques [198], making it easy to develop reliable and robust codes rapidly. Also, OpenFOAM has one of the largest, if not the largest, user base in open source CFD solutions. Furthermore, other methods such as the LS and PS methods as implement in the FEM commercial software COMSOL Multiphysics [131] were tested (using the LS and PF methods) for basic test cases, e.g. benchmark of a 2D rectangular channel, and showed unreasonable simulation and convergence time with important mass losses.

Surface tension effects are calculated from the curvature of the phase field in Eq. 2.7, which is obtained from the CSF formulation [65], and is defined according to Eq. 2.72. The phase field, α , is advected by a simple first order transport equation and the interface is calculated using the compression scheme described in Eq. 2.68. All simulations in this thesis take $C_\gamma = 1$ (Eq. 2.69) as

recommended by Deshpande *et al.* [199].

In OpenFOAM, the pressure-momentum equations are solved using the PIMPLE (PIso-siMPLE) algorithm [200], a combination of the PISO (Pressure-Implicit with Splitting of Operators) for transient flows and SIMPLE (Semi-Implicit Method for Pressure Linked Equations) algorithm for steady flows [201]. However, for non-inertial loop, the PIMPLE algorithm has a single inner loop which is equivalent to the PISO algorithm. In pseudo-code, the PISO algorithm with interface evolution reads:

```

Initialize fields
Start computational loop
  while  $t < t_{\text{end}}$ 
    while momentum not converged (PISO loop)
      Momentum prediction: Solve for velocity field based on  $p$ 
      Pressure correction: Solve for  $p$  based on momentum predictions
      Momentum correction: Update velocity field from pressure correction
      Interface evolution from velocity field
      Interface reconstruction/smoothing
      Calculate time step  $dt$  from the Courant number
      Update time  $t = t + dt$ 
    End computational loop
  End computational loop

```

2.3 Thesis Structure

The main objectives of this thesis are to 1) understand and characterize newly discovered self-coalescing flows, which allows reagent reconstitution with minimal dispersion, 2) develop a numerical framework for modelling complex capillary driven flows in microstructures, which can be used as a tool to predict behavior of liquids in microsystems and optimize their design where analytical tools are limited, and 3) predict, understand, and characterize new types of capillary flow providing enhanced control over passive flows in microchannels.

The general thesis structure is as follow. In Chapter 3, I detail my contributions with regard to our publication in Nature [197] (available in Appendix A). I discuss the characteristics of the flow in the SCMs which prevents the accumulation and smearing of reagents when resuspended. The different methods of analysis and their conclusions are briefly presented and a link with Saffman-Taylor Viscous Fingering (STVF) is made. Second, challenges in modelling capillary flows are presented and a solution is provided (Chapter 4 and publication in Computers & Fluids [202]). Finally, I describe how modelling tools can help predict and characterize new phenomena in microfluidics,

such as accelerating capillary flows (Chapter 5 and submitted in *Physical Review Fluids*).

It is important to acknowledge that some of the work in my thesis wouldn't have been possible without collaborations with other incredible scientists, engineers, and researchers. In Chapter 3, Emmanuel Delamarche (E.D.) conceived the research. Onur Gökçe (O.G.) discovered self-coalescing flows, designed SCMs and experiments, and conducted the experiments. Thomas Gervais (T.G.) developed the theoretical framework and contributed to the experimental design. I performed the conformal mapping calculations and the numerical simulations, and contributed to the theoretical framework. O.G., I and T.G. analysed the data. Yuksel Temiz (Y.T.) fabricated microfluidic chips and documented them using scanning electron microscopy. O.G., T.G. and E.D. wrote the manuscript. All authors discussed and provided input to the manuscript. Finally, the Nature manuscript was supplemented by over 20 figures and a 20 page long appendix describing the mathematical derivation leading to the analysis of self-coalescence, which I wrote alone under the supervision of T.G. The application section of Chapter 3 is part of a publication by Marco Rocca (M.R.) *et al.* [203]. In this work, M.R. and E.D. conceived the research, T.G. developed the theoretical model, and I wrote the software for running simulations and validated theoretical results with numerical experiments. In Chapter 4, I conceptualized and visualized the research, established the methodology, conducted the formal analysis, and wrote the original draft. T.G. supervised the research, and T.G. and I reviewed and edited the manuscript. In Chapter 5, I conceived the research, developed the theoretical models, conducted the numerical simulations, analysed experimental results, and compared theoretical, numerical, and experimental results. Y.T. and I designed the SCMs. Y.T. designed and conducted the experiments, and fabricated the SCMs. T.G. supervised the research. All authors discussed the results. T.G. and I wrote, reviewed, and edited the paper with inputs from all authors.

CHAPTER 3 SELF-COALESCING FLOWS IN MICROFLUIDICS FOR PULSE-SHAPED DELIVERY OF REAGENTS

Chapter Overview

In this theme, I detail my contributions with respect to our publication in Nature [197] regarding self-coalescing flows in microfluidics for pulse-shaped delivery of reagents (Appendix A). The characteristics of SC flows are discussed and the accurate resuspension of reagents in SCMs, i.e. prevention of accumulation and smearing of reagents, is explained. Analytical and numerical analyses are conducted and results show SC flow behaviour is mathematically akin to Saffman-Taylor Viscous Fingering (STVF). In this research, I performed all conformal mapping calculations and numerical simulations, and co-developed the theoretical framework with my advisor Thomas Gervais. Emmanuel Delamarche conceived the research, Onur Gökçe discovered self-coalescing flows, designed SCMs and experiments, and conducted the experiments, and Yuksel Temiz fabricated microfluidic and documented them using scanning electron microscopy. The chapter ends with an application section for which I wrote the software for running simulations and validated theoretical results with numerical experiments. This research was led by Marco Rocca and Emmanuel Delamarche, and the results are published in Lab on a Chip [203].

3.1 Introduction

Methods for the integration and release of reagents in microsystems are numerous [204] and are ubiquitous when designing BioMEMS. A key method for the integration of reagents in microstructures is by inkjet printing [205–207]. Picograms of deposited reagents dry quickly [208, 209] and have long shelf life, which is critical in the pharmaceutical and diagnostic industries [210]. Release methods include paper networks [211], degradation of hydrogels [212] and rehydration of dried reagents [213]. However, no reported methods provide a precise control over the release of reagents in microstructures, and releasing reagents still proves to be a challenge [204].

When wetting printed reagents in microchannels, a strong accumulation of reagents occurs at the capillary filling front (Fig. 3.1) because of convection, and a spreading of reagents in the direction of the flow occurs because of an increase in effective diffusivity due to strong local shear flows. This is known as the Taylor-Aris dispersion (TAD) effect, and is a challenge for any applications where dispersion has to be precisely controlled in microchannels, e.g. rapid diagnostic tests (RDT) and lateral flow immunoassay, lab-on-chip devices (LOCD), point-of-care and precision diagnostics, and integrated security features on chip [26, 55]. In BioMEMS, the challenge arises when precise

quantity of reagents are needed in controlled volume of samples for accurate and effective diagnosis or analysis.



Figure 3.1 Resuspension of printed amaranth dye in a microchannel. Accumulation of dye at the capillary front because of convection and spreading of the concentration profile by TAD.

The reagent resuspension challenge can be tackled by confining a drop of water in a microstructure, wetting printed reagents in a manner which prevents the accumulation of reagents at the filling front. By controlling the flow rate, TAD can be minimized in such a way as to maximize the spatiotemporal resolution of reagent concentration profiles and send pulses of reagents downstream of microchannels. Filling of the microstructure occurs in 3 phases: 1) water is confined in one part of the device where no reagents are printed (Fig. 3.2), confinement occurs from a capillary pinning line (CPL), 2) the capillary filling front reaches the end of the CPL, and 3) the capillary interface “folds” back onto itself in a process we call self-coalescence (SC). This phenomenon will be discussed at length in the following sections. Because dispersive effects are intrinsically linked to flow dynamics, characterizing the transport of reagents in self-coalescence modules (SCM) requires characterizing flow dynamics in the SC phase. Physical hints from experimental velocity maps (e.g. Fig. 3.3) and simulations were used to build an accurate model of SC flows.

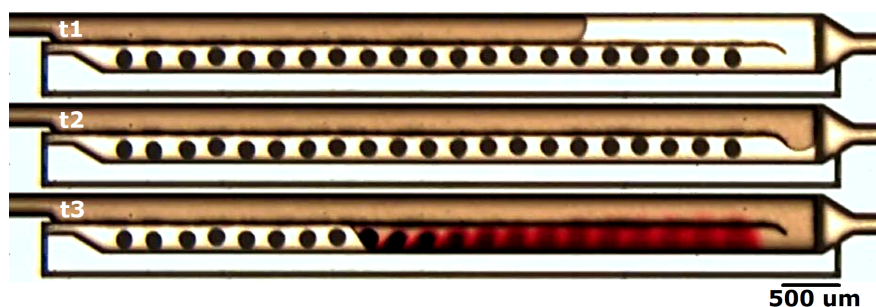


Figure 3.2 Experimental resuspension of amaranth dye deposited by inkjet printing in the SCM. The fluid fills the upper part of the device (t_1) to reach the end of the CPL (t_2) and start filling in the orthogonal flow mode (t_3) preventing the accumulation of reagents at the capillary front. (See Video A.16)

In order to determine the key properties of SC flows and extract key behavior and scaling laws, we performed several approximations to reduce the full 3D, time-dependent free boundary Stokes flow into a form tractable analytically. In this section, we provide a step by step development of the key



Figure 3.3 Fluorescent microspheres (4.8 μm diameter) revealing stagnancy of the flow far from the receding meniscus. (See Video A.15)

results obtained in Eq. A.1 and A.2 in the paper and a step by step construction of Fig. A.1e by using Hele-Shaw theory and conformal mapping to solve this type of time-dependent free-boundary flow problem.

3.2 Background : Hele-Shaw approximation in self-coalescence

In physical terms, a 3D Navier-Stokes flow can be converted to a Hele-Shaw cell with minimal error (concentrated along the domain boundaries) if three conditions are respected: i) the flow is planar; ii) the Reynolds number is small (Stokes flow); iii) the path followed by a fluid element in the flow field is much larger than the cell depth (that is: $H^2 \ll L_c^2$, where $L_c \sim W$). SCMs can be conveniently described by a quasi 2D flow in a Hele-Shaw cell, since the above conditions should be respected for several practical reasons. First, the stability of the meniscus over the CPL and the Laplace burst pressure at the diversion rail will be increased as the channel depth is made smaller. Secondly, making the device wider increases possibilities for printing reagents as the printing surface becomes larger. Thirdly, upon reconstitution, the spotted reagent concentration increases in the fluid when the ratio of H/W is kept small.

In this paper, we consider the height-averaged Hele-Shaw cell, with the governing equations:

$$\mathbf{v}_{ave}(x,y) = \frac{1}{H} \int_{z=0}^{z=H} \mathbf{v}(x,y,z) dz = -\frac{H^2}{12\eta} \nabla p(x,y) \quad (3.1)$$

Furthermore, for incompressible fluids (*e.g.* water), conservation of mass requires that the divergence of the flow field be zero ($\nabla \cdot \mathbf{v}_{ave} = 0$) outside of flow sources, yielding Laplace's equation

$$\nabla^2 p(x,y) = 0 \quad (3.2)$$

In purely 2D flows governed by Laplace equation, the pressure can be generalized to a complex potential function of the form $\Psi(z) = \phi(x,y) + i\psi(x,y)$, where $z = x + iy$, and $\phi(x,y) =$

$-(H^2/12\eta)p(x,y)$ is the velocity potential and $\psi(x,y)$ is the stream function [80]. Thus, Laplace's equation can be written using a single complex variable z , as

$$\nabla_z^2 \Psi(z) = 0 \quad (3.3)$$

with $\nabla_z^2 = d/dz(d/d\bar{z})$. This equation is well known to be conformally invariant and a rich body of literature is dedicated to solving this type of 2D Laplace problem using conformal mapping [214].

3.3 SC free boundary problem formulation

In studying self-coalescence (SC), we first observe experimentally (Video A.15) that, when a constant flow rate is introduced in a thin, elongated microstructure, the velocity of the meniscus (the leading air/water interface) moves at constant speed U_m (Fig. 3.4a). Therefore the shape of the meniscus does not vary and propagates as a kinematic wave (or shock) inside the channel. Spectacular progress since the early work of Polubarinova-Kochina and Galin (1945) have been made to study free boundary flow in Hele-Shaw cells using conformal mapping, a powerful analytical technique that uses transformations in the complex plane to map a geometry onto another simpler one, while leaving Laplace's equation invariant [214, 215].

In general, solutions to free boundary problems are challenging to obtain. Typically, one seeks a mapping of the expanding reference domain (the physical domain) onto a simpler one (typically the unit circle) with fixed boundaries. The problem is then solved in this fixed domain and the inverse mapping is used to find the solution in the physical domain.

In the self-coalescing flow problem, we are in the presence of an expanding domain (the water-filled part of the channel) and the unknown complex potential associated to the problem is time-dependent ($\Psi(z) \rightarrow \Psi(z,t)$). The boundary conditions (Fig. 3.4a) are also defined on a moving wall $\Gamma(z,t)$:

$$\operatorname{Re} \left\{ \frac{d\Psi}{dz} \right\} = \begin{cases} U, & z \rightarrow -\infty; \\ -U_m, & z = \Gamma_2; \\ 0, & z \rightarrow +\infty, \end{cases} \quad \operatorname{Im} \left\{ \frac{d\Psi}{dz} \right\}_{z=\{\Gamma_1, \Gamma_2\}} = 0, \quad \operatorname{Re} \{ \Psi \} = -\frac{H^2}{12\eta} p_{\text{cap}}, \quad (3.4)$$

where Γ_1 and Γ_2 are respectively the upper and lower boundary of the SCM.

Instead of solving the mixed boundary condition problem directly, we exploit the translational symmetry of the structure and observe that by adding a linear potential term of the form $\Psi'(z,t) = A_1 z + A_2(t)$, Eq. 3.3 remains invariant. Furthermore, in the reference frame of the moving meniscus, the translational invariance of the problem suggests that $\Psi^* = \Psi^*(z^*)$, with $z^* = z + U_m t$. By

selecting the potential associated to the reference change to be exactly $\Psi'(z, t) = U_m(z + U_m t) = U_m z^*$, the new potential becomes $\Psi^*(z^*) = \Psi(z, t) + U_m(z + U_m t)$ and the boundary conditions expressed above in Eq. 3.4 simplify to:

$$\operatorname{Re} \left\{ \frac{d\Psi^*}{dz^*} \right\} = \begin{cases} U + U_m, & z^* \rightarrow -\infty; \\ U_m, & z^* \rightarrow +\infty, \end{cases} \quad \text{and} \quad \operatorname{Re} \left\{ \frac{\partial \Psi^*}{\partial n} \right\}_{z^*=\{\Gamma_1, \Gamma_2\}} = 0, \quad (3.5)$$

where we introduce here the operator $\partial/\partial n$, the derivative in the direction normal to the boundary $\Gamma(z^*)$, with $\partial/\partial n = 0$ representing a boundary condition of the Neumann type.

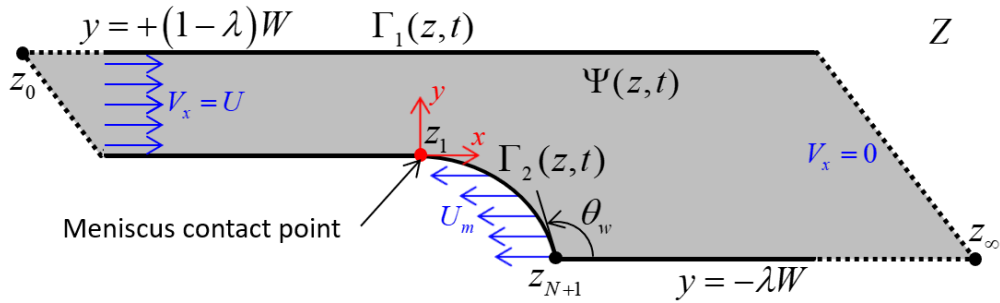
Physically, we observe that the addition of the potential $\Psi'(z^*)$ corresponds to a Galilean transform in a reference frame moving at constant velocity $-U_m$ with respect to the laboratory reference frame (Fig. 3.4b). The problem can therefore now be solved in the reference frame of the moving meniscus using a standard conformal map $z^* = f(\omega)$ to map the physical plane Z^* onto the upper half complex plane Ω with regular Neumann boundary conditions everywhere on $\Gamma(z^*)$ except at $\pm\infty$ (Fig. 3.4c). This property applies to all flows studied in this article and stems directly from the invariance of the Navier-Stokes equation under a Galilean Transform for the particular elongated geometry studied.

These two findings, 1) using the fact that Navier-Stokes equation is invariant under a Galilean transformation, and 2) that the appropriate reference frame suggested leaves the domain regular with only Neumann boundary conditions, the only kind tractable using conformal mapping, are the two key physical observations required to implement our analytical strategy. Even though they are simple, finding and formalizing them took significant efforts and was, in some way, a lucky turn of events.

3.4 Numerical solution of the flow inside a SCM

Several numerical methods can be used to analyze SC in elongated geometries. FEM provide an accurate description of the flow profile. However, it yields no insight on the relationship between the flow properties and the geometrical parameter. Simple scaling arguments offer asymptotic solutions in certain specific flow regimes, but offer no possibility to connect these regimes together. In this view, conformal mapping offers an attractive approach to model SC as it provides both. First, it yields a quasi-analytical solution with arbitrary precision of the phenomenon (Section 3.5). Secondly, this map can be approximated locally to yield asymptotic solutions at every point of interest (as in Sections 3.6.1 and 3.6.3). The general solution strategy is to observe that the circular arc of the meniscus can be approximated by a series of N linear segments (Fig. 3.5). Thus, the Z^* domain can be mapped onto Ω using Schwarz-Christoffel transformation [72] and every vertex

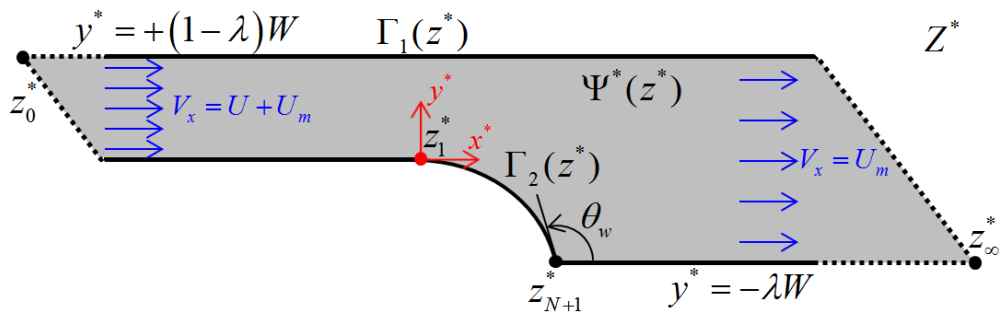
(a)



$$\Psi^*(z^*) = \Psi(z, t) + U_m z^* \quad \Leftrightarrow \quad \Psi(z, t) = \Psi^*(z^*) - U_m z^*$$

$$z^* = z + U_m t \quad \quad \quad z = z^* - U_m t$$

(b)



$$z^*(\omega) \quad \Leftrightarrow \quad \omega(z^*)$$

(c)

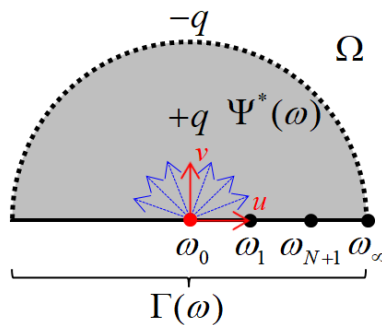


Figure 3.4 Reference frame change $Z \rightarrow Z^*$ and Schwarz-Christoffel mapping $Z^* \rightarrow \Omega$.

$z_n \in Z^*$ can be mapped from an associated prevertex $\omega_n \in \Omega$. It follows that an infinite number of segments would form a perfect circle. In practice, yet, an N -sided polygon with arbitrarily large N is sufficient. The expression for the circle's radius and the z_{N+1}^* vertex location are respectively given by

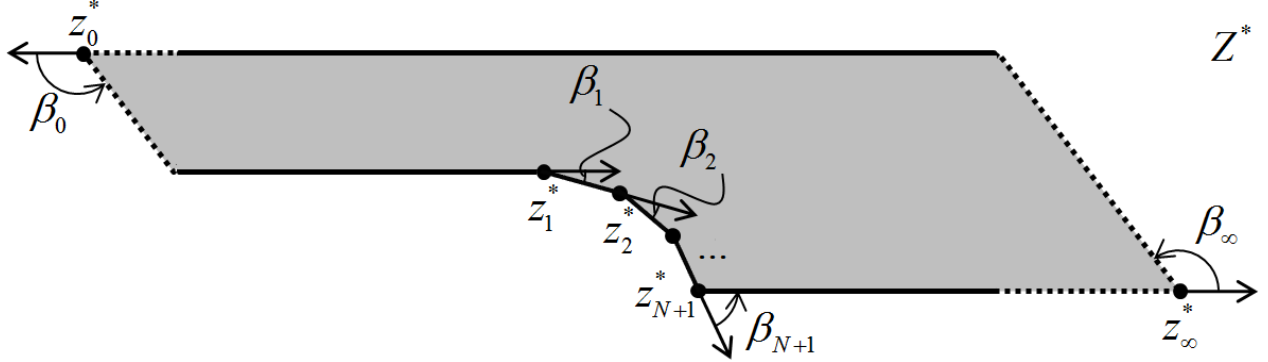


Figure 3.5 Geometry of the curved meniscus in a SCM.

$$r = \frac{\lambda W}{1 + \cos \theta_w}, \quad z_{N+1}^* = \lambda W \left(\tan \frac{\theta_w}{2} - i \right) \quad (3.6)$$

where θ_w is the dynamic contact angle at constant velocity U_m and λ is the ratio between the width of the returning flow zone and the total width of the SCM. The exterior angle β_{N+1} tends towards $\beta \equiv \pi - \theta_w$ as the number of vertices N gets larger, and the exterior angles along the meniscus are given by $\beta_{2 \leq n \leq N} = -\beta/N$ and $\beta_1 = -\beta/2N$. According to the Riemann mapping theorem [216, 217], we can arbitrarily fix three prevertices in Ω to map any points in Z^* as long as the ordering is kept the same. Choosing $\omega_0 = 0$, $\omega_{N+1} = 1$ and $\omega_\infty \rightarrow \infty$, we are left with N unknown prevertices located in the interval $(0, 1)$. Thus, the function mapping Ω to Z^* can be written as

$$z^*(\omega) = C_1 + C_2 \int_1^\omega \frac{1}{\omega'} \left\{ \frac{\prod_{n=1}^N (\omega' - \omega_n)^{\frac{1}{N}}}{\omega' - 1} \right\}^{1 - \frac{\theta_w}{\pi}} d\omega' \quad (3.7)$$

wherein $z^*(1) = C_1 = z_{N+1}^*$. The two source terms are located at $\pm\infty$ in the Z^* plane. Using Eq. 3.7, they are mapped at 0 and ∞ in the Ω plane. It ensues that the potential in Ω is

$$\Psi^*(\omega) = \frac{2q}{2\pi} \ln(\omega) \quad (3.8)$$

where q is the volume of fluid going through the system per second in unit height, i.e. $q = Q^*/H$ where $Q^* = Q/\lambda$ is the flow rate in the moving reference frame. The point source at ω_0 has for value $2q$ since only the upper complex plane is included (Fig. 3.4c). From the boundary conditions

expressed in Eq. 3.5, we find $q = U_m W$. Knowing the expression for the complex velocity:

$$\bar{V} = V_x - iV_y = \frac{d\Psi}{dz} = \left(\frac{d\Psi^*}{d\omega} \frac{d\omega}{dz^*} - \frac{d\Psi'}{dz^*} \right) \frac{dz^*}{dz} = \frac{q}{\pi\omega} \left(\frac{dz^*}{d\omega} \right)^{-1} - U_m \quad (3.9)$$

it follows that

$$\bar{V}^*(\omega) = \bar{V} + U_m = \frac{WU_m}{\pi\omega} \left(\frac{dz^*}{d\omega} \right)^{-1} \quad (3.10)$$

and from Eq. 3.7 we get

$$\bar{V}^*(\omega) = \frac{q}{\pi C_2} \left\{ \frac{\omega - 1}{\prod_{n=1}^N (\omega - \omega_n)^{\frac{1}{N}}} \right\}^{1 - \frac{\theta_w}{\pi}} \quad (3.11)$$

Since $\bar{V}^* = U_m$ when $\omega \rightarrow \infty$, we find the second integration constant to be $C_2 = W/\pi$. Subsequently, the complex velocity can be expressed as

$$\boxed{\bar{V}^*(\omega) = U_m \left\{ \frac{\omega - 1}{\prod_{n=1}^N (\omega - \omega_n)^{\frac{1}{N}}} \right\}^{1 - \frac{\theta_w}{\pi}}} \quad (3.12)$$

with the mapping solution

$$\boxed{z^*(\omega) = z_{N+1}^* + \frac{W}{\pi} \int_1^\omega \frac{1}{\omega'} \left\{ \frac{\prod_{n=1}^N (\omega' - \omega_n)^{\frac{1}{N}}}{\omega' - 1} \right\}^{1 - \frac{\theta_w}{\pi}} d\omega'} \quad (3.13)$$

Thus, from Eq. 3.13 we can map any point of Ω to Z^* . Yet, we still have to define the N unknown prevertices. The values of ω_n are found by equating the known values of z^* to the integral form of z^* , i.e.

$$|z_j^* - z_i^*| = \frac{W}{\pi} \int_{\omega_i}^{\omega_j} \frac{1}{\omega'} \left\{ \frac{\prod_{n=1}^N (\omega' - \omega_n)^{\frac{1}{N}}}{\omega' - 1} \right\}^{1 - \frac{\theta_w}{\pi}} d\omega' \quad (3.14)$$

Thus, we proceed by building a set of N equations with N unknowns (the prevertices). This process is known as the *parameter problem* and can be solved numerically [218]. Once we have the location of all the prevertices, we proceed by inverting Eq. 3.13 to find $\omega(z^*)$ and substitute it in Eq. 3.12 to get the complex velocity as a function of z^* . Comparison of this quasi-analytical solution with uPIV data and a 3D laminar incompressible Navier-Stokes model reveals the accuracy of this approach (Supl. Fig. 3.6). The FEM model and the quasi-analytical model are evaluated at half-height ($H/2$) whereas the uPIV experiment data are taken on the full height of the SCM, hence the two models

forming a velocity envelope over the experiment.

Thus, SCMs can be accurately modelled when converted to a Hele-Shaw cell when far from the boundaries at the side walls. More details regarding the calculation of the prevertices ω_n for Eq. 3.13 are presented in following section.

3.5 Solving the Schwarz-Christoffel mapping

The map from Eq. 3.13, although compact, is not appropriate for numerical treatment. Indeed, the unknown vertices ω_n spread exponentially in Ω in such a way that they are extremely close towards $\omega = 0$. With a relatively high N , which is required to capture the behavior of the flow near the origin (Fig. 3.6), it becomes impossible to solve with finite precision arithmetic. This is known as the *crowding phenomenon* [218]. To prevent this effect, we would like to map from a domain closer in resemblance to the original geometry. In this case, that would be an infinite strip open at both ends.

Mapping from the bi-infinite strip of width δ/π introducing $\omega = \exp(\delta t)$, we find

$$z^*(t) = z_{N+1}^* + \delta \frac{W}{\pi} \exp \left[\frac{\delta}{2} \left(1 - \frac{\theta_w}{\pi} \right) \sum_{n=1}^N t_n \right] \int_0^t \left\{ \frac{\prod_{n=1}^N \sinh^{\frac{1}{N}} \left[\frac{\delta}{2} (t' - t_n) \right]}{\sinh \left(\frac{\delta}{2} t' \right)} \right\}^{1 - \frac{\theta_w}{\pi}} dt' \quad (3.15)$$

with

$$\bar{V}^*(t) = U_m \exp \left[-\frac{\delta}{2} \left(1 - \frac{\theta_w}{\pi} \right) \sum_{n=1}^N t_n \right] \left\{ \frac{\sinh \left(\frac{\delta}{2} t' \right)}{\prod_{n=1}^N \sinh^{\frac{1}{N}} \left[\frac{\delta}{2} (t' - t_n) \right]} \right\}^{1 - \frac{\theta_w}{\pi}} \quad (3.16)$$

In this map the prevertices t_n are spread linearly instead of exponentially, hence getting around the crowding of prevertices close to the origin. Then, by the same process introduced in the last section, we build and solve a system of N equations with the N unknown prevertices, invert the map and substitute the result in the complex velocity. A comparison of the quasi-analytical result with a finite element model and uPIV experiments are shown in Fig. 3.6.

The FEM platform COMSOL Multiphysics[®] was used to model simulate 3D and 2D flows in SCMs. Both geometries were defined using COMSOL's CAD tools. The parameters used in the models are shown in Tab. 3.1. 3D laminar and 2D potential flows were respectively defined using COMSOL's *Laminar Flow* and *Mathematics* modules, i.e. the incompressible Navier-Stokes equations and the Laplace equation. In both cases, the problem is solved in the reference frame of the moving meniscus (the Z^* domain in Section 3.3) and plotted in the laboratory reference frame (the Z domain) with the transformation $z^* = z + Ut$. This equivalence specifically implies the in-

variance property of the Navier-Stokes equation under a Galilean transformation. These equations were both solved using the built-in steady-state fully coupled solver. Elements were manually refined on the meniscus' boundary to obtain sufficient numerical accuracy. Parametric sweeps were used to study the impact of the total width, contact angle and flow rate on the velocity field. The orthogonal velocity component was taken from a line going through the SCM along the x -axis at different y -positions and at mid-height in the Navier-Stokes case.

Preliminary 3D laminar flow simulations were also conducted to understand the general behaviour of flow decay in SCMs. The effects of topological changes in the SCM such as trenches versus rails, channel width and height, meniscus topology and others, were investigated. It was found that trenches were preferable to rails, as far as the flow is concerned, because of the flow constriction occurring above rails. Furthermore, the flow was found to decay exponentially regardless of the shape of the meniscus, and the decay scales with the width of the system. These results were valuable to give early design rules for SCMs, and helped to develop the theoretical framework explaining how the flow behaves [219].

Table 3.1 Parameter description and values used in COMSOL simulations.

Parameter	Description	Value
H	Channel height	50 μm
W	Channel total width	500 μm
L	Channel length	1 cm
θ_w	Contact angle (experimentally measured)	varies (default 116 deg)
Q	Flow rate	0.5 – 1.5 $\mu\text{L min}^{-1}$
ρ	Water density at NTP	1 kg m^{-3}
μ	Water viscosity at NTP	1 mPa s

3.6 Asymptotic solutions and self-coalescing flow modes

To elicit the flow properties of self-coalescing flows would require solving Eq. 3.13 analytically, which is not possible as the integral does not possess a primitive, nor would the resulting function be invertible. Although numerical solutions can be provided, to extract the length and time scales of the phenomenon, we proceed to find asymptotic solutions of fully developed flow regions near and past the meniscus.

3.6.1 Flow profile far from the meniscus

Far past the meniscus the flow velocity decreases to zero, but it is the functional form of this decay to zero that will reveal the scales relevant to the problem. To find the asymptotic solution when

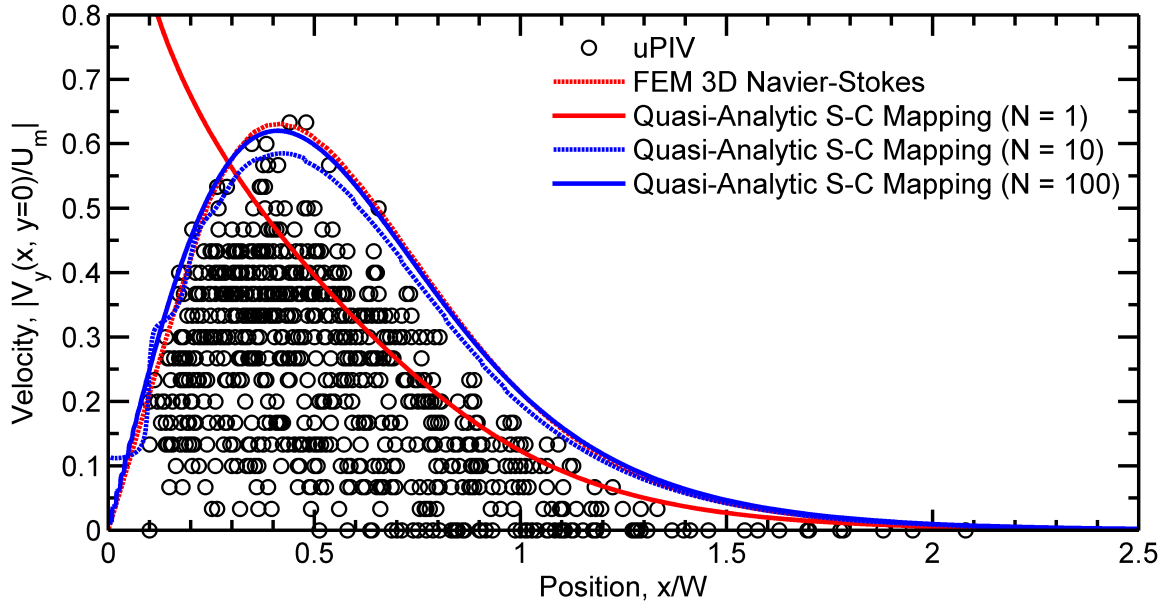


Figure 3.6 Comparison of a uPIV experiment with a 3D Navier-Stokes finite element model and the simplified case of a Hele-Shaw cell using conformal mapping for different number of vertices N . The $N = 1$ problem approximates a circle arc with a line and the problem solved in that case is simply the flow near a slanted back drop as described in Section 2.1.2 above. The experimental and numerical parameters are $U = 1$ mm/s, $H = 50$ μ m, $W = 500$ μ m, $\lambda = 0.5$, $\theta_w = 116^\circ$.

$z \gg z_{N+1}$ ($\omega \gg 1$), we introduce the variable changes $\varepsilon = 1/\omega$, where $d\omega = -d\varepsilon/\varepsilon^2$, in Eq. 3.13:

$$z^*(\omega) = z_{N+1}^* - \frac{W}{\pi} \int_1^\varepsilon \frac{1}{\varepsilon'} \left\{ \frac{\prod_{n=1}^N (1 - \omega_n \varepsilon')^{\frac{1}{N}}}{1 - \varepsilon'} \right\}^{1 - \frac{\theta_w}{\pi}} d\varepsilon' \quad (3.17)$$

Applying a Laurent series expansion at $\varepsilon = 0$ yields

$$g(\varepsilon) = \left\{ \frac{\prod_{n=1}^N (1 - \omega_n \varepsilon')^{\frac{1}{N}}}{1 - \varepsilon'} \right\}^{1 - \frac{\theta_w}{\pi}} = \sum_{k=0}^{\infty} \frac{a_k}{k!} \varepsilon^k \quad (3.18)$$

where $a_k = g^{(k)}(0)$ and $a_0 = 1$. Using the above approximation, Eq. 3.17 reduces to:

$$z^*(\varepsilon) = z_{N+1}^* - \frac{W}{\pi} \left[-\alpha + \ln \varepsilon + \sum_{k=1}^{\infty} \frac{a_k}{kk!} \varepsilon^k \right] \quad (3.19)$$

and substitution of ω back into Eq. 3.19 yields

$$z^*(\omega) = z_{N+1}^* + \frac{W}{\pi} \left[\alpha + \ln \omega - \sum_{k=1}^{\infty} \frac{a_k}{kk!} \left(\frac{1}{\omega^k} \right) \right] \quad (3.20)$$

where $\alpha = \sum_{k=1}^{\infty} a_k/kk!$ is a real constant composed of all the prevertices of the polygonal meniscus. The position of these prevertices can only be found numerically. Nevertheless, we know by definition that $\omega_n(n)$ is a monotonically increasing function of value comprised between $\omega_0 = 0$ and $\omega_{N+1} = 1$. Furthermore, the exact position of the prevertices will also depend on the system's contact angle since a higher contact angle will spread them over a longer meniscus in Z^* .

From equations 3.10 and 3.20, the complex velocity is calculated to be

$$\bar{V}^*(\omega) = U_m \left[1 + \sum_{k=1}^{\infty} \frac{a_k}{k! \omega^k} \right]^{-1} \quad (3.21)$$

Looking for the leading order of the complex velocity when $\omega \gg 1$, we get

$$\bar{V}^*(\omega) = U_m \left[1 - \frac{a_1}{\omega} \right] + \mathcal{O} \left(\frac{1}{\omega^2} \right) \quad (3.22)$$

In a similar manner, looking for the leading order of the map for large ω yields

$$z^*(\omega) = z_{N+1}^* + \frac{W}{\pi} (\alpha + \ln \omega) + \mathcal{O} \left(\frac{1}{\omega} \right) \quad (3.23)$$

which can be inverted to

$$\omega(z^*) = \exp \left[\frac{\pi}{W} (z^* - z_{N+1}^*) - \alpha \right] \quad (3.24)$$

It follows from equations 3.24 and 3.22 that the velocity behaves asymptotically as

$$\bar{V}^*(z^*) = U_m \left[1 + A \exp \left(-\frac{\pi}{W} z^* - i\lambda \pi \right) \right] \quad (3.25)$$

where the real dimensionless geometric constant for large N is given by

$$A \equiv A(W, \lambda, \theta_w) = - \left(1 - \frac{\theta_w}{\pi} \right) \left(1 - \sum_{n=1}^N \frac{\omega_n}{N} \right) \exp \left[\alpha + \lambda \pi \tan \frac{\theta_w}{2} \right] \quad (3.26)$$

The parameter A is only composed of geometric parameters, hence geometric constant, such as the contact angle θ_w , the width of the SCM and the position of all the prevertices of the polygonal

meniscus. In this analysis, numerically finding a lumped value for A is sufficient as the individual values of a_k and ω_n do not appear anywhere else.

Going back into the laboratory reference frame, i.e. $\bar{V} = \bar{V}^* - U_m$ with $z^* \rightarrow z + U_m t$, the complex velocity profile can be compactly written as

$$\bar{V}(x, y, t) = U_m A \exp \left[-\frac{\pi}{W} (x + i(y + \lambda W) + U_m t) \right], \quad x + iy + U_m t \rightarrow \infty. \quad (3.27)$$

From Eq. 3.27, we observe that the leading order of the velocity profile is purely imaginary when $y + \lambda W = W/2$, that is orthogonal to the propagation velocity of the meniscus (Fig. 3.7). Since Eq. 3.27 clearly demonstrates that the exponential decay profile always scales with W/π regardless of the position of the CPL inside the channel or any other physical parameters (Fig. 3.8), SCMs can be engineered with $\lambda \sim 1$, such as to leave maximum space for reagent printing while negligibly affecting dispersion.

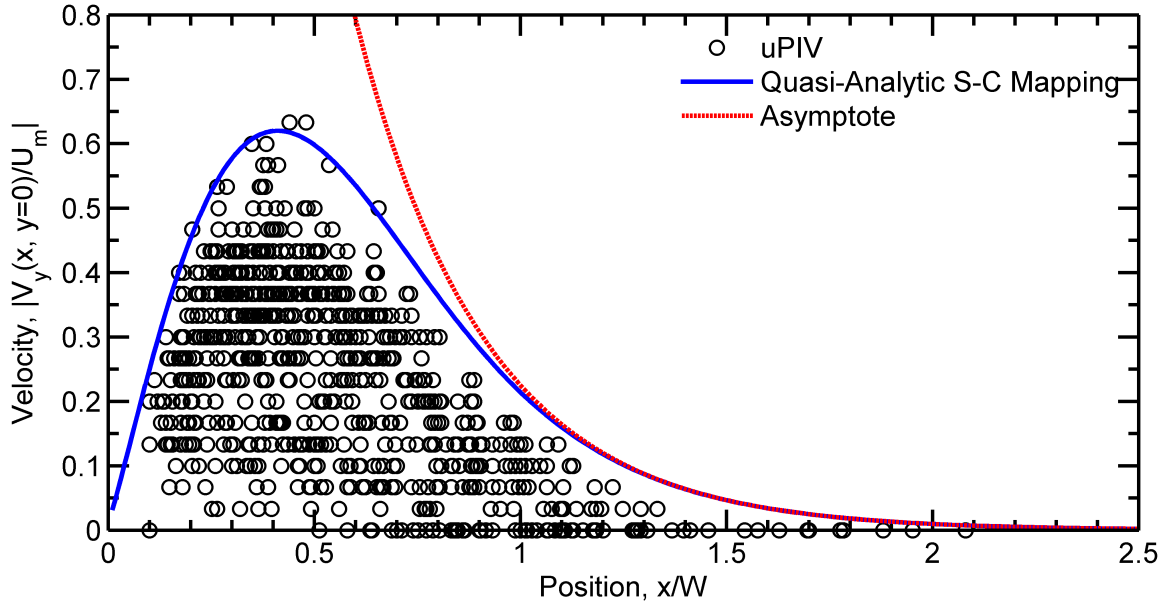


Figure 3.7 Comparison of the asymptotic exponential velocity decay when far from the meniscus with the conformal mapping solution and experimental uPIV. The experimental and numerical parameters are $U = 1$ mm/s, $H = 50$ μ m, $W = 500$ μ m, $\lambda = 0.5$, $\theta_w = 116^\circ$, $N = 100$.

3.6.2 Flow profile far from the meniscus: link with Saffman-Taylor viscous fingering

When a fluid penetrates a Hele-Shaw cell containing a fluid of higher viscosity, the interface between the two phases may, under some stability criteria, form a stable surface [100]. In an

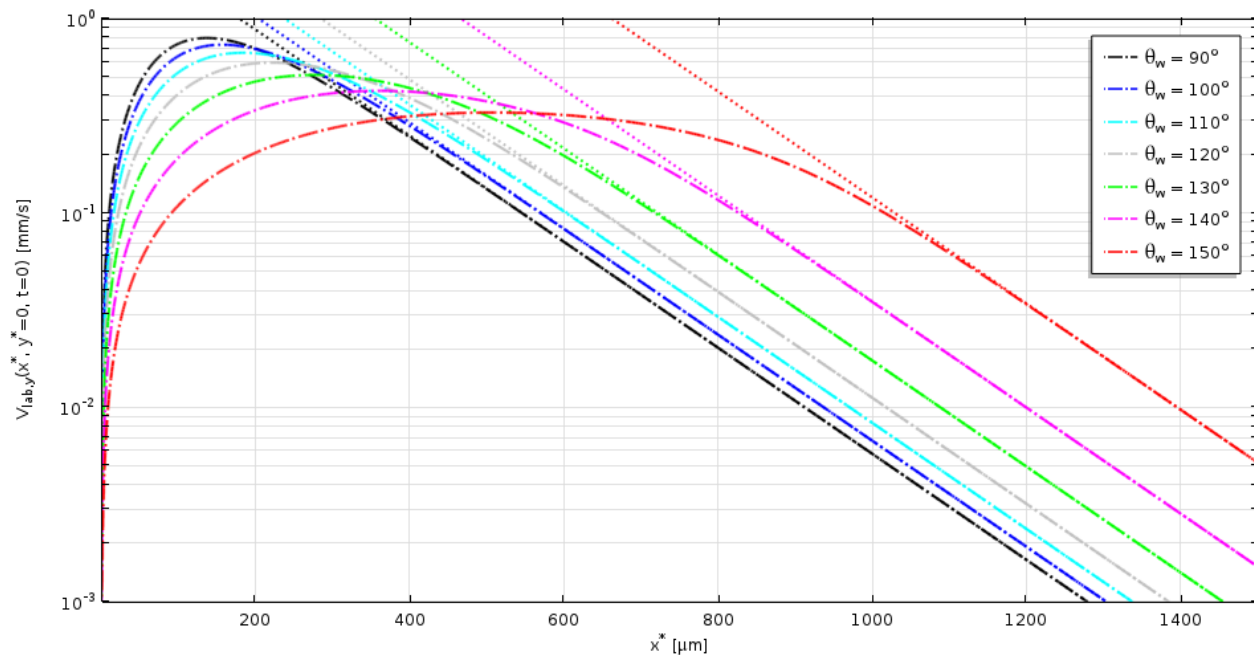


Figure 3.8 Numerical (dash-dot) and asymptotic (dot) solutions of the orthogonal velocity in the SCM as a function of position along the CPL for various contact angles θ_w and $\lambda = 0.5$.

elongated channel, that surface can take the shape of a single stable finger, also known as the Saffman-Taylor viscous fingering (STVF) phenomenon. To obey Laplace's equation and for the pressure to decay to zero far downstream the cell, the velocity must behave as

$$\bar{V}(z^*) = C \exp(-z^*/L_c) \quad (3.28)$$

where C is a complex proportionality constant and L_c the characteristic length of the velocity decay [101]. For a cell of width $2W$ and a single finger of width $2\lambda W$, L_c is calculated to be

$$L_c = \frac{W}{\pi} \quad (3.29)$$

Indeed, when viewing the no flux boundary condition at the bottom channel wall as a mirror symmetry, the link between SC and a receding form of STVF becomes obvious (Fig. 3.9, Video A.17). Yet, there are many fundamental differences between SC and STVF which suggest they are two separate, albeit mathematically related, phenomena. First, SC implies two discontinuities in the free surface to occur, respectively at the meniscus contact points with the CPL and the wall, while STVF studies the expansion/contraction of a smooth free surface.

Second, due to capillary pinning, SC can be engineered for any value of λ while Saffman and Taylor have made the well-known observation that values of $\lambda < 1/2$ never occur in STVF for low

capillary number flows ($Ca \sim 10^{-5}$ in our study).

Third, SC is in general contact angle-dependent, and similar to STVF only for the particular case of $\theta_w = \pi/2$ used in combination with a straight CPL. The conformal mapping approach employed here yields a general analytic framework to study and control SC over straight CPLs but the method can handle multiple shapes of CPLs, such as those used to create phaseguides [195]. It reveals the form of the dependence of the proportionality constant A on the meniscus velocity, the contact angle, and the geometry of the system. This asymptotic decay behavior is also observed for a large class of problems where a given potential is fixed at two opposite points of an elongated structure. A few examples are provided in Fig. 3.10. This is suggesting that for sufficiently well behaved menisci shapes, i.e. no obstruction of the flow path, an exponential velocity decay may be recovered far away from the meniscus. This is important from a design perspective as this suggests CPLs and SCMs can be given any shape, provided the Concus-Finn criterion holds, and SC will occur with an exponential velocity decay.

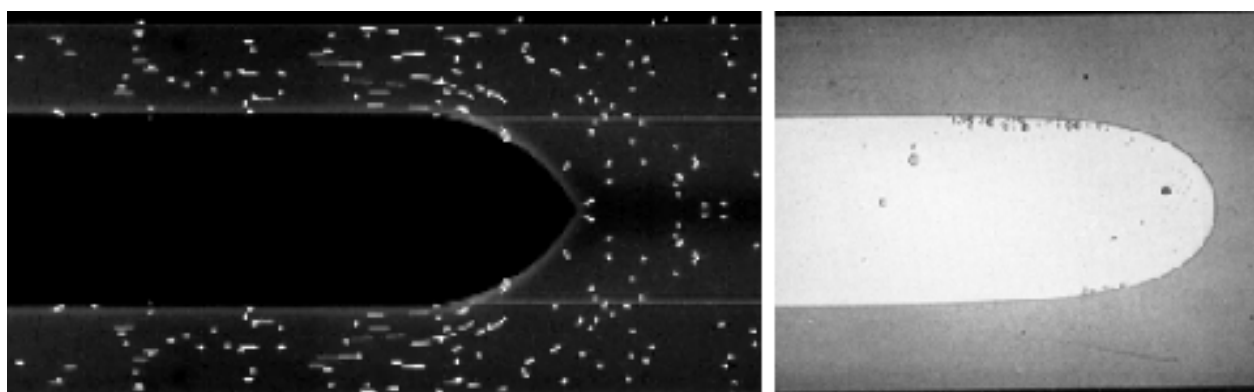


Figure 3.9 Filling of a SCM observed in fluorescence with a mirror symmetry at the lower boundary (left) and oil STVF in glycerin [100].

3.6.3 Entrance region flow profile

Another important distinction between SC and STVF is revealed when studying the flow near the meniscus contact point with the CPL. Due to a 2nd order discontinuity in the free surface absent in STVF, the y -component of the velocity profile is exactly zero at the contact point and is experimentally observed to increase linearly when moving downstream. This linear velocity increase past the contact point and its persistence downstream also plays an important role in determining the reagent reconstitution length scale and time scale. These, in turn, will determine the maximum resolution achievable during reconstitution.

When our Schwarz-Christoffel map is used to probe the solution near the origin, we observe a

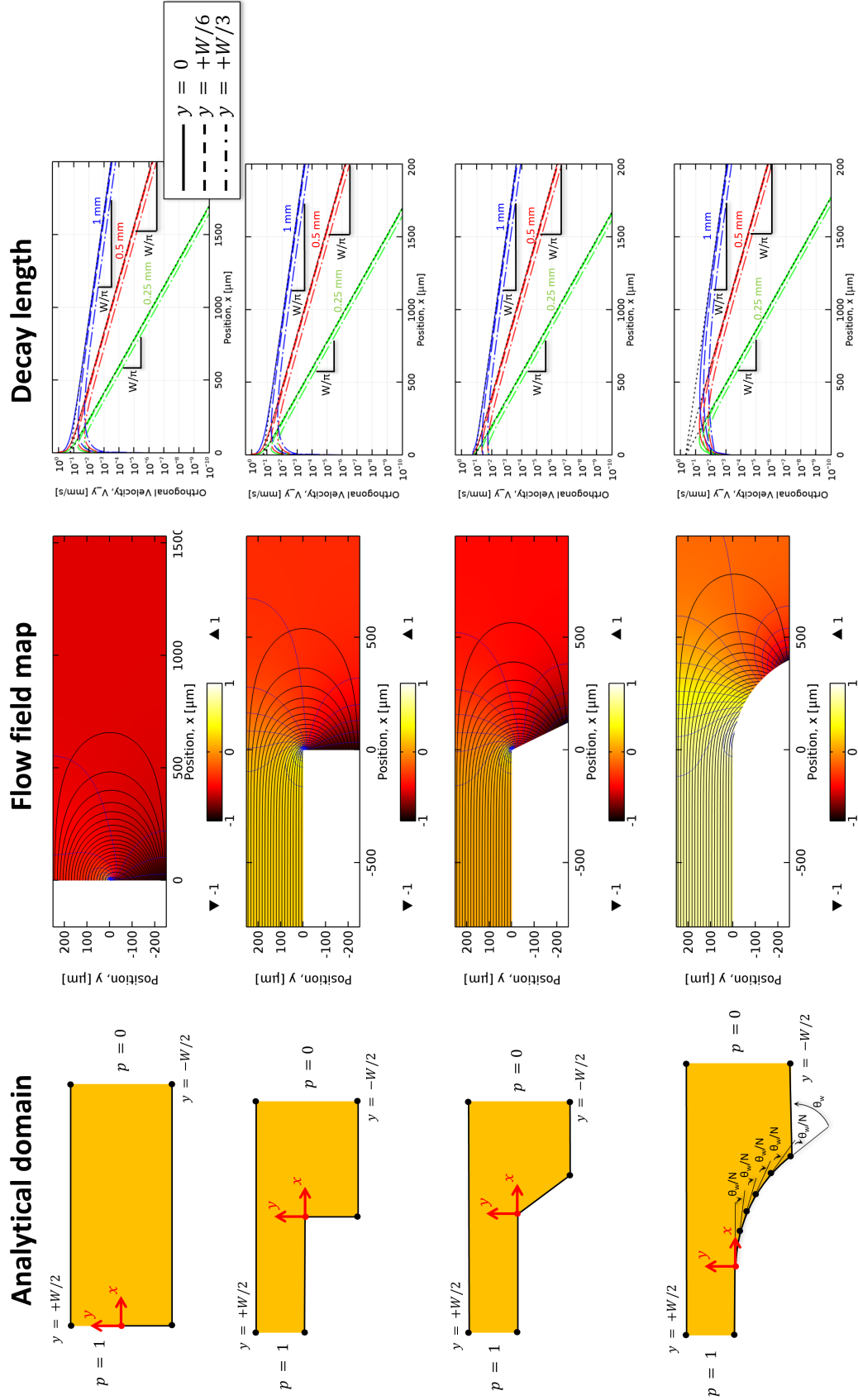


Figure 3.10 Different analytical maps providing an exponential velocity decay far from the inlet with characteristic decay lengths proportional to W/π . Analytical solutions are provided in Eq. 2.27 for the semi-infinite strip, Eq. 2.36 for the back step, and Eq. 2.47 for the inclined back step. The last map is that of the SCM derived herein.

self-similarity of the flow with respect to λ when the radius of the meniscus is kept constant (Fig. 3.11.)

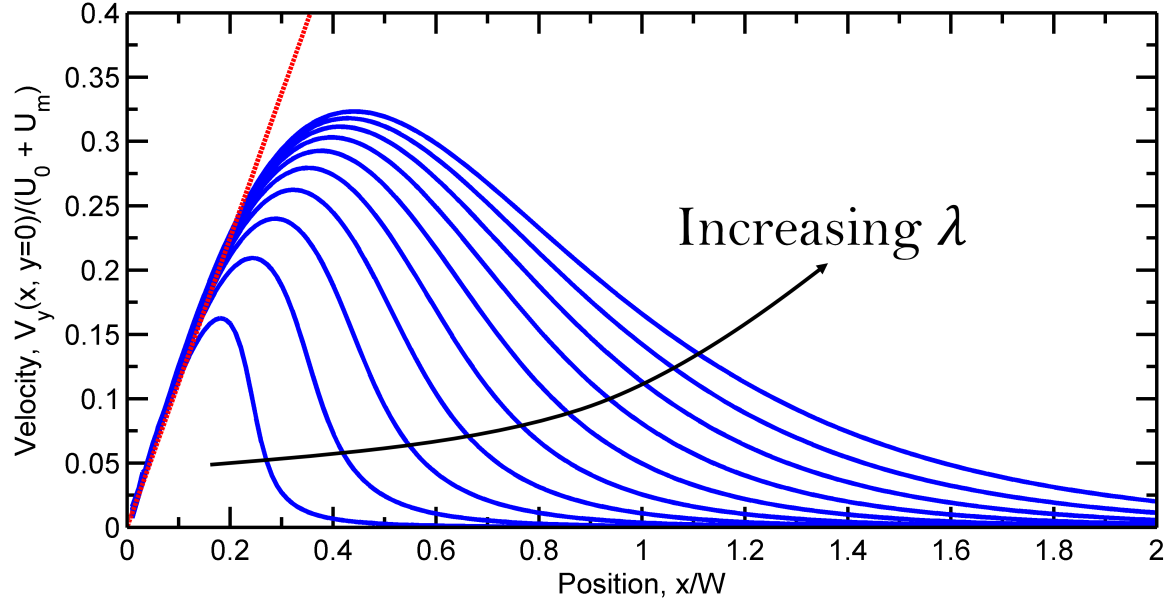


Figure 3.11 Self-similarity of the velocity near the origin with respect to λ with constant r . The parameters are $U = 1$ mm/s, $H = 50$ μ m, $\theta_w = 116^\circ$ and $N = 100$.

This suggests a flow map asymptotically akin to the flow map around a circular cylinder (Fig. 3.12). To elucidate that property, we use a Joukowski transformation $w = (1/2)(z + 1/z)$ for a circle of radius r centered in $z^* = -ir$ with an upstream flow velocity of $U + U_m$. This map is given by

$$w(z^*) = \frac{(U + U_m)r}{2} \left(\frac{z^* + ir}{r} + \frac{r}{z^* + ir} \right) \quad (3.30)$$

from which we get the complex velocity in the moving reference frame

$$\bar{V}^*(z^*) = \frac{U + U_m}{2} \left(1 - \frac{r^2}{(z^* + ir)^2} \right) \quad (3.31)$$

Computing the map and comparing with Eq. 3.31 makes clear that the flow near the tip of the meniscus connecting with the CPL can be approximated in this way (Fig. 3.12). Proceeding with a Taylor expansion of first order on Eq. 3.31 we extract the linear behavior of the velocity near the origin:

$$\bar{V}^*(z^*) = (U + U_m) \left(1 + i \frac{z^*}{r} \right) + \mathcal{O}(z^2) \quad (3.32)$$

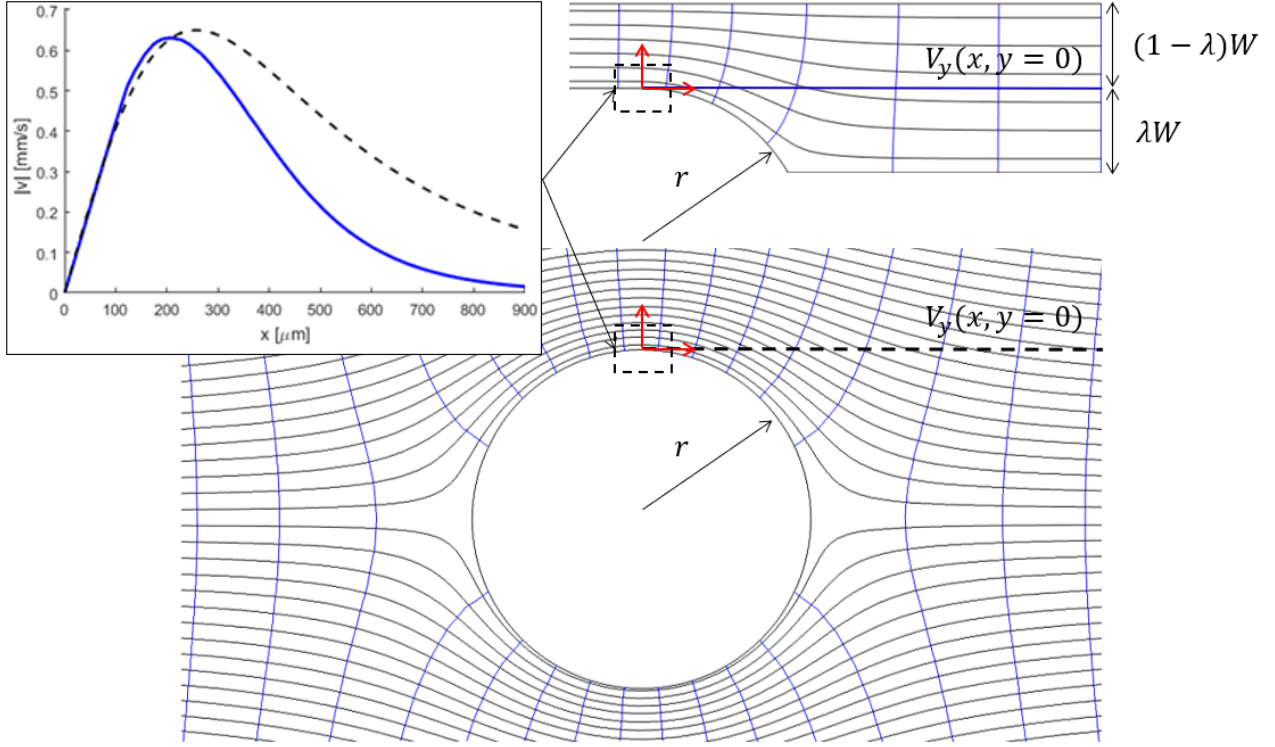


Figure 3.12 Comparison between the orthogonal flow profile within the SCM (blue solid line) and the flow over a cylinder (black dashed line) with identical radii. The velocity is zero at the meniscus contact point with the CPL and at the top of the cylinder. Downstream of z_1 , the velocity increases linearly in both cases and with the same slope. The radii are given by $r/W = 0.89$ with $W = 500 \mu\text{m}$, $H = 50 \mu\text{m}$, $\lambda = 0.5$, $\theta_w = 116^\circ$, $U = 1 \text{ mm/s}$ and $N = 100$.

Thus, we find the expression for the linear behavior presented in Fig. 3.11 which makes clear the self-similarity of the solution and provides a simple solution for the flow near the tip of the meniscus connecting with the CPL. In the laboratory reference frame, we obtain

$$\bar{V}(x, 0, t) = (U + U_m) \left(1 + i \frac{x + U_m t}{r} \right) - U, \quad (3.33)$$

where $r = \lambda W / (1 + \cos \theta_w)$ is the radius of the meniscus and U is the flow velocity at the inlet.

3.6.4 Physical interpretation of Self-Coalescence

At last we have a full solution to the problem and asymptotic flow behaviors to the leading order both right upstream and right downstream of the moving meniscus. Together, the simple Eq. 3.27 and Eq. 3.33 provide insight into the complex phenomenon of self-coalescence (Fig. 3.13). They reveal that (i) SC flow is a kinematic wave propagating at the velocity of the air/water interface,

(ii) the magnitude of the velocity field decays exponentially to zero past the meniscus regardless of its shape (step function, circular arc, etc.), the straight path followed downstream, or the position of the horizontal CPL relative to the channel centre, (iii) downstream from the meniscus SC flow decay scales with only one parameter, the width of the channel, and is always of characteristic length $L_d = W/\pi$ and time $t_d = W/(U_m\pi)$ (respectively $159\ \mu\text{m}$ and $238\ \text{ms}$ in experiments with $H = 50\ \mu\text{m}$, $W = 500\ \mu\text{m}$, $\lambda = 1/2$ and $Q_{\text{in}} = 0.5\ \mu\text{L/s}$, Fig. 1d). (iv) at the meniscus contact point with the CPL, the orthogonal velocity v_y is exactly zero and increases linearly (Eq. 3.33) before peaking and decaying exponentially.

The solutions provide useful scaling laws, e.g. exponential decay of the velocity as a function of the width of the channel, but physical limits exist bounding the scalability of devices. For instance, the model assumes a flow continuum requiring a small Knudsen number [126], i.e. the average distance a molecule or particle travels before a collision with another molecule or particle must be smaller than the characteristic length of the device. Thus, molecular flows would not abide by the same scaling laws. At the other end of the scale, volume forces such as gravity impose an upper bound on the scalability of devices as per Bond's number (Tab. 2.1). If devices were fabricated such as to have a Bond number closer to or higher than unity, capillary forces would not be strong enough to drive the liquid mass and other inertial effects might prevent proper functioning of devices.

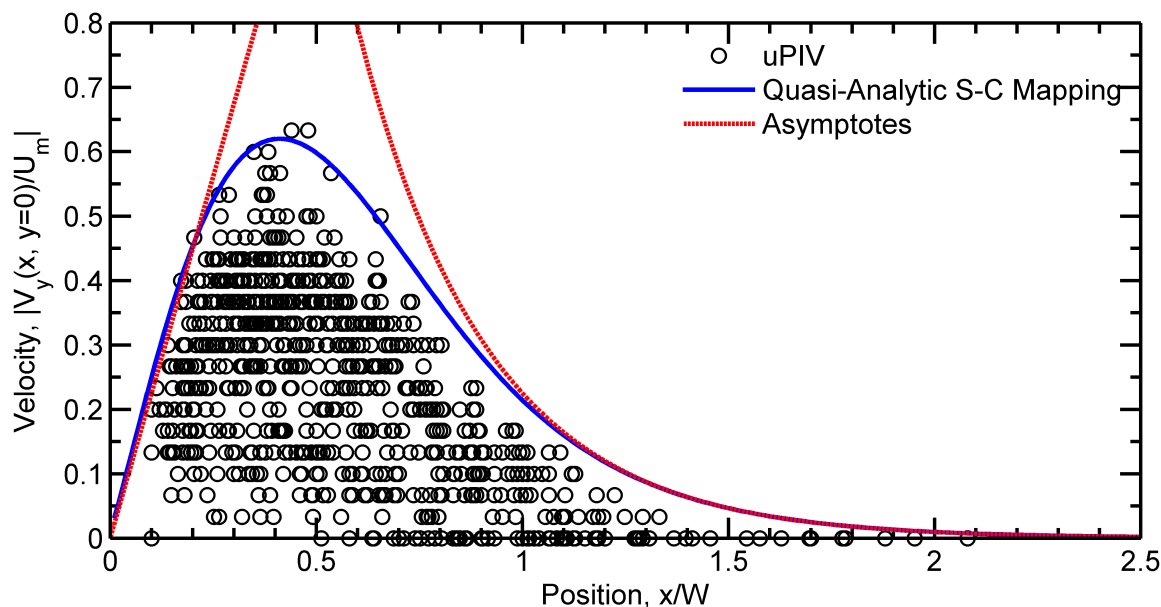


Figure 3.13 Linear asymptote near the origin and exponential asymptote far from the meniscus. Comparison with the quasi-analytic S-C solution and experimental uPIV. The experimental and numerical parameters are $U = 1\ \text{mm/s}$, $H = 50\ \mu\text{m}$, $W = 500\ \mu\text{m}$, $\lambda = 0.5$, $\theta_w = 116^\circ$, $N = 100$.

3.7 Additional details regarding the conformal mapping methodology

In the following section, we provide additional details regarding the conformal mapping methodology, i.e. 1) obtaining the Schwarz-Christoffel mapping numerical solutions, 2) converting the obtained pressure map into velocity in the physical frame of reference, 3) reverse-engineering the parameter problem when a flow solution is already known, and 4) introducing the open problem of mapping the SCM exactly, i.e. with curves, using the Schwarzian operator. Points 1-3 are critical for comparison of the analytical results with experiments and simulations, and point 4 establishes the theoretical framework for an exact mapping of SCMs which abstains from converting a circle into a polygon.

3.7.1 Schwarz-Christoffel mapping numerical solution

The numerical determination of the Schwarz-Christoffel (SC) transformation is a well-known computational problem which consists into solving a system of nonlinear equations for some *unknowns*. In other words, we must find all the ω_j parameters of the conformal transformation

$$z(\omega) = \mathbf{C}_1 + \mathbf{C}_2 \int_{\omega_0}^{\omega} \prod_{j=1}^N (\omega' - \omega_j)^{-\phi_j/\pi} d\omega' \quad (3.34)$$

This is known is commonly know as it *parameter problem*. One possible formulation of that problem is to solve the path length difference between two known points in the Z plane, i.e.

$$|z_i - z_j| = |z(\omega_i) - z(\omega_j)| = \mathbf{C}_2 \int_{\omega_i}^{\omega_j} \prod_{j=1}^N (\omega' - \omega_j)^{-\phi_j/\pi} d\omega' \quad (3.35)$$

Extracting $N + 2$ equations from Eq. 3.35, N equations for $\omega_{j=[1,N]}$ and 2 for \mathbf{C}_1 and \mathbf{C}_2 , or other possible formulations, we have to solve a constrained system of $N + 2$ nonlinear equations. For numerical purposes, it is often preferable to use the disk mapping formulation of the SC transformation,

$$z(\omega) = \mathbf{C}_1 + \mathbf{C}_2 \int_{\omega_0}^{\omega} \prod_{j=1}^N \left(1 - \frac{\omega'}{\omega_j}\right)^{-\phi_j/\pi} d\omega' \quad (3.36)$$

to avert singularities.

The parameter problem can be solved using the *Schwarz-Christoffel toolbox for MATLAB* developed by Driscoll [218]. Let us first define a vector of complex coordinates \mathbf{z} defining a bounded polygon \mathcal{P} in the Z plane. The function `polygon()` returns a structure containing the coordinates z_j with their respective exterior angles ϕ_j . The function `hplmap()` returns a compound function

that transforms \mathcal{P} into the complex upper half plane Ω . We can extract the ω_j values of the parameter problem from that function. The default formulation of the system with this function considers $\omega_1 = -1$, $\omega_{[2,N-2]} \in (-1, 1)$, $\omega_{N-1} = 1$ and $\omega_N = \infty$. We can also solve Laplace's equation using `lapsolve()` by fixing proper Dirichlet and Neumann conditions on the domain.

Although this toolbox is very efficient and accurate, it has numerical limits. Numerical instabilities occur in the case of elongated structures (high aspect ratios) and when evaluated points are near the z_j values (singularities). Furthermore, in geometries where vertices are closely packed, a crowding phenomenon occurs near ω_1 as values of $\omega_{[2,N-2]}$ tend towards ω_1 , and these values can get so close that their difference with ω_1 is smaller than machine epsilon.

3.7.2 Defining velocity numerically in the physical frame of reference

Let us find the numerical solution to Laplace's equation in the domain of the SCM as shown in Fig. 3.14. For simplicity, consider the labeling of the vortices as $\partial\mathcal{P}_i = \overline{z_i z_{i+1}}$. A constant pressure condition (Dirichlet condition) is set at the inlet and outlet, i.e. $p = p_0$ on $\partial\mathcal{P}_1$ and $p = 0$ on $\partial\mathcal{P}_{N+4}$. All other boundaries are set to Neumann conditions.

Computing the pressure field with `lapsolve()` function from Driscoll's toolbox yields a function which we evaluate in discrete space. In this case, a square grid discretization of the space is considered. Let us label the coordinates as $(x_{i,j}, y_{i,j}) \in \mathcal{P} \forall [i, j] \in \mathbb{N}$. Evaluating p for every discrete coordinates in \mathcal{P} gives us a pressure matrix of elements $p_{i,j}$.

Knowing from Hele-Shaw theory that

$$\mathbf{u} = -\frac{H^2}{12\mu} \nabla p_{i,j} \quad (3.37)$$

the velocity field can be computed by taking the gradient of p_{ij} using the finite difference method

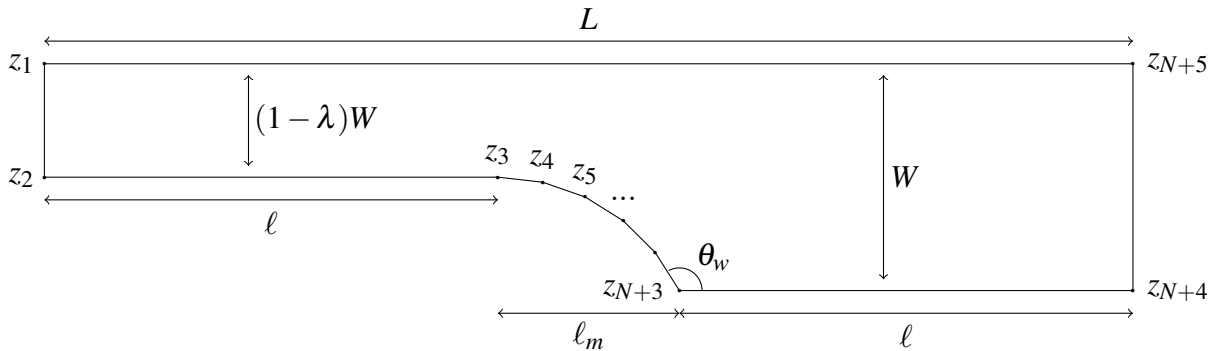


Figure 3.14 Numerical domain of the SCM.

(FDM). In this case, a simple central difference is used (Eq. 3.38).

$$\nabla p_{i,j} = \left(\frac{\partial p_{i,j}}{\partial x_{i,j}}, \frac{\partial p_{i,j}}{\partial y_{i,j}} \right) = \left(\frac{p_{i+1,j} - p_{i-1,j}}{x_{i+1,j} - x_{i-1,j}}, \frac{p_{i,j+1} - p_{i,j-1}}{y_{i,j+1} - y_{i,j-1}} \right) \quad (3.38)$$

To obtain the maximal velocity in the channel, i.e. $\mathbf{u}(z = H/2)$, simply multiply Eq. 3.37 by $3/2$.

Fixing the proper velocity at the inlet is the next problem in line. For now, the pressure is fixed at an arbitrary value, e.g. $p_0 = 1$. We know from Hagen-Poiseuille law that the pressure drop in laminar flows is proportional to the product between the flow rate and the hydraulic resistance:

$$\Delta p = QR_{hyd} \quad (3.39)$$

Solving the system a first time using an arbitrary inlet pressure and finding the velocity at the inlet (or outlet), we can find the proper Dirichlet condition to get a specific inlet velocity. Put simply,

$$p_1 = p_0 \frac{u_1}{u_0} \quad (3.40)$$

The next step is to change the reference frame of the velocity field back into the laboratory reference frame. In other words, subtracting the velocity of the meniscus U_m to the x -component of \mathbf{u} . From that field, we compute the pressure map by integrating the gradient of pressure. This is done using the MATLAB function `intgrad2()` developed by John D'Errico [220]. This function takes in two fields, in this case x - and y -components of the velocity, with mesh dimensions and returns the integrated gradient using FDM.

3.7.3 Solving the parameter problem *a posteriori*

We can also reverse engineer the parameter problem from a known solution to validate asymptotic flow solutions in SCMs. Knowing

$$\bar{V}(x,y,t) \approx U_m \tilde{A} \exp \left[-\frac{\pi}{W} (x + iy + U_m t) \right] \quad (3.41)$$

where \tilde{A} is a complex dimensionless constant (equivalent but slightly different from Eq. 3.26) defined as

$$\tilde{A} = \alpha \left(1 - \frac{\theta_w}{\pi} \right) \exp \left[\alpha \left(1 - \frac{\theta_w}{\pi} \right) + \lambda \pi \tan \left(\frac{\theta_w}{2} \right) - i \lambda \pi \right] \quad (3.42)$$

and α is a function of the sum of vertices in the Ω map approximating the meniscus, i.e ω_3 to ω_{N+3} according to Fig. 3.14.

$$\alpha = 1 - \sum_{j=3}^{N+2} \frac{\omega_j^{(j-1)(N-j)}}{N+1} \quad (3.43)$$

The value of α converges as the number of vertices and domain length increases (perfect circle and infinite domain approximation) as shown in Fig. 3.15.

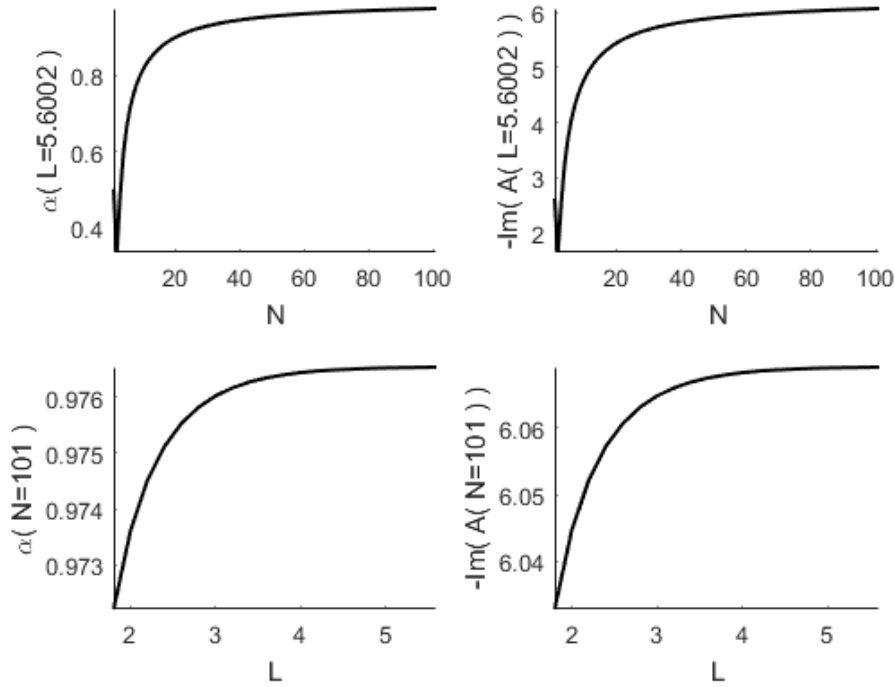


Figure 3.15 Convergence of α and \tilde{A} with respect to the domain length L and number of vertices N .

3.7.4 Exact mapping of the SCM with the Schwarzian operator (open problem)

Shortly after the discovery of Schwarz-Christoffel transforms, Schwarz also provided a method to map domains made of circular arcs rather than linear segments. Realizing that the self-coalescence geometry is composed of three straight lines (circular arcs with infinite radii of curvature) and one circular arc or radius $r = \lambda W / (1 + \cos \theta_w)$, we put some more efforts in trying to exploit this method to achieve an exact map which eschews the need to convert a circle into a polygon as we did in the previous section. Finding the function f that Maps the region of a polygon containing circular arcs in the Z complex plane to the upper half complex plane Ω can be done using the

Schwarzian operator

$$\{f, \omega\} = \left(\frac{f''(\omega)}{f'(\omega)} \right)' - \frac{1}{2} \left(\frac{f''(\omega)}{f'(\omega)} \right)^2 \quad (3.44)$$

Using the properties of $\{f, \omega\}$ and Liouville's Theorem,

$$\{f, \omega\} = \frac{1}{2} \sum_{n=1}^N \frac{(1 - \alpha_n^2)}{(\omega - \omega_n)^2} + \frac{1}{2} \sum_{n=1}^N \frac{\gamma_n}{\omega - \omega_n} + c \quad (3.45)$$

where $\alpha_n \equiv \theta_n/\pi$ are the interior angles of the polygon, c is a constant, and

$$\gamma_n = \frac{1 - \alpha_n^2}{\alpha_n} \frac{g'(\omega_n)}{g(\omega_n)} \quad (3.46)$$

where

$$f(\omega) = (\omega - \omega_n)^{\alpha_n} g(\omega) \quad (3.47)$$

The mapping function $f(\omega)$ is given by

$$f(\omega) = \frac{y_1(\omega)}{y_2(\omega)} \quad (3.48)$$

where $y_1(\omega)$ and $y_2(\omega)$ are two linearly independent solutions of the Schwarzian differential equation

$$y''(\omega) + \frac{1}{2} \{f, \omega\} y(\omega) = 0 \quad (3.49)$$

In cases of open polygons with vertices located at infinities, it may be preferable to map from the bi-infinite strip

$$\omega(t) = e^{\delta t} \quad (3.50)$$

Assuming $t_0 = -\infty$ and $t_\infty = +\infty$, the Schwarzian operator becomes

$$\frac{1}{\delta^2} \{f, t\} = -\frac{1}{2} \alpha_0 + \frac{1}{2} \sum_{n=1}^N \frac{1 - \alpha_n^2}{(1 - e^{-\delta(t-t_n)})^2} + \sum_{n=1}^N \frac{\gamma_n''}{1 - e^{-\delta(t-t_n)}} \quad (3.51)$$

and γ_n'' obeys

$$(1 - \alpha_0^2) + \sum_{n=1}^N [2\gamma_n'' + (1 - \alpha_n^2)] = (1 - \alpha_\infty^2) \quad (3.52)$$

More details regarding the Schwarzian operator, and a more detailed development of the previous equations can be found in Howell's work [221, 222] and [223]. The SCM mapping problem can

then be written as

$$\begin{aligned}
z_0 &= -\infty, & \alpha_0 &= 0, & \omega_0 &= 0, & t_0 &= -\infty; \\
z_1 &= 0, & \alpha_1 &= 1, & \omega_1 &\in (0, 1), & t_1 &\in (-\infty, 0); \\
z_2 &= \lambda W [\tan(\theta/2) - i], & \alpha_2 &= \theta/\pi, & \omega_2 &= 1, & t_2 &= 0; \\
z_\infty &= \infty, & \alpha_\infty &= 0, & \omega_\infty &= \infty, & t_\infty &= \infty.
\end{aligned} \tag{3.53}$$

Put explicitly, the Schwarzian operator becomes

$$\frac{1}{\delta^2} \{f, t\} = \frac{1}{2} \left[\frac{1 - (\theta/\pi)^2}{(1 - e^{-\delta t})^2} \right] + \frac{\gamma_1''}{1 - e^{-\delta(t-t_1)}} + \frac{\gamma_2''}{1 - e^{-\delta t}} \tag{3.54}$$

where from condition 3.52

$$\gamma_1'' + \gamma_2'' = \frac{(\theta/\pi)^2 - 1}{2} \tag{3.55}$$

From the Riemann mapping theorem [216, 217], only 3 of 4 vertices can be defined and we are left with one unknown, i.e. t_1 . Schwarz's initial analysis shows that the mapping of the strip into any polygons involving 3 circular arcs or less will yield conformal maps in terms of Appell's hypergeometric function. However, when 4 circular arcs are involved in our case, the mapping is not as straightforward. Such geometries are known to generate conformal maps in the form of Heun functions [224–226] (a generalization of the hypergeometric function). However, these functions, as the number of singularities they content is larger than 3, will have several isomorphisms due to the fact that the position of singularities in the complex plane can be permuted using Riemann's mapping theorem. There are 192 symmetries for the Heun Function [227], and finding the ones that pertain to the nature of my problem was found to be a fundamental mathematical problem outside the scope of this thesis and certainly outside the scope of my expertise in conformal mapping. This is still an open problem to be solved. The analytical framework developed in Section 3.6 suggests that the general flow solution will decay exponentially asymptotically far from the origin, and increase linearly for large λ values asymptotically close to the origin. Fig. 3.10 also suggests that the general solution will decay exponentially regardless of the shape of the meniscus, provided the shape of the meniscus is well behaved.

3.8 Rapid quantitative assays using SCMs

Other researchers at IBM Research Zurich were concentrating on applications of the SCM. Yet one key challenge remained. Now that the hydrodynamics of SC flows is well understood, there remains to account for the diffusion, dispersion and reaction of reagents spotted in these devices. As it turns

out, SCM devices were found to be effective to measure the activity of certain human enzymes, such as Glucose-6-phosphate dehydrogenase (G6PD), and to identify their deficiencies. This process involved the conversion of enzymatic substrates into detectable fluorescent compounds. Understanding the diffusion of enzymes, and substrates within the SCM and their reaction to generate fluorescence compounds via a Michaelis-Menten kinetics [64] was key to make an enzymatic rapid diagnostic test for G6PD deficiency using small blood samples. My work in this section has been to solve numerically within SCM geometries the reaction-diffusion model proposed by the IBM team and developed by my advisors T. Gervais and E. Delamarche. The results from this work have been published in [203].

3.8.1 Reactive flows in SCMs

The convection-diffusion-reaction equation describes reactive flows occurring from a combination of passive molecular diffusion, convection from a flow field, and a reaction (source or sink) term. Assuming n species of concentration C_n diffusing at a rate D_n in a flow field $\mathbf{u} \equiv (u, v, w)$, the reactive flow can be described by n equations of the form

$$\frac{\partial C_n}{\partial t} = \underbrace{\nabla \cdot (D_n \nabla C_n)}_{\text{Diffusion}} - \underbrace{\nabla \cdot (\mathbf{u} C_n)}_{\text{Convection}} + \underbrace{R_n}_{\text{Reaction}} \quad (3.56)$$

where R_n is the reaction term creating or annihilating C_n that can be a function of all species, i.e. $R_n \equiv R_n(C_1, C_2, C_3, \dots)$. *A priori* Eq. 3.56 is three-dimensional, and could be solved numerically as is, but in the case of reactive flows occurring in SCMs it can be tremendously simplified. Assuming immediate lateral and vertical homogenization, i.e. infinite diffusion speed in y and z when $H \ll W \gg L$, Eq. 3.56 can be reduced to

$$\frac{\partial C_n}{\partial t} = D_n \frac{\partial^2 C_n}{\partial x^2} - \frac{\partial}{\partial x} (u C_n) + R_n \quad (3.57)$$

where here we also assumed D_n to be constant. From Eq. 3.27, we know that in a SCM flow decays exponentially as $u(x, t) \sim \exp(-\pi(x + U_m t)/W)$ as in a shock wave behaviour, i.e. exponential decay with translational symmetry in time. Again, in cases where the SCM's width is much smaller than its length, $W \ll L$, $u(x, t)$ decays rapidly towards zero and the flow can be assumed inexistant, and Eq. 3.57 can be further reduced to

$$\frac{\partial C_n}{\partial t} = D_n \frac{\partial^2 C_n}{\partial x^2} + R_n \quad (3.58)$$

In the next section, an example of reactive flow occurring in a SCM is given in the scope of rapid

quantitative assays for determining G6PD deficiency, a widespread metabolic disorder causing hemolytic anemia [203]. Although I will be making use of technical terms explaining the coupled enzyme reaction cascades, I want to reiterate that the reaction-diffusion model was proposed by the IBM team and developed by my advisors. My outlook on this section is purely as a modeller, and as the model is required for me to explain the simulation procedure, I have no choice but to detail the equations.

3.8.2 Resorufin production from two coupled enzyme reaction cascades

The conversion of RZ into RF* by DP requires NADPH, which is provided from the reduction of NADP⁺ during the conversion of G6P into 6PGL by the enzyme G6PD as described by Eqs 3.59-3.60, Tab. 3.2 and Fig. 3.16. Initially, G6P, NADP⁺, RZ, and DP are spotted into the SCM and dried. The enzyme G6PD is brought in the SCM with the reconstitution buffer and the reaction starts. Expressed in the form of Eq. 3.58, and following the same assumptions to obtain said equation, Eq. 3.59-3.60 can be written as a set of 11 coupled diffusion-reaction equations. The reaction terms in Eqs 3.61-3.71 represent a series of enzymatic reactions described by bimolecular binding kinetics and Michaelis-Menten kinetics [64]. More details regarding how to obtain these reactive terms are provided in [203]. Diffusion and reaction coefficients are provided in Tab. 3.3 and Tab. 3.4. References for all values are provided in [203].



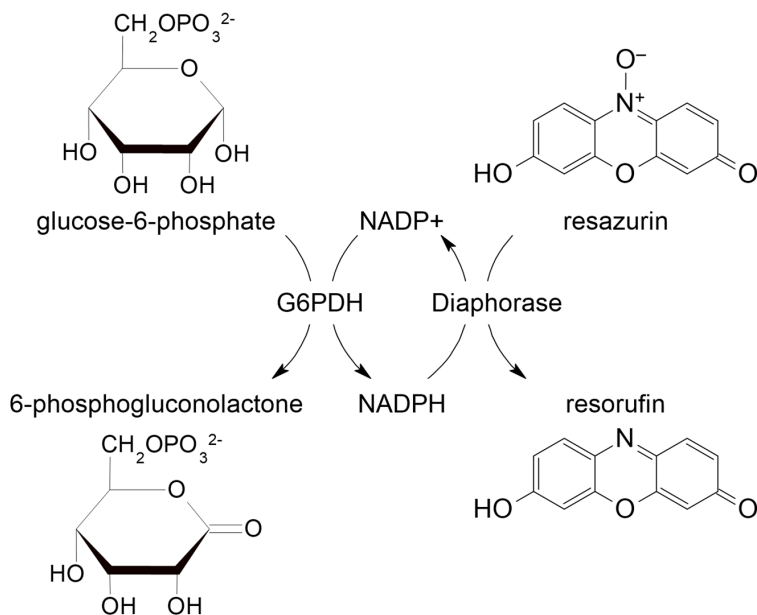


Figure 3.16 Schematic of resorufin production from two coupled enzyme reaction cascades.

$$\frac{\partial[\text{G6P}]}{\partial t} = D_{\text{G6P}} \nabla^2 [\text{G6P}] - \frac{k_{\text{cat},1} [\text{G6PD}^*] [\text{G6P}]}{K_{\text{M},1} + [\text{G6P}]} \quad (3.61)$$

$$\frac{\partial[6\text{PGL}]}{\partial t} = D_{6\text{PGL}} \nabla^2 [6\text{PGL}] + \frac{k_{\text{cat},1} [\text{G6PD}^*] [\text{G6P}]}{K_{\text{M},1} + [\text{G6P}]} \quad (3.62)$$

$$\frac{\partial[\text{NADP}^+]}{\partial t} = D_{\text{NADP}^+} \nabla^2 [\text{NADP}^+] - \frac{k_{\text{cat},1} [\text{G6PD}^*] [\text{G6P}]}{K_{\text{M},1} + [\text{G6P}]} + \frac{k_{\text{cat},2} [\text{DP}^*] [\text{RZ}]}{K_{\text{M},2} + [\text{RZ}]} \quad (3.63)$$

$$\frac{\partial[\text{NADPH}]}{\partial t} = D_{\text{NADPH}} \nabla^2 [\text{NADPH}] + \frac{k_{\text{cat},1} [\text{G6PD}^*] [\text{G6P}]}{K_{\text{M},1} + [\text{G6P}]} - \frac{k_{\text{cat},2} [\text{DP}^*] [\text{RZ}]}{K_{\text{M},2} + [\text{RZ}]} \quad (3.64)$$

$$\frac{\partial[\text{RZ}]}{\partial t} = D_{\text{RZ}} \nabla^2 [\text{RZ}] - \frac{k_{\text{cat},2} [\text{DP}^*] [\text{RZ}]}{K_{\text{M},2} + [\text{RZ}]} \quad (3.65)$$

$$\frac{\partial[\text{RF}^*]}{\partial t} = D_{\text{RF}^*} \nabla^2 [\text{RF}^*] + \frac{k_{\text{cat},2} [\text{DP}^*] [\text{RZ}]}{K_{\text{M},2} + [\text{RZ}]} \quad (3.66)$$

$$\frac{\partial[\text{G6PD}^*]}{\partial t} = D_{\text{G6PD}^*} \nabla^2 [\text{G6PD}^*] + k_{\text{on},1} [\text{G6PD}] [\text{NADP}^+] - k_{\text{off},1} [\text{G6PD}^*] \quad (3.67)$$

$$\frac{\partial[\text{G6PD}]}{\partial t} = D_{\text{G6PD}} \nabla^2 [\text{G6PD}] - k_{\text{on},1} [\text{G6PD}] [\text{NADP}^+] + k_{\text{off},1} [\text{G6PD}^*] \quad (3.68)$$

$$\frac{\partial[\text{DP}^*]}{\partial t} = D_{\text{DP}^*} \nabla^2 [\text{DP}^*] + k_{\text{on},2} [\text{G6PD}] [\text{NADP}^+] - k_{\text{off},2} [\text{DP}^*] \quad (3.69)$$

$$\frac{\partial[\text{DP}]}{\partial t} = D_{\text{DP}} \nabla^2 [\text{DP}] - k_{\text{on},2} [\text{G6PD}] [\text{NADP}^+] + k_{\text{off},2} [\text{DP}^*] \quad (3.70)$$

$$\frac{\partial[\text{H}^+]}{\partial t} = D_{\text{H}^+} \nabla^2 [\text{H}^+] + \frac{k_{\text{cat},1} [\text{G6PD}^*] [\text{G6P}]}{K_{\text{M},1} + [\text{G6P}]} - \frac{k_{\text{cat},2} [\text{DP}^*] [\text{RZ}]}{K_{\text{M},2} + [\text{RZ}]} \quad (3.71)$$

Table 3.2 Definition of species and example of initial values.

Species	Initial value	Definition
G6P	43 460 μM	Glucose-6-phosphate, substrate of G6PD enzyme
6PGL	0	6-phosphogluconolactone, product of G6P conversion
NADP ⁺	2173 μM	Cofactor binding to G6PD, product of DP RZ conversion
NADPH	0	Cofactor binding to DP, product of G6PD G6P conversion
RZ	2173 μM	Resazurin, fluorescence precursor and substrate of DP
RF*	0	Resorufin, fluorescent molecule, product of RZ conversion by DP
G6PD*	0	Activated G6PD
G6PD	0.012 μM	Enzyme which needs to be quantified in the assay
DP*	0	Activated DP
DP	388 μM	Diaphorase enzyme
H ⁺	0	Hydrogen ion, inert

3.8.3 Model implementation using finite differences

The characteristic diffusion time for the selected geometric scales with ℓ/D in every independent dimension. Knowing that the thickness of the SCM is much smaller than the width, which is smaller than the length, we can approximate that $t_m \approx L^2/D \gg W^2/D \gg H^2/D$ where t_m is the measurement window. With this assumption, a 1D model is sufficiently accurate to capture all the physics of the problem as argued in the previous section. In extreme cases where reagents are heavier, time scales widthwise could reach the same order of magnitude as time scales lengthwise. The current model implementation does not treat such cases, but a second dimension could easily be added if need be.

Numerical simulations of Eqs 3.61-3.71 are completed using Finite Differences (FD) with a second order central FD scheme in space and an explicit first order FD scheme in time. Space is discretized on a uniform grid of size Δx and time steps Δt are defined using two tolerance criterions. First, to correctly capture the physics of the problem we set a tolerance factor on the amount of mass that can react within a time interval Δt . This is to ensure smooth mass changes even when reactions are fast. The second tolerance criterion is a simple upper limit set by the von Neumann stability condition, i.e. the diffusion stability limit. An example of time step evolution through a simulation is given in Fig. 3.17.

The discretized FD equations read

$$C_{n,i}^{t+\Delta t} = C_{n,i}^t + \Delta t \left[D_n \frac{C_{n,i-1}^t - 2C_{n,i}^t + C_{n,i+1}^t}{\Delta x^2} + R_{n,i}^t \right] \quad (3.72)$$

where $C_{n,i}$ and $R_{n,i}$ are respectively the concentration and reaction rate at time t and grid node i

Table 3.3 Diffusion coefficient for the coupled enzymatic reactions from Eq. 3.61-3.71.

Parameter	Value	Units
D_{G6P}	534	$\mu\text{m}^2 \text{s}^{-1}$
D_{6PGL}	534	$\mu\text{m}^2 \text{s}^{-1}$
D_{NADP^+}	420	$\mu\text{m}^2 \text{s}^{-1}$
D_{NADPH}	420	$\mu\text{m}^2 \text{s}^{-1}$
D_{RZ}	480	$\mu\text{m}^2 \text{s}^{-1}$
D_{RF^*}	480	$\mu\text{m}^2 \text{s}^{-1}$
D_{G6PD^*}	74	$\mu\text{m}^2 \text{s}^{-1}$
D_{G6PD}	74	$\mu\text{m}^2 \text{s}^{-1}$
D_{DP^*}	74	$\mu\text{m}^2 \text{s}^{-1}$
D_{DP}	74	$\mu\text{m}^2 \text{s}^{-1}$
D_{H^+}	1000	$\mu\text{m}^2 \text{s}^{-1}$

Table 3.4 Reaction coefficients for the coupled enzymatic reactions from Eq. 3.61-3.71.

Parameter	Value	Units
$k_{\text{cat},1}$	222.21	s^{-1}
$k_{\text{cat},2}$	3.73	s^{-1}
$k_{\text{on},1}$	1	$\text{s}^{-1} \mu\text{M}^{-1}$
$k_{\text{on},2}$	1	$\text{s}^{-1} \mu\text{M}^{-1}$
$k_{\text{off},1}$	7	s^{-1}
$k_{\text{off},2}$	350	s^{-1}
$K_{\text{M},1}$	52	μM
$K_{\text{M},2}$	1500	μM

for the n th specie. Diffusion constants and reaction rates are taken from Tab. 3.3 and Tab. 3.4. Neumann boundary conditions are set at both ends of the 1D domain and initial concentrations are set by the user. In this study, G6PD is homogeneous throughout the domain and the other solutions are constant by parts with steps widths defined by the spotting diameter such as to mimic experiments. An example of initial concentration values is presented in 3.2. Convergence analyses in space and time and comparison with analytical asymptotic solutions were done to ensure the code is reliable. Simulation speed is highly dependent of reactions speed. Assuming an initial set of concentrations as portrayed in 3.2 with a discretized 1D space of 1000 nodes, simulations for 10 min of physical time takes roughly 120-130s on a single CPU on a laptop. Time steps in this case are largely reaction limited. The FD method was selected for its implementation speed and the non-existence of geometrical complexities for the problem at hand. The code was built in-house from scratch and written using MATLAB R2018a. A pseudocode of the routine for EnzModSimulator (EMS) is presented as follow:

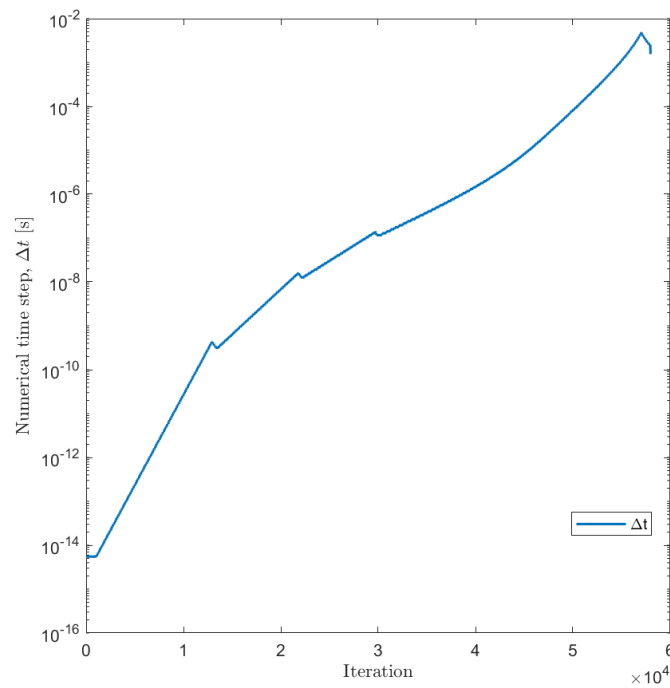


Figure 3.17 Time step throughout a simulation.

```

Program start
Read parameters
Initialize fields
Start computational loop
  while  $t < t_{\text{end}}$ 
    if Approximations on reactions exist
      Initialize fields accordingly
    else
      Initialize all fields
    Calculate reaction limiters  $RLim$ 
    Initialize source terms  $R$ 
    while  $R > RLim$ 
      Reduce time step  $dt$ 
      Calculate source terms  $R$ 
    if  $dt > dt_D$  (von Neumann stability condition)
       $dt = dt_D$ 
    Calculate diffusion and update fields

```

Update time $t = t + dt$
 End computational loop
 Post-processing
 End of program

Five level of approximations are also available with the code in conjunction with the full 11 equations model: 1) quasi steady state of enzyme-cofactor complex, 2) well mixed volumes, 3) approximations on G6PDH enzymatic kinetics, 4) approximations on diaphorase enzymatic kinetics, and 5) approximate asymptotic solution (analytic).

In 1, the equilibrium between co-factors and enzyme is rapidly achieved such that $[\text{NADPH}^*]$ and $[\text{DP}^*]$ can be considered in quasi-steady state at all times, i.e.

$$[\text{NADPH}^*] = [\text{NADPH}]_0 \frac{[\text{NADP}^+]}{K_{d,1} + [\text{NADP}^+]} \quad (3.73)$$

$$[\text{DP}^*] = [\text{DP}]_0 \frac{[\text{NADPH}]}{K_{d,2} + [\text{NADPH}]} \quad (3.74)$$

where $K_{d,1} = k_{\text{off},1}/k_{\text{on},1}$ and $K_{d,2} = k_{\text{off},2}/k_{\text{on},2}$. In 2, we suppose that all volumes are well mixed, with the effect of canceling all Laplacian terms in Eqs 3.61-3.71. In 3, NADP^+ is assumed overabundant with respect to G6PDH, and that $[\text{G6P}]$ is always much larger than $K_{M,1}$. Put in mathematical form

$$\frac{d[\text{G6P}]}{dt} = -k_{\text{cat},1}[\text{G6PDH}]_0 \quad (3.75)$$

which has for solution

$$[\text{G6P}](t) = [\text{G6P}]_0 - k_{\text{cat},1}[\text{G6PDH}]_0 t \quad (3.76)$$

In 4, we are neglecting the saturation of the DP enzyme leading to

$$\frac{d[\text{RF}^*]}{dt} = -k_{\text{cat},2}[\text{DP}]_0 \left(\frac{[\text{G6P}]_0 - [\text{G6P}] - [\text{RF}^*]}{K_{d,2}} \right) \left(\frac{[\text{RZ}]_0 - [\text{RF}^*]}{K_{M,2} + [\text{RZ}]_0 - [\text{RF}^*]} \right) \quad (3.77)$$

and combining this results with 3 we obtain

$$\frac{d[\text{RF}^*]}{dt} = -k_{\text{cat},2}[\text{DP}]_0 \left(\frac{k_{\text{cat},1}[\text{G6PDH}]_0 t - [\text{RF}^*]}{K_{d,2}} \right) \left(\frac{[\text{RZ}]_0 - [\text{RF}^*]}{K_{M,2} + [\text{RZ}]_0 - [\text{RF}^*]} \right) \quad (3.78)$$

Finally, in 5, an asymptotic development of last equation is done for initial times, i.e. when $[\text{RF}^*] \gg [\text{RZ}]_0$. The solution is given by

$$X(\tau) \approx \left(\frac{K+1}{\alpha} \right)^2 \left(\frac{\alpha\tau}{K+1} - (1 - e^{-\alpha\tau/(K+1)}) \right) \quad (3.79)$$

where

$$X = \frac{[\text{RF}^*]}{[\text{RZ}]_0}; \tau = \frac{t}{\tau_0}; \tau_0 = \frac{[\text{RZ}]_0}{k_{\text{cat},1}[\text{G6PDH}]_0}; \alpha = \frac{k_{\text{cat},2}[\text{DP}]_0}{k_{\text{cat},1}[\text{G6PDH}]_0} \frac{[\text{RZ}]_0}{K_{\text{d},2}}; K = \frac{K_{\text{M},2}}{[\text{RZ}]_0} \quad (3.80)$$

Simple validation steps [228] were conducted by comparing simplified models to numerical results. A validation case is presented in Appendix ?? with a text input file example in Appendix ?. This code was also used to produce all numerical results in Rocca *et al.* [203]. Concentration of species in time and space for the full model with the initial conditions presented in Tab. 3.2 are presented in Fig. 3.18.

3.9 Conclusion

Flows within elongated capillary-driven microstructures devices can be solved using advanced numerical methods for multiphase flows. However, by using the invariance property of the Navier-Stokes equations under Galilean transformations, the flow can be analysed in a reference frame where the meniscus is static in space. Thus, reducing the domain of analysis to the water domain with static boundaries. Consequently, simpler numerical methods can be used to find flow solutions. However, this is limited to elongated structures with translational symmetries.

In the particular case of SC along a straight CPL, we describe how a Galilean transform placing oneself in the reference frame of the moving meniscus transforms all moving boundary conditions (Stefan) into regular (Neumann) boundary conditions. The Hele-Shaw approximation of the flow in self-coalescence is used in conjunction with the Galilean transformation to formulate a SC free boundary problem that can be solved using conformal mapping. Conformal mapping solutions of the flow inside a SCM are provided using the Schwarz-Christoffel mapping and mapping over an infinite cylinder.

Asymptotic solutions and self-coalescing flow modes are provided in the vicinity and far away from the CPL-meniscus contact point. By combination of the two asymptotes (Eq. 3.27 and 3.32), the general formulation of the complex velocity in the laboratory reference frame can be encompassed between two simple expressions, i.e. a linear increase followed by an exponential decrease of the velocity as we get further away from the CPL-meniscus contact point. We then describe how flow orthogonality (Eq. 3.27) and its characteristic decay length W/π is invariant no matter the choice of contact angle, meniscus shape, flow velocity, or the horizontal path followed downstream of the obstacle, and as such, is a key signature of self-coalescing flows as described here.

A mathematical analogy between the theory of Saffman-Taylor and SC flows is found when far from the curved interface. Indeed, a SCM with a mirror symmetry in SC mode does look somewhat

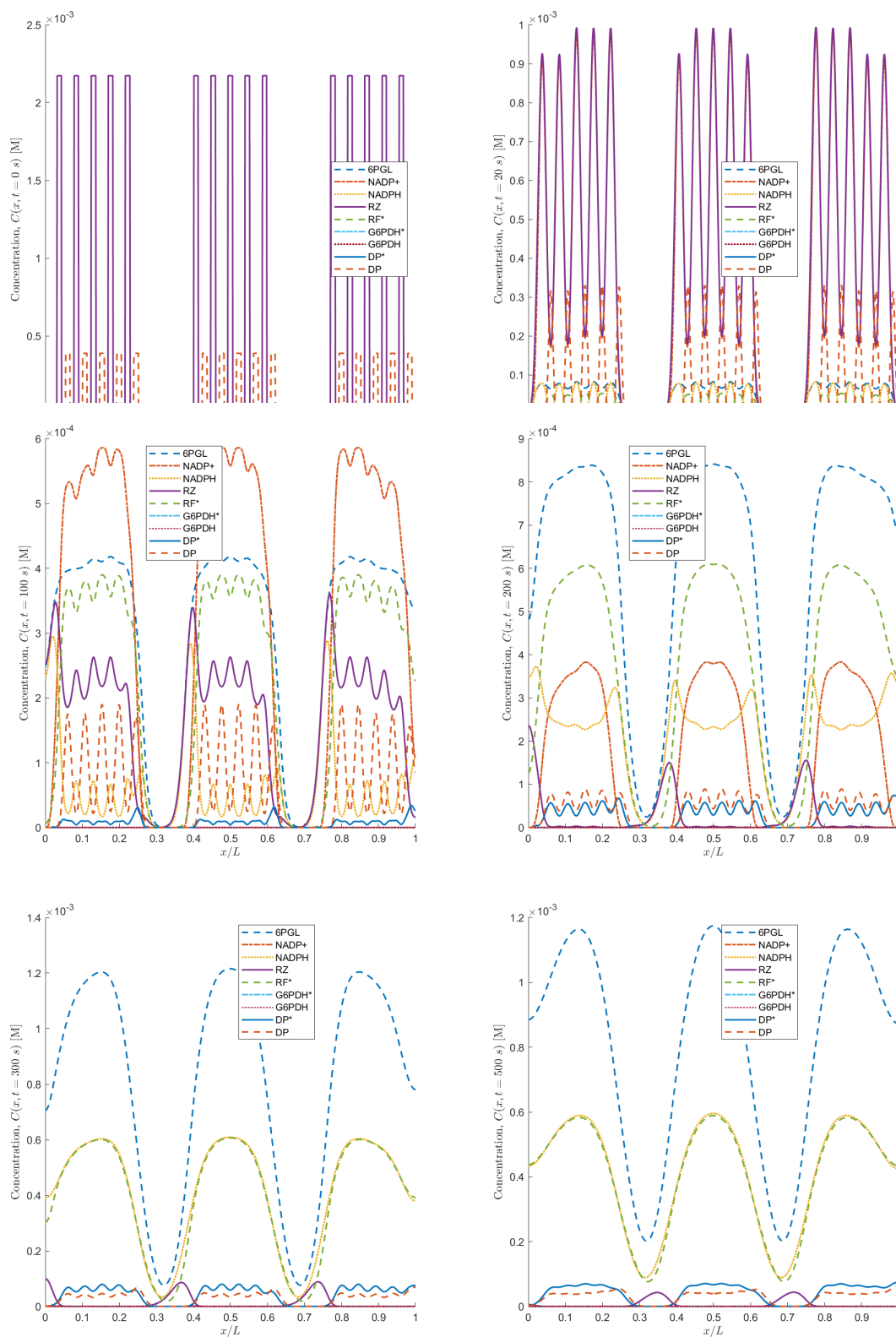


Figure 3.18 Spatial and temporal evolution of species from initially spotted region. From left to right and top to bottom: 0 s, 20 s, 100 s, 200 s, 300 s, and 500 s.

like a receding STVF (Fig. 3.9). Yet, there are some key differences. For instance, SC arises from a capillary pinning of the air/water interface which is not smooth at the contact point of the meniscus with the CPL. SC can also be achieved for arbitrary λ values compared to STVF were only values of $\lambda < 1/2$ were recorded for small capillary numbers ($Ca \sim 10^{-5}$ in our study). Furthermore, SC can be accurately modelled using a simple conformal map in a static domain while STVF cannot. We also describe how SC can take any value of contact angle at its tip while STVF arises from the specific case where the contact angle is $\pi/2$, i.e. when the tip of the finger is smooth.

The SCM is a key solution regarding the resuspension and control of release of reagents in microchannels. An example of how SCMs can be used for rapid quantitative assays in the context glucose-6-phosphatedehydrogenase (G6PD) and hemoglobin combination on a capillary-driven microfluidic chip is provided. A quick description of the FD-based CFD software that was written and used for this work is given.

CHAPTER 4 ARTICLE 1: A SIMPLE STATIC CONTACT ANGLE-BASED MESH-DEPENDENCY CORRECTION FOR 3D CAPILLARY FLOW SIMULATIONS

Authors: Samuel Castonguay, Thomas Gervais

Chapter Overview

In this theme, I develop a numerical framework for modelling complex capillary driven flows in microstructures. This methodology can be used to predict behavior of liquids in microsystems and optimize their design where analytical tools are limited. In this work, I conceptualized and visualized the research, established the methodology, conducted the formal analysis, and wrote the original draft. My advisor Thomas Gervais supervised the research, and we both reviewed and edited the manuscript. This work was published in *Computers & Fluids*, June 27, 2021 [202].

Abstract

Precise modelling of contact angle is ubiquitous in capillary driven multiphase flow simulations. From a simple 2D rectangular capillary benchmark, we demonstrate and discuss the dependence of capillary dynamics on the mesh size with respect to Washburn's equation. Mesh-dependency is dominated by an underestimation of viscous losses for coarser meshes and transits to ever increasing stress-related errors due the Navier-Stokes equations breaking down in the vicinity of moving contact lines subjected to several known boundary conditions. Furthermore, computational limits generally impose mesh sizes for which none of the errors are negligible. We show that for Washburn-like flows, a simple modification of the static contact angle value is adequate to correct the dynamics of the flow. This semi-analytic correction has the advantage of requiring no modification of the source code or implementation of new boundary conditions, and thus can be easily used with any codes whether commercial or not. Simulations of a self-coalescence module and a capillary pump are presented as 3D verification test cases of the method.

4.1 Introduction

With an increasing interest for capillary flows and their applications in recent years, it is important to develop engineering and modelling tools to predict and control precisely the behavior of capillary flows in numerous contexts. Some of the most prominent fields include petroleum engineering [229], micro process engineering [13] and lab-on-chip devices [230, 231]. In the case of

microfluidic systems, we find capillary flows in capillary pumps [232], valves [233], phaseguides [195], and more recently self-coalescence modules [197]. Since complex capillary phenomena cannot be modelled analytically, we need to rely on powerful numerical tools taking into account all physically relevant phenomena to achieve realistic predictions.

It is well established in fluid mechanics that the Navier-Stokes (NS) equations describe the flow dynamics of incompressible Newtonian liquids such as water in normal temperature and pressure conditions. However, it is not the case for multiphase flows because of intrinsic multiscale effects that come into play [234].

For instance, interface tracking methods using Eulerian descriptions of the flow predominantly use a continuous representation of the multiphase interface with a phase transition length of the order of the local mesh size. Since mesh sizes are generally orders of magnitude larger than the physical multiphase transition thickness, Eulerian-based interface tracking is highly mesh dependent. Furthermore, any continuum formulation of fluid dynamics is prompt to mesh dependencies due to improper treatment of wall stresses in the vicinity of moving contact lines on walls with Dirichlet boundary conditions such as no-slip boundary conditions [190, 191, 235, 236]. This error occurs because the classical continuum description of fluid mechanics breaks down at the mesoscopic and microscopic scales.

Since stress-related errors increase with mesh refinement and hydrodynamics-related errors and interface thickness decrease with mesh refinement, we must find a systematic method to correct the different errors or find an acceptable compromise between them for the problem at hand.

Reducing or correcting mesh-dependency is generally done using either partial slip boundary conditions or localized body forces that reduce wall stress or mesh-dependent contact angle boundary conditions that compensate for stress increases [173, 237–239]. However, these methods either are not appropriate for capillary flow cases, require mesh sizes and time steps considerably smaller than what can be achieved in practice, or use pre-factors that are not *a priori* known. This is even more true for simulations with high geometric aspect ratios as commonly encountered in microfluidics.

In this work, we propose a simple static contact angle-based mesh-dependency correction to compensate for non physical stresses in the case of capillary flows behaving as per Washburn's equation. We calculate a correction factor from a simple *a posteriori* semi-analytical match of Washburn's equation for a 2D rectangular capillary benchmark, and use this correction *a priori* for complex capillary flows in 3D microstructures. In this study, we use this method for 3D simulations of complex capillary devices such as self-coalescence modules [197] and capillary pumps [232].

Capillary flow simulations in this paper are done using `interFoam`, an incompressible two-phase flow solver part of the open source finite volume library `OpenFOAM` (Open Field Operation and

Manipulation) that uses cell-centered finite volume formulations [240,241]. However, the presented correction method is valid for any CFD approach using a continuum formulation of fluid dynamics.

The performance of `interFoam` has already been investigated in the case of surface tension-dominated flows [199], segmented liquid-gas flows in microchannels [176] and spontaneous flows in capillary pumps [179,242]. More recently, `interFoam` and modified versions thereof was successful at simulating droplet coalescence [243], micro-jets [244], corner flows in square capillaries [245] and pore waterflooding [246,247]. However, we find a lack of an in-depth analysis of mesh-dependency and grid convergence in the case of capillary-dominated flows in microchannels.

The solution procedure utilises the PISO (pressure-implicit with splitting of operators) algorithm for transient pressure-velocity coupling [248]. The transient term is solved using a first order Euler scheme with a fixed maximal Courant number to define time steps.

In this work, we first draw a quick summary of the constitutive equations and numerical procedure. We then conduct a validation procedure [228] by proxy using Washburn's equation to explore mesh-dependency and grid convergence issues for a 2D rectangular capillary benchmark from which we build our correction methodology. Finally, we test the correction method for the simulation of a self-coalescence module and a capillary pump.

4.2 Numerical methodology

We solve the Navier-Stokes equations for an incompressible flow of two immiscible Newtonian fluids. The mass and momentum conservation equations for a fluid of density ρ and viscosity μ are respectively

$$\nabla \cdot \mathbf{u} = 0 \quad (4.1)$$

$$\frac{\partial \rho \mathbf{u}}{\partial t} + \nabla \cdot (\rho \mathbf{u} \mathbf{u}) = -\nabla p + \mu \nabla^2 \mathbf{u} + \mathbf{F} \quad (4.2)$$

where \mathbf{u} is the velocity vector field, p the pressure scalar field, and \mathbf{F} accounts for additional body forces on the fluid. Because of scaling laws in microfluidics, gravity can be neglected and only surface tension effects, \mathbf{F}_γ , are significant. The surface tension body force is calculated from the curvature of interfaces forming between the two liquids. Calculating this term requires additional information regarding the transport of phases from which we can track multiphase interfaces and calculate their curvature. For an extensive review on the subject, we refer to [109].

In the VOF formulation [201], we solve a single set of NS equations (Eq. 4.1-4.2) coupled with a phase field α from which we derive density and viscosity fields as follow :

$$\rho = \alpha \rho_1 + (1 - \alpha) \rho_2 \quad (4.3)$$

$$\mu = \alpha\mu_1 + (1 - \alpha)\mu_2 \quad (4.4)$$

where $\alpha \in [0, 1]$ is a scalar field referring to the fraction between the cell volume occupied by one phase and the total volume of the control cell. The phase field is advected by a simple first order transport equation given by

$$\frac{\partial \alpha}{\partial t} + \nabla \cdot (\alpha \mathbf{u}) = 0 \quad (4.5)$$

As a consequence of the Eulerian nature of the method it is difficult to resolve sharp fluid interfaces on arbitrary meshes. For instance, solving the transport equations with Eq. 4.5 as is would result in strong numerical diffusion of multiphase interfaces. To counter this numerical artifact, a compression term [249] is introduced in the phase transport equation from which Eq. 4.5 becomes

$$\frac{\partial \alpha}{\partial t} + \nabla \cdot (\alpha \mathbf{u}) - \nabla \cdot [\alpha(1 - \alpha)\mathbf{u}_r] = 0 \quad (4.6)$$

with

$$\mathbf{u}_r = \mathbf{n}_f \min \left[C_\gamma \frac{|\phi_f|}{|S_f|}, \max \frac{|\phi_f|}{|S_f|} \right] \quad (4.7)$$

where ϕ_f , S_f and \mathbf{n}_f are respectively the volume flux across the surface f , the surface area and the unit vector of that surface, and $C_\gamma \in [0, 4]$ is a constant. For $C_\gamma = 0$ there is no compression and for $C_\gamma > 1$ compression is enhanced. All simulations in this work take $C_\gamma = 1$ since other values are known to worsen interface diffusion and curvature errors [199].

Surface tension body forces \mathbf{F}_γ are calculated using the continuum surface force (CSF) formulation [65] :

$$\mathbf{F}_\gamma = \gamma \kappa (\nabla \alpha) \quad (4.8)$$

where $\kappa = \nabla \cdot (\nabla \alpha / |\nabla \alpha|)$ is the curvature of the phase field. The CSF model has been selected for its extensive use in the literature [243, 245, 250]. For other surface force formulations and their assessment we refer to [178].

Constant pressure boundary conditions, $p = 0$, are imposed on all inlets and outlets and constant pressure gradients, $\nabla p = 0$, are imposed on all walls. It has been shown by [242] that static contact angle boundary conditions are best for the simulation of capillary flows in microsystems such as capillary pumps, thus constant contact angle boundary conditions for α are set throughout this study. This is done by updating the surface vector to the multiphase interface in the first cell layer using the dot product relation with the surface vector to the wall and the cosine of the contact angle. Boundary conditions for \mathbf{u} will be specified in Section 4.3.

Meshes for benchmark cases and self-coalescence modules are respectively 2D and 3D structured cartesian grids constructed using OpenFOAM's built-in utility `blockMesh`. Capillary pump

meshes are unstructured and constructed from 3D structured cartesian grids snapped to the geometry using `blockMesh` and `snappyHexMesh` utilities. Most simulations are conducted in parallel on a homebrewed server with 2 Intel Xeon CPUs. Simulations with ~ 0.5 M cells or more are run on Calcul Québec’s supercomputers Mammouth Parallèle II and Béluga.

4.3 Benchmark case and the mesh-dependency problem

We first begin our analysis of the effect of meshing on capillary flows with the benchmark case of a 2D rectangular capillary (Fig. 4.1) of dimensions $L \times H$ for which we know analytically the displacement $x(t)$ of the liquid-gas interface. All simulations use the same set of physical parameters as displayed in Tab. 4.1. The choice of parameters is made from, but not limited to, commonly encountered water-air capillary microsystems under standard conditions for temperature and pressure.

4.4 The dynamics of capillary flow

Moving inertialess fluids due to capillary pumping in small conduits have been described by Lucas and Washburn [82, 251] from a balance between viscous losses and capillary action. Assuming a fully developed Poiseuille flow profile in a 2D rectangular capillary tube (Fig. 4.1), the pressure balance equation reads

$$\frac{12\mu}{H^2}x\dot{x} = \frac{2\gamma}{H} \cos \theta \quad (4.9)$$

where the left-hand side of the equation is the Hagen-Poiseuille law, akin to Ohm’s law in electrodynamics, and the right-hand side the Young-Laplace pressure drop. Solving Eq. 4.9 assuming

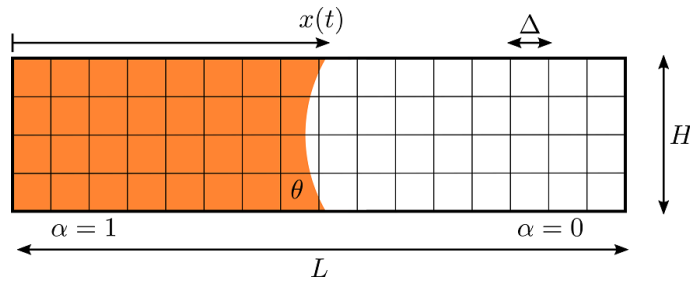


Figure 4.1 Benchmark case of spontaneous imbibition in a 2D rectangular microchannel. The microchannel dimensions are $L \times H$ with $L/H = 100$. θ is the contact angle and Δ the mesh size.

Table 4.1 Physical parameters for the simulations.

Parameter	Description	Value
θ	Contact angle	$40^\circ - 80^\circ$
γ	Surface tension	72 J m^{-2}
ρ_1	Liquid density	1000 kg m^{-3}
μ_1	Liquid viscosity	1 mPa s
ρ_2	Gas density	1 kg m^{-3}
μ_2	Gas viscosity	$14.8 \mu\text{Pa s}$

$x(0) = 0$ leads to Washburn's equation [68] :

$$x = H \sqrt{\frac{t}{\tau}} \quad (4.10)$$

with the Washburn characteristic time

$$\tau = \frac{3\mu H}{\gamma \cos \theta} \quad (4.11)$$

These approximations are true in cases where both the Reynolds and the Capillary numbers are smaller than unity. In the case of capillary driven flow in a 2D rectangular microchannel, we have

$$\text{Re} = \frac{\rho U H^2}{\mu L}, \quad \text{Ca} = \frac{\mu U}{\gamma} \quad (4.12)$$

Assuming $U = \dot{x}$, we can take from Eq. 4.9 that $U = H^2/2\tau x$. Because Washburn's equation for velocity is monotonously decreasing and is singular at $x = 0$ due to the absence of inertia, we take the maximum velocity to be at a distance $5H$ in the channel and the minimal velocity to be at a distance L . For $\theta = 60^\circ$, we have $\text{Re} \in [0.036, 0.72] < 1$ and $\text{Ca} \in [0.00083, 0.017] \ll 1$.

4.5 Boundary conditions and mesh-dependent results

In this section, we present and discuss results that are mesh dependent regardless of the velocity boundary conditions applied. Simulations of the benchmark case when implementing no-slip boundary conditions are shown in Fig. 4.2. This figure illustrates the volume fraction, measured for every time step and equivalent to $x(t)/L$, from which we measure the Washburn characteristic time presented in Fig. 4.3. Three different convergence zones are observed when τ evolves with Δ : (i) when $H/\Delta \lesssim 3$, errors due to capillary pressure and hydraulic resistance underestimation dominate which results in smaller Washburn characteristic times which increase logarithmically with respect to the mesh size, (ii) when $3 \lesssim H/\Delta \lesssim 8$, the Washburn characteristic time convergence transits

from a the pre-asymptotic region dominated by pressure-related and hydrodynamics-related errors to a region dominated by stress-related errors due to improper treatment of wall stress by continuum mechanics, and (iii) when $H/\Delta \gtrsim 8$, the flow slows down due to an increase in stress which is measured as a steady logarithmic increase in τ . This is made evident by measuring stress as a function of Δ as presented in Fig. 4.4. Stress was found to increase as a power of $3/2$ with respect to Δ . The general behavior depicted by the three zones in Fig. 4.2 is invariant of the contact angle as shown in Fig. 4.5. The only noted difference is a decrease in the logarithmic steepness of τ in region (iii) with an increase in θ .

Logarithmic dependence of contact lines position with respect to the mesh size has also been observed and treated using a contact angle-based method by [238] for two test cases : 1) a 2D withdrawing plate, and 2) a 2D spreading droplet. However, 3D capillary flows introduce additional degrees of complexity making this approach inappropriate. For instance, 3D simulations of microsystems rarely permit meshes finer than $\Delta \sim H/10$ due to high aspect ratios and computational limits. We find ourselves most of the time in region (ii) of Fig. 4.3. This in turn makes a systematic correction method difficult to develop as numerical and modelling errors in the transitory convergence region are of the same order. An other difficulty arises when modelling devices that are contact angle-sensitive due to pinning on sharp corners such as self-coalescence modules [197] and phaseguides [252] since we cannot correct θ at will. Indeed, contact angle-based corrections must be small enough to ensure the Concus-Finn criterion [83] is respected. This criterion states that a stable interface in an edge can only exists if the wall's contact angle does not exceed the so-called critical contact angle given by the surface properties and topology of the channel. The critical contact angle on a sharp edge of angle $\pi - \delta$ (e.g. Fig. 4.9b) can be written as

$$\theta_c = \frac{\pi - \delta}{2} \quad (4.13)$$

Another approach amongst scientists and engineers to resolve this challenge has been to introduce partial slip, also known as Navier-slip, boundary conditions on walls to obtain bounded solutions [191, 253]. Introducing the physical boundary's normal n , we define the partial slip boundary condition as

$$f\mathbf{u} + (f - 1)\frac{\partial\mathbf{u}}{\partial n} = \mathbf{0} \quad (4.14)$$

wherefor $f = 1$ and $f = 0$ we respectively impose a Dirichlet boundary condition $\mathbf{u} = \mathbf{0}$ and a Neumann boundary condition $\partial\mathbf{u}/\partial n = \mathbf{0}$. However, partial slip boundary conditions do not solve the mesh-dependency problem in the case of capillary flows in microchannels as displayed in Fig. 4.6. We also observe that a decrease in f , i.e. an increase in slip length, speeds up the flow due to reduced viscous losses and tends to worsen the mesh-dependency steepness.

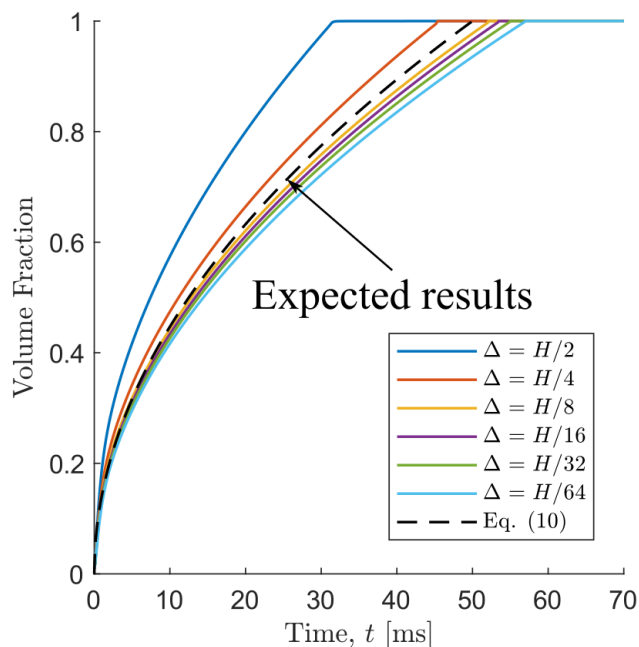


Figure 4.2 Volume fraction as a function of time for the benchmark case with $\theta = 60^\circ$.

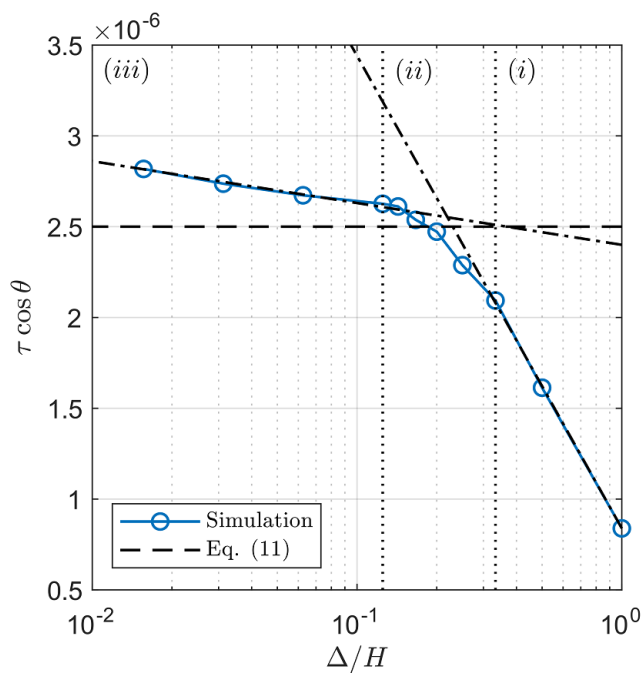


Figure 4.3 Evaluated Washburn characteristic time as a function of mesh size for the benchmark case with $\theta = 60^\circ$. We delimit three regions of interest: (iii) the asymptotic logarithmic convergence towards stress singularity, (ii) the transitory convergence, and (i) the pre-asymptotic logarithmic convergence.

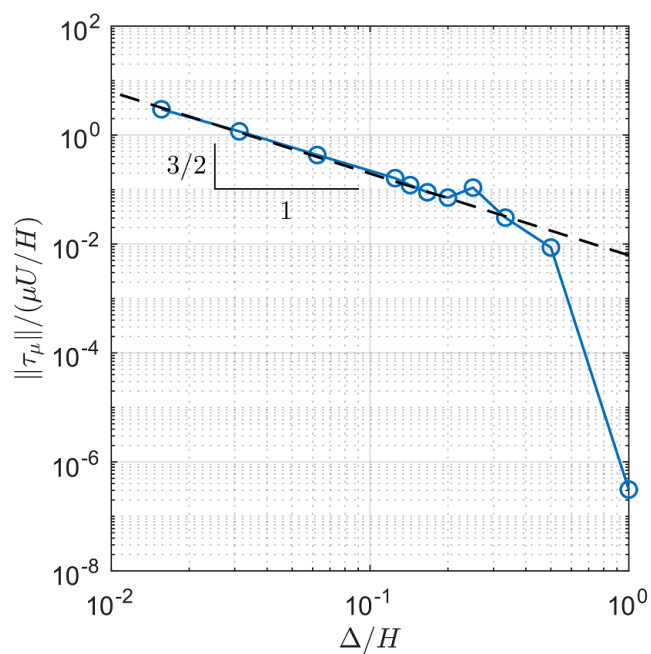


Figure 4.4 Normalized stress on the walls $\|\tau_{xy}\|$ with respect to the mesh size Δ near the contact line.

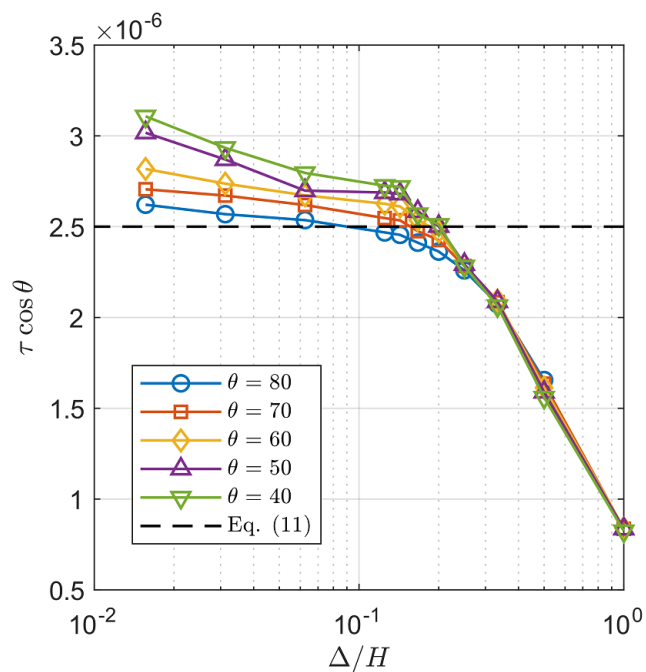


Figure 4.5 Evaluated Washburn characteristic time normalized with respect to $\cos \theta$ as a function of the mesh size Δ and the contact angle θ .

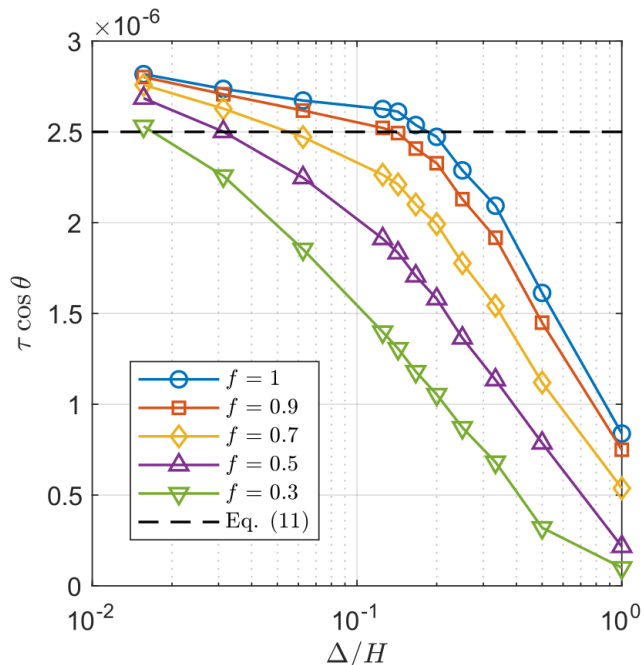


Figure 4.6 Evaluated Washburn characteristic time normalized with respect to $\cos \theta$ as a function of the mesh size Δ for different partial slip values f .

As proposed by [173] we could select a mesh dependent slip length to solve the problem. However, this type of correction can only be applied when the numerical value for τ is above the theoretical value, making it a one-way correction only. Furthermore, a mesh size of $H/32$ would require a correction of $f \approx 0.5$ as seen in Fig. 4.6. Such a high slip value on walls puts us far from a Poiseuille-like flow and prompt to numerical instabilities such as increased spurious currents [199], which in turn slows down simulations and increases flow errors in the vicinity of capillary interfaces.

An other important issue many CFD codes suffer from, including `interFoam`, are parasitic currents in surface tension dominated flows [199]. Parasitic currents were quantified and are shown to increase with mesh refinement and decrease with larger contact angles. This error does not show any influence on the shape of the flow rate, but it could contribute to the numerical discrepancies made evident above. However, parasitic currents bring serious concerns in capillary flows with velocities smaller than parasitic currents due to time step limitations imposed by the Courant number.

In light of the reasons stated above, a novel approach is evidently essential to accurately model capillary flows. This is even more true for 3D simulations exhibiting high geometric aspect ratios, as often encountered in many applications. We proceed next to develop a static contact angle-based correction that is both versatile and easy to use without requiring access to the source code.

4.6 Contact angle-based correction and mesh optimization

As proposed by [238], we search for a mesh-dependency corrector $G(\Delta)$ of the form

$$\cos \theta_{\text{num}} = \cos \theta + G(\Delta) \quad (4.15)$$

where θ_{num} is the measured numerical contact angle, θ is the physical static contact angle. Ideally, that correction should be invariant of geometry and physical parameters. Furthermore, $G(\Delta)$ should be as small as possible to ensure the Concus-Finn criterion is respected as discussed in the previous section. In [238], $G(\Delta)$ is based on the theoretical analysis of Cox [254]. However, this model assumes an asymptotic logarithmic convergence as depicted in Fig. 4.3iii which is not realizable for most 3D capillary flow simulations in microfluidics with high geometrical aspect ratios nor does it minimize $G(\Delta)$. Our approach is to measure *a posteriori* the exact correction needed to correspond to a known solution of the flow for a simple test case which is then used *a priori* for large 3D simulation cases. From Eq. 4.11 and Eq. 4.15 we can write

$$G(\Delta) = \cos \theta \left(\frac{\cos \theta_{\text{num}}}{\cos \theta} - 1 \right) = \cos \theta \left(\frac{\tau}{\tau_{\text{num}}} - 1 \right) \quad (4.16)$$

where τ_{num} is the measured Washburn characteristic time. $G(\Delta)$ is then injected back into Eq. 4.15 to find the corrected contact angle θ_{corr} . This process can be repeated to refine the value of θ_{corr} using the relation

$$\cos \theta_i = \cos \theta_{i-1} + G_i(\Delta), \quad i \in \mathbb{N}^* \quad (4.17)$$

where $\cos \theta_0 \equiv \cos \theta$ and θ_{corr} would be equal to the last value of θ_i calculated. Because this correction method is based on the ratio of the numerical and physical Washburn characteristic times (Eq. 4.11), it is valid as long as Washburn's assumptions for Eq. 4.9 hold and it is independent of geometry and physical parameters other than the contact angle itself.

We test this procedure for the benchmark case and display the corrected contact angle θ_{corr} in Fig. 4.7a and the associated corrected Washburn characteristic time τ_{corr} in Fig. 4.7b as a function of the mesh size. The finer the mesh gets, the larger the gap between the physical and numerical contact angles gets as a result of the increase in stress error. We calculate the relative error on τ_{corr} with respect to Eq. 4.11 and show that the error diminishes on average by an order of magnitude per iteration of Eq. 4.17 as displayed in Fig. 4.7c. Simulations are repeated using the corrected static contact angle for wall boundary conditions and mesh-independent results are obtained as presented in Fig. 4.7d. We repeat this procedure with different contact angles to measure the influence of θ on $G(\Delta)$ and conclude from Fig. 4.8 that a decrease in θ leads to an increase in $G(\Delta)$. This is to be expected since an increase in θ worsens the steepness of the logarithmic increase in stress as

previously depicted in Fig. 4.5. Extreme cases where the corrected contact angle reaches either half or double the physical contact angle happens when $\Delta \sim H/64$ and $\Delta \sim H/2$ for $\theta = 40^\circ$. For all physical contact angles, the optimal grid size to minimize $G(\Delta)$ is in-between $\Delta \sim H/4$ and $\Delta \sim H/6$. Excluding $\theta = 40^\circ$, all corrected contact angles are within a $\pm 5^\circ$ gap with respect to their associated physical contact angle in the interval from $\Delta \sim H/4$ to $\Delta \sim H/16$. This leaves us enough leeway to optimize $G(\Delta)$ whilst having a small enough interface thickness to properly capture the physics of most capillary microfluidics problems. The correction methodology was tested and can be used for contact angles smaller than 40° if the Washburn equation assumptions are respected and as long as the contact angle correction is smaller than the physical contact angle.

4.7 3D simulation results

To demonstrate that the *a posteriori* correction proposed in the previous chapter can be used *a priori* for larger 3D simulations, we proceed with simulations of a Self-Coalescence Module (SCM) [197] and a capillary pump [232]. All physical constants are the same as presented in Tab. 4.1 and a contact angle $\theta = 60^\circ$ is used for both cases.

The SCM's schematic is displayed by the two cross-sections in Fig. 4.9a-b and snapshots of the simulation are shown in Fig. 4.9c respectively in the initialisation, transition and self-coalescence stages. A full video of the simulation is available in Supplementary Video 4.13. The aspect ratio of the device is $L/H = 100$ which makes a correction approach assuming asymptotic convergence towards stress singularity (Fig. 4.3iii) unfathomable because of computational costs. We would require more than 5 million cells only to reach $H/\Delta = 16$ and tens of millions of cells to reach $H/\Delta = 32$. In addition, because the meniscus pinning stability on the trench (Fig. 4.9b) is contact angle sensitive as per Concus-Finn's criterion, contact angle corrections must not exceed nor be close to $(\pi - \delta)/2$ to properly model the pinning. Thus, an increase in mesh refinement past the transitory convergence zone (Fig. 4.3ii) is not physically nor computationally viable. We repeat the simulation for three different grids with and without the *a priori* correction and measure the volume fraction. The results are displayed respectively in Fig. 4.10a and Fig. 4.10b. With the correction applied, we reach an outstanding match between the simulations results for all three meshes and Eq. 4.10 in the initialization stage. This could be expected to some degree because the mesh is a uniform structured grid and the geometry is not much different from a 2D capillary assuming $W \gg H$. Nonetheless, because of this strong match with theory, SCMs could potentially be the basis for new benchmark test cases for incompressible two-phase flow solvers involving both capillary flow dynamics and pinning stability.

The second test case is a capillary pump as depicted in Fig. 4.11a. The grid for this second case is unstructured and not uniform. Meshing details are presented in Tab. 4.2 and the aspect ratio of

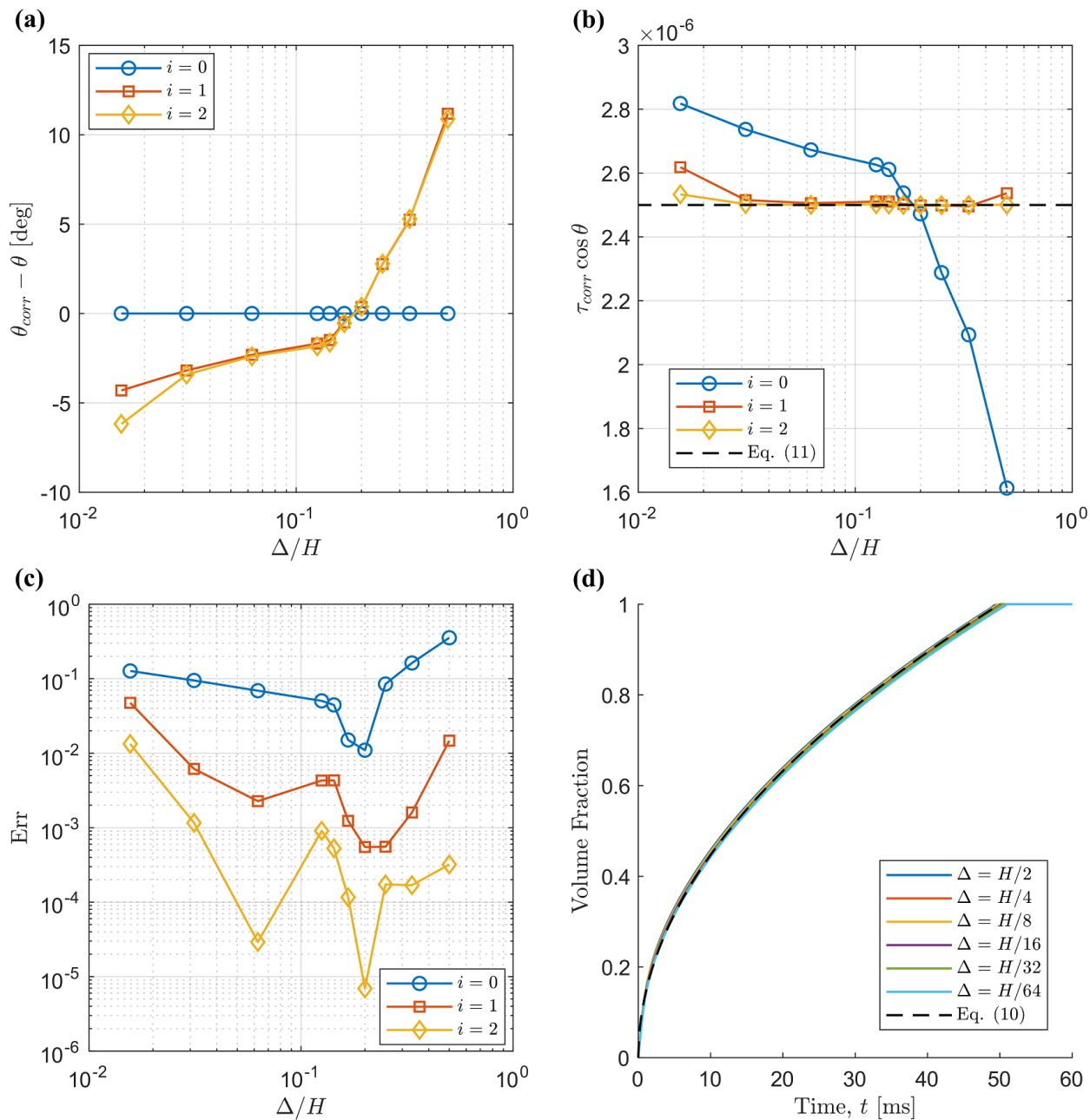


Figure 4.7 Correction procedure for the 2D rectangular microchannel benchmark case with $\theta = 60^\circ$. θ_{corr} and τ_{corr} (a-b) are calculated *a posteriori* repeatedly, showing an overall decrease in the error $\text{Err} = |\tau_{\text{corr}} - \tau|/\tau$ as i increases (c). The $i = 2$ correction is kept and used *a priori* to fix mesh-dependencies of the same case (d).

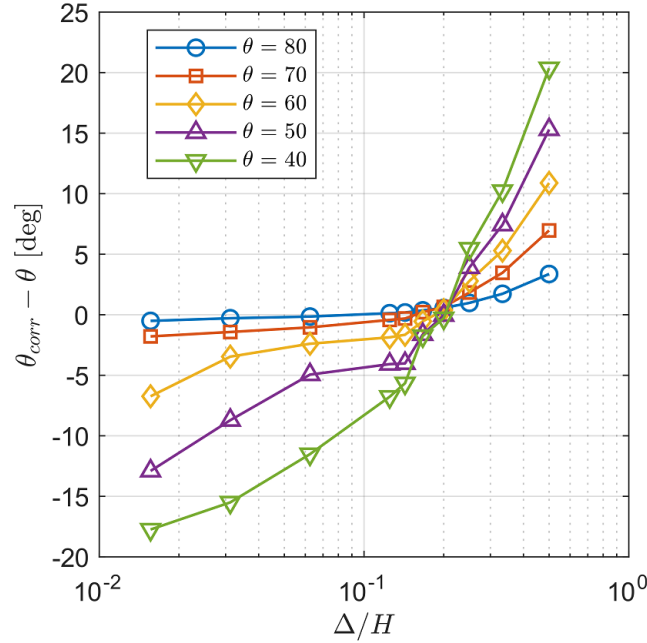


Figure 4.8 Corrected contact angle $\theta_{\text{corr}}(i = 2)$ with respect to the mesh size Δ for different physical contact angles θ .

the device is $L/H \approx 65$, where L is the diagonal length. As for the SCM, this makes a correction approach assuming asymptotic convergence towards stress singularity not possible. Snapshots of the simulation are displayed in Fig. 4.11b and a full video is available in Supplementary Video 4.14. We repeat the same procedure as with the first case by comparing the results with and without correction. The volume fraction measurements are respectively displayed in Fig. 4.12a and Fig. 4.12b. Here again, we observe a substantive reduction of the mesh dependency effect on the volume fraction in time, however less than for the SCM. This is because the capillary pump mesh is not regular with constant H/Δ everywhere and the fact that we use a single correction value. To consider different cell sizes, we would have to implement a boundary condition that reads the local cell size Δ and returns the proper value for θ_{num} locally. Nevertheless, even for an unstructured non uniform mesh the mesh-dependency is still reduced significantly.

4.8 Conclusion

The VOF method can serve to model complex capillary flows in 3D microstructures such as SCMs, capillary pumps and micro-valves. However, the results are highly mesh-dependent due to intrinsic multiscale effects not considered by continuum mechanics. To make this point evident, we verified the code using a 2D rectangular capillary benchmark case for which we know analytically the

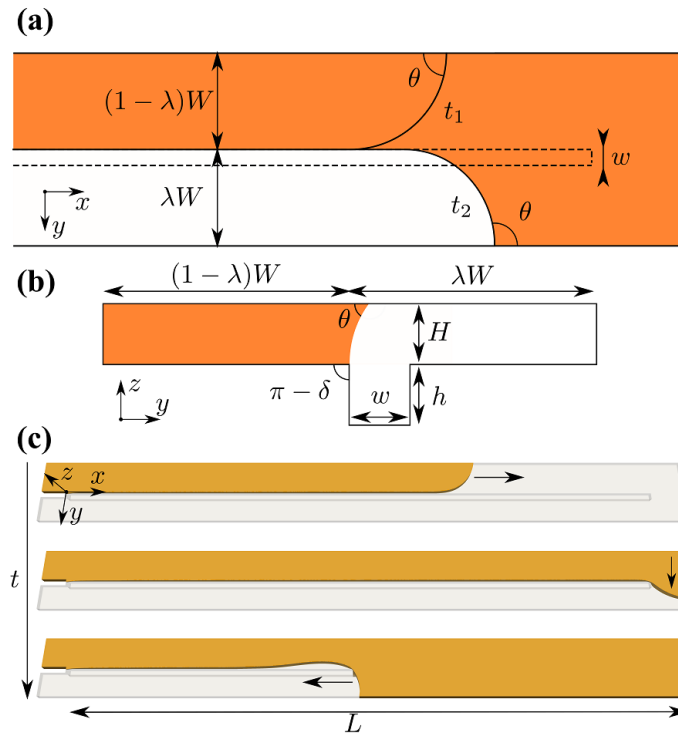


Figure 4.9 Top view of a self-coalescence module schematic (a) in the initialization stage (t_1) and self-coalescence stage (t_2), cross-sectional view of the schematic (b) and simulation snapshots (c) taken at $t = 35$ ms, 85 ms and 122 ms. The main channel dimensions are $L \times W \times H = 6000 \times 600 \times 60 \mu\text{m}^3$, the trench dimensions are $L \times w \times h = 6000 \times 60 \times 60 \mu\text{m}^3$ with $\delta = \pi/2$, the contact angle is $\theta = 60^\circ$ and $\lambda = 0.5$.

Table 4.2 Mesh details for the capillary pump case.

	$\Delta = H/4$	$\Delta = H/6$	$\Delta = H/8$
Number of cells	103,920	350,712	834,256
Max aspect ratio	3.47992	3.52884	3.47588
Max mesh non-orthogonality	25.8235	26.5289	27.1862
Average mesh non-orthogonality	2.98406	2.15215	1.61587
Max skewness	1.98284	1.57256	1.30628

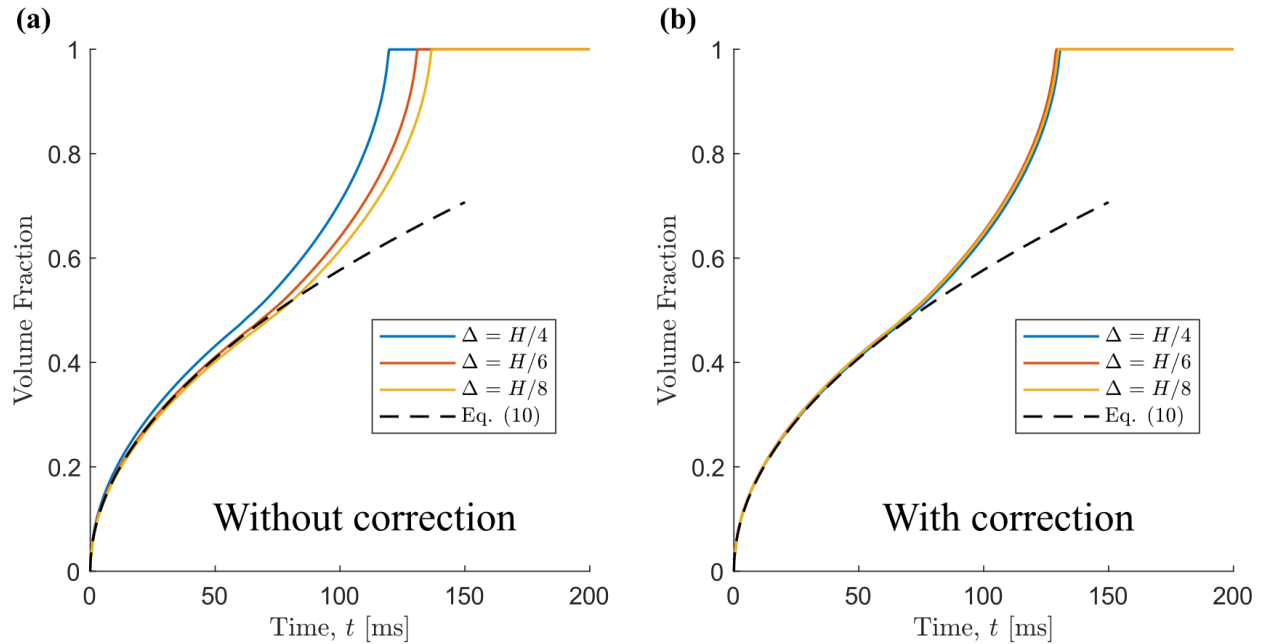


Figure 4.10 Capillary filling of the self-coalescence module (a) without correction, and (b) with correction. The number of cells for the three meshes are 72,960; 246,240 and 583,680.

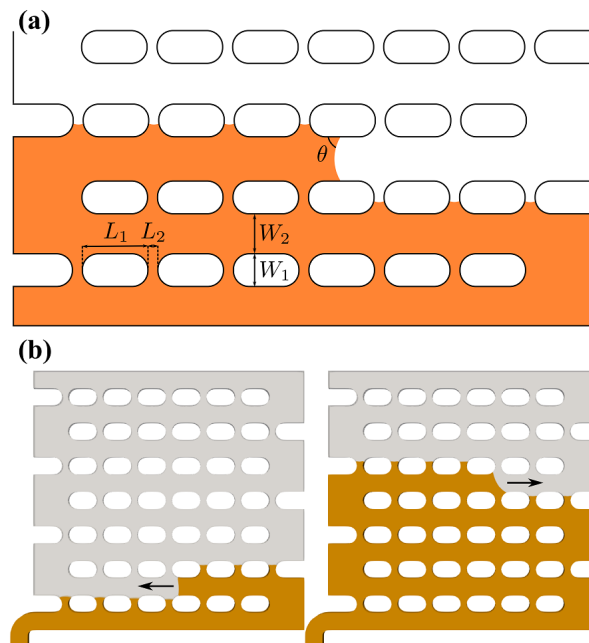


Figure 4.11 Top view of a capillary pump schematic (a) and simulation snapshots (b) taken at $t = 21$ ms (left) and 64 ms (right). The cross-sectional area of pillars is $L_1 \times W_1 = 75 \times 45 \mu\text{m}^2$ with rounded corners of radii $W_1/2$, the longitudinal gap between pillars is $L_2 = 15 \mu\text{m}$, the lateral gap between pillars is $W_2 = 45 \mu\text{m}$, the height of the capillary pump is $H = 15 \mu\text{m}$ and the contact angle is $\theta = 60^\circ$.

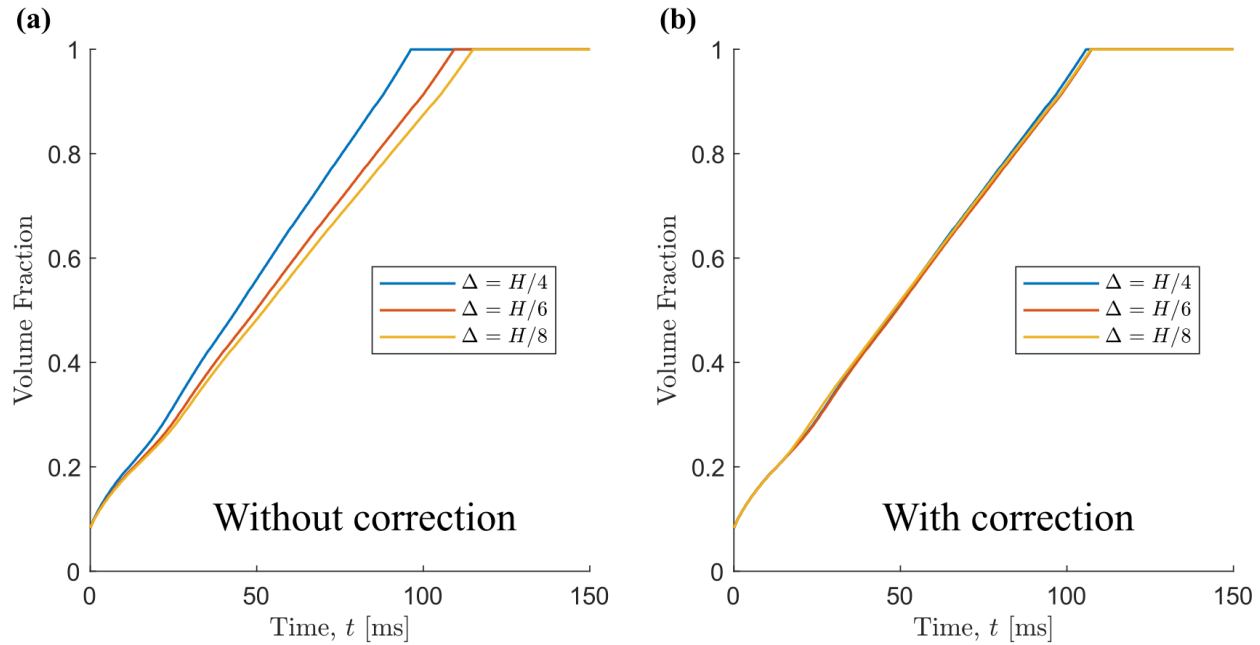


Figure 4.12 Capillary filling of a capillary pump (a) without correction, and (b) with correction.

solution for the displacement of the meniscus. Several verification steps were done using different partial slip and contact angle values showing a dependence of the results on mesh size regardless of boundary conditions.

To remediate the situation, we developed a novel correction approach for capillary flows abiding by Washburn's equation hypotheses. A static contact angle-based correction is found *a posteriori* from a simple 2D benchmark case which is in turn used *a priori* for complex 3D simulations. This methodology was successfully applied to the simulations of a SCM and a capillary pump. The correction procedure proves to be efficient at reducing the mesh-dependency even for unstructured non uniform meshes. In addition, we introduced the notion of optimal grid to minimize the error caused by improper treatment of stress at walls which implies a compromise between interfaces' sharpness and the proximity of corrected and physical contact angles. With the correction procedure, the VOF method gives us a solid framework to optimize and design new generations of capillary autonomous microsystems.

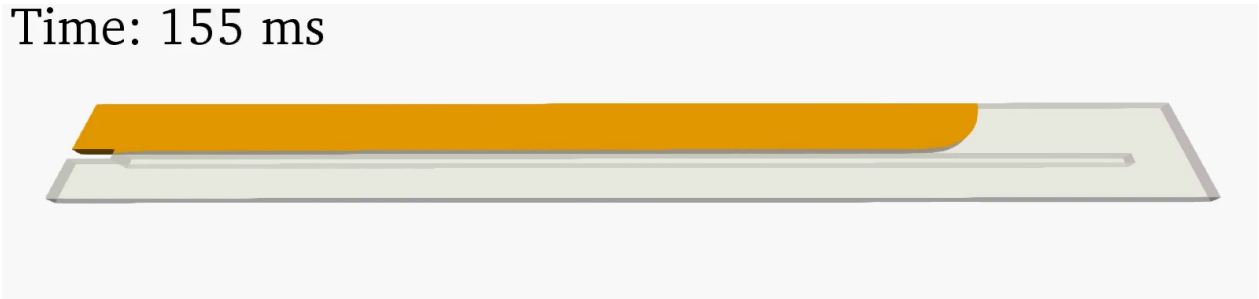
Simulation results of the SCM shows that it could serve as a basis for future 3D benchmark test cases to study the performance of incompressible two-phase flow solver. A great variety of capillary phenomena are involved in understanding how SCMs work including Washburn's law, the Concus-Finn criterion and the Bosanquet law [255] in cases where inertia is dominant. For its close relation with Saffman-Taylor viscous fingers [100], a SCM-based benchmark could also be used to provide further insights into the modelling of receding Saffman-Taylor viscous fingers with

forced geometrical configurations using pinning lines.

Lastly, the correction procedure introduced in this work is not limited to the VOF method and can be used for any continuum based CFD method. Furthermore, this method has the advantage of not requiring any access to the internal code of the CFD software or library used, i.e. it can be used with any commercial, open source or in-house codes.

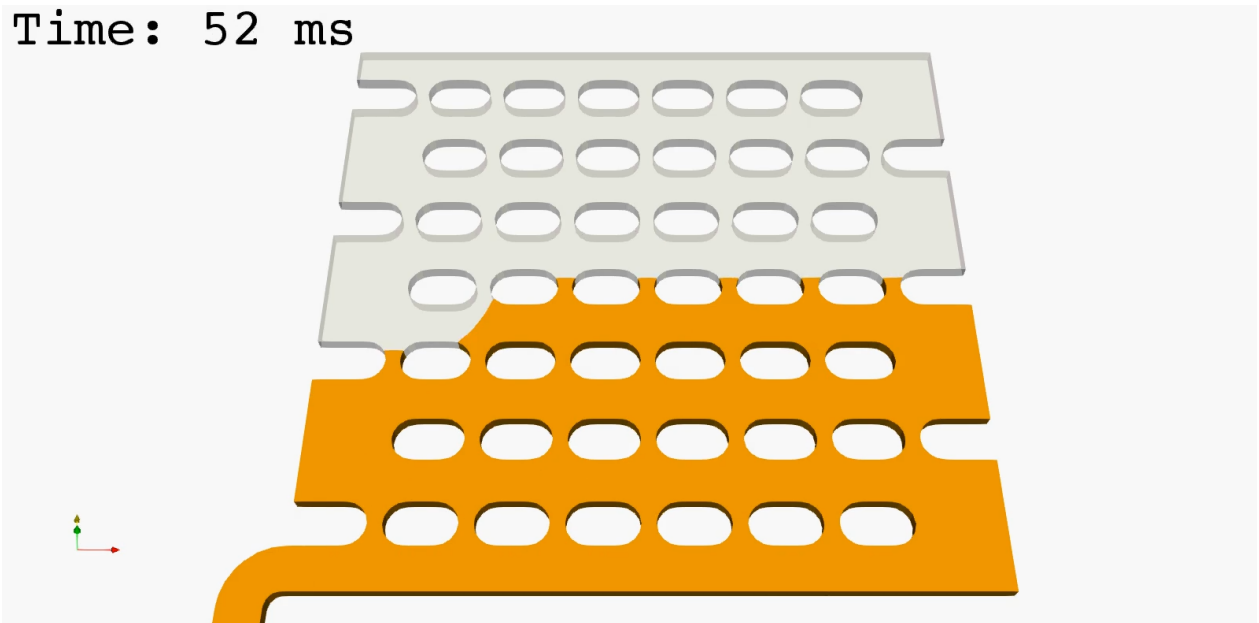
4.9 Supplementary videos

Time: 155 ms



Video 4.13 Water volume fraction of a filling SCM. (Flash Player required)

Time: 52 ms



Video 4.14 Water volume fraction of a filling capillary pump. (Flash Player required)

CHAPTER 5 ARTICLE 2: DYNAMICS OF ACCELERATING CAPILLARY FLOW

Authors: Samuel Castonguay, Yuksel Temiz, Emmanuel Delamarche, Thomas Gervais

Chapter Overview

In this theme, I used numerical modelling to discover and characterise Reverse-Washburn flows, and I lay down the theoretical framework describing them. This novel type of capillary flow provides a superior control over passive flows in microchannels. In this work, I conceived the research, developed the theoretical models, conducted the numerical simulations, analysed experimental results, and compared theoretical, numerical, and experimental results. Yuksel Temiz and I designed the SCMs. Yuksel also designed and conducted the experiments, and fabricated the SCMs. My advisor Thomas Gervais supervised the research. All authors discussed the results. Thomas and I wrote, reviewed, and edited the paper with inputs from all authors. This work was submitted in *Physical Review Fluids*, March 8, 2022.

Abstract

We present an important corollary to Washburn's equation in capillary dynamics. We show that, during capillary filling, in cases where flow path decreases with time, an accelerating capillary flow or reverse-Washburn flow regime occurs. We provide a description of this phenomenon following Washburn's classic analysis and characterize a "reverse-Washburn" capillary flow regime in both inertial and viscous regimes. This regime is observed and characterized in experiments and numerical simulations of recently discovered self-coalescence flows, opening the door to engineering devices with naturally accelerating capillary inflows.

5.1 Introduction

The penetration of liquids into capillaries and porous bodies is ubiquitous in many natural and industrial processes. The first analytical assessment of the dynamics of capillary flow was done by Lucas and Washburn [82, 251] a century ago and its governing equation is commonly referred to as Washburn's equation. However, an important corollary to this equation has been omitted. In situations where the flow path shortens, viscous losses decrease with respect to time resulting in an accelerating flow. These shortening flow paths can simply be due to the spontaneous dewetting of fluids, in which case the fluid is receding in an emptying channel. However, more interesting cases

have been discovered recently in which a net positive flow can be introduced in a channel, all the while inducing capillary acceleration. In this letter, we follow the classic derivation of Washburn's equation and generalize it to characterize such capillary inflow. We also derive the inertial equivalent of this expression, namely the generalized Bosanquet equation for accelerating capillary flows. Finally, we use our model to describe the experimental behavior of accelerating capillary inflows as evidenced in self-coalescence flow - or zipper flow - physics [197] with supporting experiments and numerical simulations.

Capillary Flows are found in soil water retention [256], petroleum engineering [229, 257], autonomous microfluidic systems [197, 232], rapid diagnostic tests [258], anticounterfeiting features [26] and fuel cells [259, 260] to name a few. Decelerating capillary flow is a critical issue in many systems where precise spontaneous imbibition is limited by an upstream hydraulic resistance build-up [261, 262], and any convection-limited transport problems [263, 264] where the flow is driven by surface tension. In the later case, accelerating capillary flows could be used to engineer thinner boundary layers resulting in enhanced heat and mass transport to the surfaces.

The dynamics of capillary flow can be controlled through engineering of a specific device topology or by introducing external forces. Some examples include electro-osmotic pumping [265], geometric constrictions [266, 267] and solid-liquid surface tension manipulations such as wettability gradients and thermal gradients [28]. However, none apply to unaltered passive systems where the dynamic is simply defined by a pressure balance between capillary pressure and viscous losses, as per Washburn's classic derivation. The aim of this letter is to i) develop the general equation of motion for accelerating capillary flow with and without inertia, and ii) use it to describe the experimental behavior of accelerating flows with net capillary filling as evidenced in self-coalescence flow - or zipper flow - physics [197] with supporting experiments and numerical simulations. In the following work, self-coalescence is achieved using a straight capillary pinning line, but can be generalized to any shapes where coalescence occurs in a confined area, e.g. spirals, sharp turns, and slow meanders. This process also describes the filling dynamics of other capillary microsystems such as capillary pumps and microfluidic phaseguides.

5.2 The Dynamics of Capillary Flow

Washburn-like flows, as discovered by Lucas and Washburn 101 years ago [82, 251], occur when an imbalance exists between free surface energy change rate and viscous dissipations, yielding a net time varying force driving the fluid in a filling channel. The analytical model is derived as per the original paper by Washburn [82], and we refer to [68] for more details on capillary flow theory in general.

Disregarding any influence other than an increase in surface energy F_S and a decrease in pressure-volume Helmholtz free energy F_{pV} , the variation of the total Helmholtz free energy F at equilibrium dictates the balance between these forces

$$\delta F = \delta F_S + \delta F_{pV} = \delta F_S + \delta V \Delta p_S = 0 \quad (5.1)$$

where δV is the variation in volume (Fig. 5.1) and Δp_S is the capillary pressure also known as the Young-Laplace pressure drop.

Viscous dissipation of energy in a fully developed Poiseuille flow is given by the hydraulic analog of Ohm's law, i.e. the Hagen-Poiseuille law

$$\Delta p = RQ \quad (5.2)$$

where R is the hydraulic resistance and Q is the flow rate. The hydraulic resistance can be decomposed in several components varying along the length of the capillary with respect to several factors such as geometry and physical properties [268,269]. Here, we will focus on general systems where the hydraulic resistance can be decomposed in a constant part, R_0 , and a linearly varying one in space, xR_x , where x is the moving capillary interface's position and R_x is the hydraulic resistance per unit length. The constant part can be expressed as an effective pre-filled length we define as $L_0 = R_0/R_x$. Introducing the effective displacement $\xi = L_0 + x$ and the adimensional variables $\tilde{x} = x/\ell$, $\tilde{\xi} = \xi/\ell$ and $\tilde{t} = t/\tau$ with ℓ an arbitrary length and $\tau = \mathcal{A}R_x\ell^2/2\Delta p_S$ the Washburn characteristic time constant, and combining Eq. 5.1-5.2 we obtain the following equation of motion

$$\tilde{\xi} \frac{d\tilde{\xi}}{d\tilde{t}} = \pm \frac{1}{2} \quad (5.3)$$

where the \pm sign denotes when the flow is accelerating (negative) and decelerating (positive). Solving Eq. 5.3 assuming $\tilde{\xi}(0) = \tilde{\xi}_0$ yields

$$\tilde{\xi}^2 - \tilde{\xi}_0^2 = \pm \tilde{t} \quad (5.4)$$

With $\tilde{\xi}_0 = 0$ and taking the positive branch of the solution, we recover the canonical form of Washburn's classic equation $\tilde{\xi} = \sqrt{\tilde{t}}$. In honor of the previous work by Washburn [82] on this topic a century ago and for its direct relation with the former equation, we label the negative branch of this result as the "Reverse-Washburn equation". This present analysis assumes an identical system for the Washburn and Reverse-Washburn (R-W) regimes. However, in practice, the presence of topological asymmetries and different wetting dynamics complexifies the analysis, and two different Washburn characteristic time constants arises (SCM derivation details in Appendix C).

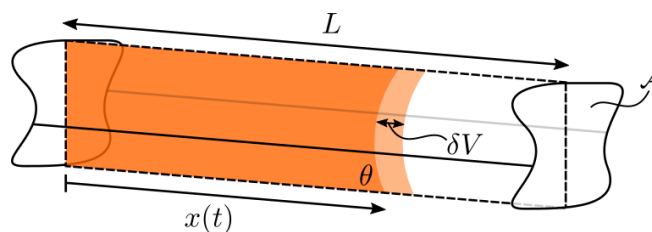


Figure 5.1 Schematic of a filling capillary of arbitrary cross-sectional shape, cross-sectional area \mathcal{A} and length L . Cut-plane along the x -axis in dashed lines.

Following the analysis by Rideal and Bosanquet [255, 270] we can further extend the model to take into account inertial effects, thus removing the non-physical singular velocity occurring in Washburn's equation when $x \rightarrow 0$ (see Appendix A).

5.3 Methodology

Self-coalescence flow modules (SCM) can be readily fabricated using standard silicon micromachining techniques. A brightfield image of the SCM device is presented in Fig. 5.2(a), and cross-sectional schematics with all relevant parameters for numerical simulations are presented in Fig. 5.2(b-c).

SCM chips were fabricated on 4-inch single-side-polished Si wafers (Si-Mat, Germany) using photolithographic patterning of two SU-8 layers (MicroChem Corp.). Two layouts to pattern rails (clear mask) and microfluidic channels (dark mask) were designed in L-Edit software and transferred to glass/Cr masks using a direct laser writing system (DWL 2000, Heidelberg Instruments, Germany). For the rails, SU-8 3025 was spin-coated and patterned at a thickness of about $33 \mu\text{m}$ following the recipe provided by the supplier. A second SU-8 layer for the microchannels was then patterned using the same SU-8 photoresist but with a slightly modified recipe to achieve $57 \mu\text{m}$ -deep channels (Suppl. Fig. 5.5-5.6). The chips were then diced after protecting the wafer surface using a thin photoresist layer. Following cleaning of individual chips in acetone and then isopropanol, the chips were dried using N_2 and their surface was sealed using a DF-1050 dry film resist (Nagase ChemteX, USA) laminated at 45°C , forming close rectangular microchannels. A simple holder with liquid loading reservoirs was 3D-printed to accommodate the chip and load samples (Suppl. Fig. 5.7). After applying about $20 \mu\text{L}$ liquid sample to the reservoir (Suppl. Fig. 5.8), videos of the capillary filling were acquired at 60fps using Nikon 1 J3 camera connected to a stereo microscope (Leica MZ16). Data was acquired by tracking the meniscus position manually frame-by-frame using MATLAB. High quality images were taken using a Nikon 90i microscope, for planar views, and a custom-built microscope, for slanted image planes.

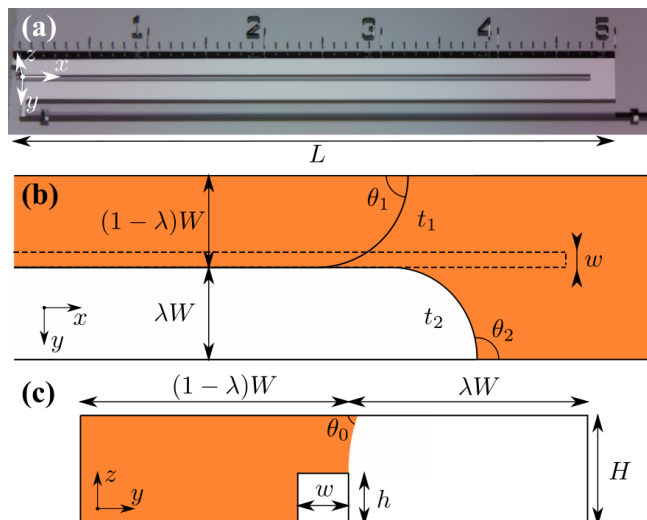


Figure 5.2 Brightfield image of the self-coalescence module (a) using the microscope at an angle of 45° , self-coalescence module schematic in the Washburn and R-W regimes ((b) at t_1 and t_2 respectively) and cross-section of the device along the capillary pinning line (c). The materials are SU-8 on silicon wafer. The channel dimensions are $L \times W \times H = 5200 \times 500 \times 57 \mu\text{m}^3$, the rail's position is $\lambda = 0.5$ and its cross-sectional area is $w \times h = 25 \times 33 \mu\text{m}^2$. θ_0 , θ_1 and θ_2 are effective contact angles determined from each individual experiment.

Full 3D dynamics of R-W flows under the continuum limit approximation has been further carried out using a Volume-of-flow (VOF) method. Singular stresses in the vicinity of moving contact lines due to the continuum formalism breaking down at the molecular scale are dealt with using a recently developed semi-analytic static contact angle correction [202]. The position is tracked at every time step using the volume fraction of water in the whole domain and scaled from 0 to L using probes at the end of the channel for proper adimensionalization. The domain is discretized from a regular orthogonal grid that is snapped on the device's geometry, and the problem is solved using the "interFoam" solver from OpenFOAM. Details regarding numerical modelling are provided in Appendix B.

5.4 Results & Discussion

Experiments and simulations were performed for two different liquids, i) deionized (DI) water, and ii) a glucose standard solution of 1 mg/mL (Sigma-Aldrich) to mimic Newtonian organic liquids. The viscosity of water, density and air/water interfacial tension are respectively 1 mPas, 1000 kg and 72 mJ/m^2 at $\approx 20^\circ\text{C}$. At 0.1%(w/w), physical properties of the glucose solution are not expected to divert significantly from water [271,272]. However, an increase in glucose concentration is expected to increase density, viscosity and surface tension. Because other factors, such as surface

roughness, have greater impact on the flow dynamics, we use the same physical properties for both liquids and take into account all variations in the Washburn time constants by mean of the effective contact angle calculation.

Experiment and simulation snapshots are presented in Fig. 5.3. Contact angles on the SU-8 side walls θ_1 and θ_2 are dynamic in nature due to surface roughness and impacts wettability [273,274]. However, an effective static contact angle can be extracted, as per Cassie's law [275], from a fit of Washburn's characteristic time and the rate of increase of ξ^2 . With $\theta_0 = 85^\circ$, the measured average effective contact angles on the SU-8 walls and standard error interval in both regimes are respectively $\theta_1 = 91.0 \pm 1.2^\circ$ and $\theta_2 = 108.3 \pm 1.4^\circ$ ($n = 8$) for DI water and $\theta_1 = 86.5 \pm 0.8^\circ$ and $\theta_2 = 103.3 \pm 0.9^\circ$ ($n = 7$) for the glucose solution. This is in agreement with observations in Fig. 5.3(a) where the wetting dynamics of SU-8 is slightly hydrophobic for DI water. We also observed that the glucose displayed slightly lower contact angles with the surface than DI water in general, resulting in shorter filling times as made evident in Fig. 5.4. All data sets are presented in Sup. Fig. 5.9. When the moving front reaches positions near the inlet and outlet ($x \rightarrow 0$), we observe a discrepancy with the theory due to additional liquid-surface energy gains and losses not considered by the model. Our experimental results show that there is a match between theory and experiments to within 16% and 2% respectively for the Washburn time constant and Reverse-Washburn time constant. Contact angles are given within 1.3% and 0.9%. Numerical results are also in agreement with both theory and experiments in the Washburn and Reverse-Washburn regimes.

5.5 Conclusion

To conclude, we have observed and characterized here at least one instance in which capillary velocity accelerates during filling without resorting to channel branching or making changes in the surface properties of the device. Also, there is a significant advantage of using self-coalescence as the acceleration is continuous, easily controllable, and occurs without using high resolution branching which takes large amount of space on a chip and requires high precision fabrication. Furthermore, self-coalescence can be generalized to any geometries where coalescence occurs in confined areas.

The setup is also useful with most liquids with high surface tension that spontaneously wet a surface. Alternatively, the system can be biased with a positive pressure to introduce liquids that do not spontaneously wet the surface, such as water in hydrophobic channels, as done in Gökçe *et al.* [197]. In this work, DI water and a glucose solution were used to simulate biological liquids that are ubiquitous in lab on chip devices.

Thus self coalescence flow modules provide a simple way towards engineering accelerating flows

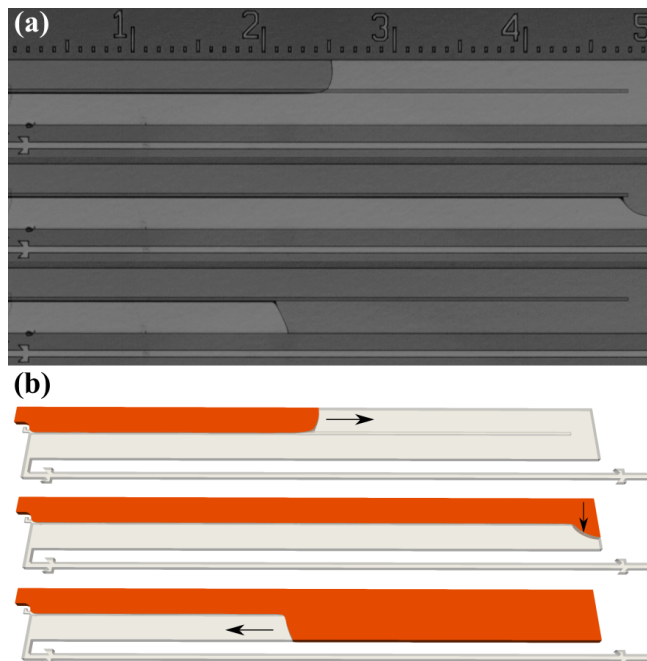


Figure 5.3 Side-by-side comparison of experiments (a) and simulations (b). From top to bottom, i) the meniscus moves forward and decelerates in time due to an increase in path length, ii) the meniscus enters the transition zone towards self-coalescence, and iii) the meniscus moves backward whilst accelerating due to a reduction in the length of the flow path. We can observe in (a) that SU-8 is slightly hydrophobic, as taken into account in our theoretical and numerical models.

to enhance mass transfer and compensate for binding site depletion in surface-based sensors [263, 264], or to speed up lengthy steps in capillary assays. Finally, the pumping capability of SCMs can be scaled up by placing several modules in parallel to generate accelerating flows of arbitrary volumes [276].

5.6 Appendix

5.6.1 Derivation of the Bosanquet and Reverse-Bosanquet equations

In the following section, we derive the theoretical form of the Reverse-Bosanquet equation, thus extending the work of Rideal and Bosanquet [255, 270] to account for inertia in accelerating capillary flows. Introducing the density of the liquid, ρ , the new equation of motion reads

$$\text{La} \frac{d}{d\tilde{t}} \left(\tilde{\xi} \frac{d\tilde{\xi}}{d\tilde{t}} \right) + \tilde{\xi} \frac{d\tilde{\xi}}{d\tilde{t}} = \pm \frac{1}{2} \quad (5.5)$$

where, again, the \pm sign denotes when the flow path increases (positive) and decreases (negative), and

$$\text{La} = \frac{\gamma\rho L_c}{\mu^2} \quad (5.6)$$

is the Laplace number with a characteristic length $L_c = 2\kappa\mu^2/(\mathcal{AR}_x\ell)^2$. The Laplace number characterises inertia and surface tension with respect to momentum transport. Thus, the leftmost part of Eq. 5.5 accounts for inertial effects, and the remaining terms are equivalent to Washburn's equation (Eq. 5.3), i.e. the capillary pressure and viscous losses where the negative sign denotes a decrease in hydraulic resistance. Substituting $u = \tilde{\xi}d\tilde{\xi}/d\tilde{t}$ in Eq. 5.5 and assuming $u(0) = u_0$, we obtain

$$u = \left(u_0 \mp \frac{1}{2}\right) e^{-\tilde{t}/\text{La}} \pm \frac{1}{2} \quad (5.7)$$

Reinjecting $\tilde{\xi}$ into 5.7 and solving assuming $\xi(0) = \xi_0$ yields

$$\tilde{\xi}^2 - \xi_0^2 = \text{La}(\pm 1 - 2u_0) \left(e^{-\tilde{t}/\text{La}} - 1\right) \pm \tilde{t} \quad (5.8)$$

Finally, introducing the adimensional velocity $\tilde{v} = d\tilde{\xi}/d\tilde{t}$, we can rewrite Eq. 5.8 as

$$\tilde{\xi}^2 - \xi_0^2 = \text{La} \left(\pm 1 - 2\xi_0\tilde{v}_0\right) \left(e^{-\tilde{t}/\text{La}} - 1\right) \pm \tilde{t} \quad (5.9)$$

where \tilde{v}_0 is the initial velocity of the meniscus. Eq. 5.9 clearly shows the equivalence of the Bosanquet and Washburn equations and the Reverse-Bosanquet and Reverse-Washburn equations when inertia is neglected, i.e. when the Laplace number is null.

5.6.2 Digital twins and numerical methodology

For a laminar incompressible isothermal flow of a liquid mixture with a spatially defined density, $\rho \equiv \rho(\mathbf{x})$, and viscosity, $\mu \equiv \mu(\mathbf{x})$, the conservation of momentum, $\rho\mathbf{u}$, with an external body force \mathbf{F} can be written as

$$\frac{\partial \rho\mathbf{u}}{\partial t} + \nabla \cdot (\rho\mathbf{u}\mathbf{u}) = -\nabla p + \mu\nabla^2\mathbf{u} + \mathbf{F} \quad (5.10)$$

with the incompressible mass conservation condition $\nabla \cdot \mathbf{u} = 0$. For a two-phase mixture, we can define a phase field $\alpha \in [0, 1]$ which is advected in space using the simple first order transport equation

$$\frac{\partial \alpha}{\partial t} + \nabla \cdot (\alpha\mathbf{u}) = 0 \quad (5.11)$$

This is known as the volume of fluid (VOF) method. In practice, a compression term has to be added to Eq. 5.11 to mitigate numerical diffusion and smearing of the interface [249]. Physical properties

of the mixture are simply obtained from a linear combination of the two fluids' individual properties with the phase field acting as a weight function, i.e. $\rho = \alpha\rho_1 + (1 - \alpha)\rho_2$ and $\mu = \alpha\mu_1 + (1 - \alpha)\mu_2$, where the subscripts 1 and 2 denotes the two liquids. Assuming no external force other than the capillary force is exerted on the system, we can write \mathbf{F} using the continuum surface force (CSF) formulation [65] as $\mathbf{F} = \gamma\kappa(\nabla\alpha)$ where $\kappa = \nabla \cdot (\nabla\alpha/|\nabla\alpha|)$ is the curvature of the multiphase interface. Singular stress' in the vicinity of moving contact lines due to the continuum formalism breaking down at the molecular scale are dealt with using a simple semi-analytic static contact angle correction [202]. We solve these equations numerically using "interFoam", a solver from the open source library OpenFOAM using the finite volume method (FVM). The mesh is generated and snapped on the geometry using the meshing utilities "blockMesh" and "snappyHexMesh" from the same library. Compromising between simulation time and results quality, we opt for an initial grid of uniform mesh size $\Delta = H/6$ for a total of 205,914 cells after the snapping iterations.

5.6.3 Derivation of the Washburn and reverse-Washburn equations for a self-coalescence module

In the following section, we solve the equations of motion for a moving meniscus in a SCM as depicted in Fig. 5.2 in the accelerating and decelerating regimes. The symbols "+" and "-" are used to label variables and parameters in the decelerating and accelerating regimes respectively, i.e. positive and negative velocity. Introducing the dimensionless variables $\tilde{x}_{\pm} = x_{\pm}/\ell$ and $\tilde{t}_{\pm} = t/\tau_{\pm}$, and the capillary pinning line (rail) height h and width w , we first calculate the variation of the total Helmholtz free energy at equilibrium. Assuming a translation symmetry of the capillary interface when moving along the x -axis by an infinitesimal displacement δx , the variations in surface energy are given by

$$\delta F_S^+ = (\gamma_{sl} - \gamma_{sg})\delta x [2(1 - \lambda)W + H + h] + \gamma_g\delta x(H - h) \quad (5.12)$$

and

$$\delta F_S^- = (\gamma_{sl} - \gamma_{sg})\delta x [2\lambda W + H + h] - \gamma_g\delta x(H - h) \quad (5.13)$$

where γ_{sl} , γ_{sg} and γ_g are respectively the solid-liquid, solid-gas and liquid-gas surface tensions. The variations in volume are simply given by $\delta V^+ = \delta x[(1 - \lambda)WH - hw]$ and $\delta V^- = \delta x\lambda WH$. With these quantities defined, we can calculate the Laplace pressure drop from Eq. 5.1 knowing that $\cos\theta = (\gamma_{sl} - \gamma_{sg})/\gamma_g$ and $\gamma_g \equiv \gamma$. We define all relevant parameters and variables according to Fig. 5.2 in Tab. 5.1.

In the R-W equation of Tab. 5.1, $\Delta\tilde{t}_d$ is a normalized delay time (with respect to \tilde{t}_-) that takes into account the Washburn filling time Δt_+ and the transition time in-between the Washburn and R-W regimes when the meniscus moves along the wall at $x = L$. We also assumed in Tab. 5.1 that

Table 5.1 Definition of parameters and variables for a SCM as shown in Fig. 5.2.

Definition	Washburn	Reverse-Washburn
Section width	$W_+ = (1 - \lambda)W$	$W_- = \lambda W$
Cross-sectional area	$\mathcal{A}_+ = HW_+ - hw$	$\mathcal{A}_- = HW_-$
Curvature	$\kappa_+ = [2W_+ \cos \theta_0 + (H + h) \cos \theta_1 + (H - h)] / \mathcal{A}_+$	$\kappa_- = [2W_- \cos \theta_0 + (H + h) \cos \theta_2 - (H - h)] / \mathcal{A}_-$
Variable hydraulic resistance	$R_x = \frac{12\mu}{H^3 W_+} \left(\frac{f}{1 - (w + 0.63H)/W_+} + \frac{1 - f}{1 - 0.315H/W_+} \right)$	
Characteristic time	$\tau_+ = \frac{\mathcal{A}_+ R_x \ell^2}{2\gamma \kappa_+}$	$\tau_- = \frac{\mathcal{A}_- R_x \ell^2}{2\gamma \kappa_-}$
Filling time	$\Delta t_+ = \tau_+ \left(1 - \tilde{\xi}_0^2 \right)$	$\Delta t_- = \tau_- \left(1 - \tilde{\xi}_0^2 \right)$
Meniscus position	$\tilde{\xi}_+ = \sqrt{\tilde{\xi}_0^2 + \tilde{t}_+}$	$\tilde{\xi}_- = \sqrt{\tilde{\xi}_0^2 + \Delta \tilde{t}_d - \tilde{t}_-}$

no liquid spills over in the $y < 0$ region above the rail. To take into account each individual surfaces' physical properties, we simply have to recalculate Eq. 5.12-5.13 accordingly. The variable hydraulic resistance can be bounded within a defined interval. The maximal value of the interval is obtained when $h \rightarrow H$, where the hydraulic resistance is approximated by a closed rectangular channel of width $W_+ - w$. The minimal value is obtained when $h \rightarrow 0$, where the hydraulic resistance is obtained from a rectangular channel of width W_+ with a symmetry plane on the side of the liquid-gas interface. The exact value of the hydraulic resistance can be expressed as a linear combination of both extremes weighted by a factor f . This weight factor is calculated numerically using finite element analysis (COMSOL Multiphysics) of a laminar stationary single phase flow in the approximated flow path geometry. Solid-liquid interfaces are set to zero velocity Dirichlet boundary conditions and the liquid-gas interface to a Neumann boundary condition. The resulting weight factor is $f = 0.8207$ for $H = 57\mu\text{m}$ and $h = 33\mu\text{m}$.

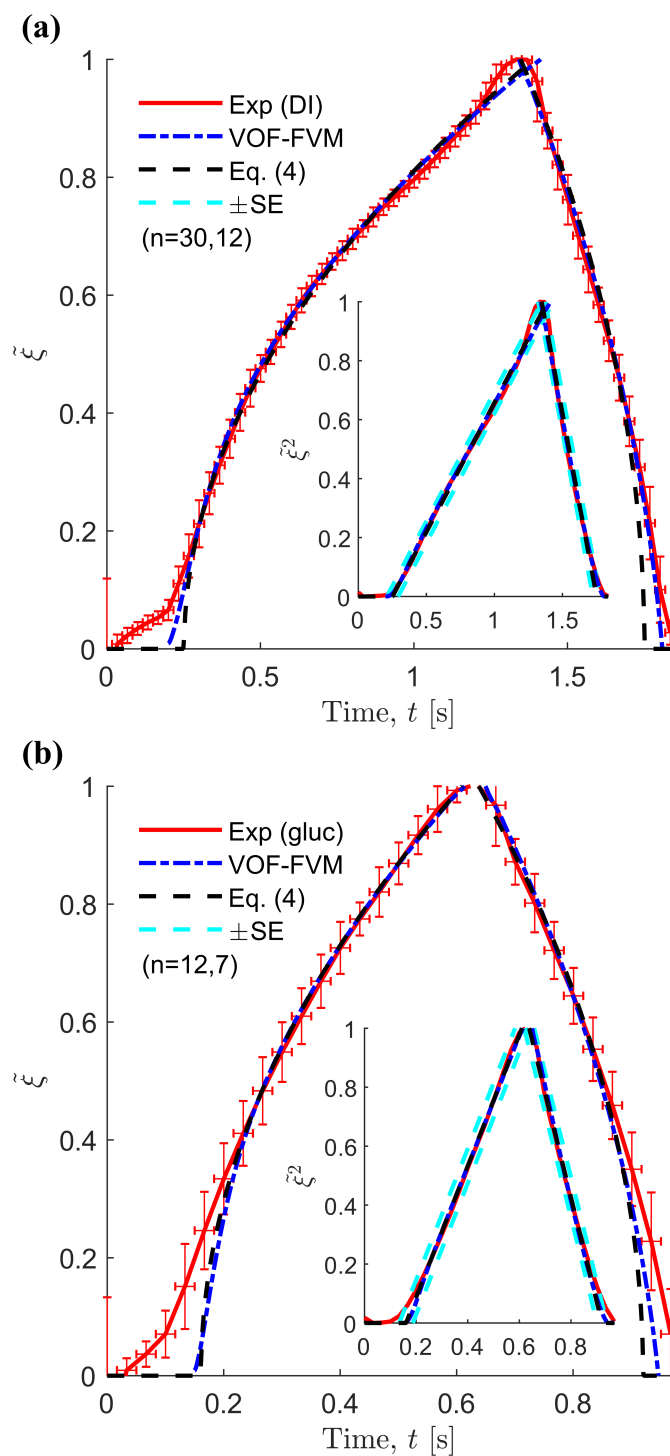


Figure 5.4 Superposition of the experimental (red), numerical (blue) and theoretical (black) results for a Washburn- Reverse-Washburn cycle in a capillary structure. The inset is the same data set squared to emphasize the square root behavior of the Washburn and R-W regimes. Experimental error bars are obtained from the frame rate of the camera and the distance travelled by the meniscus within the exposure time. The cyan dashed lines are obtained from the standard error of the linear fit in both regimes with n being the number of points used for the fits.

5.7 Supplementary Material

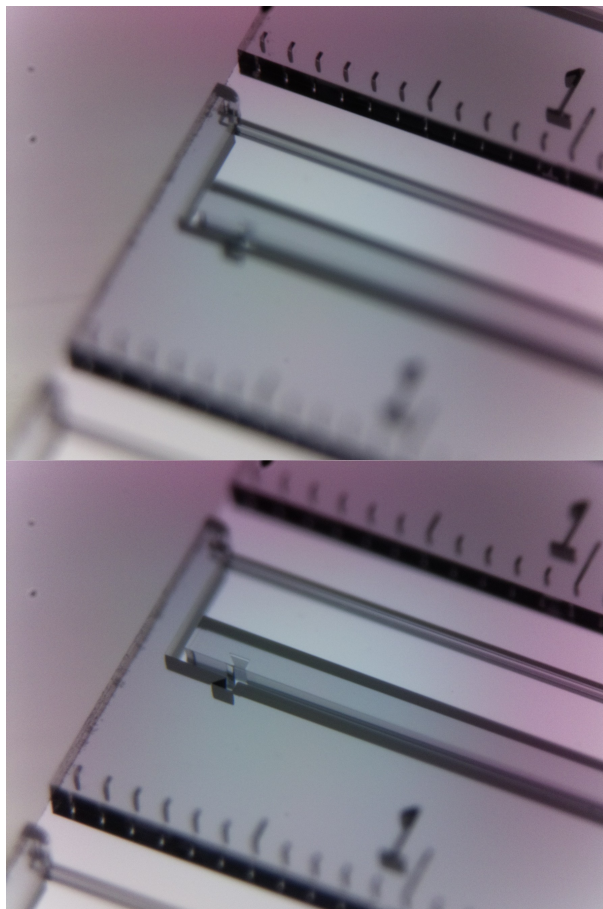


Figure 5.5 Brightfield image of the chip with a focus on the chip's inlet (top) and outlet valve (bottom) using the Lego microscope, a custom-designed and full-motorized microscopy system that can take images at different angles. Instructions, software and all design files are open source and can be found at <https://github.com/IBM/Microscopy>.



Figure 5.6 Brightfield image of the entire chip with control channels (high inlet hydraulic resistance on the right side).



Figure 5.7 Chip placed on the loading pad.

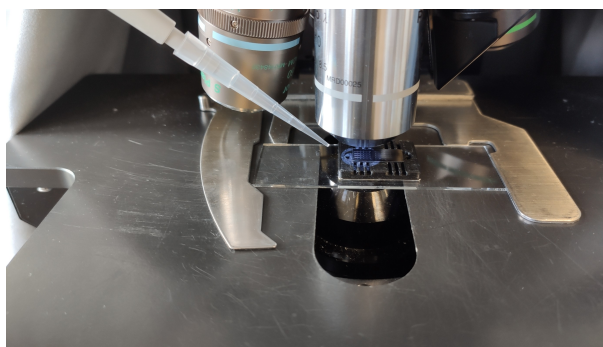


Figure 5.8 Experimental setup for pipetting under a microscope.

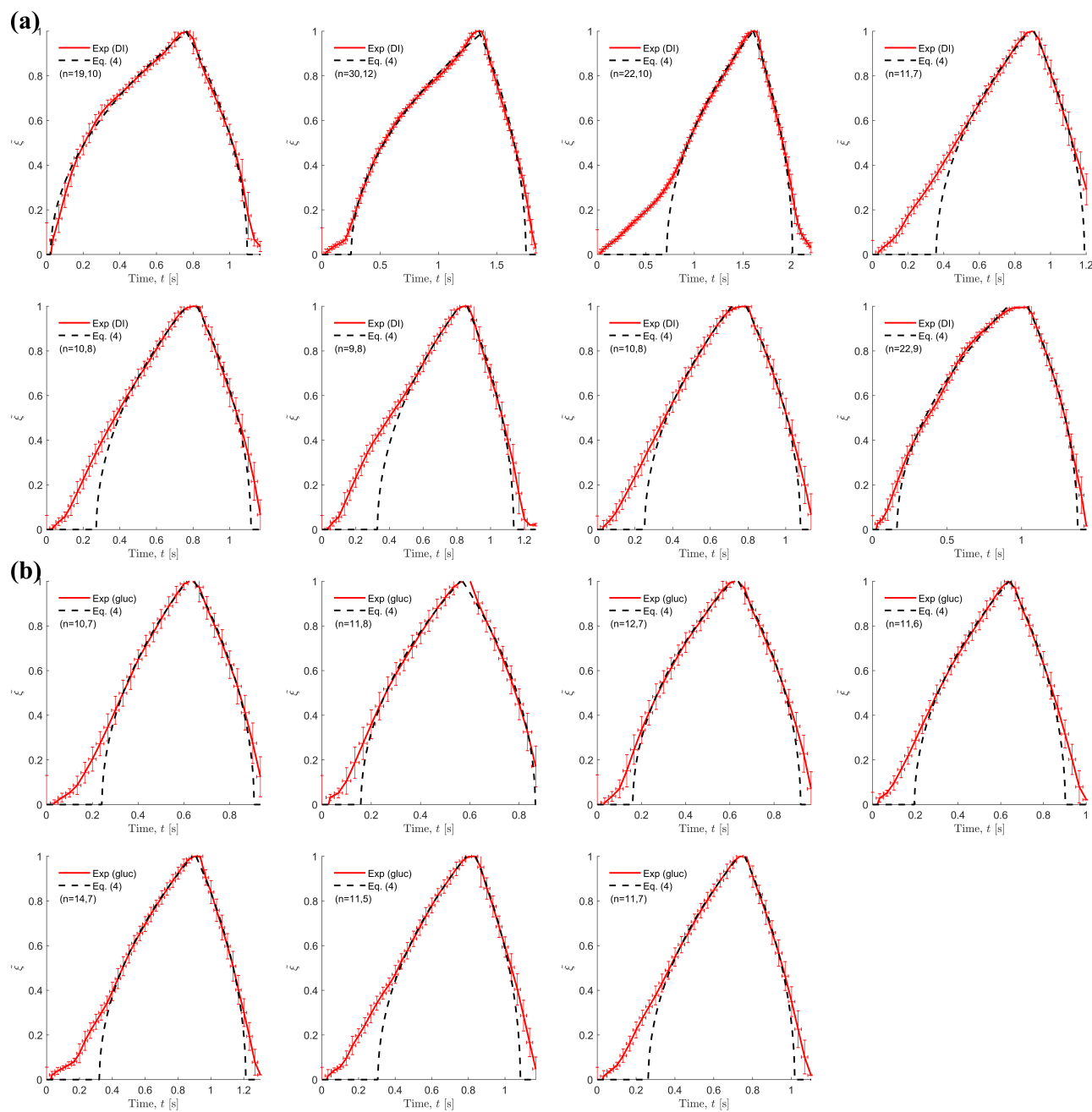


Figure 5.9 Experimental data sets for DI water (a) and the glucose solution (b). When the meniscus is near the inlet or outlet, additional liquid-surface energy terms not considered in the model creates a discrepancy between experiments and theory. Energy is used to stretch the meniscus near the inlet, which reduces its speed, and this energy is given back near the outlet, which increases its speed.

CHAPTER 6 GENERAL DISCUSSION

6.1 Self-coalescing flows in microfluidics for pulse-shaped delivery of reagents

The delivery of high spatiotemporal resolution pulses of reagents in microsystems is ubiquitous in BioMEMS applications, and more recently in embedded security features in microfluidic systems. The self-coalescence module (SCM) confines a droplet of water in a microstructure and make it fold onto itself by SC. This type of flow prevents reagent accumulation at the capillary filling front.

Boundary conditions are regularized by using the invariance property of the Navier-Stokes equations under Galilean transformations, and the resulting flow problem is simplified using potential flow theory in a Hele-Shaw cell. Approximating the circular arc of the returning meniscus with a polygon of N segments, we use the Schwarz-Christoffel transformation to map the original domain onto the upper half complex plane.

Finding the position of the vertices, known as the parameter problem, may be done analytically up to a given number of vertices as per the Riemann mapping theorem. If the number of vertices prevent finding an explicit general solution, numerical methods are required to find the vertices. However, as $N \rightarrow \infty$ it is numerically challenging to find the vertices in the complex map as they spread exponentially around the origin, i.e. the crowding phenomenon. To get around this challenge, instead of mapping from the upper half plane, we map from the bi-infinite strip using an additional conformal transformation, thus finding the map solution for the SCM.

We proceed with an asymptotic analysis of the general implicit solution to find key characteristics of SC flows in the vicinity of the moving meniscus and far away from it. The asymptotic study far from the meniscus reveals that the flow decays exponentially, and that a single parameter value—the width of the system—is required characterize the decay length. This is a characteristic of solutions obeying Laplace's equation and reflects the behavior of evanescent waves. On the other hand, the asymptotic study in the vicinity of the moving meniscus reveals a linearly increasing velocity and self-similarity with respect to λ . This suggests that the flow around the meniscus is alike that of the classical 2D flow over a cylinder.

Conformal mapping is a powerful tool that can be used to study SC flows in elongated structures in the moving reference frame of the meniscus and by approximating the meniscus as an N -sided curve. Using analytical methods gives us the possibility of finding elegant asymptotic solutions that can lead to simple design rules, i.e. the flow velocity increases linearly close to the meniscus and decays asymptotically towards zero as we get further from it. Lastly, this study reveals link to Saffman-Taylor viscous fingering (STVF) and we describe how SC and STVF are analogous and

how they differ.

6.2 A simple static contact angle-based mesh-dependency correction for 3D capillary flow simulations

Capillary driven multiphase flow simulations do not converge with mesh refinement due to viscous losses underestimation for coarse meshes, and contact line dynamics singularities when the mesh is refined. This is because the continuum formulation of fluid mechanics breaks down at the molecular level and does not capture wetting dynamics occurring at that scale. Physically, molecules attach, detach, and collide with the solid wall, allowing the capillary interface to move.

We provide a semi-analytical correction function based on the Washburn equation to easily correct the singular contact line behaviour in a small Reynolds and Capillary numbers limit. This methodology can be used with any CFD codes as it does not require modification or implementation in the source code directly. Although, this methodology could also be automated by implementing it in available software packages.

The correction methodology consists in calculating a corrected static contact angle from simple 2D simulations *a-posteriori*, and use that correction for complex 3D capillary flow simulations *a-priori*. This methodology was shown to be effective even in complex geometries such as capillary pumps. 3D simulations of two microfluidic devices were conducted to demonstrate mesh-independency using the method.

6.3 The dynamics of accelerating capillary flow

An important corollary to Washburn's equation is presented in cases where viscous losses diminish in time, resulting in accelerating capillary flow. We label this phenomenon the "Reverse-Washburn" capillary flow regime in the low Laplace number limit, and "Reverse-Bosanquet" capillary flow regime in the high Laplace number limit. RW was first discovered through simulations, and subsequently observed and characterized in experiments. The theoretical framework is derived as per the original papers by Washburn [82] and Bosanquet [255] in their respective non-inertial and inertial formulations. The resulting theory holds for any given channel as long as viscous losses change linearly (positively or negatively) along the channel (i.e. constant, or periodic, change in hydraulic resistance). The net Laplace pressure on the meniscus is described from a free energy formulation as described by Gibbs' free energy.

Accelerating flows are studied in the case of self-coalescence occurring in a passive SCM, but can be generalized to any shapes where coalescence occurs in a confined area, e.g. sharp turns, spirals,

and slow meanders. This process also describes the behaviour of filling dynamics in other capillary microsystems such as capillary pumps and microfluidic phaseguides.

Accelerating flows could compensate for boundary layer depletion in surface-based reactions with the acceleration of the flow replenishing the captured species near the surface, and major applications have been found in reagent reconstitution on chip and have been established [197].

6.4 Limitations

In Chapter 3, the general mapping solution (Eq. 3.12-3.13) uses a piecewise linear approximation of the meniscus and needs to be solved numerically. This model could be improved using a more appropriate transformation such as the modified Schwarz-Christoffel transformation for polygons with circular arcs [222]. This would also solve the problem of requiring a numerical input to obtain the amplitude of the exponential decay for the asymptotic solution far from the meniscus, and the limit of small λ values for the asymptotic solution in the vicinity of the moving meniscus.

In Chapter 4, the contact angle correction methodology is fundamentally issued from physics, but requires an empiric (numeric) input to quantify the amplitude of the correction. Although the values could be tabulated and a simple interpolation could be used to make the correction general for any cases, provided the correction does not exceed the contact angle itself, it would be preferable to obtain a simple equation that can account for the correction without an empiric input or tabulated data. However, producing the tabulated data can be tedious as correction values are dependent on both the contact angle and the mesh size, and simulation time increases significantly with mesh refinement.

The correction methodology is only valid for small Reynolds numbers and small capillary numbers limit. In cases where $Re \gg 1$ the flow is not fully developed and the Hagen-Poiseuille law does not hold. On the other hand, when $Ca \gg 1$ visco-capillary effects might distort the shape of the meniscus and the constant radius approximation used to calculate the Laplace pressure might not hold. The correction method relies on those two quantities being lower than or close to unity.

For devices with more than one length scale, we select the dimension for which the impact on the flow is greatest. However, this might not be appropriate in cases where the length scales are of the same order of magnitude. For instance, in SCMs there are two length scales: H and λW . We take H to compute the correction function because this is the dimension with the greatest impact on viscous losses and capillary pressure. The same idea would follow for any other device. The method was not tested for cases where $H/W \approx 1$ where an additional length scale would have to be added or for cases with irregular and more complex geometries. However, we should expect a correction function bounded by the values for the smallest and longest dimension in the flow path

cross-section, and from a first estimation the correction function should follow a relation akin to that for hydraulic radii calculations. However, further research is required for the general case. Nonetheless the capillary pump test case shows that even for $H/W \approx 5$ and a relatively complex geometry, a single length scale simplification works fine.

Most CFD codes suffer from parasitic currents when modeling capillary dominated flows, including interFoam. Parasitic currents were quantified and are shown to increase with mesh refinement and decrease with larger contact angles (see Fig. 6.1). The currents amplitude stays within a factor of 2 in general and a factor of 6 at worst. This error does not influence flow behavior in power $1/2$, but it could contribute to the value of the correction function. Spurious currents can bring serious concerns when one wants to compute slower capillary flows due to the physical and computational times scaling linearly when $U < U_s$ due to time step limitations imposed by the Courant number (Appendix H). For instance, this is a problem encountered in Chapter 5.

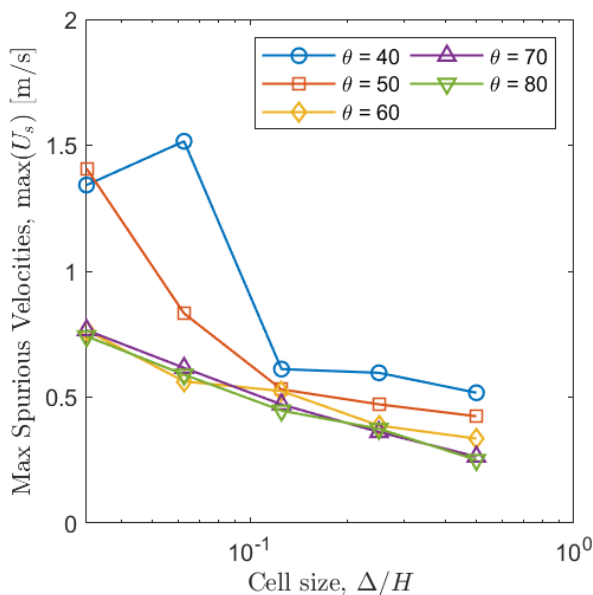


Figure 6.1 Spurious currents as a function of cell size for different contact angles with interFoam (VOF-FVM) and compressive CSF.

In Chapter 5, Washburn and Reverse-Washburn flow regimes were difficult to reproduce experimentally due to surface roughness, which has for effect a reduction in the effective contact angle and uneven filling rates. Groves caused by DRIE etching on the side walls could also be a potential cause for discrepancies observed between theory, simulations, and experiments. The effective contact angles were all close to 90° which makes simulations extremely intensive due to spurious currents (100+ CPUs for more than a week of computing) and slow filling rates. Nonetheless, evidence of the Reverse-Washburn effect was provided, but results could be improved substantially.

The Reverse-Bosanquet effect (Eq. 5.9) would require re-thinking the experiment from scratch.

A phenomenon that has been observed numerically, and has yet to be observed in experiments, is the "bubble" shape the meniscus takes when SC starts at the end of a CPL. A possible explanation is that the bubble is resulting from a balance between hydraulic pressure and capillary pressure. The bubble expands to minimize its surface energy, and doing so shrinks the flow path (Fig. 6.2-6.3) which increase the hydraulic resistance and the pressure locally. The width of the bubble might be described by a power law akin to Bretherton's law for the motion of long bubbles in tubes [277], but would have to be investigated further.

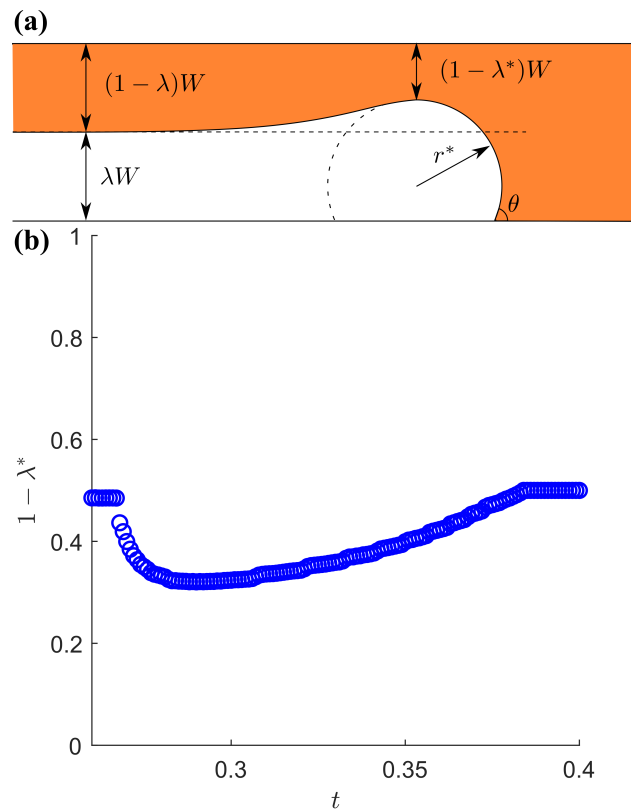


Figure 6.2 Schematic of the formation of a bubble in SCMs (a), and numerical results of the width of the bubble with respect to time (b) using VOF-FVM with the compressive CSF model.

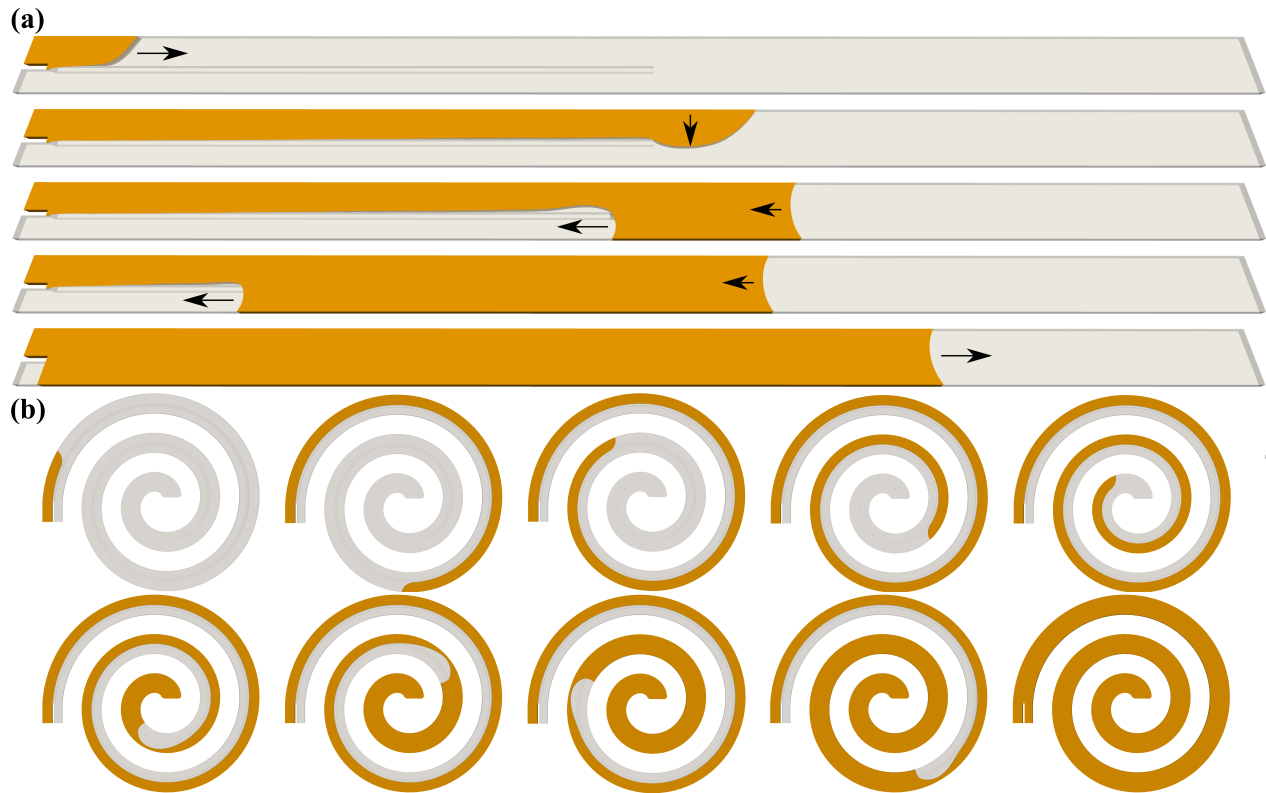


Figure 6.3 Simulation snapshots of (a) a SCM without diversion barrier, and (b) design of a SCM in the shape of an Archimedean spiral with the "buble" shape made evident when self-coalescence occurs. These are also examples of WRW cycles.

CHAPTER 7 CONCLUSION

7.1 Thesis contributions

The three main contributions of this thesis are as follow: 1) a full characterization of self-coalescing flows in microfluidics for pulse-shaped delivery of reagents using conformal mapping, 2) the development of a simple static contact angle-based mesh-dependency correction for 3D capillary flow simulations which allowed for the simulation of SCMs, phaseguides, and capillary pumps, and 3) a generalization of the Washburn equation for accelerating flows with supporting numerical, made possible from de second contribution, and experimental results. More details are provided on each theme here below. Finally, this thesis is concluded by a discussion on limitations of this work and recommendations for future research.

7.2 Future research

During the course of those past five years of research, several projects arose, and ideas explored, without them making the cut for this thesis. Nonetheless, here are some recommendations of topics that could be further explored following the work from this thesis. Notably, 1) a complete SC solution using the Schwarzian differential equation, 2) WRW flow cycling, 3) SCM-based electrocapillary-driven microfluidics, 4) benchmarking the SCM for numerical tests, 5) compare and asses the performance of different CFD software packages, and 6) couple capillary flow modelling with additional transport equation for dispersive and reactive species.

7.2.1 Towards a complete SC solution

The mapping solution to the SCM (Eq. 3.27) is not complete as it still requires an input of numerical data. In addition, the asymptotic solution close to the meniscus (Eq. 3.33) are only valid for large meniscus radii and when $\lambda \gtrsim 0.1$, which is fortunately the case for the applications we make of SCMs, i.e. large spotting areas are sought. A possible approach to resolve this challenge is to use a modified Schwarz-Christoffel transformation directly mapping polygons with circular arcs [222] instead of regular polygons. The conformal map f is then found by solving the Schwarzian differential equation

$$y''(\omega) + \frac{1}{2} \{f, \omega\} y(\omega) = 0 \quad (7.1)$$

where $\{f, \omega\}$ is the Schwarzian operator (see discussion in Section 3.7.4). With an asymptotic analysis of the Schwarzian differential equation, the theoretical model could be refined. From our

analysis in this paper, we expect the solution to be akin to the Gamma function, or more precisely Appell's hypergeometric function (as in Eq. 2.44 for the inclined back step).

7.2.2 Washburn-Reverse-Washburn cycles

Flows in capillary pumps are known to decrease in speed the more they are filled up due to an increase in viscous losses and a constant, or periodic, capillary pressure. In a SCM, viscous losses increase as liquid fills the first part of the channel, and once SC begins when the liquid reaches the end of the CPL, viscous losses decrease. Thus, the flow accelerates, and we introduced in this thesis RW flows. By the combination of both Washburn and Reverse-Washburn flows we can engineer flows that are cycling between the two modes (WRW cycles). Thus, giving us a superior control over the speed at which fluids move in capillary-driven microstructures. We can also quantify the efficiency at which a surface can be wetted using WRW cycles. Simple back of the envelope calculations reveal that filling an arbitrary surface with N straight channels takes between N times (in serial) to twice (in parallel) as much time than it would take to fill the same surface with N SCMs. This has potential applications for capillary pumping, and surface reaction engineering [263].

7.2.3 Customizable flows with electrocapillary-driven microfluidics

Using electrowetting in combination with autonomous capillary pumping —Washburn-type flows and WRW cycles—we could engineer devices providing even greater control over the flow. The flow rate in a passively filling channel through capillarity can be given as a function of the contact angle, and the change in contact angle under an applied potential, V , is given by $(\cos \theta - \cos \theta_0) \sim V^2$, where θ_0 is the initial contact angle without electric potential. Combining the two phenomena, we can engineer flow rates exceeding the limits of electrowetting and under the threshold of electrolysis. The module could be used to minimize TAD in capillary-driven microstructures, and to enhance the capabilities of capillary pumping, e.g. filling in otherwise impossible configurations and controllable pumping. However, by introducing electrodes in the system for electrowetting we lose some of the autonomy (passive nature) of the device.

7.2.4 SCM-based benchmark tests

SCMs rely on three very important concepts in microfluidics: 1) self-coalescence, 2) Washburn and Reverse-Washburn flows, and 3) the Concus-Finn criterion. By benchmarking SCMs for numerical simulations, we could test different solvers and measure their performance in simulating these features. For instance, test cases in OpenFOAM showed that meniscus pinning fails when the

meshing resolution of a CPL is less than 4 times its height due to interface diffusion reaching over the rail. Furthermore, analytical description of all these concepts are given in this thesis, i.e. Eq. 3.12-3.13 for the flow within SCMs during self-coalescence with asymptotes given by Eq. 3.27 and Eq. 3.33, Eq. 5.4 for the position, velocity, and acceleration of the meniscus during Washburn and Reverse flows, and Eq. 2.64 for the Concus-Finn criterion.

SCMs could also be used to study Kelvin–Helmholtz (KH) instabilities [11] in microenvironments as fluid velocities go in opposite directions in the initial filling stage, i.e. liquid 1 moves in the positive direction, and liquid 2 in the negative opposite direction. In a water-air system, this effect is negligible because of the low Capillary and Webber number (Tab. 2.1), but experiments could be run where that is not the case. And if not physically, this is a numerical experiment that can be run to test stability of some solvers. For example, SCM test cases with mesh refinement across the interface showed KH-like instabilities forming in some flow regimes, whereas no refinement didn't. If observed experimentally, the "bubble" effect described in the limitations of this work (Fig. 6.2-6.3) could also be used as a benchmark test criteria with structures akin to SCMs.

7.2.5 A comparative study between different CFD software packages

As presented in Section 2.2, several open-source and commercial CFD software platforms exist, with different approaches with respect to modelling surface evolution and surface tension. A comparative study comparing the pros and cons, the performance, and the accuracy of the different methods would be valuable to understand what better tool to use for a given problem in capillary dynamics. Notably, potential software platforms include OpenFOAM [128], discussed at length in this thesis, Ansys-Fluent [130], Gerris [129], COMSOL Multiphysics [131], and STAR-CCM+ [132] to name a few.

7.2.6 Full coupling of capillary dynamics with mass transport

Coupling mass transport equations with VOF and study the recirculation of reagents at the capillary front when in reconstitution would be an interesting and valuable avenue following this work. The open source solver `interMixingFoam` from OpenFOAM, using a three-phase formulation of VOF with one dispersive phase, and has recently been used to model double-flow liquid injectors [278]. However, the available literature on that subject is very sparse, and rigorous validation work in a microfluidics framework has yet to be done. Test cases with the `interMixingFoam` solver were done for reconstitution of dispersive species in SCMs and straight microchannels, however spurious currents were significantly disrupting reconstitution at the capillary interface due to the non-physical velocities. This should be investigated further. Ultimately, a complete free-surface model with multiple dispersive and reactive species could be implemented and numerical results

could be compared with experimental results from [203].

7.3 Final words

Contributions presented in this thesis helped understand self-coalescing flows, which allows reagent reconstitution with minimal dispersion and pointed, thanks to the dedicated work of E. Delamarche and his team at IBM, to meaningful applications in point-of-care diagnostics and security in the diagnostic test industry. A full characterisation of the flow has been developed and provide tools to understand and use this novel type of flow for precision diagnostics and the integration of security features on chip. A numerical framework for modelling complex capillary driven flows in microstructures was also developed. These tools are useful to predict the behavior of liquids in microsystems and optimize their design where analytical methods cannot. Analytical, and numerical modelling were used to predict, understand, and characterize Reverse-Washburn flows, a new capillary flow regime providing enhanced control over passive flows in microchannels. These flows have potential applications in better engineering surface reactions on chip by providing enhanced control over the flow.

Spurious currents and contact line singularities are a main issue in modelling capillary driven flows, although they can be mitigated or corrected in specific cases. It would be valuable to find a general solution to these problems. Ideally, these solutions should be computationally unintensive and not restricted to structured meshes and adaptive solvers.

Critical steps modellers should always take, in my opinion, are to 1) understand problems from a physical point of view, 2) understand the limits of a given model (e.g. continuum mechanics and contact line dynamics), 3) reduce the complexity of the model as much as possible, but not too much, 4) understand where modelling might fail and how to adapt numerical models accordingly, and 5) always validate results (convergence analyses, compare with theory and experiments). In this way, modellers prevent committing GIGO, i.e. "garbage in, garbage out" [279]. It is of my opinion that more modellers should take Charles Babbage's view on computational work^{1,2}.

Open-source CFD software packages like OpenFOAM provide powerful community-based tools and help pushing the frontier of knowledge in computational physics and surpasses in many ways commercial options. I am looking forward to seeing what the open-source CFD community will become, and how community-based CFD software packages will evolve.

¹Charles Babbage (1791-1871) seeded the idea of digital programmable computers.

²Excerpt from *Passages from the Life of a Philosopher* [280]: On two occasions I have been asked, "Pray, Mr. Babbage, if you put into the machine wrong figures, will the right answers come out?" ... I am not able rightly to apprehend the kind of confusion of ideas that could provoke such a question.

REFERENCES

- [1] P. S. Laplace, *Traité de mécanique céleste*. de l'Imprimerie de Crapelet, 1799.
- [2] T. Young, "An essay on the cohesion of fluids," *Philosophical transactions of the royal society of London*, no. 95, pp. 65–87, 1805.
- [3] F. Hauksbee, "Several experiments touching the seeming spontaneous ascent of water," *Philosophical Transactions of the Royal Society of London*, vol. 26, no. 319, pp. 258–266, 1709.
- [4] J. Jurin, "An account of some experiments shown before the royal society; with an enquiry into the cause of the ascent and suspension of water in capillary tubes." *Philosophical Transactions of the Royal Society of London*, vol. 30, no. 355, pp. 739–747, 1718.
- [5] J. E. Jones, "On the determination of molecular fields. i. from the variation of the viscosity of a gas with temperature," *Proceedings of the Royal Society of London. Series A, Containing Papers of a Mathematical and Physical Character*, vol. 106, no. 738, pp. 441–462, 1924.
- [6] J. E. Jones, "On the determination of molecular fields. ii. from the equation of state of a gas," *Proceedings of the Royal Society of London. Series A, Containing Papers of a Mathematical and Physical Character*, vol. 106, no. 738, pp. 463–477, 1924.
- [7] L. Boltzmann, "Zur theorie der elastischen nachwirkung," *Annalen der Physik*, vol. 241, no. 11, pp. 430–432, 1878.
- [8] C. Navier, "Mémoire sur les lois du mouvement des fluides," *Mémoires de l'Académie Royale des Sciences de l'Institut de France*, vol. 6, no. 1823, pp. 389–440, 1823.
- [9] G. Stokes, "On the effect of the internal friction of fluids on the motion of pendulums," *Transactions of the Cambridge Philosophical Society*, vol. 9, p. 8, 1851.
- [10] S. Chibbaro, E. Costa, D. I. Dimitrov, F. Diotallevi, A. Milchev, D. Palmieri, G. Pontrelli, and S. Succi, "Capillary Filling in Microchannels with Wall Corrugations: A Comparative Study of the Concus-Finn Criterion by Continuum, Kinetic, and Atomistic Approaches," *Langmuir*, vol. 25, no. 21, pp. 12 653–12 660, nov 2009.
- [11] S. Chandrasekhar, "Hydrodynamic and hydromagnetic stability," *International Series of Monographs on Physics*, 1961.

- [12] K. Schubert, J. Brandner, M. Fichtner, G. Linder, U. Schygulla, and A. Wenka, "Microstructure devices for applications in thermal and chemical process engineering," *Microscale Thermophysical Engineering*, vol. 5, no. 1, pp. 17–39, 2001.
- [13] V. Hessel, S. Hardt, and H. Löwe, *Chemical Micro Process Engineering*. Weinheim, FRG: Wiley, jan 2004.
- [14] T. Dietrich, *Microchemical engineering in practice*. John Wiley & Sons, 2011.
- [15] W. Ehrfeld, V. Hessel, and V. Haverkamp, "Microreactors," *Ullmann's encyclopedia of industrial chemistry*, 2000.
- [16] V. Hessel, H. Löwe, and F. Schönfeld, "Micromixers—a review on passive and active mixing principles," *Chemical engineering science*, vol. 60, no. 8-9, pp. 2479–2501, 2005.
- [17] G. N. Doku, W. Verboom, D. N. Reinhoudt, and A. Van Den Berg, "On-microchip multiphase chemistry—a review of microreactor design principles and reagent contacting modes," *Tetrahedron*, vol. 61, no. 11, pp. 2733–2742, 2005.
- [18] O. Geschke, H. Klank, and P. Telleman, *Microsystem Engineering of Lab-on-a-chip Devices*. Wiley Online Library, 2004.
- [19] S. Saliterman, *Fundamentals of BioMEMS and medical microdevices*. SPIE press, 2006, vol. 153.
- [20] A. Folch, *Introduction to BioMEMS*. CRC Press, 2013.
- [21] A. K. Yetisen, M. S. Akram, and C. R. Lowe, "based microfluidic point-of-care diagnostic devices," *Lab on a Chip*, vol. 13, no. 12, pp. 2210–2251, 2013.
- [22] F. A. Gomez, *Biological applications of microfluidics*. John Wiley & Sons, 2008.
- [23] L. Y. Yeo, H.-C. Chang, P. P. Chan, and J. R. Friend, "Microfluidic devices for bioapplications," *small*, vol. 7, no. 1, pp. 12–48, 2011.
- [24] S. Han, H. J. Bae, J. Kim, S. Shin, S.-E. Choi, S. H. Lee, S. Kwon, and W. Park, "Lithographically Encoded Polymer Microtaggant Using High-Capacity and Error-Correctable QR Code for Anti-Counterfeiting of Drugs," *Advanced Materials*, vol. 24, no. 44, pp. 5924–5929, nov 2012.
- [25] S. S. Ali, M. Ibrahim, O. Sinanoglu, K. Chakrabarty, and R. Karri, "Microfluidic encryption of on-chip biochemical assays," in *2016 IEEE Biomedical Circuits and Systems Conference (BioCAS)*. IEEE, 2016, pp. 152–155.

- [26] O. Gökçe, C. Mercandetti, and E. Delamarche, “High-Content Optical Codes for Protecting Rapid Diagnostic Tests from Counterfeiting,” *Analytical Chemistry*, vol. 90, no. 12, pp. 7383–7390, jun 2018.
- [27] S. Pekdemir, H. H. Ipekci, M. Serhatlioglu, C. Elbuken, and M. S. Onses, “Sers-active linear barcodes by microfluidic-assisted patterning,” *Journal of Colloid and Interface Science*, vol. 584, pp. 11–18, 2021.
- [28] T. M. Squires and S. R. Quake, “Microfluidics: Fluid physics at the nanoliter scale,” *Reviews of Modern Physics*, vol. 77, no. 3, pp. 977–1026, oct 2005.
- [29] G. M. Whitesides, “The origins and the future of microfluidics,” *Nature*, vol. 442, no. 7101, pp. 368–373, jul 2006.
- [30] R. E. Baker, A. S. Mahmud, I. F. Miller, M. Rajeev, F. Rasambainarivo, B. L. Rice, S. Takahashi, A. J. Tatem, C. E. Wagner, L.-F. Wang *et al.*, “Infectious disease in an era of global change,” *Nature Reviews Microbiology*, vol. 20, no. 4, pp. 193–205, 2022.
- [31] “Who coronavirus (covid-19) dashboard,” 07 2022. [Online]. Available: <https://covid19.who.int/>
- [32] P. K. Drain, “Rapid diagnostic testing for sars-cov-2,” *New England journal of medicine*, vol. 386, no. 3, pp. 264–272, 2022.
- [33] C. Dye, “After 2015: infectious diseases in a new era of health and development,” *Philosophical Transactions of the Royal Society B: Biological Sciences*, vol. 369, no. 1645, pp. 20130426–20130426, may 2014.
- [34] M. Naghavi, A. A. Abajobir, C. Abbafati, K. M. Abbas, F. Abd-Allah, S. F. Abera, V. Aboyans, O. Adetokunboh, A. Afshin, A. Agrawal *et al.*, “Global, regional, and national age-sex specific mortality for 264 causes of death, 1980–2016: a systematic analysis for the global burden of disease study 2016,” *The lancet*, vol. 390, no. 10100, pp. 1151–1210, 2017.
- [35] P. K. Drain, E. P. Hyle, F. Noubary, K. A. Freedberg, D. Wilson, W. R. Bishai, W. Rodriguez, and I. V. Bassett, “Diagnostic point-of-care tests in resource-limited settings,” *The Lancet Infectious Diseases*, vol. 14, no. 3, pp. 239–249, mar 2014.
- [36] N. M. Pham, W. Karlen, H.-P. Beck, and E. Delamarche, “Malaria and the last parasite: how can technology help?” *Malaria Journal*, vol. 17, no. 1, p. 260, 2018.
- [37] P. Yager, G. J. Domingo, and J. Gerdes, “Point-of-Care Diagnostics for Global Health,” *Annual Review of Biomedical Engineering*, vol. 10, no. 1, pp. 107–144, aug 2008.

- [38] “Point of care rapid diagnostics market,” Mar 2022. [Online]. Available: <https://www.marketsandmarkets.com/Market-Reports/point-of-care-diagnostic-market-106829185.html>
- [39] F. Clark, “Rise in online pharmacies sees counterfeit drugs go global,” *The Lancet*, vol. 386, no. 10001, pp. 1327–1328, 2015.
- [40] A. Lavorgna, “The online trade in counterfeit pharmaceuticals: new criminal opportunities, trends and challenges,” *European Journal of Criminology*, vol. 12, no. 2, pp. 226–241, 2015.
- [41] P. N. Newton, M. D. Green, and F. M. Fernández, “Impact of poor-quality medicines in the developing world,” *Trends in Pharmacological Sciences*, vol. 31, no. 3, pp. 99–101, mar 2010.
- [42] B. Glass, “Counterfeit drugs and medical devices in developing countries,” *Research and Reports in Tropical Medicine*, vol. 2014, no. 5, p. 11, mar 2014.
- [43] Kate Kelland, “Global healthcare fraud costs put at \$ 260 billion,” 2010.
- [44] P. N. Newton, M. D. Green, F. M. Fernández, N. P. Day, and N. J. White, “Counterfeit anti-infective drugs,” *The Lancet Infectious Diseases*, vol. 6, no. 9, pp. 602–613, sep 2006.
- [45] P. M. Rudolf and I. B. Bernstein, “Counterfeit Drugs,” *New England Journal of Medicine*, vol. 350, no. 14, pp. 1384–1386, apr 2004.
- [46] M. Mori, R. Ravinetto, and J. Jacobs, “Quality of medical devices and in vitro diagnostics in resource-limited settings,” *Tropical Medicine & International Health*, vol. 16, no. 11, pp. 1439–1449, nov 2011.
- [47] C. for Devices and R. Health, “Counterfeit at-home otc covid-19 diagnostic tests,” Apr 2022. [Online]. Available: <https://www.fda.gov/medical-devices/coronavirus-covid-19-and-medical-devices/counterfeit-home-otc-covid-19-diagnostic-tests>
- [48] H. D. Larkin, “Warning against counterfeit at-home covid-19 tests,” Jun 2022. [Online]. Available: <https://jamanetwork.com/journals/jama/fullarticle/2792997>
- [49] O. Akoni, “Ebola: Lagos alerts on sale of fake evd cassettes, test kits,” Sep 2014. [Online]. Available: <https://www.vanguardngr.com/2014/09/ebola-lagos-alerts-sale-fake-evd-cassettes-test-kits/>
- [50] T. Rowley, “Warning over hiv tests sold online,” Oct 2011. [Online]. Available: <http://www.independent.co.uk/life-style/health-and-families/health-news/warning-over-hiv-tests-sold-online-2376208.html>

- [51] F. Kapama, “Tanzania: Msd imports fake hiv testing kits,” Oct 2014. [Online]. Available: <https://allafrica.com/stories/201410100867.html>
- [52] A. D. Frank and L. Rapaport, “Faulty diabetes tests tracked to china,” Aug 2007. [Online]. Available: <https://www.nysun.com/article/national-faulty-diabetes-tests-tracked-to-china>
- [53] D. Kirkova, “‘pregnancy pranking’ kits sold online: Positive tests, fake dna results, prosthetic bellies and ultrasounds marketed as ‘gags’,” Jan 2014. [Online]. Available: <https://www.dailymail.co.uk/femail/article-2539946/Pregnancy-pranking-kits-sold-internet-Positive-tests-fake-DNA-results-prosthetic-bellies-ultrasounds-marketed-gags.html>
- [54] D. Bansal, “Anti-Counterfeit Technologies: A Pharmaceutical Industry Perspective,” *Scientia Pharmaceutica*, vol. 81, no. 1, pp. 1–13, 2013.
- [55] T. F. Scherr, S. Gupta, D. W. Wright, and F. R. Haselton, “An embedded barcode for “connected” malaria rapid diagnostic tests,” *Lab Chip*, vol. 17, pp. 1314–1322, 2017. [Online]. Available: <http://dx.doi.org/10.1039/C6LC01580H>
- [56] T. K. Mackey and G. Nayyar, “A review of existing and emerging digital technologies to combat the global trade in fake medicines,” *Expert Opinion on Drug Safety*, vol. 16, no. 5, pp. 587–602, may 2017.
- [57] A. T. Ciftlik, D. G. Dupouy, and M. A. M. Gijs, “Programmable parylene-C bonding layer fluorescence for storing information on microfluidic chips,” *Lab on a Chip*, vol. 13, no. 8, p. 1482, 2013.
- [58] D.-H. Park, C. J. Han, Y.-G. Shul, and J.-H. Choy, “Avatar DNA Nanohybrid System in Chip-on-a-Phone,” *Scientific Reports*, vol. 4, no. 1, p. 4879, may 2015.
- [59] V. J. Cadarso, S. Chosson, K. Sidler, R. D. Hersch, and J. Brugger, “High-resolution 1D moirés as counterfeit security features,” *Light: Science & Applications*, vol. 2, no. 7, pp. e86–e86, jul 2013.
- [60] L. Gervais and E. Delamarche, “Toward one-step point-of-care immunodiagnostics using capillary-driven microfluidics and PDMS substrates,” *Lab on a Chip*, vol. 9, no. 23, p. 3330, 2009.
- [61] “Crypto-Anchors and Blockchain, <https://www.research.ibm.com/5-in-5/crypto-anchors-and-blockchain/>,” 2018.
- [62] “Five innovations that will help change our lives within five years, <http://research.ibm.com/5-in-5/>,” 2018.

- [63] “Ink Spots to Put an End to Counterfeit Diagnostic Tests,” <https://www.ibm.com/blogs/research/2018/06/ink-spots-end-counterfeit-diagnostics/>, 2018.
- [64] L. Michaelis and M. Menten, “Die Kinetik der Invertinwirkung,” *Biochemische Zeitschrift*, 1913.
- [65] J. Brackbill, D. Kothe, and C. Zemach, “A continuum method for modeling surface tension,” *Journal of Computational Physics*, vol. 100, no. 2, pp. 335–354, jun 1992.
- [66] A. Vaschy, “Sur les lois de similitude en physique,” in *Annales télégraphiques*, vol. 19, 1892, pp. 25–28.
- [67] E. Buckingham, “On physically similar systems; illustrations of the use of dimensional equations,” *Physical review*, vol. 4, no. 4, p. 345, 1914.
- [68] H. Bruus, *Theoretical Microfluidics*. Oxford Master Series in Condensed Matter Physics, 2008.
- [69] H. S. HELE-SHAW, “The Flow of Water,” *Nature*, vol. 58, no. 1489, pp. 34–36, may 1898.
- [70] W. M. Deen, *Analysis of Transport Phenomena*. Oxford University Press, 1998.
- [71] J. Poiseuille, “Ecoulement des liquides: Societe phi/omatique de paris,” *Extraits des Procès-Verbaux des Seances Pendant l’Annee*, vol. 3, pp. 77–81, 1838.
- [72] R. V. Churchill, “Introduction to Complex Variables and Applications,” p. 216, 1948.
- [73] E. B. Christoffel, “Sul problema delle temperature stazionarie e la rappresentazione di una data superficie [on the problem of stationary temperatures and the representation of a given surface].” *Annali di Matematica Pura ed Applicata (1867-1897)*, vol. 1, no. 1, pp. 89–103, 1867.
- [74] H. A. Schwarz, “Ueber einige abbildungsaufgaben [about some mapping problems].” *Journal für die reine und angewandte Mathematik*, pp. 46–70, 1869.
- [75] R. Schinzinger and P. A. Laura, *Conformal mapping: methods and applications*. Courier Corporation, 2012.
- [76] P. Appell and J. K. De Fériet, *Fonctions hypergéométriques et hypersphériques: polynomes d’Hermite*. Gauthier-villars, 1926.

- [77] M. Abramowitz and I. A. Stegun, *Handbook of mathematical functions with formulas, graphs, and mathematical tables*. US Government printing office, 1964, vol. 55.
- [78] G. Taylor, "Dispersion of soluble matter in solvent flowing slowly through a tube," *Proceedings of the Royal Society of London. Series A. Mathematical and Physical Sciences*, vol. 219, no. 1137, pp. 186–203, aug 1953.
- [79] R. Aris, "On the dispersion of a solute in a fluid flowing through a tube," *Proceedings of the Royal Society of London. Series A. Mathematical and Physical Sciences*, vol. 235, no. 1200, pp. 67–77, 1956.
- [80] R. Bharadwaj, D. E. Huber, T. Khurana, and J. G. Santiago, "Taylor dispersion in sample pre-concentration methods," in *Handbook of Capillary and Microchip Electrophoresis and Associated Microtechniques*, J. P. Landers, Ed. CRC Press, 2008, ch. 38, pp. 1085–1120.
- [81] J. W. Gibbs, *Scientific Papers of J. Willard Gibbs, in Two Volumes*. Longmans, Green, 1906, vol. 1.
- [82] E. W. Washburn, "The Dynamics of Capillary Flow," *Physical Review*, vol. 17, no. 3, pp. 273–283, mar 1921.
- [83] P. Concus and R. Finn, "ON THE BEHAVIOR OF A CAPILLARY SURFACE IN A WEDGE," *Proceedings of the National Academy of Sciences*, vol. 63, no. 2, pp. 292–299, jun 1969.
- [84] P. Concus and R. Finn, "On capillary free surfaces in a gravitational field," *Acta Mathematica*, vol. 132, no. 1, pp. 207–223, 1974.
- [85] R. Finn, "Existence and Non Existence of Capillary Surfaces," *Manuscripta Mathematica*, vol. 28, no. 1-3, pp. 1–11, 1979.
- [86] R. Finn, "Local and global existence criteria for capillary surfaces in wedges," *Calculus of Variations and Partial Differential Equations*, vol. 4, no. 4, pp. 305–322, jun 1996.
- [87] T. Ransohoff and C. Radke, "Laminar flow of a wetting liquid along the corners of a predominantly gas-occupied noncircular pore," *Journal of colloid and interface science*, vol. 121, no. 2, pp. 392–401, 1988.
- [88] M. Dong and I. Chatzis, "The imbibition and flow of a wetting liquid along the corners of a square capillary tube," *Journal of colloid and interface science*, vol. 172, no. 2, pp. 278–288, 1995.

- [89] L. Romero and F. Yost, “Flow in an open channel capillary,” *Journal of Fluid Mechanics*, vol. 322, pp. 109–129, 1996.
- [90] M. M. Weislogel and S. Lichter, “Capillary flow in an interior corner,” *Journal of Fluid Mechanics*, vol. 373, pp. 349–378, 1998.
- [91] J. Bico and D. Quéré, “Rise of liquids and bubbles in angular capillary tubes,” *Journal of colloid and Interface Science*, vol. 247, no. 1, pp. 162–166, 2002.
- [92] S. Herminghaus, M. Brinkmann, and R. Seemann, “Wetting and Dewetting of Complex Surface Geometries,” *Annual Review of Materials Research*, vol. 38, no. 1, pp. 101–121, aug 2008.
- [93] F.-M. Chang, S.-J. Hong, Y.-J. Sheng, and H.-K. Tsao, “Wetting Invasion and Retreat across a Corner Boundary,” *The Journal of Physical Chemistry C*, vol. 114, no. 3, pp. 1615–1621, jan 2010.
- [94] F. Dutka, M. Napiórkowski, and S. Dietrich, “Mesoscopic analysis of Gibbs’ criterion for sessile nanodroplets on trapezoidal substrates,” *The Journal of Chemical Physics*, vol. 136, no. 6, p. 064702, feb 2012.
- [95] L. Clime, D. Brassard, J. P. Pezacki, and T. Veres, “Self-priming of liquids in capillary autonomous microfluidic systems,” *Microfluidics and Nanofluidics*, vol. 12, no. 1-4, pp. 371–382, jan 2012.
- [96] A. T. Paxson and K. K. Varanasi, “Self-similarity of contact line depinning from textured surfaces,” *Nature communications*, vol. 4, no. 1, pp. 1–8, 2013.
- [97] B. Zhao, C. W. MacMinn, and R. Juanes, “Wettability control on multiphase flow in patterned microfluidics,” *Proceedings of the National Academy of Sciences*, vol. 113, no. 37, pp. 10 251–10 256, 2016.
- [98] G. Taylor, “The Instability of Liquid Surfaces when Accelerated in a Direction Perpendicular to their Planes. I,” *Proceedings of the Royal Society A: Mathematical, Physical and Engineering Sciences*, vol. 201, no. 1065, pp. 192–196, mar 1950.
- [99] D. J. Lewis, “The Instability of Liquid Surfaces when Accelerated in a Direction Perpendicular to their Planes. II,” *Proceedings of the Royal Society A: Mathematical, Physical and Engineering Sciences*, vol. 202, no. 1068, pp. 81–96, jun 1950.

- [100] P. G. Saffman and G. Taylor, "The Penetration of a Fluid into a Porous Medium or Hele-Shaw Cell Containing a More Viscous Liquid," *Proceedings of the Royal Society A: Mathematical, Physical and Engineering Sciences*, vol. 245, no. 1242, pp. 312–329, jun 1958.
- [101] D. Bensimon, L. P. Kadanoff, S. Liang, B. I. Shraiman, and C. Tang, "Viscous flows in two dimensions," *Reviews of Modern Physics*, vol. 58, no. 4, pp. 977–999, oct 1986.
- [102] K. E. Gubbins and J. D. Moore, "Molecular modeling of matter: Impact and prospects in engineering," *Industrial & Engineering Chemistry Research*, vol. 49, no. 7, pp. 3026–3046, 2010.
- [103] C. J. Cramer, *Essentials of computational chemistry: theories and models*. John Wiley & Sons, 2013.
- [104] F. Jensen, *Introduction to computational chemistry*. John wiley & sons, 2017.
- [105] D. Frenkel and B. Smit, *Understanding molecular simulation: from algorithms to applications*. Elsevier, 2001, vol. 1.
- [106] M. P. Allen and D. J. Tildesley, *Computer simulation of liquids*. Oxford university press, 2017.
- [107] S. Chen and G. D. Doolen, "Lattice boltzmann method for fluid flows," *Annual review of fluid mechanics*, vol. 30, no. 1, pp. 329–364, 1998.
- [108] T. Chung *et al.*, *Computational fluid dynamics*. Cambridge university press, 2002.
- [109] M. Wörner, "Numerical modeling of multiphase flows in microfluidics and micro process engineering: a review of methods and applications," *Microfluidics and Nanofluidics*, vol. 12, no. 6, pp. 841–886, may 2012.
- [110] R. B. Ferreira, D. Falcão, V. Oliveira, and A. Pinto, "Numerical simulations of two-phase flow in proton exchange membrane fuel cells using the volume of fluid method—a review," *Journal of Power Sources*, vol. 277, pp. 329–342, 2015.
- [111] A. Sharma, "Level set method for computational multi-fluid dynamics: A review on developments, applications and analysis," *Sadhana*, vol. 40, no. 3, pp. 627–652, 2015.
- [112] S. Haase, D. Y. Murzin, and T. Salmi, "Review on hydrodynamics and mass transfer in minichannel wall reactors with gas–liquid taylor flow," *Chemical Engineering Research and Design*, vol. 113, pp. 304–329, 2016.

- [113] H. Wang, X. Yuan, H. Liang, Z. Chai, and B. Shi, “A brief review of the phase-field-based lattice boltzmann method for multiphase flows,” *Capillarity*, vol. 2, no. 3, pp. 33–52, 2019.
- [114] K. Kadau, J. L. Barber, T. C. Germann, B. L. Holian, and B. J. Alder, “Atomistic methods in fluid simulation,” *Philosophical Transactions of the Royal Society A: Mathematical, Physical and Engineering Sciences*, vol. 368, no. 1916, pp. 1547–1560, apr 2010.
- [115] S. Chen and G. D. Doolen, *Lattice Boltzmann Modeling*. Berlin, Heidelberg: Springer Berlin Heidelberg, 2006, vol. 30, no. Kadanoff 1986.
- [116] J. Hardy and Y. Pomeau, “de pazzis. o,(1973). time evolution of twodimensional model system. i. invariant states and time correlation functions,” *J. Math. Phys*, vol. 14, no. 12, pp. 1746–1759, 1973.
- [117] D. H. Rothman and J. M. Keller, “Immiscible cellular-automaton fluids,” *Journal of Statistical Physics*, vol. 52, no. 3-4, pp. 1119–1127, aug 1988.
- [118] L. Clime, D. Brassard, and T. Veres, “Numerical modeling of the splitting of magnetic droplets by multiphase lattice boltzmann equation,” *Journal of Applied Physics*, vol. 105, no. 7, p. 07B517, 2009.
- [119] L. Clime, D. Brassard, and T. Veres, “Numerical modeling of electrowetting processes in digital microfluidic devices,” *Computers & Fluids*, vol. 39, no. 9, pp. 1510–1515, oct 2010.
- [120] M. J. Krause, A. Kummerländer, S. J. Avis, H. Kusumaatmaja, D. Dapelo, F. Klemens, M. Gaedtker, N. Hafen, A. Mink, R. Trunk *et al.*, “Openlb—open source lattice boltzmann code,” *Computers & Mathematics with Applications*, vol. 81, pp. 258–288, 2021.
- [121] J. Latt, O. Malaspinas, D. Kontaxakis, A. Parmigiani, D. Lagrava, F. Brogi, M. B. Belgacem, Y. Thorimbert, S. Leclaire, S. Li *et al.*, “Palabos: parallel lattice boltzmann solver,” *Computers & Mathematics with Applications*, vol. 81, pp. 334–350, 2021.
- [122] S. Lishchuk, C. Care, and I. Halliday, “Lattice boltzmann algorithm for surface tension with greatly reduced microcurrents,” *Physical review E*, vol. 67, no. 3, p. 036701, 2003.
- [123] M. M. Dupin, I. Halliday, and C. M. Care, “Simulation of a microfluidic flow-focusing device,” *Physical review E*, vol. 73, no. 5, p. 055701, 2006.
- [124] C. Pooley and K. Furtado, “Eliminating spurious velocities in the free-energy lattice boltzmann method,” *Physical Review E*, vol. 77, no. 4, p. 046702, 2008.

- [125] T. Lee, “Effects of incompressibility on the elimination of parasitic currents in the lattice boltzmann equation method for binary fluids,” *Computers & Mathematics with Applications*, vol. 58, no. 5, pp. 987–994, 2009.
- [126] M. Gad-el Hak, “The Fluid Mechanics of Microdevices - The Freeman Scholar Lecture,” *Journal of Fluids Engineering*, vol. 121, no. 1, p. 5, 1999.
- [127] T. J. Chung, *Computational Fluid Dynamics*. Cambridge: Cambridge University Press, 2002.
- [128] “The openfoam foundation.” [Online]. Available: <https://openfoam.org/>
- [129] “Gerris flow solver.” [Online]. Available: <http://gfs.sourceforge.net/>
- [130] “Ansys fluent | fluid simulation software.” [Online]. Available: <https://www.ansys.com/products/fluids/ansys-fluent>
- [131] “Multiphysics software for optimizing designs.” [Online]. Available: <https://www.comsol.com/>
- [132] “Multiphysics computational fluid dynamics (cfd) simulation software: Siemens software.” [Online]. Available: <https://www.plm.automation.siemens.com/global/en/products/simcenter/STAR-CCM.html>
- [133] F. H. Harlow and J. E. Welch, “Numerical calculation of time-dependent viscous incompressible flow of fluid with free surface,” *The physics of fluids*, vol. 8, no. 12, pp. 2182–2189, 1965.
- [134] F. H. Harlow and J. E. Welch, “Numerical study of large-amplitude free-surface motions,” *The Physics of Fluids*, vol. 9, no. 5, pp. 842–851, 1966.
- [135] B. J. Daly, “Numerical study of two fluid rayleigh-taylor instability,” *The Physics of Fluids*, vol. 10, no. 2, pp. 297–307, 1967.
- [136] S. O. Unverdi and G. Tryggvason, “A front-tracking method for viscous, incompressible, multi-fluid flows,” *Journal of computational physics*, vol. 100, no. 1, pp. 25–37, 1992.
- [137] G. Tryggvason, B. Bunner, A. Esmaeeli, D. Juric, N. Al-Rawahi, W. Tauber, J. Han, S. Nas, and Y.-J. Jan, “A front-tracking method for the computations of multiphase flow,” *Journal of computational physics*, vol. 169, no. 2, pp. 708–759, 2001.
- [138] C. W. Hirt, A. A. Amsden, and J. Cook, “An arbitrary lagrangian-eulerian computing method for all flow speeds,” *Journal of computational physics*, vol. 14, no. 3, pp. 227–253, 1974.

- [139] S. Quan, J. Lou, and D. P. Schmidt, "Modeling merging and breakup in the moving mesh interface tracking method for multiphase flow simulations," *Journal of Computational Physics*, vol. 228, no. 7, pp. 2660–2675, apr 2009.
- [140] B. Nichols and C. Hirt, "Methods for calculating multi-dimensional, transient free surface flows past bodies," Los Alamos Scientific Lab., N. Mex.(USA), Tech. Rep., 1975.
- [141] B. Nichols, C. Hirt, and R. Hotchkiss, "Sola-vof: A solution algorithm for transient fluid flow with multiple free boundaries," Los Alamos National Lab.(LANL), Los Alamos, NM (United States), Tech. Rep., 1980.
- [142] C. Hirt and B. Nichols, "Volume of fluid (VOF) method for the dynamics of free boundaries," *Journal of Computational Physics*, vol. 39, no. 1, pp. 201–225, jan 1981.
- [143] W. F. Noh and P. Woodward, "Slic (simple line interface calculation)," in *Proceedings of the fifth international conference on numerical methods in fluid dynamics June 28–July 2, 1976 Twente University, Enschede*. Springer, 1976, pp. 330–340.
- [144] K. Yokoi, "Efficient implementation of thinc scheme: a simple and practical smoothed vof algorithm," *Journal of Computational Physics*, vol. 226, no. 2, pp. 1985–2002, 2007.
- [145] Y. Renardy and M. Renardy, "Prost: a parabolic reconstruction of surface tension for the volume-of-fluid method," *Journal of computational physics*, vol. 183, no. 2, pp. 400–421, 2002.
- [146] R. Scardovelli and S. Zaleski, "Analytical relations connecting linear interfaces and volume fractions in rectangular grids," *Journal of Computational Physics*, vol. 164, no. 1, pp. 228–237, 2000.
- [147] X. Yang, A. J. James, J. Lowengrub, X. Zheng, and V. Cristini, "An adaptive coupled level-set/volume-of-fluid interface capturing method for unstructured triangular grids," *Journal of Computational Physics*, vol. 217, no. 2, pp. 364–394, 2006.
- [148] X. Lv, Q. Zou, Y. Zhao, and D. Reeve, "A novel coupled level set and volume of fluid method for sharp interface capturing on 3d tetrahedral grids," *Journal of Computational Physics*, vol. 229, no. 7, pp. 2573–2604, 2010.
- [149] H. G. Weller, "A new approach to vof-based interface capturing methods for incompressible and compressible flow," *OpenCFD Ltd., Report TR/HGW*, vol. 4, p. 35, 2008.
- [150] C. Greenshields, "Interface capturing in openfoam," Oct 2021. [Online]. Available: <https://cfd.direct/openfoam/free-software/multiphase-interface-capturing/>

- [151] I. Ginzburg and G. Wittum, “Two-phase flows on interface refined grids modeled with vof, staggered finite volumes, and spline interpolants,” *Journal of Computational Physics*, vol. 166, no. 2, pp. 302–335, 2001.
- [152] J. López, J. Hernández, P. Gómez, and F. Faura, “A volume of fluid method based on multidimensional advection and spline interface reconstruction,” *Journal of Computational Physics*, vol. 195, no. 2, pp. 718–742, 2004.
- [153] S. Diwakar, S. K. Das, and T. Sundararajan, “A quadratic spline based interface (quasi) reconstruction algorithm for accurate tracking of two-phase flows,” *Journal of Computational Physics*, vol. 228, no. 24, pp. 9107–9130, 2009.
- [154] S. Osher and J. A. Sethian, “Fronts propagating with curvature-dependent speed: Algorithms based on hamilton-jacobi formulations,” *Journal of computational physics*, vol. 79, no. 1, pp. 12–49, 1988.
- [155] M. Sussman, P. Smereka, and S. Osher, “A level set approach for computing solutions to incompressible two-phase flow,” *Journal of Computational physics*, vol. 114, no. 1, pp. 146–159, 1994.
- [156] J. A. Sethian, P. Smereka *et al.*, “Level set methods for fluid interfaces,” *Annual review of fluid mechanics*, vol. 35, no. 1, pp. 341–372, 2003.
- [157] F. Ilinca, K. R. Yu, and B. Blais, “The effect of viscosity on free surface flow inside an angularly oscillating rectangular tank,” *Computers & Fluids*, vol. 183, pp. 160–176, 2019.
- [158] Y.-C. Chang, T. Hou, B. Merriman, and S. Osher, “A level set formulation of eulerian interface capturing methods for incompressible fluid flows,” *Journal of computational Physics*, vol. 124, no. 2, pp. 449–464, 1996.
- [159] G. Son and V. K. Dhir, “A level set method for analysis of film boiling on an immersed solid surface,” *Numerical Heat Transfer, Part B: Fundamentals*, vol. 52, no. 2, pp. 153–177, 2007.
- [160] Y. Zhang, Q. Zou, and D. Greaves, “Numerical simulation of free-surface flow using the level-set method with global mass correction,” *International Journal for Numerical Methods in Fluids*, vol. 63, no. 6, pp. 651–680, 2010.
- [161] R. F. Ausas, E. A. Dari, and G. C. Buscaglia, “A geometric mass-preserving redistancing scheme for the level set function,” *International journal for numerical methods in fluids*, vol. 65, no. 8, pp. 989–1010, 2011.

- [162] E. Olsson and G. Kreiss, “A conservative level set method for two phase flow,” *Journal of computational physics*, vol. 210, no. 1, pp. 225–246, 2005.
- [163] E. Olsson, G. Kreiss, and S. Zahedi, “A conservative level set method for two phase flow ii,” *Journal of Computational Physics*, vol. 225, no. 1, pp. 785–807, 2007.
- [164] M. Kronbichler, A. Diagne, and H. Holmgren, “A fast massively parallel two-phase flow solver for microfluidic chip simulation,” *The International Journal of High Performance Computing Applications*, vol. 32, no. 2, pp. 266–287, 2018.
- [165] D. Jacqmin, “Calculation of two-phase navier–stokes flows using phase-field modeling,” *Journal of computational physics*, vol. 155, no. 1, pp. 96–127, 1999.
- [166] J. W. Cahn and J. E. Hilliard, “Free energy of a nonuniform system. i. interfacial free energy,” *The Journal of chemical physics*, vol. 28, no. 2, pp. 258–267, 1958.
- [167] S. Popinet and S. Zaleski, “A front-tracking algorithm for accurate representation of surface tension,” *International Journal for Numerical Methods in Fluids*, vol. 30, no. 6, pp. 775–793, 1999.
- [168] S. Shin and D. Juric, “Modeling three-dimensional multiphase flow using a level contour reconstruction method for front tracking without connectivity,” *Journal of Computational Physics*, vol. 180, no. 2, pp. 427–470, 2002.
- [169] C. S. Peskin, “The immersed boundary method,” *Acta numerica*, vol. 11, pp. 479–517, 2002.
- [170] C. Galusinski and P. Vigneaux, “On stability condition for bifluid flows with surface tension: Application to microfluidics,” *Journal of Computational Physics*, vol. 227, no. 12, pp. 6140–6164, 2008.
- [171] S. Hysing, “A new implicit surface tension implementation for interfacial flows,” *International Journal for Numerical Methods in Fluids*, vol. 51, no. 6, pp. 659–672, 2006.
- [172] M. Raessi, M. Bussmann, and J. Mostaghimi, “A semi-implicit finite volume implementation of the csf method for treating surface tension in interfacial flows,” *International journal for numerical methods in fluids*, vol. 59, no. 10, pp. 1093–1110, 2009.
- [173] M. Renardy, Y. Renardy, and J. Li, “Numerical Simulation of Moving Contact Line Problems Using a Volume-of-Fluid Method,” *Journal of Computational Physics*, vol. 171, no. 1, pp. 243–263, jul 2001.

- [174] S. Popinet, “An accurate adaptive solver for surface-tension-driven interfacial flows,” *Journal of Computational Physics*, vol. 228, no. 16, pp. 5838–5866, 2009.
- [175] A. Q. Raeini, M. J. Blunt, and B. Bijeljic, “Modelling two-phase flow in porous media at the pore scale using the volume-of-fluid method,” *Journal of Computational Physics*, vol. 231, no. 17, pp. 5653–5668, 2012.
- [176] D. A. Hoang, V. van Steijn, L. M. Portela, M. T. Kreutzer, and C. R. Kleijn, “Benchmark numerical simulations of segmented two-phase flows in microchannels using the Volume of Fluid method,” *Computers & Fluids*, vol. 86, pp. 28–36, nov 2013.
- [177] J. Sivasamy, T.-N. Wong, N.-T. Nguyen, and L. T.-H. Kao, “An investigation on the mechanism of droplet formation in a microfluidic t-junction,” *Microfluidics and nanofluidics*, vol. 11, no. 1, pp. 1–10, 2011.
- [178] S. Pavuluri, J. Maes, and F. Doster, “Spontaneous imbibition in a microchannel: analytical solution and assessment of volume of fluid formulations,” *Microfluidics and Nanofluidics*, vol. 22, no. 8, p. 90, aug 2018.
- [179] A. A. Saha, S. K. Mitra, M. Tweedie, S. Roy, and J. McLaughlin, “Experimental and numerical investigation of capillary flow in SU8 and PDMS microchannels with integrated pillars,” *Microfluidics and Nanofluidics*, vol. 7, no. 4, pp. 451–465, 2009.
- [180] B. Lafaurie, C. Nardone, R. Scardovelli, S. Zaleski, and G. Zanetti, “Modelling merging and fragmentation in multiphase flows with surfer,” *Journal of computational physics*, vol. 113, no. 1, pp. 134–147, 1994.
- [181] R. Courant, K. Friedrichs, and H. Lewy, “Über die partiellen Differenzgleichungen der mathematischen Physik,” *Mathematische Annalen*, vol. 100, no. 1, pp. 32–74, dec 1928.
- [182] P. Lax, “Systems of conservation laws,” LOS ALAMOS NATIONAL LAB NM, Tech. Rep., 1959.
- [183] C. Runge, “Über die numerische auflösung von differentialgleichungen,” *Mathematische Annalen*, vol. 46, no. 2, pp. 167–178, 1895.
- [184] W. Kutta, “Beitrag zur näherungsweise integration totaler differentialgleichungen,” *Z. Math. Phys.*, vol. 46, pp. 435–453, 1901.
- [185] E. Aulisa, S. Manservigi, and R. Scardovelli, “A novel representation of the surface tension force for two-phase flow with reduced spurious currents,” *Computer methods in applied mechanics and engineering*, vol. 195, no. 44-47, pp. 6239–6257, 2006.

- [186] D. J. Harvie, M. Davidson, and M. Rudman, “An analysis of parasitic current generation in volume of fluid simulations,” *Applied mathematical modelling*, vol. 30, no. 10, pp. 1056–1066, 2006.
- [187] D. Fuster, G. Agbaglah, C. Josserand, S. Popinet, and S. Zaleski, “Numerical simulation of droplets, bubbles and waves: state of the art,” *Fluid dynamics research*, vol. 41, no. 6, p. 065001, 2009.
- [188] M. M. Francois, S. J. Cummins, E. D. Dendy, D. B. Kothe, J. M. Sicilian, and M. W. Williams, “A balanced-force algorithm for continuous and sharp interfacial surface tension models within a volume tracking framework,” *Journal of Computational Physics*, vol. 213, no. 1, pp. 141–173, mar 2006.
- [189] G. Taylor, “On scraping viscous fluid from a plane surface,” *The Scientific Papers of Sir Geoffrey Ingram Taylor*, no. 1971, pp. 410–413, 1962.
- [190] H. K. Moffatt, “Viscous and resistive eddies near a sharp corner,” *Journal of Fluid Mechanics*, vol. 18, no. 1, pp. 1–18, jan 1964.
- [191] C. Huh and L. Scriven, “Hydrodynamic model of steady movement of a solid/liquid/fluid contact line,” *Journal of Colloid and Interface Science*, vol. 35, no. 1, pp. 85–101, jan 1971.
- [192] J. Roenby, H. Bredmose, and H. Jasak, “A computational method for sharp interface advection,” *Royal Society open science*, vol. 3, no. 11, p. 160405, 2016.
- [193] L. Gamet, M. Scala, J. Roenby, H. Scheufler, and J.-L. Pierson, “Validation of volume-of-fluid openfoam® isoadvector solvers using single bubble benchmarks,” *Computers & Fluids*, vol. 213, p. 104722, 2020.
- [194] D. Dai and A. Y. Tong, “Analytical interface reconstruction algorithms in the plic-vof method for 3d polyhedral unstructured meshes,” *International Journal for Numerical Methods in Fluids*, vol. 91, no. 5, pp. 213–227, 2019.
- [195] P. Vulto, S. Podszun, P. Meyer, C. Hermann, A. Manz, and G. A. Urban, “Phaseguides: a paradigm shift in microfluidic priming and emptying,” *Lab on a Chip*, vol. 11, no. 9, p. 1596, 2011.
- [196] H. Cho, H.-Y. Kim, J. Y. Kang, and T. S. Kim, “How the capillary burst microvalve works,” *Journal of Colloid and Interface Science*, vol. 306, no. 2, pp. 379–385, feb 2007.

- [197] O. Gökçe, S. Castonguay, Y. Temiz, T. Gervais, and E. Delamarche, “Self-coalescing flows in microfluidics for pulse-shaped delivery of reagents,” *Nature*, vol. 574, no. 7777, pp. 228–232, oct 2019.
- [198] H. G. Weller, G. Tabor, H. Jasak, and C. Fureby, “A tensorial approach to computational continuum mechanics using object-oriented techniques,” *Computers in physics*, vol. 12, no. 6, pp. 620–631, 1998.
- [199] S. S. Deshpande, L. Anumolu, and M. F. Trujillo, “Evaluating the performance of the two-phase flow solver interFoam,” *Computational Science & Discovery*, vol. 5, no. 1, p. 014016, nov 2012.
- [200] E. Robertson, V. Choudhury, S. Bhushan, and D. K. Walters, “Validation of openfoam numerical methods and turbulence models for incompressible bluff body flows,” *Computers & Fluids*, vol. 123, pp. 122–145, 2015.
- [201] J. H. Ferziger and M. Perić, *Computational Methods for Fluid Dynamics*. Berlin, Heidelberg: Springer Berlin Heidelberg, 2002.
- [202] S. Castonguay and T. Gervais, “A simple static contact angle-based mesh-dependency correction for 3D capillary flow simulations,” *Computers & Fluids*, vol. 228, no. May, p. 105060, oct 2021.
- [203] M. Rocca, Y. Temiz, M. L. Salva, S. Castonguay, T. Gervais, C. M. Niemeyer, and E. Delamarche, “Rapid quantitative assays for glucose-6-phosphate dehydrogenase (G6PD) and hemoglobin combined on a capillary-driven microfluidic chip,” *Lab on a Chip*, pp. 1037–1043, 2021.
- [204] M. Hitzbleck and E. Delamarche, “Reagents in microfluidics: an in and out challenge,” *Chemical Society Reviews*, vol. 42, no. 21, p. 8494, 2013.
- [205] P. Calvert, “Inkjet Printing for Materials and Devices,” *Chemistry of Materials*, vol. 13, no. 10, pp. 3299–3305, oct 2001.
- [206] J. A. Lim, W. H. Lee, H. S. Lee, J. H. Lee, Y. D. Park, and K. Cho, “Self-Organization of Ink-jet-Printed Triisopropylsilylethynyl Pentacene via Evaporation-Induced Flows in a Drying Droplet,” *Advanced Functional Materials*, vol. 18, no. 2, pp. 229–234, jan 2008.
- [207] M. Singh, H. M. Haverinen, P. Dhagat, and G. E. Jabbour, “Inkjet Printing-Process and Its Applications,” *Advanced Materials*, vol. 22, no. 6, pp. 673–685, feb 2010.

- [208] I. Langmuir., “The evaporation of small spheres,” *Physical Review*, vol. 12, pp. 368–370, 11 1918. [Online]. Available: <https://link.aps.org/doi/10.1103/PhysRev.12.368>
- [209] I. Langmuir, “The adsorption of gases on plane surfaces of glass, mica and platinum.” *Journal of the American Chemical Society*, vol. 40, pp. 1361–1403, 9 1918. [Online]. Available: <https://pubs.acs.org/doi/abs/10.1021/ja02242a004>
- [210] M. C. Manning, D. K. Chou, B. M. Murphy, R. W. Payne, and D. S. Katayama, “Stability of protein pharmaceuticals: an update,” *Pharmaceutical research*, vol. 27, no. 4, pp. 544–575, 2010.
- [211] E. Fu, B. Lutz, P. Kauffman, and P. Yager, “Controlled reagent transport in disposable 2D paper networks,” *Lab on a Chip*, vol. 10, no. 7, p. 918, 2010.
- [212] H. Z. An, M. E. Helgeson, and P. S. Doyle, “Nanoemulsion Composite Microgels for Orthogonal Encapsulation and Release,” *Advanced Materials*, vol. 24, no. 28, pp. 3838–3844, jul 2012.
- [213] G. E. Fridley, H. Q. Le, E. Fu, and P. Yager, “Controlled release of dry reagents in porous media for tunable temporal and spatial distribution upon rehydration,” *Lab on a Chip*, vol. 12, no. 21, p. 4321, 2012.
- [214] S. D. Howison, “Complex variable methods in Hele–Shaw moving boundary problems,” *European Journal of Applied Mathematics*, vol. 3, no. 03, p. 209, sep 1992.
- [215] L. J. Cummings, S. D. Howison, and J. R. King, “Two-dimensional Stokes and Hele-Shaw flows with free surfaces,” *European Journal of Applied Mathematics*, vol. 10, no. 6, dec 1999.
- [216] B. Riemann, *Grundlagen für eine allgemeine Theorie der Funktionen einer veränderlichen complexen Grösse [An alternative basis for a general theory of the functions of complex variables]*. Ph. D. thesis, University of Göttingen, 1851.
- [217] W. F. Osgood, “On the existence of the green’s function for the most general simply connected plane region,” *Transactions of the American Mathematical Society*, vol. 1, no. 3, pp. 310–314, 1900.
- [218] T. A. Driscoll and L. N. Trefethen, *Schwarz-Christoffel Mapping*. Cambridge: Cambridge University Press, 2002.

- [219] S. Castonguay, O. Gökçe, T. Gervais, and E. Delamarche, “Characterization of Self-Coalescence in Microfluidic Capillary Flow via Finite Element Method,” in *14th U.S. National Congress on Computational Mechanics, USNCCM14*, 2017.
- [220] J. D’Errico, “Inverse (integrated) gradient,” URL: <https://de.mathworks.com/matlabcentral/fileexchange/9734-inverse-integrated-gradient>, 2009.
- [221] L. H. Howell, “Computation of Conformal Maps by Modified Schwarz-Christoffel Transformations,” Ph.D. dissertation, MASSACHUSETTS INSTITUTE OF TECHNOLOGY, 1990.
- [222] L. H. Howell, “Numerical conformal mapping of circular arc polygons,” *Journal of Computational and Applied Mathematics*, vol. 46, no. 1-2, pp. 7–28, jun 1993.
- [223] M. J. Ablowitz, A. S. Fokas, and A. S. Fokas, *Complex variables: introduction and applications*. Cambridge University Press, 2003.
- [224] K. Heun, “Zur theorie der riemann’schen functionen zweiter ordnung mit vier verzweigungspunkten,” *Mathematische Annalen*, vol. 33, no. 2, pp. 161–179, 1888.
- [225] F. M. Arscott, S. Y. Slavyanov, D. Schmidt, G. Wolf, P. Maroni, and A. Duval, *Heun’s Differential Equations*. Clarendon Press, 1995.
- [226] F. W. Olver, D. W. Lozier, R. F. Boisvert, and C. W. Clark, *NIST handbook of mathematical functions*. Cambridge university press, 2010.
- [227] R. Maier, “The 192 solutions of the heun equation,” *Mathematics of Computation*, vol. 76, no. 258, pp. 811–843, 2007.
- [228] W. L. Oberkampf and C. J. Roy, *Verification and Validation in Scientific Computing*. Cambridge: Cambridge University Press, 2010.
- [229] J. M. Wood and H. Sanei, “Secondary migration and leakage of methane from a major tight-gas system,” *Nature Communications*, vol. 7, no. 1, p. 13614, dec 2016.
- [230] E. Hemmig, Y. Temiz, O. Gökçe, R. D. Lovchik, and E. Delamarche, “Transposing Lateral Flow Immunoassays to Capillary-Driven Microfluidics Using Self-Coalescence Modules and Capillary-Assembled Receptor Carriers,” *Analytical Chemistry*, vol. 92, no. 1, pp. 940–946, jan 2020.
- [231] Y. Zhai, A. Wang, D. Koh, P. Schneider, and K. W. Oh, “A robust, portable and backflow-free micromixing device based on both capillary- and vacuum-driven flows,” *Lab on a Chip*, vol. 18, no. 2, pp. 276–284, 2018.

- [232] M. Zimmermann, H. Schmid, P. Hunziker, and E. Delamarche, “Capillary pumps for autonomous capillary systems,” *Lab Chip*, vol. 7, no. 1, pp. 119–125, sep 2007.
- [233] M. Zimmermann, P. Hunziker, and E. Delamarche, “Valves for autonomous capillary systems,” *Microfluidics and Nanofluidics*, vol. 5, no. 3, pp. 395–402, sep 2008.
- [234] R. H. Sampieri, A. Prosperetti, and G. Tryggvason, *Computational Methods for Multiphase Flow*. Cambridge: Cambridge University Press, 2007.
- [235] E. B. Dussan, “On the Spreading of Liquids on Solid Surfaces: Static and Dynamic Contact Lines,” *Annual Review of Fluid Mechanics*, vol. 11, no. 1, pp. 371–400, jan 1979.
- [236] J. H. Snoeijer and B. Andreotti, “Moving Contact Lines: Scales, Regimes, and Dynamical Transitions,” *Annual Review of Fluid Mechanics*, vol. 45, no. 1, pp. 269–292, jan 2013.
- [237] L. M. Hocking, “A moving fluid interface. Part 2. The removal of the force singularity by a slip flow,” *Journal of Fluid Mechanics*, vol. 79, no. 2, pp. 209–229, feb 1977.
- [238] S. Afkhami, S. Zaleski, and M. Bussmann, “A mesh-dependent model for applying dynamic contact angles to VOF simulations,” *Journal of Computational Physics*, vol. 228, no. 15, pp. 5370–5389, aug 2009.
- [239] F. Schönfeld and S. Hardt, “Dynamic contact angles in CFD simulations,” *Computers & Fluids*, vol. 38, no. 4, pp. 757–764, apr 2009.
- [240] H. Jasak, “Error Analysis and Estimation for the finite volume method with applications to fluid flows.” Ph.D. dissertation, Imperial College of Science, Technology and Medicine, 1996.
- [241] H. G. Weller, G. Tabor, H. Jasak, and C. Fureby, “A tensorial approach to computational continuum mechanics using object-oriented techniques,” *Computers in Physics*, vol. 12, no. 6, p. 620, 1998.
- [242] A. Ashish Saha and S. K. Mitra, “Effect of dynamic contact angle in a volume of fluid (VOF) model for a microfluidic capillary flow,” *Journal of Colloid and Interface Science*, vol. 339, no. 2, pp. 461–480, nov 2009.
- [243] S. Li, F. Chu, J. Zhang, D. Brutin, and D. Wen, “Droplet jumping induced by coalescence of a moving droplet and a static one: Effect of initial velocity,” *Chemical Engineering Science*, vol. 211, p. 115252, jan 2020.

- [244] V. Inguva, R. Graceffa, J. Schulz, O. Bilsel, and B. J. Perot, “Creating round focused microjets from rectangular nozzles,” *Journal of Mechanical Science and Technology*, vol. 33, no. 9, pp. 4281–4289, sep 2019.
- [245] V. Thammanna Gurumurthy, D. Rettenmaier, I. V. Roisman, C. Tropea, and S. Garoff, “Computations of spontaneous rise of a rivulet in a corner of a vertical square capillary,” *Colloids and Surfaces A: Physicochemical and Engineering Aspects*, vol. 544, no. December 2017, pp. 118–126, may 2018.
- [246] H. S. Rabbani and T. D. Seers, “Inertia Controlled Capillary Pressure at the Juncture between Converging and Uniform Channels,” *Scientific Reports*, vol. 9, no. 1, p. 13870, dec 2019.
- [247] R. Aziz, V. Joekar-Niasar, P. J. Martínez-Ferrer, O. E. Godinez-Brizuela, C. Theodoropoulos, and H. Mahani, “Novel insights into pore-scale dynamics of wettability alteration during low salinity waterflooding,” *Scientific Reports*, vol. 9, no. 1, p. 9257, dec 2019.
- [248] H. Rusche, “Computational Fluid Dynamics of Dispersed Two-Phase Flows at High Phase Fractions,” Ph.D. dissertation, Imperial College of Science, Technology & Medicine, London, 2002.
- [249] O. Ubbink and R. Issa, “A Method for Capturing Sharp Fluid Interfaces on Arbitrary Meshes,” *Journal of Computational Physics*, vol. 153, no. 1, pp. 26–50, jul 1999.
- [250] H. S. Rabbani, V. Joekar-Niasar, and N. Shokri, “Effects of intermediate wettability on entry capillary pressure in angular pores,” *Journal of Colloid and Interface Science*, vol. 473, pp. 34–43, jul 2016.
- [251] R. Lucas, “Ueber das Zeitgesetz des kapillaren Aufstiegs von Flüssigkeiten,” *Kolloid-Zeitschrift*, vol. 23, no. 1, pp. 15–22, jul 1918.
- [252] P. Vulto, S. Podszun, P. Meyer, and G. Urban, “Phaseguide patterns for advanced liquid handling in Lab-on-a-Chip systems,” in *TRANSDUCERS 2009 - 2009 International Solid-State Sensors, Actuators and Microsystems Conference*. IEEE, jun 2009, pp. 409–412.
- [253] Y. Sui, H. Ding, and P. D. Spelt, “Numerical Simulations of Flows with Moving Contact Lines,” *Annual Review of Fluid Mechanics*, vol. 46, no. 1, pp. 97–119, jan 2014.
- [254] R. G. Cox, “The dynamics of the spreading of liquids on a solid surface. Part 1. Viscous flow,” *Journal of Fluid Mechanics*, vol. 168, no. -1, p. 169, jul 1986.

- [255] C. Bosanquet, “LV. On the flow of liquids into capillary tubes,” *The London, Edinburgh, and Dublin Philosophical Magazine and Journal of Science*, vol. 45, no. 267, pp. 525–531, mar 1923.
- [256] H. Czachor, S. Doerr, and L. Lichner, “Water retention of repellent and subcritical repellent soils: New insights from model and experimental investigations,” *Journal of Hydrology*, vol. 380, no. 1-2, pp. 104–111, jan 2010.
- [257] T. W. Patzek, “Verification of a Complete Pore Network Simulator of Drainage and Imbibition,” *SPE Journal*, vol. 6, no. 02, pp. 144–156, jun 2001.
- [258] M. M. Gong and D. Sinton, “Turning the Page: Advancing Paper-Based Microfluidics for Broad Diagnostic Application,” *Chemical Reviews*, vol. 117, no. 12, pp. 8447–8480, jun 2017.
- [259] K. Jiao and X. Li, “Water transport in polymer electrolyte membrane fuel cells,” *Progress in Energy and Combustion Science*, vol. 37, no. 3, pp. 221–291, jun 2011.
- [260] T. G. Tranter, J. T. Gostick, A. D. Burns, and W. F. Gale, “Capillary Hysteresis in Neutrally Wettable Fibrous Media: A Pore Network Study of a Fuel Cell Electrode,” *Transport in Porous Media*, vol. 121, no. 3, pp. 597–620, feb 2018.
- [261] D. Juncker, H. Schmid, U. Drechsler, H. Wolf, M. Wolf, B. Michel, N. de Rooij, and E. Delamarche, “Autonomous Microfluidic Capillary System,” *Analytical Chemistry*, vol. 74, no. 24, pp. 6139–6144, dec 2002.
- [262] G. Mason and N. R. Morrow, “Developments in spontaneous imbibition and possibilities for future work,” *Journal of Petroleum Science and Engineering*, vol. 110, pp. 268–293, oct 2013.
- [263] T. Gervais and K. F. Jensen, “Mass transport and surface reactions in microfluidic systems,” *Chemical Engineering Science*, vol. 61, no. 4, pp. 1102–1121, feb 2006.
- [264] T. M. Squires, R. J. Messinger, and S. R. Manalis, “Making it stick: convection, reaction and diffusion in surface-based biosensors,” *Nature Biotechnology*, vol. 26, no. 4, pp. 417–426, apr 2008.
- [265] T. Rosenfeld and M. Bercovici, “Dynamic control of capillary flow in porous media by electroosmotic pumping,” *Lab on a Chip*, vol. 19, no. 2, pp. 328–334, 2019.
- [266] H.-Y. KIM and L. MAHADEVAN, “Capillary rise between elastic sheets,” *Journal of Fluid Mechanics*, vol. 548, no. -1, p. 141, feb 2006.

- [267] D. Shou, L. Ye, and J. Fan, “Treelike networks accelerating capillary flow,” *Physical Review E*, vol. 89, no. 5, p. 053007, may 2014.
- [268] J. Berthier, D. Gosselin, and E. Berthier, “A generalization of the Lucas–Washburn–Rideal law to composite microchannels of arbitrary cross section,” *Microfluidics and Nanofluidics*, vol. 19, no. 3, pp. 497–507, sep 2015.
- [269] J. Berthier, D. Gosselin, A. Pham, F. Boizot, G. Delapierre, N. Belgacem, and D. Chaussy, “Spontaneous capillary flows in piecewise varying cross section microchannels,” *Sensors and Actuators B: Chemical*, vol. 223, pp. 868–877, feb 2016.
- [270] E. K. Rideal, “CVIII. On the flow of liquids under capillary pressure,” *The London, Edinburgh, and Dublin Philosophical Magazine and Journal of Science*, vol. 44, no. 264, pp. 1152–1159, dec 1922.
- [271] V. Telis, J. Telis-Romero, H. Mazzotti, and A. Gabas, “Viscosity of Aqueous Carbohydrate Solutions at Different Temperatures and Concentrations,” *International Journal of Food Properties*, vol. 10, no. 1, pp. 185–195, jan 2007.
- [272] E. Aumann, L. Hildemann, and A. Tabazadeh, “Measuring and modeling the composition and temperature-dependence of surface tension for organic solutions,” *Atmospheric Environment*, vol. 44, no. 3, pp. 329–337, jan 2010.
- [273] D. Quéré, “Wetting and Roughness,” *Annual Review of Materials Research*, vol. 38, no. 1, pp. 71–99, aug 2008.
- [274] D. Bonn, J. Eggers, J. Indekeu, J. Meunier, and E. Rolley, “Wetting and spreading,” *Reviews of Modern Physics*, vol. 81, no. 2, pp. 739–805, may 2009.
- [275] A. B. D. Cassie and S. Baxter, “Wettability of porous surfaces,” *Transactions of the Faraday Society*, vol. 40, no. 5, p. 546, 1944.
- [276] T. Gervais, Y. Temiz, L. Aubé, and E. Delamarche, “Large-scale dried reagent reconstitution and diffusion control using microfluidic self-coalescence modules,” *Small*, vol. 18, no. 16, p. 2105939, 2022. [Online]. Available: <https://onlinelibrary.wiley.com/doi/abs/10.1002/sml.202105939>
- [277] F. P. Bretherton, “The motion of long bubbles in tubes,” *Journal of Fluid Mechanics*, vol. 10, no. 02, p. 166, mar 1961.

- [278] D. Oberthuer, J. Knoška, M. O. Wiedorn, K. R. Beyerlein, D. A. Bushnell, E. G. Kovaleva, M. Heymann, L. Gumprecht, R. A. Kirian, A. Barty, V. Mariani, A. Tolstikova, L. Adriano, S. Awel, M. Barthelmess, K. Dörner, P. L. Xavier, O. Yefanov, D. R. James, G. Nelson, D. Wang, G. Calvey, Y. Chen, A. Schmidt, M. Szczepek, S. Frielingsdorf, O. Lenz, E. Snell, P. J. Robinson, B. Šarler, G. Belšak, M. Maček, F. Wilde, A. Aquila, S. Boutet, M. Liang, M. S. Hunter, P. Scheerer, J. D. Lipscomb, U. Weierstall, R. D. Kornberg, J. C. H. Spence, L. Pollack, H. N. Chapman, and S. Bajt, “Double-flow focused liquid injector for efficient serial femtosecond crystallography,” *Scientific Reports*, vol. 7, no. 1, pp. 1–10, dec 2017.
- [279] W. D. Mellin, “Work with new electronic ‘brains’ opens field for army math experts,” *The Hammond Times*, vol. 10, p. 66, 1957.
- [280] C. Babbage, *Passages from the life of a philosopher*. Longman green, 1864.
- [281] P. Yager, T. Edwards, E. Fu, K. Helton, K. Nelson, M. R. Tam, and B. H. Weigl, “Microfluidic diagnostic technologies for global public health,” *Nature*, vol. 442, no. 7101, pp. 412–418, 2006.
- [282] T. R. Hughes, M. Mao, A. R. Jones, J. Burchard, M. J. Marton, K. W. Shannon, S. M. Lefkowitz, M. Ziman, J. M. Schelter, M. R. Meyer *et al.*, “Expression profiling using microarrays fabricated by an ink-jet oligonucleotide synthesizer,” *Nature biotechnology*, vol. 19, no. 4, pp. 342–347, 2001.
- [283] B. Derby, “Printing and prototyping of tissues and scaffolds,” *science*, vol. 338, no. 6109, pp. 921–926, 2012.
- [284] H. Sirringhaus, T. Kawase, R. Friend, T. Shimoda, M. Inbasekaran, W. Wu, and E. P. Woo, “High-resolution inkjet printing of all-polymer transistor circuits,” *Science*, vol. 290, no. 5499, pp. 2123–2126, 2000.
- [285] M. Beck, S. Brockhuis, N. van der Velde, C. Breukers, J. Greve, and L. W. Terstappen, “On-chip sample preparation by controlled release of antibodies for simple cd4 counting,” *Lab on a Chip*, vol. 12, no. 1, pp. 167–173, 2012.
- [286] M. Hitzbleck, L. Gervais, and E. Delamarche, “Controlled release of reagents in capillary-driven microfluidics using reagent integrators,” *Lab on a Chip*, vol. 11, no. 16, p. 2680, 2011.
- [287] E. Garcia, J. R. Kirkham, A. V. Hatch, K. R. Hawkins, and P. Yager, “Controlled microfluidic reconstitution of functional protein from an anhydrous storage depot,” *Lab on a Chip*, vol. 4, no. 1, p. 78, 2004.

- [288] J. Oliver, C. Huh, and S. Mason, “Resistance to spreading of liquids by sharp edges,” *Journal of Colloid and Interface Science*, vol. 59, no. 3, pp. 568–581, 1977.
- [289] P.-G. de Gennes, F. Brochard-Wyart, and D. Quéré, *Capillarity and Wetting Phenomena: Drops, Bubbles, Pearls, Waves*. Springer, 2004.
- [290] P.-A. Goyette, É. Boulais, F. Normandeau, G. Laberge, D. Juncker, and T. Gervais, “Microfluidic multipoles theory and applications,” *Nature Communications*, vol. 10, no. 1, p. 1781, dec 2019.
- [291] R. Safavieh and D. Juncker, “Capillaries: pre-programmed, self-powered microfluidic circuits built from capillary elements,” *Lab on a Chip*, vol. 13, no. 21, p. 4180, 2013.
- [292] B. Zhao, “Surface-Directed Liquid Flow Inside Microchannels,” *Science*, vol. 291, no. 5506, pp. 1023–1026, feb 2001.
- [293] A. M. Weiner, “Femtosecond pulse shaping using spatial light modulators,” *Review of scientific instruments*, vol. 71, no. 5, pp. 1929–1960, 2000.
- [294] G. G. Guilbault and D. N. Kramer, “Fluorometric procedure for measuring the activity of dehydrogenases.” *Analytical chemistry*, vol. 37, no. 10, pp. 1219–1221, 1965.
- [295] N. LaRue, M. Kahn, M. Murray, B. T. Leader, P. Bansil, S. McGray, M. Kalnoky, H. Zhang, H. Huang, H. Jiang *et al.*, “Comparison of quantitative and qualitative tests for glucose-6-phosphate dehydrogenase deficiency,” *The American journal of tropical medicine and hygiene*, vol. 91, no. 4, p. 854, 2014.
- [296] M. D. Cappellini and G. Fiorelli, “Glucose-6-phosphate dehydrogenase deficiency,” *The lancet*, vol. 371, no. 9606, pp. 64–74, 2008.
- [297] O. Piepenburg, C. H. Williams, D. L. Stemple, and N. A. Armes, “Dna detection using recombination proteins,” *PLoS biology*, vol. 4, no. 7, p. e204, 2006.
- [298] B. M. Paegel, L. D. Hutt, P. C. Simpson, and R. A. Mathies, “Turn geometry for minimizing band broadening in microfabricated capillary electrophoresis channels,” *Analytical chemistry*, vol. 72, no. 14, pp. 3030–3037, 2000.
- [299] J. Schindelin, I. Arganda-Carreras, E. Frise, V. Kaynig, M. Longair, T. Pietzsch, S. Preibisch, C. Rueden, S. Saalfeld, B. Schmid *et al.*, “Fiji: an open-source platform for biological-image analysis,” *Nature methods*, vol. 9, no. 7, pp. 676–682, 2012.

- [300] T. Zimmermann, “Spectral imaging and linear unmixing in light microscopy,” *Microscopy techniques*, pp. 245–265, 2005.
- [301] W. T. Seaman, E. Andrews, M. Couch, E. M. Kojic, S. Cu-Uvin, J. Palefsky, A. M. Deal, and J. Webster-Cyriaque, “Detection and quantitation of hpv in genital and oral tissues and fluids by real time pcr,” *Virology journal*, vol. 7, no. 1, pp. 1–17, 2010.
- [302] G. E. Glock and P. McLean, “Further studies on the properties and assay of glucose 6-phosphate dehydrogenase and 6-phosphogluconate dehydrogenase of rat liver,” *Biochemical Journal*, vol. 55, no. 3, p. 400, 1953.
- [303] N. Bontoux, A. Pépin, Y. Chen, A. Ajdari, and H. A. Stone, “Experimental characterization of hydrodynamic dispersion in shallow microchannels,” *Lab Chip*, vol. 6, no. 7, pp. 930–935, 2006.
- [304] R. Chuoke, P. Van Meurs, and C. van der Poel, “The instability of slow, immiscible, viscous liquid-liquid displacements in permeable media,” *Transactions of the AIME*, vol. 216, no. 01, pp. 188–194, 1959.
- [305] X. Shan and H. Chen, “Lattice Boltzmann model for simulating flows with multiple phases and components,” *Physical Review E*, vol. 47, no. 3, pp. 1815–1819, mar 1993.
- [306] M. R. Swift, E. Orlandini, W. R. Osborn, and J. M. Yeomans, “Lattice Boltzmann simulations of liquid-gas and binary fluid systems,” *Physical Review E*, vol. 54, no. 5, pp. 5041–5052, nov 1996.
- [307] X. He, X. Shan, and G. D. Doolen, “Discrete Boltzmann equation model for nonideal gases,” *Physical Review E*, vol. 57, no. 1, pp. R13–R16, jan 1998.
- [308] L. O. E. Santos, P. C. Facin, and P. C. Philippi, “Lattice-Boltzmann model based on field mediators for immiscible fluids,” *Physical Review E*, vol. 68, no. 5, p. 056302, nov 2003.
- [309] H. Huang, M. C. Sukop, and X.-Y. Lu, *Multiphase Lattice Boltzmann Methods: Theory and Application*. Chichester, UK: John Wiley & Sons, Ltd, jul 2015.
- [310] S. R. A. Salinas, *Introduction to Statistical Physics*, ser. Graduate Texts in Contemporary Physics. New York, NY: Springer New York, 2001.
- [311] S. Leclaire, A. Parmigiani, O. Malaspinas, B. Chopard, and J. Latt, “Generalized three-dimensional lattice Boltzmann color-gradient method for immiscible two-phase pore-scale imbibition and drainage in porous media,” *Physical Review E*, vol. 95, no. 3, p. 033306, mar 2017.

- [312] T. Reis and T. N. Phillips, “Lattice Boltzmann model for simulating immiscible two-phase flows,” *Journal of Physics A: Mathematical and Theoretical*, vol. 40, no. 14, pp. 4033–4053, apr 2007.
- [313] S. Leclaire, M. Reggio, and J.-Y. Trépanier, “Isotropic color gradient for simulating very high-density ratios with a two-phase flow lattice Boltzmann model,” *Computers & Fluids*, vol. 48, no. 1, pp. 98–112, sep 2011.
- [314] S. Leclaire, M. Reggio, and J.-Y. Trépanier, “Numerical evaluation of two recoloring operators for an immiscible two-phase flow lattice Boltzmann model,” *Applied Mathematical Modelling*, vol. 36, no. 5, pp. 2237–2252, may 2012.
- [315] S. Leclaire, M. Reggio, and J.-Y. Trépanier, “Progress and investigation on lattice Boltzmann modeling of multiple immiscible fluids or components with variable density and viscosity ratios,” *Journal of Computational Physics*, vol. 246, pp. 318–342, aug 2013.
- [316] S. Leclaire, N. Pellerin, M. Reggio, and J.-Y. Trépanier, “Enhanced equilibrium distribution functions for simulating immiscible multiphase flows with variable density ratios in a class of lattice Boltzmann models,” *International Journal of Multiphase Flow*, vol. 57, pp. 159–168, 2013.
- [317] S. Leclaire, N. Pellerin, M. Reggio, and J.-Y. Trépanier, “An approach to control the spurious currents in a multiphase lattice Boltzmann method and to improve the implementation of initial condition,” *International Journal for Numerical Methods in Fluids*, vol. 77, no. 12, pp. 732–746, apr 2015.
- [318] Y. Arango, Y. Temiz, O. Gökçe, and E. Delamarche, “Electrogates for stop-and-go control of liquid flow in microfluidics,” *Applied Physics Letters*, vol. 112, no. 15, p. 153701, apr 2018.

APPENDIX A SELF-COALESCEING FLOWS IN MICROFLUIDICS FOR PULSE-SHAPED DELIVERY OF REAGENTS

A.1 Abstract

Microfluidic systems can deliver portable point-of-care diagnostics without the need for external equipment or specialist operators, by integrating all reagents and manipulations required for a particular assay in one device [281]. A key approach is to deposit picogram quantities of dried reagents in microchannels with micrometre precision using specialized inkjet plotters [26, 282–284]. This means that reagents can be stored for long periods of time and reconstituted spontaneously when adding a liquid sample. But it is challenging to carry out complex operations using multiple reagents, because shear flow enhances their dispersion and they tend to accumulate at moving liquid fronts, resulting in poor spatiotemporal control over the concentration profile of the reconstituted reagents [204]. One solution is to limit the rate of release of reagents into the liquid [213, 285–287]. However, this requires the fine-tuning of different reagents, conditions and targeted operations, and cannot readily produce the complex, time-dependent multireagent concentration pulses required for sophisticated on-chip assays. Here we report and characterize a capillary flow phenomenon that we term self-coalescence, which is seen when a confined liquid with a stretched air–liquid interface is forced to ‘zip’ back onto itself in a microfluidic channel, thereby allowing reagent reconstitution with minimal dispersion. We provide a comprehensive framework that captures the physical underpinning of this effect. We also fabricate scalable, compact and passive microfluidic structures—‘self-coalescence modules’, or SCMs—that exploit and control this phenomenon in order to dissolve dried reagent deposits in aqueous solutions with precise spatiotemporal control. We show that SCMs can reconstitute multiple reagents so that they either undergo local reactions or are sequentially delivered in a flow of liquid. SCMs are easily fabricated in different materials, readily configured to enable different reagent manipulations, and readily combined with other microfluidic technologies, so should prove useful for assays, diagnostics, high-throughput screening and other technologies requiring efficient preparation and manipulation of small volumes of complex solutions.

A.2 Theory

The key to translating self-coalescence into a useful microfluidic technology is first to elicit and characterize its physical underpinnings (see also Chapter 3), in order to demonstrate how air–liquid interfaces can be manipulated such that the characteristic time and length over which dispersion oc-

curs scale with the width, W , of the microfluidic channel rather than its length, L (assuming that W is much less than L). To implement the concept, we use a shallow channel geometry (whose height, H , is much less than W) to confine the liquid within a Hele-Shaw cell—a quasi-two-dimensional planar flow model whereby flow is always considered to be locally parabolic and propagating in the direction of the pressure gradient [69]. Within the flow plane, the fluid is further confined laterally by a capillary pinning line (CPL) [288] that acts as a Laplace pressure barrier [289] and geometrically forces the liquid to self-coalesce—that is, to fold onto itself and release its surface free energy to spill over the CPL. Making the CPL straight creates a translational symmetry in the self-coalescence process that results in the fluid propagating at the velocity of the capillary front. In this process, following the path of least resistance, most of the flow occurs right behind the moving liquid front, where the fluid rapidly comes to a rest (Fig. A.1a, b and Supplementary Video A.15).

Free-boundary flows are known to be challenging to model and to compute numerically, let alone analytically [214]. A complete solution to the problem can be reached by numerical modelling. Alternatively, recognizing the conformal invariance of the advection–diffusion transport equation in shallow microfluidic devices [290], and that all boundary conditions become regular in the reference frame of the moving meniscus (Fig. A.1c), a complete solution can be obtained using a Schwarz–Christoffel mapping [218] (see section 3.3). Two simple asymptotic solutions can be further derived via this conformal mapping approach to obtain the main velocity field along the CPL both near its contact point (where x is much less than W) and far downstream of the meniscus contact point (where x is much greater than W):

$$\bar{V}_{\text{near}}(x, t) \approx U_m + i(U + U_m) \left(\frac{x + U_m t}{t} \right) \quad (\text{A.1})$$

$$\bar{V}_{\text{far}}(x, t) = A(W, \lambda, \theta_w) U_m e^{-\frac{\pi}{W}(x + U_m t + i\lambda W)} \quad (\text{A.2})$$

where the variables x and t are respectively the horizontal distance from the meniscus tip and the time elapsed; $r = \lambda W / (1 + \cos \theta_w)$ is the radius of the circular meniscus; U_m is the meniscus velocity; U is the flow velocity at the inlet; $A(W, \lambda, \theta_w)$ is a constant geometric factor that depends on the channel width and wall contact angle; λ is the width fraction of the channel cross-section at which self-coalescence occurs; i is the imaginary unit; and e is Euler’s number (section 3.6).

The exponential form of Equation A.1 has been extensively studied in the case of Saffman–Taylor viscous fingering in a long straight channel, which yields a similar exponential decay of the velocity field with characteristic decay length $L_d = W / \pi$ and time $t_d = L_d / U_m$ (Fig. A.1d) [101]. In the context of self-coalescence, this decay constant explains the short flow lifetime before stagnation is achieved (L_d is roughly 160 μm ; t_d is approximately 240ms; assuming that $W = 500 \mu\text{m}$ and

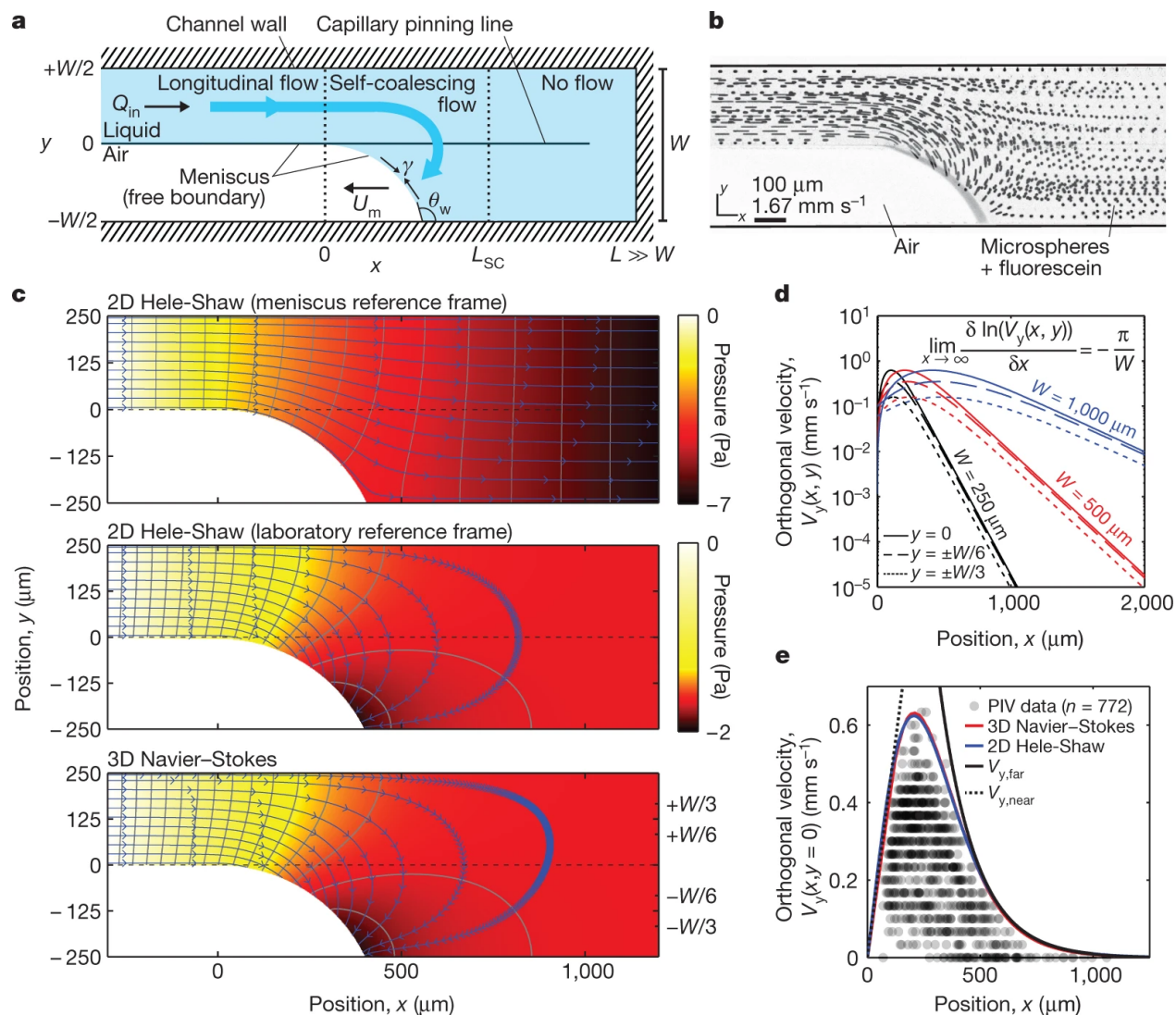


Figure A.1 Description and modelling of self-coalescence in a microchannel. **a**, Top view of a microchannel (of width W and length L) that is partially filled with a liquid. During Stokes flow (at flow rate Q_{in}), this setting fosters three flow modes: longitudinal flow (where $x < 0$), self-coalescing flow ($0 < x < L_{SC}$), and stagnancy ('no flow', where $x > L_{SC}$), with L_{SC} being the penetration length of a self-coalescing flow. U_m is the meniscus velocity, γ the surface tension, and θ_w the contact angle. **b**, Image of fluorescent microspheres (diameter $4.8 \mu\text{m}$) in $10 \mu\text{g mL}^{-1}$ fluorescein solution during self-coalescence (W is $500 \mu\text{m}$; microchannel height is $50 \mu\text{m}$; Q_{in} is 500 nL/min ; Re is roughly 0.001 ; and $\theta_w = 116^\circ$). Streaks and dots respectively reveal moving and stationary particles. The CPL, implemented with a $5\text{-}\mu\text{m}$ -wide trench, is not visible after background subtraction. **c**, Two-dimensional (2D) Hele-Shaw model (top and middle) and 3D Navier-Stokes simulation (bottom) of self-coalescence in the same channel geometry as in panel **b** and at half the channel height. The colour map shows pressure, and the middle and bottom panels share the same colour map. Blue, velocity streamlines, and grey, isobars. The gaps between arrowheads show the displacement of a particle at regular time intervals (180 ms). (Continued on the following page.)

Figure A.1 **d**, Log plots of the orthogonal velocity (V_y) of self-coalescing flows for three channel widths and at different y positions as indicated, highlighting the asymptotic form of the orthogonal velocity component: near the meniscus the flow is transitional, increasing steadily until it reaches a peak and then decaying exponentially downstream of the offset. **e**, Plotted are V_y values for particles from all z -planes at $y = 0$ from velocimetry data (semi-transparent dots, $n = 772$ from 12 locations in 3 experiments), along with the maximum V_y predicted by the 2D Hele-Shaw model (blue), the 2D asymptotic model (black, $V_{y,\text{far}} = 5.26e^{-\pi x/500}$ mm s^{-1} ; dotted, $V_{y,\text{near}} = 0.0045x$ mm s^{-1}) and the 3D Navier–Stokes simulation (red). PIV, particle image velocimetry.

$U_m = 1\text{mm s}^{-1}$). The analytical results for these two asymptotic behaviours, as well as the full Schwarz–Christoffel mapping solution (see section 3.4), reveal a strong match with finite-element-method simulations and experiments, further verifying the model (Fig. A.1e). To achieve self-coalescence the CPL can be made straight, but in general can be of any shape, from sharp turns to spirals and slow meanders. This process thus also explains the filling dynamics within capillary pumps [232] and around microfluidic phaseguides [195]—capillary structures often used to control wetting in microsystems. Even more importantly, the process reveals how the phenomena can be precisely triggered and controlled to engineer minimally dispersive flows.

A.3 Reagent reconstitution and scalability

We use the practical implementation of self-coalescence here to control reagent reconstitution under the form of a SCM. The SCM is a microchannel having two CPLs and a vent (Fig. A.2a). The first CPL (the leading barrier) ensures longitudinal flow, whereas the second (the diversion barrier) acts as a capillary burst valve [291] and prevents the liquid from exiting the SCM before the SCM is completely filled. A gap between the leading and diversion barriers forces self-coalescence to begin next to the diversion barrier. The effectiveness of reagent reconstitution using self-coalescence becomes apparent when it is compared with reconstitution in a microchannel that lacks a leading barrier, illustrated in Fig. A.2b, c using amaranth dye and water. In this case, the longitudinal flow leads to the strong accumulation of amaranth dye near the liquid filling front, which creates a concentration spike that is an order of magnitude higher than the uniform concentration attained when using self-coalescence (Fig. A.2d and Extended Data Fig. A.6). When self-coalescence is used to reconstitute reagents printed at any fixed point in that region, the Péclet number, Pé , associated with the flows depends on the local velocity above a reagent spot, which peaks linearly (Equation A.1) before decaying exponentially with time as the meniscus moves away (Equation A.2). Thus $\text{Pé} \equiv |V_{\text{far}}|H/D$, which approximates to $e^{-\pi Wt/\lambda W}$, making Taylor–Aris dispersion, whose magnitude scales roughly as Pé^2 , vanishingly small almost immediately after reagents have been wetted, and practically eliminating any form of convective reagent dispersion during reconstitution (Fig.

A.2b and Supplementary Video A.16).

There are numerous ways to implement SCMs in different materials—using, for example, silicon substrates and microfabrication or polymeric materials via hot embossing or injection moulding, and using different geometries such as depressed (trench-like) or protruding (rail-like) CPLs (Extended Data Fig. A.7). The material compatibility is further supported by the fact that the contact angle has only a mild influence on self-coalescence, and no influence at all on the exponential-decay length scale (section 3.6). Capillary pinning can also be achieved by patterning hydrophobic layers [292].

When performing chemistry at the microscale, it is a common requirement to use solutions that have a well defined composition and volumes that range from nanolitres up to a few microlitres. The volume of the SCM determines the maximum volume of the solution that can be prepared, and the amount of deposited reagent determines its resulting concentration, as demonstrated here with amaranth dye reconstitution in SCMs of different dimensions (Fig. A.3 and Extended Data Fig. A.8). We tested the stability of leading barriers using different channel geometries and filling conditions (Extended Data Fig. A.9). Modelling and experiments reveal simple rules of thumb for designing stable SCMs: wide SCMs are preferred over long SCMs that accumulate more hydraulic resistance during filling.

A.4 Reagent pulse shaping

The preparation of solutions with uniform concentration profiles is perhaps the greatest practical challenge solved by SCMs. In fact, any arbitrary concentration profile can be generated using one or several reagents and specific spotting patterns. However, a broadening of the initial reagent concentration profile is inevitable owing to Taylor–Aris dispersion once the solution sets in motion and exits the SCM (section A.9.2). The magnitude of the dispersion and the resulting concentration profile at time t and distance d from the diversion barrier can be computed exactly by convolving the spotted reagent profile with the Green’s functions that describe reagent profile evolution during SCM filling and reagent delivery (section A.9.3). The approach yields a powerful design tool, which we use for reagent pulse shaping under Taylor–Aris dispersion in a way that is conceptually analogous to optical amplitude pulse shaping in dispersive media [293], where the spatial frequency distribution of the input concentration signal replaces the frequency content of a light pulse, concentration replaces the pulse amplitude, and the dispersive channel acts as the dispersive optical medium (section A.9.4).

This modelling strategy for concentration pulse shaping allows us to define spotting patterns that will give specific concentration profiles of reconstituted amaranth and brilliant blue dye without

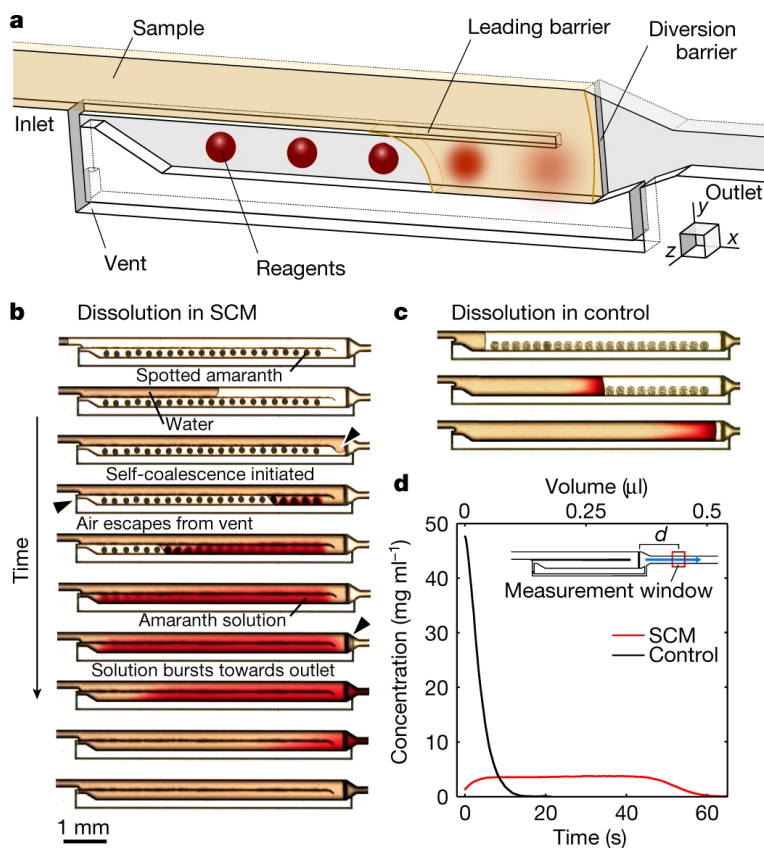


Figure A.2 SCM for reagent reconstitution. **a**, Illustration of the components forming a SCM and the locations of dried, spotted reagents. **b**, Time series of bright-field microscope images showing the reconstitution of amaranth in a SCM filled with water over the course of 75 s. **c**, Reconstitution of amaranth in a control experiment (with no self-coalescence) shows strong reagent accumulation. **d**, Mean concentration profiles of amaranth solutions using a 375-nL SCM (red, $n = 6$) and a 375-nL control microchannel (black, $n = 6$, $Q_{in} = 500$ nL/min). Inset, the amaranth concentration was measured at $d = 3$ mm downstream of the SCM outlet.

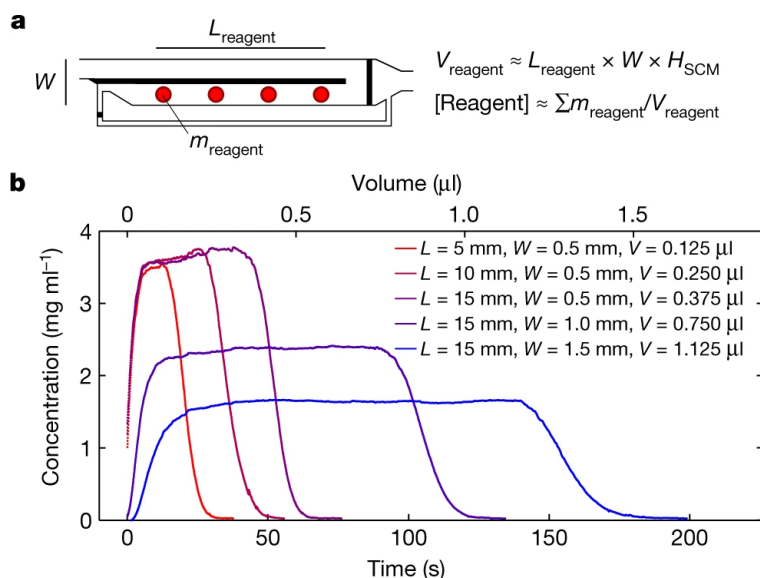


Figure A.3 Scalability of SCMs. **a**, The width (W) and depth (H_{SCM}) of a SCM and the length of the deposited reagent pattern (L_{reagent}) determine the volume in which a reagent reconstitutes (V_{reagent}). The final concentration of the reagent after reconstitution can simply be adjusted with the amount of deposited reagent (m_{reagent}). **b**, Mean concentration profiles ($n = 6$; measurement distance $d = 3 \text{ mm}$) of amaranth, reconstituted in SCMs with varied lateral dimensions ($H_{\text{SCM}} = 50 \mu\text{m}$ for all; $Q_{\text{in}} = 500 \text{ nL/min}$).

having to optimize the patterns empirically (Fig. A.4). We can readily release reagents consecutively with minimal intermixing (Fig. A.4a), achieve steady concentration ranges (Fig. A.4b), and merge reagents at preprogrammed distances downstream (Fig. A.4c). It is also possible to integrate two different reagents and release them downstream either sequentially with minimum dispersion (section A.9.5) and a separated profile (Fig. A.4d), or mixed with an intercalated profile (Fig. A.4e), or with a gradient/counter-gradient profile (Fig. A.4f), in close agreement with the theoretical predictions of our concentration pulse shaping model (Extended Data Fig. A.10 and section A.9.6).

A.5 Biochemical reactions in SCMs

SCM variants that have a modified vent to purge a surplus of liquid and no diversion barrier can maintain the distribution profiles of reconstituted reagents for long durations, with minimal diffusion effects. This allows several biochemical reactions to be run in spatially segregated regions inside single SCMs, akin to using individual wells in a microtitre plate to perform simultaneous experiments (Fig. A.5). We illustrate this with a multistep enzymatic assay that uses a fluorometric readout to quantify the activity of glucose-6-phosphate dehydrogenase (G6PDH) [294], with a

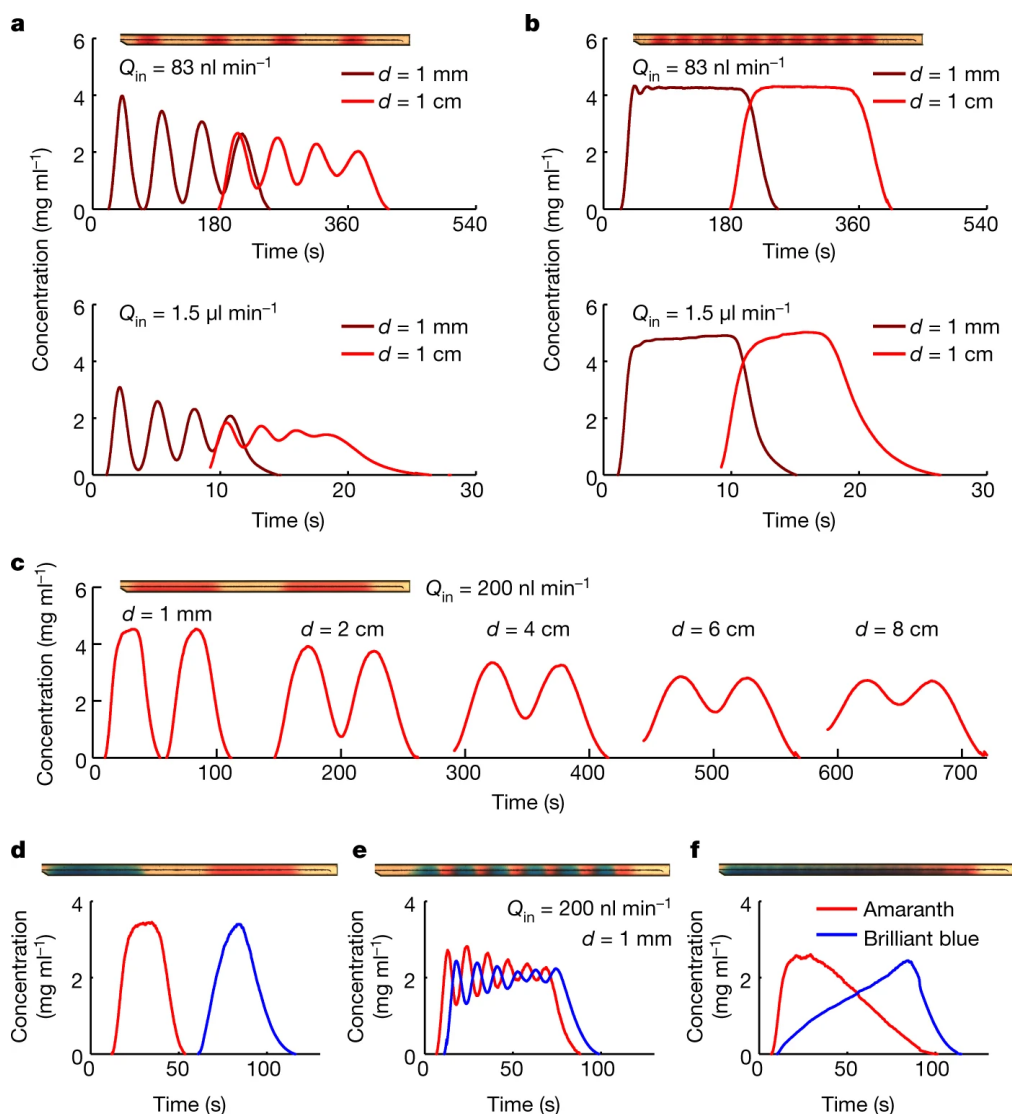


Figure A.4 Reagent pulse shaping and generation of complex concentration profiles. These mean concentration profiles of reconstituted reagent were obtained using various deposition patterns, flow rates, Q_{in} values and measurement distances, d ($n = 6$ for each plot). The experimental profiles (optical micrographs) above the plots were obtained before the liquids exited the SCM (13-mm long). **a**, Well separated reagent spots disperse and acquire a broader concentration profile as they travel in the SCM and the downstream channel, at both the optimal flow rate, 83 nL/min (top) and a fast flow rate, 1.5 μ L/min (bottom). **b**, Sufficiently dense spotting of reagents leads to homogenous concentration profiles. **c**, Evolution of the concentration domains of a reagent spotted at two main locations. **d–f**, Sequential delivery of two types of reagent, which were spotted such that they were well separated (**d**), co-homogenizing (**e**), or forming gradients (**f**).

glucose-6-phosphate (G6P) substrate, the co-factors nicotinamide adenine dinucleotide phosphate (NADP⁺) and magnesium (Mg²⁺), and a fluorescent reporter system that is based on the reduction of resazurin by diaphorase spotted in a first SCM (SCM 1) (Fig. A.5a; note that diaphorase is spotted separately from its substrates in order to avoid undesired enzymatic activity during storage of the SCM). When the carrier fluid is introduced, these reagents reconstitute homogeneously and proceed to the next SCM, where reaction kinetics (which depend on the G6PDH concentration) can be characterized using the fluorescence signal of resorufin. SCMs are also powerful tools for calibrating such an enzymatic reaction, where the ambient temperature, slight variations in the amount of deposited reagents, or the possible decay of reagents over time might alter the reaction kinetics. Such a calibration can be performed by spotting a gradient of G6PDH in SCM 2 and measuring the resulting kinetics (Fig. A.5a). The amount of deposited G6PDH and the maximum speed of the enzymatic reaction (Fig. A.5b) exhibit the expected linear relation, as shown by a calibration curve (Fig. A.5c, black). These calibration data match quantification data (Fig. A.5c, orange), which were obtained by loading a buffer spiked with various amounts of G6PDH into SCMs containing all other reagents. It was possible to measure in only 2 min as little as 0.75 $\mu\text{U}\mu\text{L}^{-1}$ of G6PDH—a concentration 130 times lower than the 10% activity cut-off used in clinical tests to diagnose inherited G6PDH deficiency [295], which affects 400 million people worldwide [296].

A.6 Conclusion

Self-coalescence is a very general concept and applicable to other biochemical assays. We use it here also to perform isothermal recombinase polymerase amplification (RPA) [297] for the detection of DNA sequences of human papilloma virus (HPV) types 16 and 18 (Fig. A.5d). For this implementation, the reaction master mix (containing enzymes, nucleotides, and so on) for RPA was deposited in SCM 1, and other reagents (primers, Mg²⁺ and SYBR Green dye) were deposited in SCM 2. The flow was paused for 3 min once SCM 1 was filled in order to allow complete reconstitution of the viscous RPA master mix. A self-timing SCM can also be used to delay the release of liquids (Extended Data Fig. A.11 and section A.9.3).

RPA is a more complicated chemical system than G6PDH quantification and requires finer optimization. For example, increasing the concentration of SYBR Green yields a better signal-to-noise ratio, but such intercalating dyes interfere with polymerase reactions and delay the onset of DNA amplification (Fig. A.5e and Extended Data Fig. A.12a). Similarly, amplification reactions accelerate with increasing Mg²⁺ concentration (Fig. A.5f and Extended Data Fig. A.12b), but too much Mg²⁺ can lead to unspecific amplification and high background noise owing to the formation of primer dimers. Reaction conditions can be readily mapped by spotting reagents in a SCM, as done here using step-function gradients of SYBR Green and Mg²⁺ (Fig. A.5d). A DNA concentration

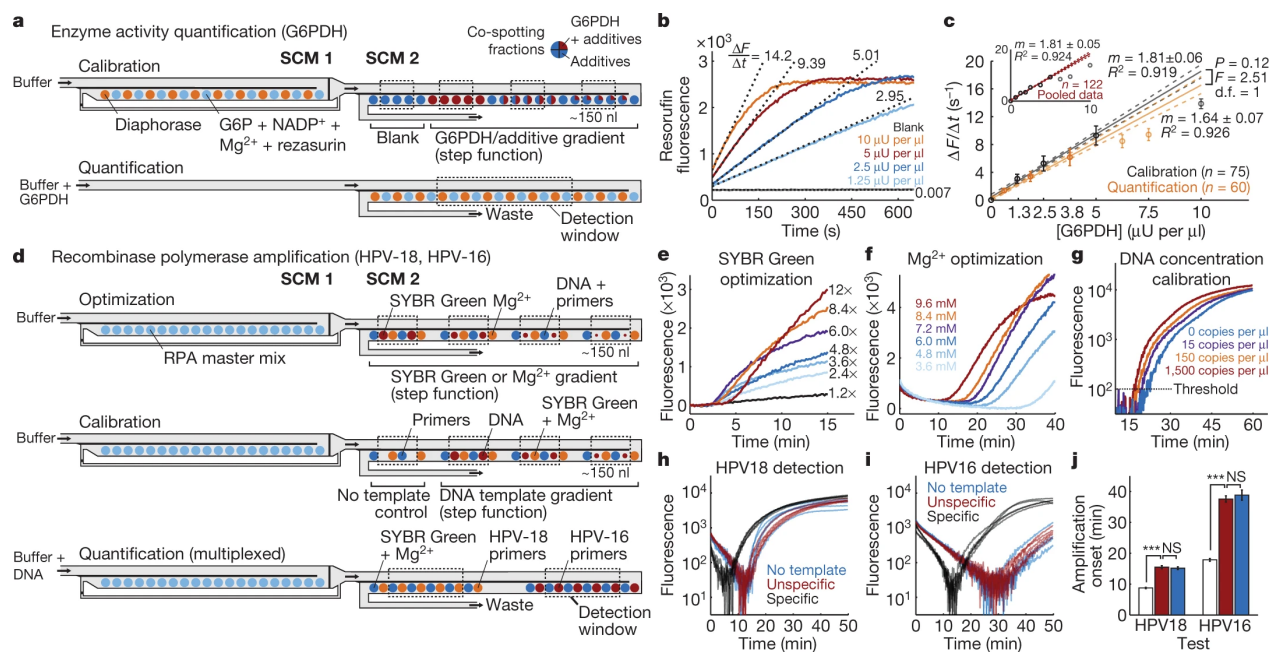


Figure A.5 Biochemical reactions in SCMs. **a**, Implementation of a fluorometric reaction for quantifying active G6PDH. To calibrate the reaction (top), all reagents except the G6PDH analyte are deposited alternatingly into SCM 1, where they reconstitute and homogenize in a buffer before filling SCM 2. SCM 2 contains a G6PDH gradient and a counter gradient of additives. To quantify active G6PDH in a buffer (bottom), only one SCM is used. Fluorescence signals are measured over separate detection windows (dashed rectangles). Extra buffer from SCM 1 is purged at the entrance of SCM 2 using a vent/waste channel. **b**, Calibration data from a single experiment, based on the highest rate of change in resorufin fluorescence ($\Delta F/\Delta t$; dashed lines) at different G6PDH concentrations (coloured lines). **c**, Data from calibration (black) and quantification assays (orange) show a linear relationship between $\Delta F/\Delta t$ and G6PDH for low concentrations, and a saturation profile for higher concentrations (faint data points, omitted from the regression analysis), as expected for such an enzyme-concentration activity curve. The calibration and assay data are not significantly different (n , number of data points; m , slope of fit; d.f., degrees of freedom; error bars, standard deviation; calibration, ten experiments or more; quantification, five experiments or more). The inset shows the regression analysis of calibration and assay data pooled together. **d**, Implementation of RPA using SCMs, where SCM 1 contains the RPA reaction master mix and SCM 2 contains the rest of the reagents. RPA reaction kinetics are characterized locally by measuring fluorescence over concentration gradients of SYBR Green, Mg²⁺ or DNA template. A multiplexed quantification of DNA concentration can be realized by depositing primers for different templates in separate areas of SCM 2. **e**, **f**, Optimization data from single experiments at different SYBR Green (**e**) and Mg²⁺ (**f**) concentrations, for amplifying ten copies per microlitre of HPV-18 DNA. **g**, DNA concentration calibration data from one experiment for HPV-18 DNA quantification (threshold, 100). **h**, **i**, Individual traces (based on five experiments) of fluorescence signals from the HPV-18 detection window (**h**) and the HPV-16 detection window (**i**) when the test was run with no template (blue), with 1,000 copies per microlitre of unmatched template (unspecific, red), or with 1,000 copies per microlitre of matching template (specific, black). **j**, Amplification onset times from different tests (white, specific; red, unspecific; blue, no template). *** $P < 0.001$; NS, not significant; error bars, standard error of the mean.

gradient in a SCM can also be used to calibrate the real-time RPA reaction for quantifying DNA (Fig. A.5g and Extended Data Fig. A.12c). Moreover, different sets of primers can be deposited at different locations of SCMs for multiplexed detection of multiple target sequences (Fig. A.5h, i) with high specificity and reproducibility (Fig. A.5j).

The minimal dispersion of reagents in SCMs enables the localization of neighbouring reactions without compartmentalization, so that complex biochemical reactions can be implemented in nanolitre volumes of liquids in a single or several combined SCMs. This capability should have far-reaching consequences for biological assays and diagnostics, but could also prove to be a game-changing technology for chemistry at the microscale, and have impacts on the synthesis and discovery of new materials and research in the life sciences.

A.7 Method

A.7.1 Chip fabrication and reagent deposition

Silicon wafers with a 600-nm thermally grown oxide layer were processed using standard photolithography and deep reactive-ion etching (DRIE) (Extended Data Fig. A.7a). Briefly, microchannels were patterned on the oxide layer using a 1.2- μm -thick AZ 6612 positive-tone photoresist and a glass/chromium photomask. Following a mild plasma cleaning to remove the photoresist residues and to activate the surface, the oxide layer was etched in buffered hydrofluoric acid (BHF). The photoresist was stripped in a plasma asher and a new layer of AZ 6612 photoresist was spin-coated and patterned to define CPL geometries. The silicon substrate was anisotropically etched for 30 μm using DRIE (Alcatel AMS 200). Following the removal of the photoresist layer, both microchannels and CPLs were etched for 50 μm using DRIE and the oxide layer as a hard mask. Subsequently, the oxide layer was removed in BHF and the wafer was diced. The quality of the fabrication was verified using scanning electron microscopy (Zeiss Leo 1550) and optical interferometry (Veeco Wyco NT1100).

We also fabricated SCMs in a polymeric photoresist (SU-8) as part of capillary-driven microfluidic chips, and designed SCMs with relaxed dimensions and rounded corners for fabrication using injection moulding. SCMs should also be compatible with other replication techniques involving polydimethylsiloxane (PDMS) moulding and hot embossing.

We prefer using narrow trenches (5- μm wide) to create leading barriers and a step down to create diversion barriers (Extended Data Fig. A.7b–f): this implementation has the advantage of not increasing the flow resistance over the CPL, is robust, and is easily fabricated in silicon channels of any thickness using standard lithography and DRIE (Extended Data Fig. A.7a). Notwithstanding, protruding leading barriers (that is, a rail-like geometry) provide better stability than trenches for the same SCM height, because the smaller liquid–vapour interface leads to a proportionally larger Laplace pinning pressure. The geometry of the diversion barrier is not critical as this barrier is challenged only when the SCM is completely filled. However, if the gap between the leading barrier and the diversion barrier is too narrow (for example, less than 200 μm in 50- μm -deep SCMs), it pins the liquid, which in turn increases the pressure on the barriers and can result in their failure.

The surface of the microfluidic chips was cleaned using an air plasma (for 2 min with a coil power of 200 W; Tepla 100-E). Within 10 min after cleaning, the chips were silanized by immersing them in a solution of 0.1% trichloro(octyl)silane (Sigma-Aldrich) in heptane (Sigma-Aldrich) for 2 min. After rinsing the chips with ethanol (Fluka) and drying them under a stream of nitrogen, solutions of erioglaucine disodium (Sigma-Aldrich, hereon referred to as brilliant blue) and amaranth (Sigma-Aldrich), each at 30 mg mL^{-1} in water, were deposited in microfluidic structures using an inkjet

spotter (Nano-Plotter 2.1, Gesim GmbH) equipped with a PicoTip-A piezoelectric pipette (Gesim GmbH). First, the reagents were spotted in two alignment marks (one visible in Extended Data Fig. A.8) located at opposite sides of the chips. The difference between the programmed spotting coordinates and the effective location of spots was used to eliminate any misalignment. After spotting specific patterns of reagents on microfluidic chips, the chips were sealed with 3-mm-thick slabs of PDMS (Dow Corning Sylgard 184). The volume of jetted droplets was measured by depositing 1,000 droplets of amaranth or brilliant blue solution at a spot on a clean surface, letting the spot dry, reconstituting the spot in 1 μL of water and measuring the concentration of the reconstitution with a spectrophotometer (Tecan Infinite M200). The volume of the droplets varied slightly from 40 pL to 60 pL between different spotting sessions, but was stable within the same session. The amount of deposited reagents was calibrated according to the droplet volume.

The patterns of reagents spotted in SCMs or control channels are detailed below. In experiments in which the dissolution in a SCM was compared with the dissolution in a control channel (Fig. A.2d) and in volume scaling experiments (Fig. A.3b), 5- to 15-mm-long lines comprising 25-ng spots (250- μm pitch) of amaranth were spotted. In experiments in which reagent pulse shaping was evaluated by using the amaranth dye (Fig. A.4a–c), either four 100-ng spots (3-mm pitch; Fig. A.4a), ten 100-ng spots (1-mm pitch; Fig. A.4b) or two 3-mm-long lines comprising 25-ng spots (250- μm pitch) were spotted with 3-mm separation between the lines (Fig. A.4c). In experiments in which the sequential delivery of multiple reagents was demonstrated (Fig. A.4d), one 3-mm-long line comprising 15-ng spots (250- μm pitch) of amaranth and another one of brilliant blue were spotted with 3-mm separation between the lines. In experiments in which in situ mixing of multiple reagents was demonstrated (Fig. A.4e), six 15-ng spots (1.5-mm pitch) of amaranth intercalated with six 15-ng spots (1.5-mm pitch) of brilliant blue were spotted. In experiments in which concentration gradients were generated (Fig. A.4f), 30 spots (300- μm pitch) of amaranth gradually decreasing in mass from 15 ng to 0 ng were spotted over 30 spots (300- μm pitch) of brilliant blue gradually increasing in mass from 0 ng to 15 ng.

In the chips in which reagent pulse shaping was evaluated (Extended Data Fig. A.13a), a narrow loop geometry [298] was used to minimize the effect of the turn on dispersion.

A.7.2 Particle image velocimetry

SCMs with a length of 15 mm, a width of 0.5 mm, a depth of 50 μm , and 5- μm -wide trenches were filled at a constant flow rate (active pumping, Kent Scientific Genie syringe pump, 0.5 $\mu\text{L}/\text{min}$) with a 10 $\mu\text{L}/\text{min}$ fluorescein sodium (Fluka) aqueous solution containing 0.02% fluorescent microspheres (size 4.8 μm ; Thermo-Scientific Fluoro-Max). The filling was imaged using a fluorescence microscope (Nikon Eclipse 90i, Nikon DS-1QM/H) at a rate of 15 frames per second (fps),

with a 60-ms exposure per frame. The displacement of particles crossing the leading barrier during the 60-ms exposure was measured manually in each frame from the particle streaks on the images. These measurements were used to calculate the velocity of the particles. The position of the measured particles was determined from the midpoint of the streaks. In order to display the velocity streamlines as in Fig. A.1b, 15 subsequent frames were aligned (taking the position of the curved meniscus as reference) in an image stack, the maximum projection of the image stack was taken, and the projected image was inverted. For this, images of the particles that sediment during longitudinal flow were manually removed from each frame for visual clarity. Fiji [299] was used for data extraction and image processing.

A.7.3 Optical measurements of reagent reconstitution

Microfluidic chips having SCMs or control microchannels spotted with reagents were placed under a stereo microscope (Leica MX16). The optical zoom, lighting intensity, and colour and exposure settings of the RGB CMOS camera (Leica MC170 HD) were identical for all experiments. Before the start of the experiments, the roll and the pitch of the microfluidic chips were corrected with a custom tiltable XY stage. A syringe pump (Kent Scientific Genie) was connected to the microfluidic chips with 1/32-inch tubing (Extended Data Fig. A.14a). Before each experiment, the rate of pumping was calibrated. During the experiments, microfluidic chips were filled with water at a constant flow rate (indicated by Q_{in} for different sets of experiments). Videos (30 fps, $1,280 \times 720$ pixels) of the liquid carrying reconstituted reagents were recorded at fixed locations. Acquisition was stopped when the reagent solution was completely flushed away from the imaging area.

Video files were processed to extract the absorbance of solutions. This was done by defining a region of interest (ROI) on each video, centred on the downstream microchannel at a fixed distance (indicated by d for different sets of experiments) away from the diversion barrier. The ROIs were 200- μm wide and covered the width of the microchannel (180–500 μm). The mean intensity value over time of individual video channels was extracted from the area defined by the ROIs. For experiments with only amaranth dye, the intensity values from the green channel were used for further analysis; for experiments with amaranth and brilliant blue dyes, the intensity values from the red and blue channels were used. The absorbance signal was calculated by taking the negative logarithm of the quotient of the intensity values over the mean value of signal coming only from water.

The absorbance signal was converted into concentration values using calibration curves taken for different sets of experiments. For this, solutions of dyes with known concentrations were filled into the microfluidic chips and the intensity values were processed as described above. The exponential fit to the calibration data was used to transform the absorbance values to concentration values

(Extended Data Fig. A.6c, d). For experiments in which both amaranth and brilliant blue dyes were used, the calibration curves and the absorbance data were used after linear spectral unmixing [300] (Extended Data Fig. A.13b–e). Matlab was used for these analyses.

A.7.4 General preparation for biochemical reactions in SCMs

To implement biochemical reactions using SCMs (Fig. A.5), we fabricated microfluidic chips containing SCMs with protruding CPLs (that is, rails instead of trenches) in silicon and silanized them as above. These chips had a channel depth of 100 μm and 40- μm -high rails (Extended Data Fig. A.7g, h). The reagents were deposited inside SCMs using the inkjet spotter equipped with a NanoTip piezoelectric pipette (GeSiM GmbH). The droplet volume for each reagent solution was characterized as above. After deposition of reagents, the chips were sealed using a PDMS that had been passivated by exposure to a 0.2% bovine serum albumin (BSA, Sigma-Aldrich) solution in 50 mM Tris-HCl (pH 7.5) for 10 min.

A.7.5 Spotting scheme for G6PDH reactions

To quantify G6PDH activity (Fig. A.5a–c), we adapted a fluorometric protocol [294] for implementation inside SCMs.

All solutions were prepared in a 20 mM Tris-HCl (pH 7.8) buffer (Fluka) containing 0.2% BSA additive. Solutions containing diaphorase and G6PDH also contained 3% trehalose (Fluka) and 1 mM tris(2-carboxyethyl)phosphine (TCEP; Thermo Scientific).

In the calibration configuration, SCM 1 (width 0.5 mm, length 33 mm, rail width 30 μm ; Extended Data Fig. A.7g) was patterned using two solutions. The first solution contained 0.1 $\text{U}\mu\text{L}^{-1}$ diaphorase (Sigma-Aldrich) and was deposited as discrete spots over a distance of 30 mm with a 1-mm pitch. Each spot was formed using four inkjet-deposited droplets (with a total volume of roughly 2.5 nl). The second solution contained the substrates and co-factors, namely 200 mM MgCl_2 (Sigma-Aldrich), 40 mM G6P (Sigma-Aldrich), 2 mM NADP^+ (Sigma-Aldrich) and 0.2 mM rezasurin (Sigma-Aldrich). The substrate solution was also deposited using a 1-mm pitch along 30 mm, but with a 0.5-mm shift relative to the diaphorase spots, and with each spot formed using eight dispensed droplets (approximately 4.5 nl).

SCM 2 (width 0.5 mm, length 30 mm) was patterned so as to have three regions with different G6PDH concentrations and one region without any G6PDH for blank measurements. Each region consisted of 5-mm-long lines of spots with a 0.5-mm pitch, and was separated from another region by 2 mm. In different experiment sets, either one (585 pL), two or four droplets of solution containing 0.52×10^{-4} $\text{U}\mu\text{L}^{-1}$ G6PDH (Sigma-Aldrich), or two, four or eight droplets of the same

solution, were deposited to form regions with increasing G6PDH concentration. In order to achieve comparable reaction kinetics from different regions, we needed to compensate for additives in the G6PDH solution that were also deposited at different amounts. This was achieved by spotting a solution containing only the additives over the spots of G6PDH to adjust the total deposited amount per spot to four or eight droplets.

In the quantification configuration, we used only SCM 2, and patterned it identically to SCM 1 in the calibration configuration.

A.7.6 Spotting scheme for recombinase polymerase amplification

We implemented isothermal recombinase polymerase DNA amplification [297] (RPA) using SCMs (Fig. A.5d–j and Extended Data Fig. A.12a–c) by adapting and applying the reagents from a commercially available kit (TwistDx TwistAmp Basic). Quantitative synthetic HPV-18 DNA (ATCC VR-3241SD) and quantitative synthetic HPV-16 DNA (ATCC VR-3240SD) were purchased and used in the amplification reactions as the template. Primer sequences were taken from the literature [301] and the primers were purchased (Integrated DNA Technologies). The following primers were used in the experiments (5'-3'):

HPV-16 forward: TTGTTGGGGTAACCAACTATTTGTTACTGTT

HPV-16 reverse: CCTCCCATGTCTGAGGTACTCCTTAAAG

HPV-18 forward: GCATAATCAATTATTTGTTACTGTGGTAGATACCACT

HPV-18 reverse: GCTATACTGCTTAAATTTGGTAGCATCATATTGC

In all experiments, SCM 1 (width 1 mm, length 28 mm, rail width 75 μm , rail split with a 15- μm -wide trench; Extended Data Fig. A.7h) was patterned with the 2 \times RPA master mix, prepared by reconstituting the pellet from the kit in 1 mM TCEP solution. The RPA master mix was deposited along a 25-mm line of spots, with a 1-mm pitch, and with each spot formed using 100 droplets (approximately 50 nl).

SCM 2 (width 0.5 mm, length 30 mm) was patterned with all other reagents necessary for the RPA reaction. For optimization of the SYBR Green concentration, a DNA-Mg mix consisting of 100 copies per microlitre of HPV-18 DNA, 140 mM magnesium acetate (MgOAc; Fluka), 5 μM of each HPV-18 primer, 3% trehalose and 0.2% BSA was deposited as a 28-mm line of spots with a 0.5-mm pitch, and with each spot formed using five droplets (approximately 3 nl). Over these spots, a step-function-like gradient of SYBR Green was created by depositing a 50 \times SYBR Green (Invitrogen) solution containing 0.2% BSA along 4-mm segments having a 0.5-mm pitch, with the segments formed either with one (roughly 600 pl), two, three, four, five, seven or ten droplets,

without additional spacing between segments.

For optimization of the Mg^{2+} concentration, a 24-mm line of spots of DNA solution, containing 250 copies per microlitre of HPV-18 DNA, 12.5 μ m of each HPV-18 primer and 3% trehalose, was patterned in SCM 2 with a 0.5-mm-pitch and with each spot formed by two droplets (approximately 1.2 nl). A similar second line, which was formed using spots (two droplets, approximately 1.2 nl) of 125 \times SYBR Green, 75 mM MgOAc, 3% trehalose and 0.2% BSA, was patterned with a 0.25-mm shift from the first line. Over the second line, a step-function-like gradient of Mg^{2+} was formed by depositing 50 mM MgOAc solution on 4-mm segments having a 0.5-mm pitch, and with the segments formed either by zero, one (roughly 600 pl), two, three, four or five droplets, and no additional spacing between segments.

For calibration of DNA concentration to amplification onset time, two 18-mm lines each with a 0.5-mm pitch and spots of two droplets (roughly 1.2 nl) were patterned with a 0.25-mm offset between them. The first line consisted of spots of 125 \times SYBR Green, 95 mM MgOAc, 3% trehalose and 0.2% BSA. The second line consisted of spots of 95 mM MgOAc, 8.4 μ m of each HPV-18 primer and 3% trehalose. Over the second line, a step-function-like gradient of HPV-18 DNA was patterned by depositing two droplets (roughly 1.2 nl) of DNA solution containing 3% trehalose along 4-mm segments with a 0.5-mm pitch, with the segments spotted from different DNA solutions having 250, 2,500 or 25,000 copies per microlitre of HPV-18 DNA. No calibration was performed for HPV-16.

For multiplexed detection of HPV-16 and HPV-18 DNA, SCM 2 was patterned similarly to the spotting scheme for DNA calibration, but without any DNA spotted. Additionally, one half of SCM 2 was patterned using HPV-16 primers and the other half using HPV-18 primers.

A.7.7 Biochemical reactions in SCMs, data acquisition and analysis

To start the biochemical reactions, spotted and sealed chips were filled only with buffer, or with buffer containing G6PDH or DNA under active pumping at varied flow rates and at room temperature (Extended Data Fig. A.14a). Each chip carried elements for five experiments. Experiments were run one after another. In all experiments, SCM 1 was filled at a rate of 1.0 μ L/min, and SCM 2 at 0.5 μ L/min during longitudinal flow and 3.5 μ L/min during self-coalescing flow. For RPA reactions, the flow was paused for 3 min after SCM 1 was filled for the rehydration and reconstitution of the RPA master mix.

For calibration of the G6PDH reaction, the chips were filled with 50 mM Tris-HCl (pH 7.8) solution. For G6PDH quantification experiments, chips were manually filled using a micropipette (Extended Data Fig. A.14b) with 50 mM Tris-HCl (pH 7.8) solutions containing 0.625–7.5 μ U μ L⁻¹

G6PDH, 0.2 mM TCEP, 0.6% trehalose and 0.04% BSA.

For calibration of the RPA reaction and for optimization of SYBR Green and MgOAc concentrations, the chips were filled with 25 mM Tris-HCl (pH 7.9) solution containing 100 mM potassium acetate (Sigma-Aldrich), 5.4% polyethylene glycol (molecular weight 35 kDa; Sigma-Aldrich) and 0.05% Tween-20 (Fluka). For the multiplexed detection of HPV-16 and HPV-18, the chips were filled with the same solution additionally containing 1,000 copies per microlitre of HPV-16 or HPV-18 DNA.

After the chips were filled, they were swiftly transferred to a microtitre plate reader (Tecan Infinite M200) using a custom-made aluminium adaptor (Extended Data Fig. A.14c). While the reactions ran, the reader scanned along SCM 2 and measured the fluorescence signal every millimetre. G6PDH reactions were run at 25 °C. The conversion of rezasurin to resorufin was measured at 560-nm excitation and 595-nm emission using a sampling time interval of 5 s. RPA reactions were run at 33-36 °C. SYBR Green fluorescence was measured using 490-nm excitation and 525-nm emission wavelengths every 10 s. Subsequent analyses were run only on the measurements taken at detection windows (roughly 150 nL, determined by the point spread function of the excitation beam of the plate reader; full width at half maximum roughly 3 mm as measured), centred over regions with different concentrations of G6PDH, SYBR Green, Mg²⁺ or DNA (for optimization and calibration), or at detection windows centred over regions with G6PDH assay reagents or primers (for quantification).

The kinetics of the G6PDH reaction was characterized from the fastest rate of fluorescence change ($\Delta F/\Delta t$) for each reaction at different G6PDH concentrations [302]. The quality of the calibration curve was assessed using linear regression (LinearModel class in Matlab). To evaluate whether calibration and quantification experiments agreed, we applied analysis of covariance (ANCOVA; 'aoctool' function in Matlab).

The amplification onset of RPA reactions was extracted first by subtracting the background from the signal and later by applying a threshold to the logarithm of the data. The quality of the calibration curve was assessed using linear regression (LinearModel class in Matlab). To test whether detection of HPV-16 or HPV-18 DNA produced signals with significantly earlier onset times than unspecific amplification, we applied a two-sample t-test ('ttest2' function in Matlab).

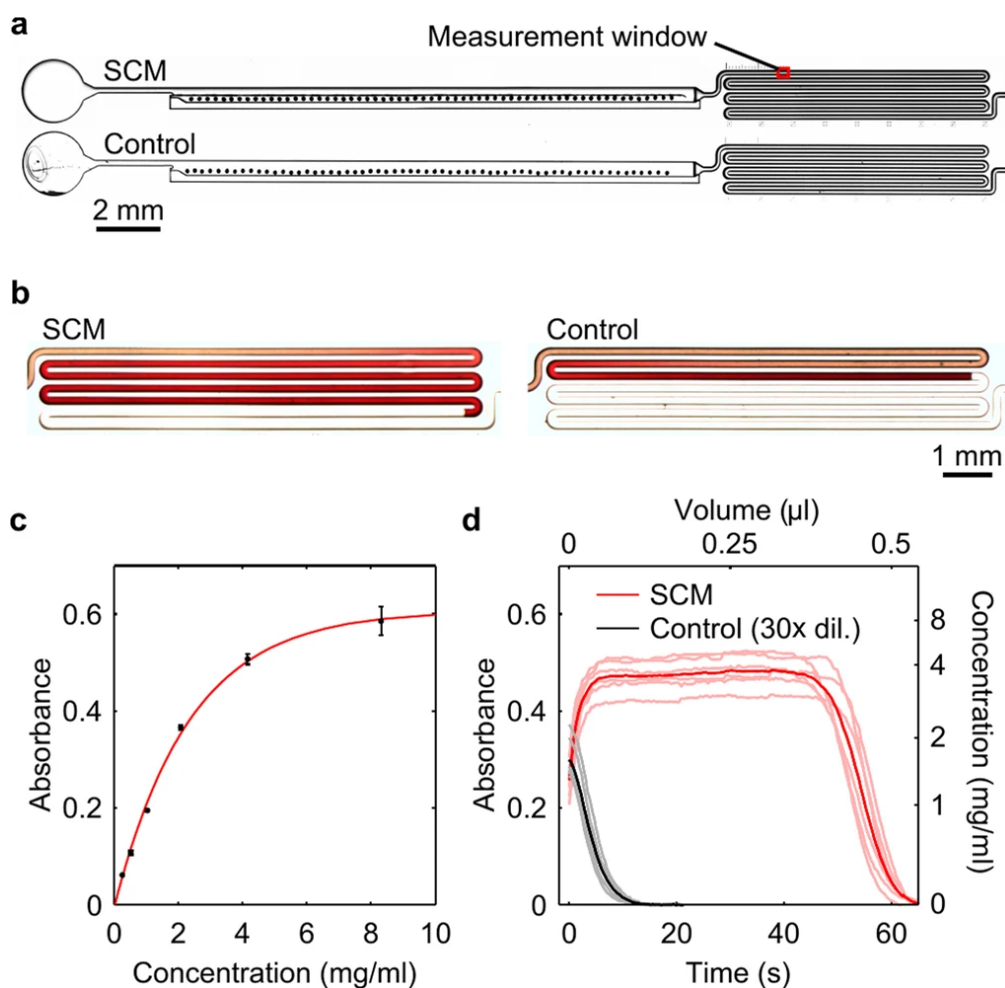


Figure A.6 Characterization of reagent dissolution in SCMs and control experiments. **a**, Bright-field microscope images of microfluidic chips in silicon, each chip being composed of a rounded inlet (left), a SCM (middle), and a meandering channel (right) used for conveniently measuring the concentration profile of the solution exiting the SCM. **b**, Amaranth solutions from a SCM (left) and in a control microchannel (right) are readily visualized using the meandering channels. **c**, Calibration curve for quantification of the concentration of reconstituted amaranth ($n = 4$ for each concentration). Error bars represent standard error of the mean. **d**, Concentration profiles of amaranth solution reconstituted in SCMs or control microchannels ($Q_{in} = 500$ nL/min). Means of individual acquisitions are displayed with dark coloured lines and individual acquisitions with a lighter shading. Amaranth solution was inkjet spotted into SCMs at 100 ng mm^{-1} ($250\text{-}\mu\text{m}$ pitch). The reagent accumulation in the control was so strong that the amaranth solution was diluted $\times 30$ before deposition to keep the absorbance signal in the dynamic range of the camera. The concentration profile from control experiments shown in Fig. A.2d is scaled up from this diluted signal.

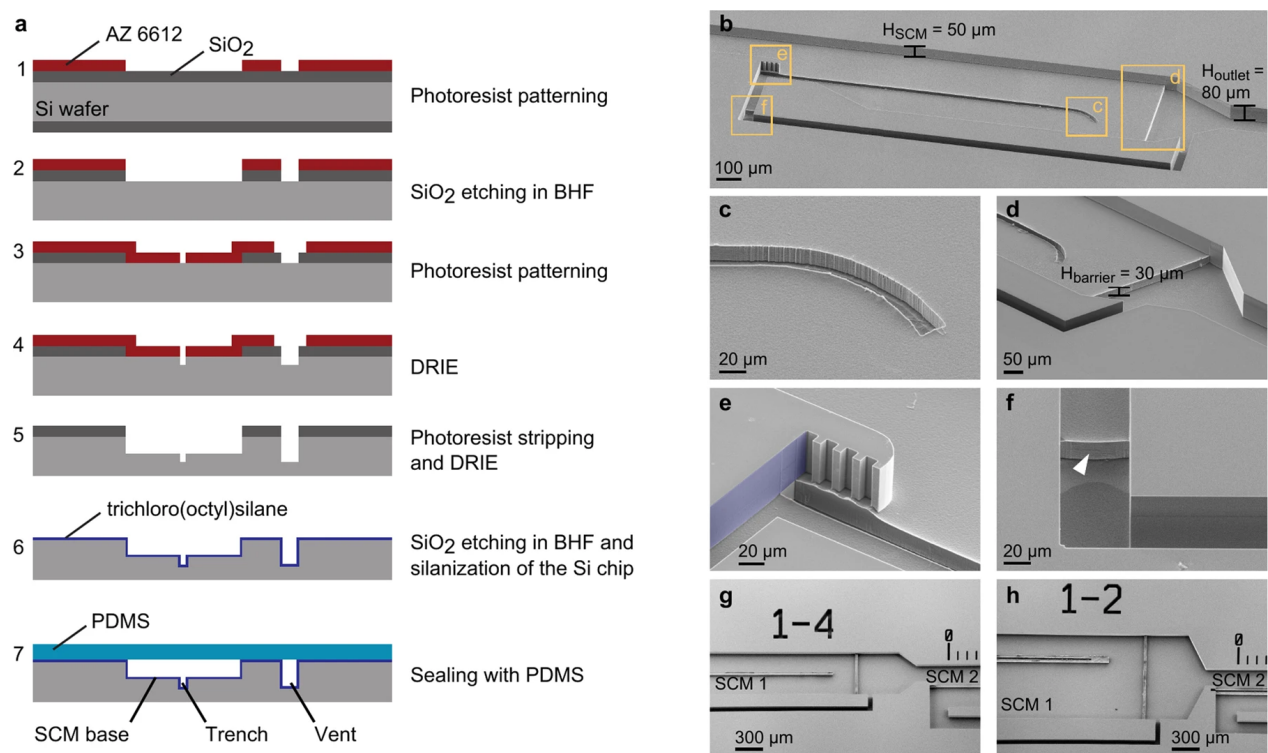


Figure A.7 Fabrication steps for SCMs with depressed barriers, and scanning electron microscopy images of representative SCMs. **a**, Silicon wafers are processed by standard photolithography and multiple steps of deep reactive-ion etching (DRIE). Specifically, a 1.2- μm -thick AZ 6612 photoresist layer is patterned (step 1) to mask the SiO_2 layer during etching in buffered hydrofluoric acid (BHF; step 2). A new layer of AZ 6621 is patterned (step 3), exposing the areas that are etched to form the trenches during the first DRIE step (step 4). Later, using the patterned SiO_2 layer as the mask, a second DRIE step forms the microchannels while preserving the trenches (step 5). After dicing, the chips are cleaned and silanized in trichloro(octyl)silane solution (step 6). After reagent deposition, chips are sealed with a layer of polydimethylsiloxane (PDMS; step 7). **b**, Image of a SCM fabricated in silicon, with yellow frames highlighting particular regions shown below. **c**, The leading barrier with a trench geometry. Here, for visual clarity, the trench width is 20 μm , but 5- μm -wide trenches were used in experiments. The curved end of the leading barrier facilitates the initiation of self-coalescing flow. **d**, Diversion barrier with a step-down geometry. **e**, Raised vertical CPLs at the entrance of the SCM help to keep the meniscus away from the side wall coloured in blue. **f**, The barrier at the vent entrance (arrowhead) ensures that liquid does not enter the vent. The depths of the SCM (H_{SCM}), outlet (H_{outlet}) and barriers (H_{barrier}) are shown on the images. **g**, **h**, Scanning electron microscopy (SEM) images of the devices used in G6PDH reactions (**g**) and in RPA reactions (**h**). (The numbers 1-2 and 1-4 are device numbers.).

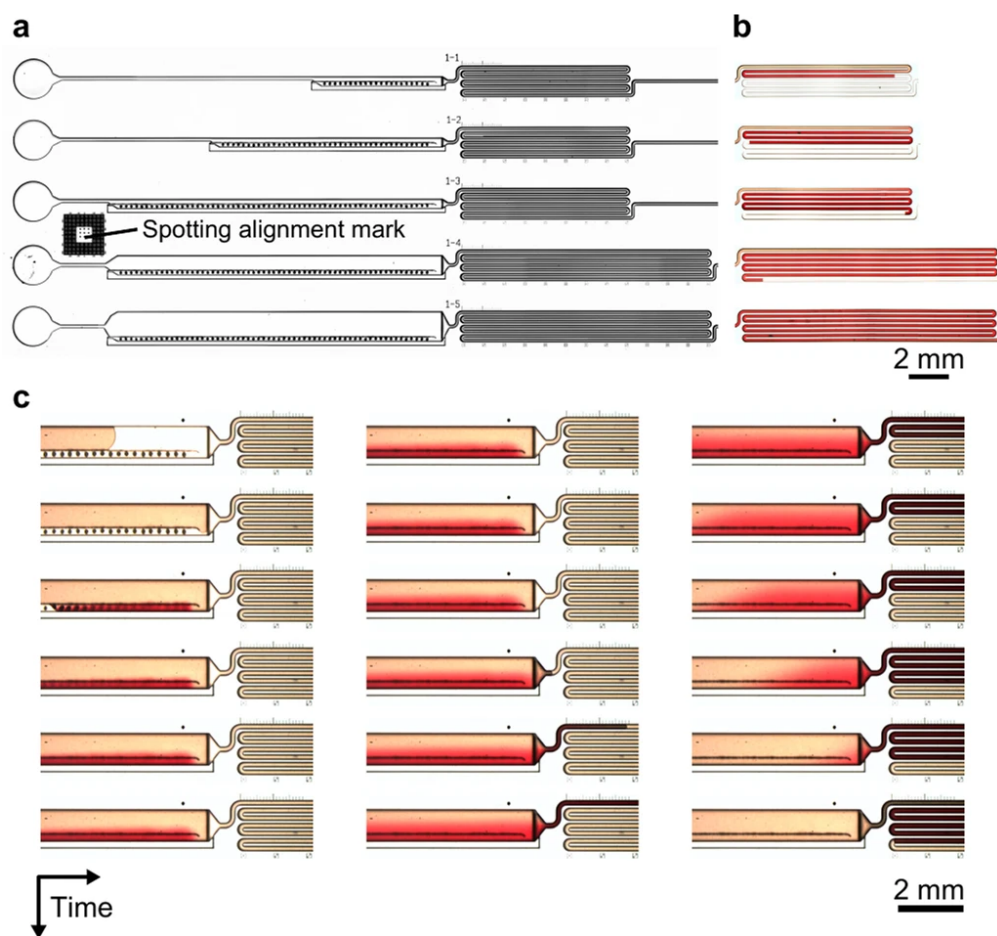


Figure A.8 SCM volume scaling experiments. **a**, Bright-field microscope images of devices fabricated in silicon (numbered 1-1 to 1-5) in which volume scaling experiments were performed. As discussed in Fig. A.1d, the velocity of the self-coalescing flow decays more quickly in narrower than in wider SCMs. In order to maintain a quick decay of the self-coalescing flow velocity in wide SCMs, the leading barrier is simply shifted towards the area in which reagents are deposited. Amaranth is deposited at 100 ng mm^{-1} ($250\text{-}\mu\text{m}$ pitch). A spotting alignment mark is used to align the inkjet spotter head with the microfluidic chips for precise targeting of the deposition location. **b**, Bright-field microscope images showing the amaranth solution in the meandering channels, reconstituted in the SCMs shown in panel **a**. **c**, Time series of bright-field microscope images showing the reconstitution of amaranth in a 1-mm-wide SCM ($Q_{\text{in}} = 500 \text{ nL/min}$). Typically, in wide SCMs (wider than 0.5 mm), lateral homogenization of the reconstituted reagent is complete at the narrow outlet of the SCM (as seen here), and can be enhanced, if necessary, by adding a Dean vortex mixer, a chaotic mixer, or a simple meandering channel. Larger volumes of solution with reconstituted reagents can also be achieved using an array of parallel SCMs. SCMs are easily scaled; however, making them longer decreases the maximum filling flow rate because the pressure at the inlet needs to be lower than the Laplace pressure over the CPL.

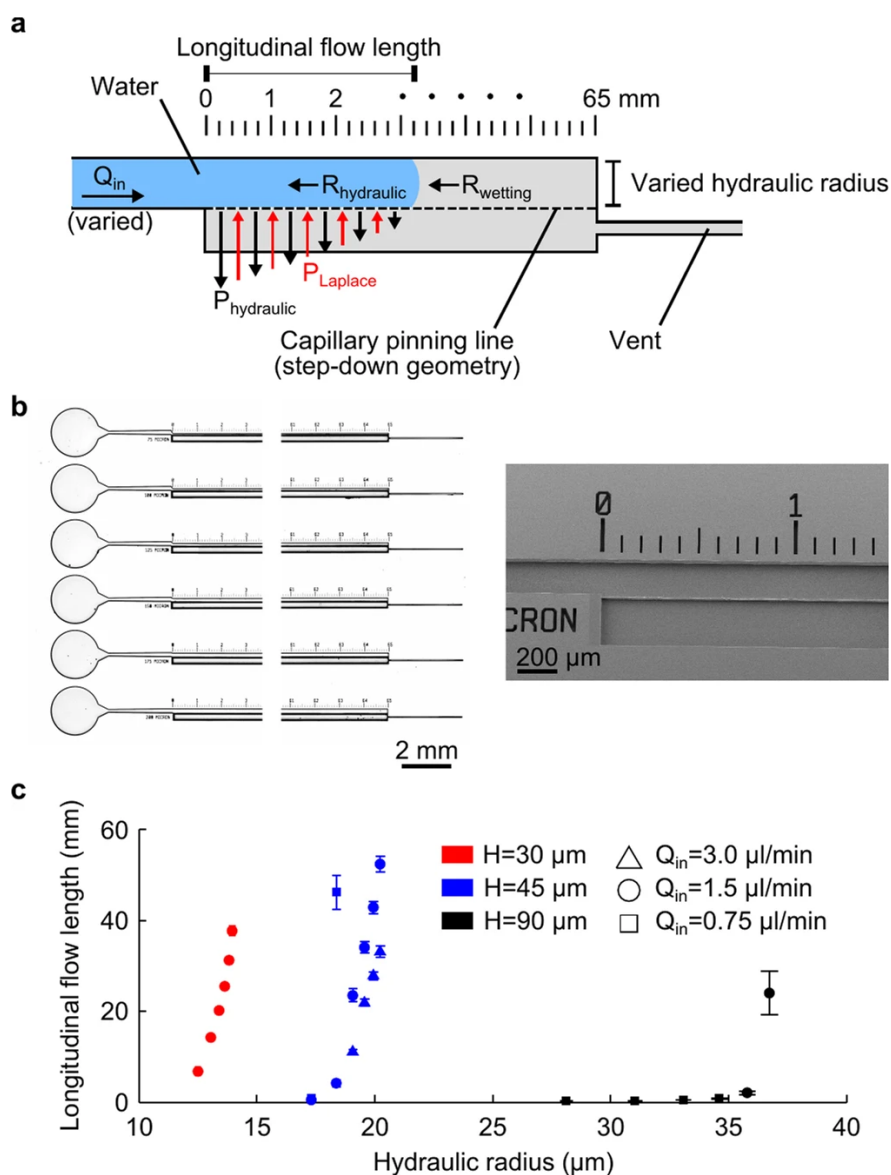


Figure A.9 Assessment of the stability of the leading barrier. **a**, During longitudinal flow, the hydraulic pressure ($P_{hydraulic}$) increases as the hydraulic resistance ($R_{hydraulic}$) increases with the distance travelled by the liquid. The leading barrier is able to preserve the longitudinal flow as long as the pinning forces ($P_{Laplace}$) can balance the increasing hydraulic pressure and the pressure exerted by the resistance to wetting ($R_{wetting}$). In order to investigate this effect, the width ($W = 75, 100, 125, 150, 175$ or $200 \mu\text{m}$) and the height ($H = 30, 45$ or $90 \mu\text{m}$) of the longitudinal flow area and the filling flow rate ($Q_{in} = 0.75, 1.5$ or $3.0 \mu\text{L}/\text{min}$) were varied. During experiments, the maximum distance along which the liquid remains pinned was measured. **b**, Bright-field (left) and SEM (right) images of devices in which stability-assessment experiments are performed. **c**, Experimental data support theoretical predictions that: first, a smaller liquid–vapour interface can bear a higher hydraulic pressure; second, the hydraulic radius of the longitudinal flow area needs to be large in order to fill deeper structures or for high filling flow rates; and third, the flow rate challenges the stability of the leading barrier. Data points are means of experiments ($n = 8$ or more; error bars represent standard error of the mean). Conditions in which the liquid was not pinned at the CPL (longitudinal flow length = 0 mm) or the liquid travelled to the end of the test device (longitudinal flow length = 65 mm) are excluded from the plot.

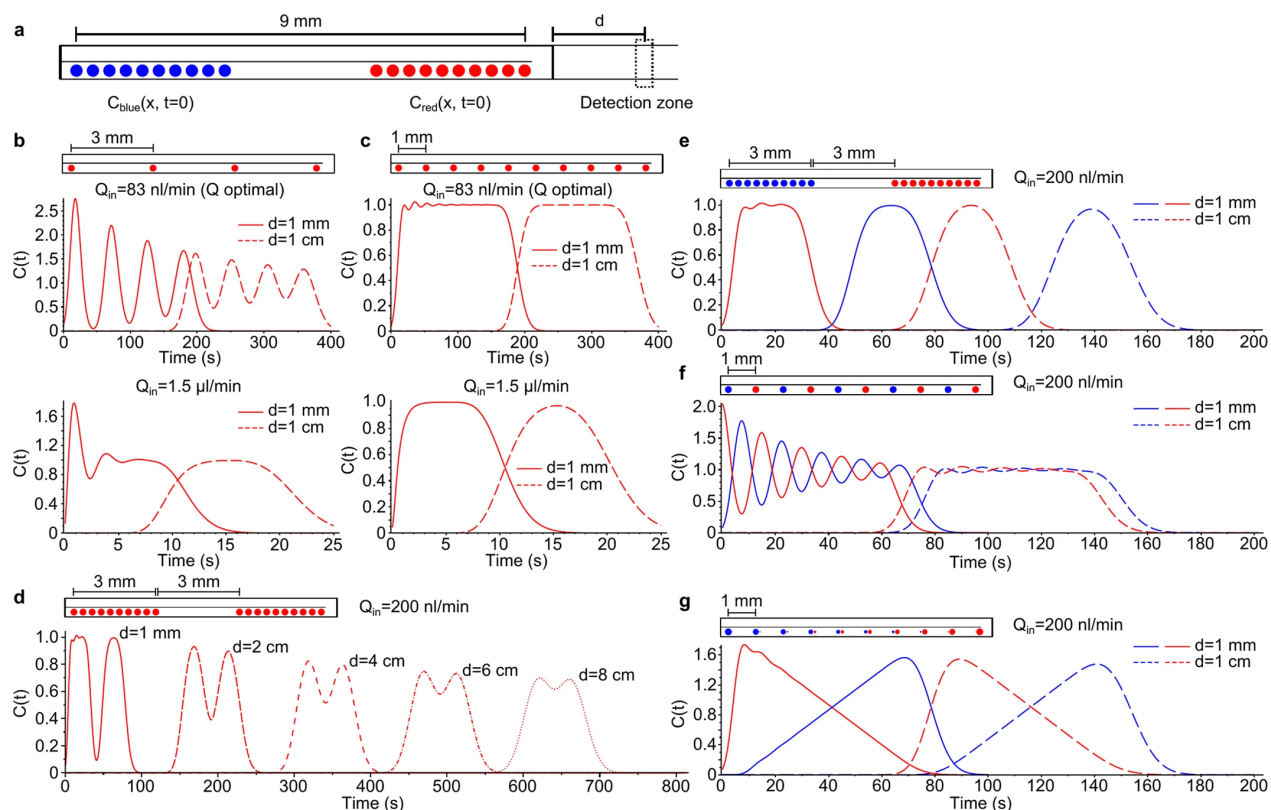


Figure A.10 Predicted complex concentration profiles from diffusion–dispersion models. **a**, Illustration of the experimental method for analysing dispersion in SCMs and in downstream channels at distance d . C , concentration. **b–g**, Predicted concentration profiles for experiments shown in Fig. A.4 ($C(t)$ in arbitrary units). **b**, **c**, Results of controlling the spotting pitch to generate spiked (**b**) or flat (**c**) concentration pulses at optimal ($Pé = 5.6$; top panels) and large ($Pé = 100$; lower panels) Péclet numbers, at constant spotted reagent mass. **d**, Signal decorrelation over time due to Taylor–Aris dispersion for several positions of the detection zone ($Pé = 13$). **e**, Pulsing of two spatially resolved different reagents ($Pé = 13$). **f**, Pulsing of a flat profile of two mixed reagents by alternated spotting and flow control ($Pé = 13$). **g**, Pulsing of two linear concentration gradients to a detection zone ($Pé = 13$).

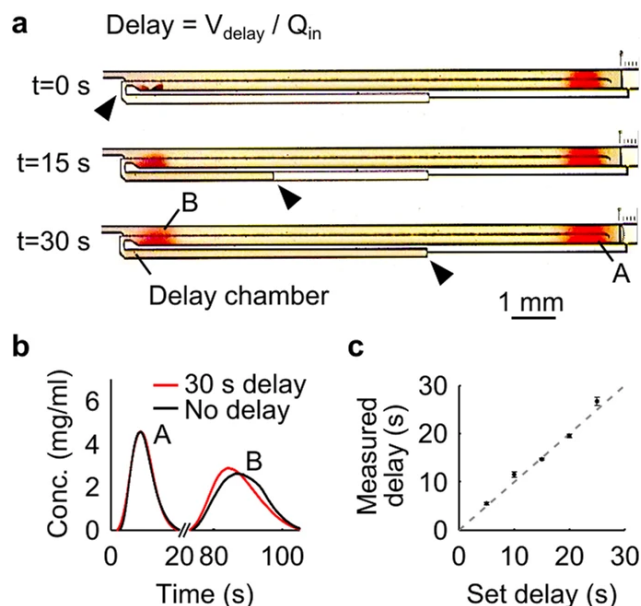


Figure A.11 Release of reconstituted reagents from a SCM with time delays. A chamber of volume V_{delay} at the entrance of the vent adds a delay before a liquid leaves the SCM. **a**, Time series of images showing filling of the delay chamber while reconstituted amaranth diffuses. Reagents in area A, but not in area B, have additional time to reconstitute/diffuse while the rest of the SCM fills ($t = 0$ s). If needed, using a delay chamber gives additional time for the reconstitution/diffusion of the B reagents. Arrowheads mark the liquid filling front in the delay chamber. **b**, Effect of delay on the concentration profile of points A and B. Without any delay, point B disperses more than it does with a delay, and its profile is broader ($n = 9$; $Q_{\text{in}} = 200$ nL/min). **c**, Measured delay provided by different delay chambers. The dashed line is the identity line; error bars represent standard error of the mean; $n = 6$; $Q_{\text{in}} = 200$ nL/min.

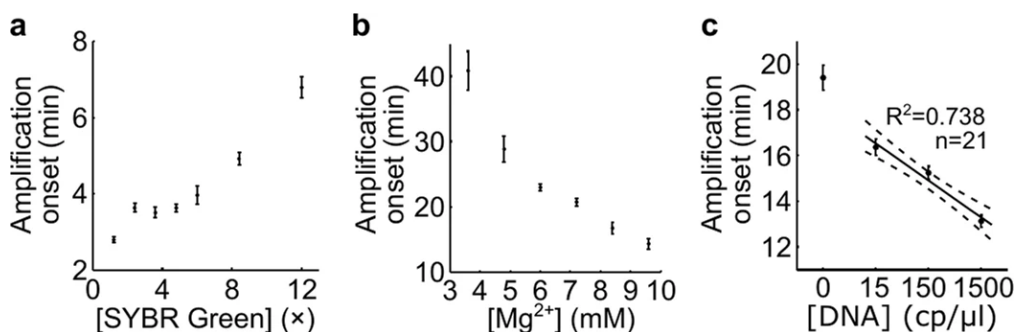


Figure A.12 Optimization and calibration of RPA reactions in SCMs. **a**, **b**, Optimization data for SYBR Green concentration (**a**; four experiments) and Mg^{2+} concentration (**b**; five experiments) for amplification of ten copies per microlitre of HPV-18 DNA. **c**, DNA concentration calibration (seven experiments) for HPV-18 DNA quantification. Plots show amplification onset time extracted from SYBR Green fluorescence signals. Error bars represent standard errors of the mean.

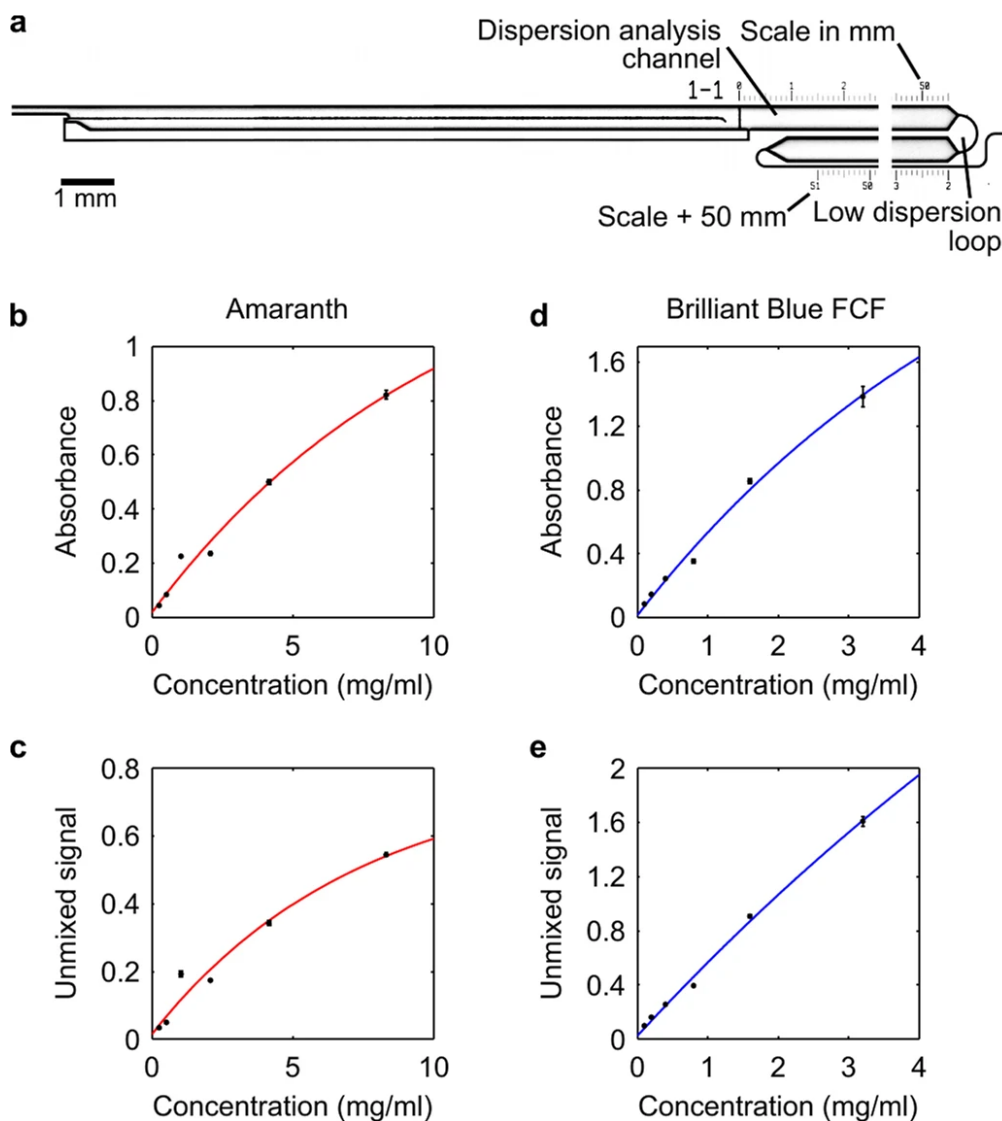


Figure A.13 Characterization of dissolution of multiple reagents in SCMs. **a**, Bright-field image of the device in which reagent pulse shaping and complex profile generation experiments were performed. The diversion barrier of these SCMs has a trench geometry in order to keep the dimensions of the dispersion analysis channel identical to the dimensions of the SCM. **b**, Absorbance calibration curve, and, **c**, the calibration curve after linear spectral unmixing of the amaranth signal. **d**, **e**, As for panels **b**, **c**, but for the brilliant blue signal. $n = 6$ for each data point. Error bars represent standard errors of the mean.

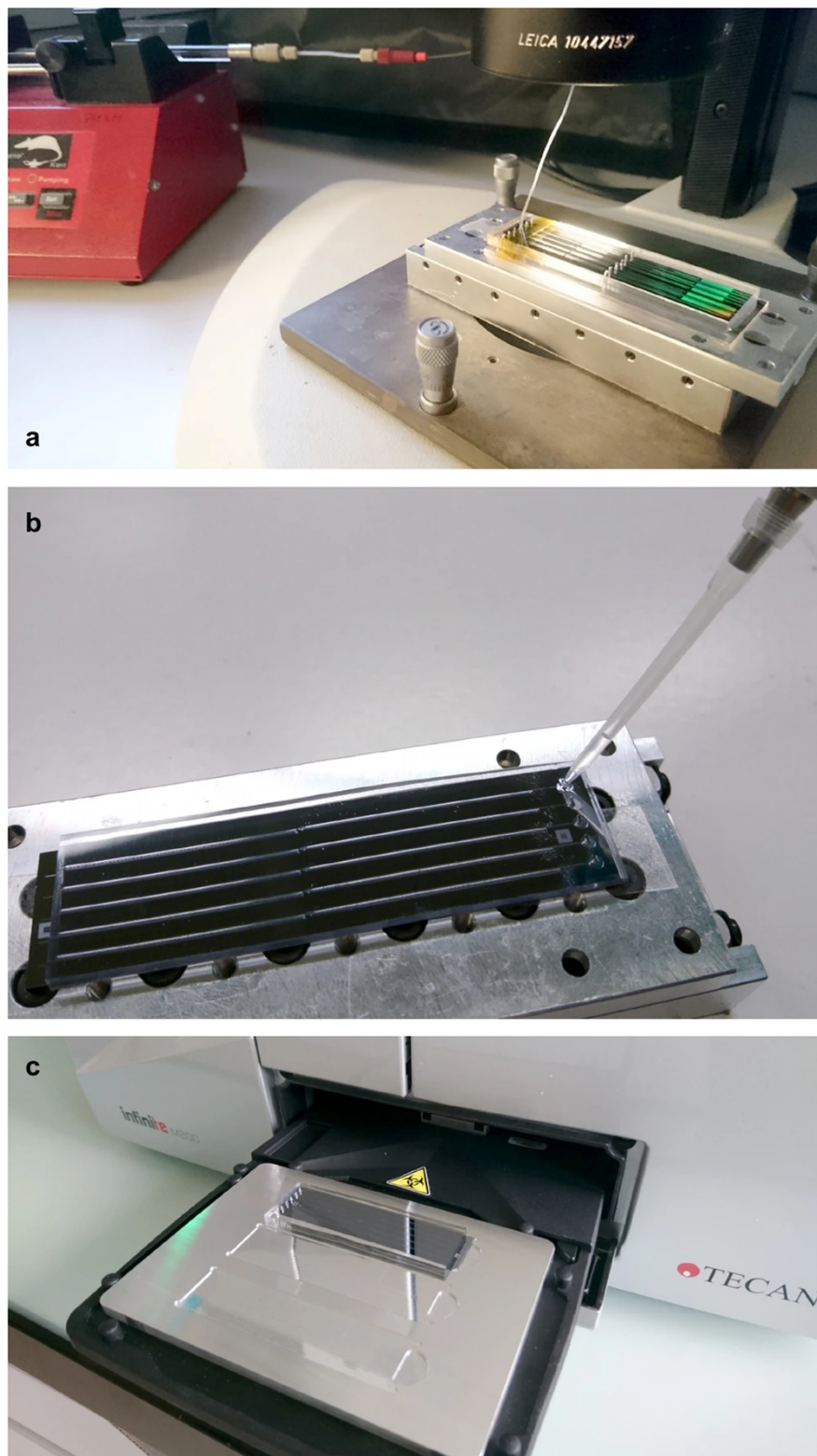
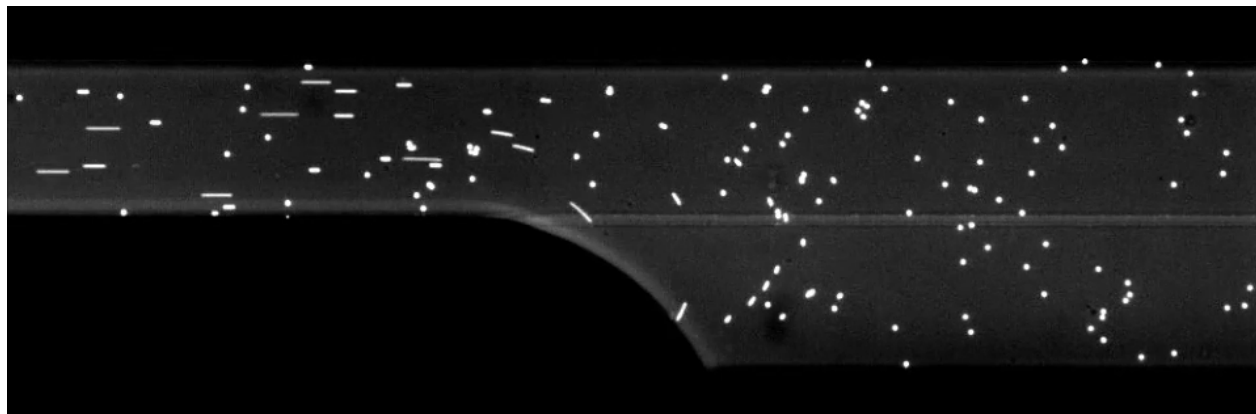
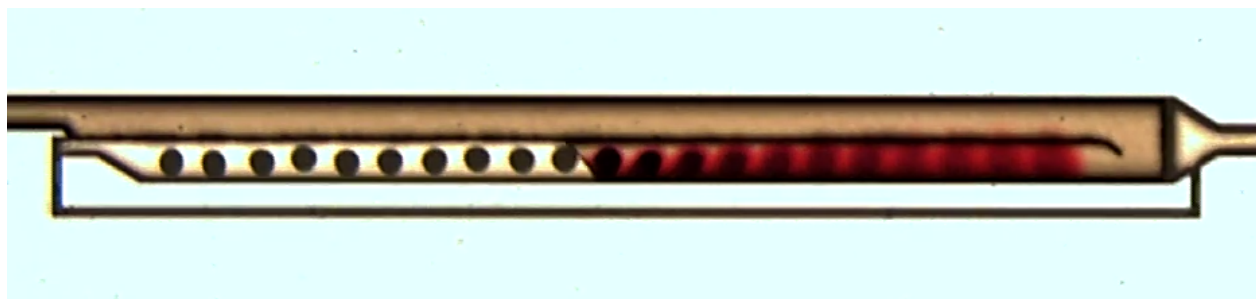


Figure A.14 Experimental setup. **a**, The setup for filling SCMs and documenting the dissolution of food dyes. **b**, Filling SCMs manually using a micropipette for G6PDH quantification experiments. **c**, Measuring the fluorescence signal from G6PDH and RPA reactions using a microtitre plate reader fitted with a custom-made aluminium adaptor.

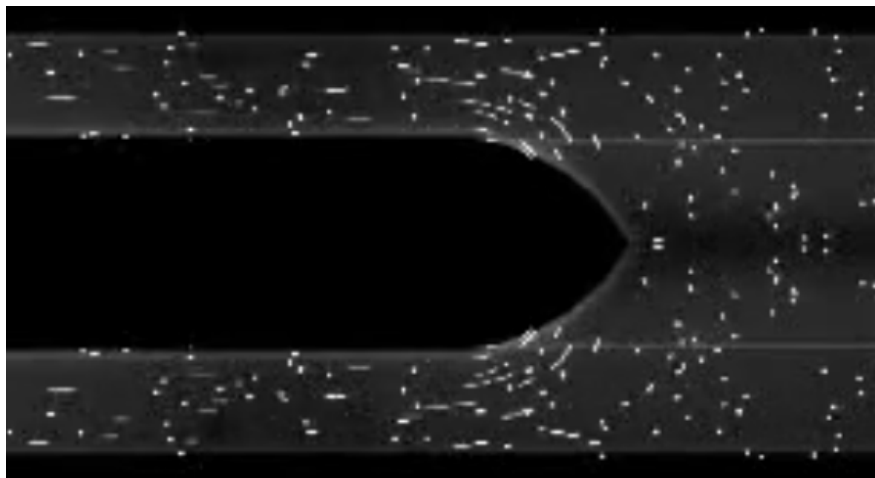
A.8 Supplementary Videos



Video A.15 Fluorescent microspheres revealing the streamlines of a self-coalescing flow. $4.8\ \mu\text{m}$ fluorescent microspheres suspended in a liquid are injected into a SCM (0.5-mm-wide) at $0.5\ \mu\text{L}/\text{min}$ flow rate. The video is in real time with each frame acquired over a 60 ms exposure. (Flash Player required)



Video A.16 Reagent reconstitution in a SCM. a SCM ($L \times W \times D$, $5\ \text{mm} \times 0.5\ \text{mm} \times 50\ \mu\text{m}$) spotted with amaranth dye is filled with water at $0.5\ \mu\text{L}/\text{min}$ flow rate. The video is accelerated ($3\times$). (Flash Player required)



Video A.17 Self-coalescence and Saffman–Taylor viscous fingering. Filling of a SCM observed using fluorescent microparticles. The experimental image is only the top half of the video. The part below the central mirror symmetry line (located at the device wall) is simply a reflection of the upper half made to highlight a similitude between self-coalescence and Saffman–Taylor viscous fingering. The height of the SCM is $50\ \mu\text{m}$ and its width is $500\ \mu\text{m}$ with a flow rate of $0.5\ \mu\text{L}/\text{min}$ and $\lambda = 1/2$. The video is shown along with the discussion in section 3.6.1. (Flash Player required)

A.9 Supplementary Information: Pulse shaping approach in channels with inherent Taylor-Aris Dispersion

This section is a complement to the section on reagent pulse shaping and Taylor-Aris dispersion (TAD) control inside a SCM and downstream of it. It is closely associated with data presented in Figure A.3 and A.4 in the paper and refers to Extended Data Figure 5 and 6. As TAD is suppressed during OF (observed in Fig. A.2b, Suppl. Vid. 2), passive diffusion is the only dispersive process acting on the samples inside the SCM. Homogenization through diffusion can have a positive impact on operation, if one seeks to produce a uniform reagent concentration from reconstituted reagents, or a negative one, if one seeks to produce patterns with high spatial frequency content. Lateral homogenization is often desired and can be further controlled and amplified by the use of a delay chamber (Extended Data Fig. A.11). Finally, once the SCM is full and the diversion rail bursts, TAD is unavoidable in the channel downstream of the SCM. We developed a software to predict the shape of the pulses at any point in time and space downstream of a SCM from the initial reagent spotting patterns. By carefully selecting the flow conditions to minimize TAD, we demonstrate that a high information content can be transported downstream of a SCM towards a detection zone (DZ), a region of interest where the reagents interact (sensor, cell culture chamber, etc.), forming an assay in the most general sense of the term. In this section, we describe each of these effects using a Green's functions approach and show how they can be used efficiently to minimize TAD

and predict reagent pulse profile. We further demonstrate, using our simple software, how this approach can be used to perform reagent “signal processing” or “amplitude pulse-shaping” using a SCM.

A.9.1 Passive diffusion inside the SCM following a reconstitution

During OF, the dried reagent dot is only briefly exposed to a moving fluid, and the corresponding orthogonal and longitudinal flow velocities quickly decay to zero. The time constant for this decay at a fixed dot position, using the module of the velocity profile found in Eq. 3.27, is of the same magnitude as the flow far from the meniscus:

$$V \sim e^{-\frac{\pi}{W}Ut} \quad (\text{A.3})$$

With the typical parameters used in our experiments ($W = 500 \mu\text{m}$, $H = 50 \mu\text{m}$, $U = 0.67 \text{ mm/s}$), the critical time scale and flow length scale over a reagent dot is respectively $t = 240 \text{ ms}$ and $L_C = 159 \mu\text{m}$, leaving very little time and space for TAD to occur before flow becomes stagnant. However, once the fluid is stagnant, diffusion immediately starts to broaden the concentration peaks produced by the reconstituted reagents.

Also, reconstitution time, i.e. $t_r = L_{SCM}/U$ ($t_r = 14 \text{ s}$ with the data above), is typically much smaller than lateral diffusion time $t_D = W^2/2D$ ($t_D = 275 \text{ s}$ for small molecules with $D = 450 \mu\text{m}^2/\text{s}$). If pulses are sent immediately after reconstitution, then diffusive blurring is minimal and pulse shape evolution can be directly inferred using the TAD associated Green’s function and following the method described in section A.9.3 below.

To further decrease the reconstitution time, we can increase the flow rate within the chamber. However, we need to keep in mind that the CPL can only withstand pressures below the Laplace pressure. We find that

$$Q_{\max} = \frac{HW}{2} \frac{dx}{dt} = \frac{\gamma L}{R_0 x} \left(\frac{1 + \cos \theta_w}{H} - \frac{2(\cos \theta_w - 1)}{W} - \frac{\cos \theta_w}{x} \right) \quad (\text{A.4})$$

where R_0 is the channel hydraulic resistance when wetted over its full length, L , H and W are the channel height and width, respectively, x is the wetted SCM length during longitudinal flow, and θ_w is the contact angle between the fluid and the SCM surface. Consequently, if the hydraulic resistance or the flow rate is too high during longitudinal flow, while free surface is created above the CPL, the liquid will cross the leading barrier before reaching the diversion barrier. Equation A.4 implies a quadratic filling time ($t \sim x^2$ when $x \gg H$) for the liquid filling flow phase, as per Washburn’s equation [82], but SCMs can still be filled within a few seconds.

A.9.2 General formulation of the diffusion problem inside the SCM

The initial concentration generated by a spotted dot of dried reagents will depend on the volume in which it is being resuspended; the shallower the SCM, the higher the concentrations achievable. For fast resuspension events in shallow channels, the concentration will quickly homogenize in the vertical direction ($t_D = H^2/2D = 2.75$ s with the above data). The initial concentration C_0 arising from a single dot of a given species shortly after resuspension is thus given by $C_0 = m_r/M_rSH$, where m_r is the mass of reagent spotted, M_r is the molecular mass of the species, S is the surface of the spot and H the channel height.

If left long enough, a point source of reagent reconstituted inside a SCM will slowly homogenize through passive diffusion, following the time-dependent diffusion equation

$$\frac{\partial G}{\partial t} = D \left(\frac{\partial^2 G}{\partial x^2} + \frac{\partial^2 G}{\partial y^2} \right) + \delta(t-t')\delta(x-x')\delta(y-y') \quad (\text{A.5})$$

where $G(x, x', y, y', t, t')$ is Green's function for a point source of reconstituted reagent concentration. The z component of the equation have been neglected as they homogenize much faster than the other two if $H \ll W \ll L$. The evolution of a general initial concentration profile $C(x, y, t = 0) = C_0(x, y)$ through pure diffusion in a SCM, can be obtained using the problem's associated Green's function in long 2D strip ($L \gg W$). Here the boundary conditions are no flux at the side walls, and a vanishing concentration profile at $L \gg W$, yielding

$$G_{x,y,t} = \frac{1}{W} \frac{e^{-\frac{(x-x')^2}{4D(t-t')}}}{\sqrt{4\pi D(t-t')}} \left\{ 1 + \sum_{n=0}^{\infty} \frac{2}{n\pi} e^{-\frac{n^2\pi^2 D}{W^2}(t-t')} \cos\left(\frac{n\pi y}{W}\right) \cos\left(\frac{n\pi y'}{W}\right) \right\} \quad (\text{A.6})$$

where $G_{x,y,t} \equiv G_{x,y,t}(x, x', y, y', t, t')$, $y \in (0, W)$ is the lateral spatial coordinate and x is the longitudinal spatial coordinate. The complete spatial concentration profile at $t = 0$ can always be computed from the initial condition, by performing a triple convolution integral:

$$C(x, y, t) = \langle C * G_{x,y,t} \rangle = \frac{1}{W} \int_{-\infty}^{\infty} \int_{-\infty}^{\infty} \int_0^W C_0(x', y') \delta(t') G_{x,y,t}(x, x', y, y', t, t') dx' dy' dt' \quad (\text{A.7})$$

A.9.3 Delay chambers as a tool to control reagent homogenization in SCM

The various stages of reagent reconstitution and dispersion inside a SCM and its subsequent delivery to a detection zone downstream are summarized in Supplementary Figure A.18.

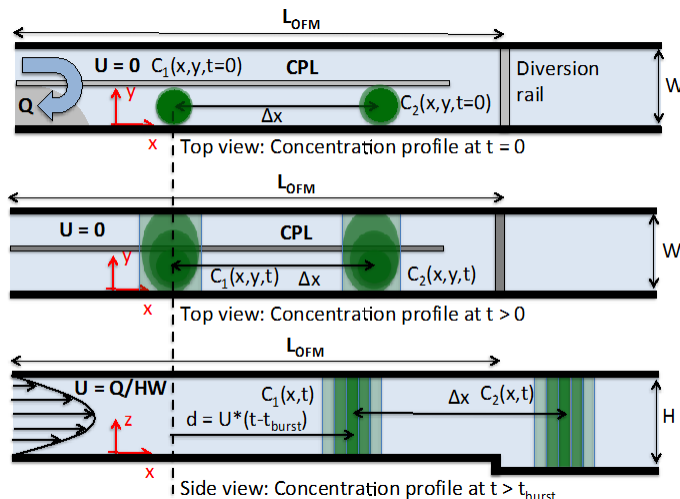


Figure A.18 Reagent transport inside a SCM. Top: Reagent resuspension ($t = 0$); Middle: Passive diffusion in stagnant flow during SCM or delay chamber filling; Bottom: Taylor dispersion during flow downstream of a SCM into a detection channel (side view).

Lateral homogenization using delay chambers

If left long enough, the complex reagent patterns reconstituted inside a SCM will slowly homogenize through passive diffusion. To study the decoupled lateral diffusion, we assume a spotting distribution independent of x , $C(x, y, 0) \equiv C_0(y)$, that is homogeneous in the longitudinal direction. Equation A.7 then simplifies to:

$$C(y, t) = \langle \rho * G_y \rangle = \frac{1}{W} \int_0^W C_0(y) G_y(y, y', t) dy' \quad (\text{A.8})$$

with

$$G_y(y, y', t) = \frac{1}{W} \left\{ 1 + \sum_{n=0}^{\infty} \frac{2}{n\pi} e^{-\frac{t}{t_n}} \cos\left(\frac{n\pi y}{W}\right) \cos\left(\frac{n\pi y'}{W}\right) \right\} \quad (\text{A.9})$$

where $t_n = W^2/(n^2\pi^2D)$. From Eq. A.9, we observe that the homogenization time scale corresponds to decay time of the first eigenvalue ($n = 1$), the slowest of all decay time constants. Thus homogenization time can be extracted and is worth

$$t_1 = \frac{W^2}{\pi^2 D} \quad (\text{A.10})$$

Three times this time constant will correspond to a lateral homogenization roughly 95% ($1 - e^{-3}$) complete no matter the initial shape of the reagent profile, and the delay chamber volume can be precisely set to add this extra time for diffusion to occur. In the diffusion of small molecules ($D \sim$

500 $\mu\text{m/s}$) in the SCM design introduced above, we find $3t_1 = 152$ s (Suppl. Fig. A.18).

Longitudinal homogenization using delay chambers: from discrete dot patterns to continuous reagent concentrations

Alternatively, in some instances, the delay chamber can be used to allow sufficient time for a concentration pattern made of printed dots to diffuse and generate a smooth concentration profile. To isolate the effect of longitudinal homogenization in the general problem formulation found in Eq. A.7, we consider here initial concentration profile that are laterally homogeneous, $C(x, y, 0) \equiv C_0(x)$. Thus, Eq. (A.7) reduces to

$$C(x, t) = \langle C * G_{x,y,t} \rangle = \frac{1}{W} \int_{-\infty}^{\infty} \int_{-\infty}^{\infty} C_0(x) \delta(t') G_{x,t}(x, x', t, t') dx' dt' \quad (\text{A.11})$$

where

$$G_{x,t}(x, x', t, t') = \frac{e^{-\frac{(x-x')^2}{4D(t-t')}}}{\sqrt{4\pi D(t-t')}} \quad (\text{A.12})$$

The latter 1D Green's function, Eq. A.12, indicates that a point source of reagents located at x' will diffuse to form a Gaussian of mean x' and standard deviation $\sigma(t) = \sqrt{2Dt}$. Therefore, it can be used to compute a minimal resolution criterion between two closely spaced reagent dots such that they remain spatially resolved after time t . To do so, we find the autocorrelation function of two reagent dots, assumed point sources without loss of generality, separated by a distance Δx . The autocorrelation function as a function of spacing Δx and time t , thus becomes:

$$AC(\Delta x, t) = \langle C(x, t) * C(x - \Delta x, t) \rangle_x = C_0^2 \int_{-\infty}^{\infty} \frac{e^{-\frac{x^2}{4Dt}} e^{-\frac{(x-\Delta x)^2}{4Dt}}}{\sqrt{4\pi Dt} \sqrt{4\pi Dt}} dx = \frac{C_0^2}{2} \frac{e^{-\frac{\Delta x^2}{4\sigma(t)^2}}}{\sqrt{\pi\sigma(t)}} \quad (\text{A.13})$$

As expected, the autocorrelation is maximum when $\Delta x = 0$ and decays strongly such that when $\Delta x = 2n\sigma$, its value is $AC(2n\sigma, t)/AC_{max} = e^{-n^2}$. The critical time under which a $2n\sigma$ peak separation is achieved for two pulses separated by a distance Δx is thus

$$t_{crit} < \frac{\Delta x^2}{8n^2 D} \quad (\text{A.14})$$

Thus, for reagents dots of amaranth separated by $\Delta x = 500$ μm , the critical time to maintain a 6σ spacing (high spatial resolution) is $t < 7.7$ s. The SCM filling must be done under this time if the goal is to elute spatially resolved peaks from the SCM.

Alternatively, in most applications, the problem is rather to achieve a smooth concentration profile

for an array of resuspended reagent dots. Then, the critical time over which two concentration dots will strongly overlap ($\Delta x = \sigma, n = 1/2$ in Eq. A.14) is given by the simple $t > \Delta x^2/2D$. For a typical spotting pitch $\Delta x = 250 \mu\text{m}$ for amaranth, we get $t > 69 \text{ s}$.

A delay chamber can be used to precisely set this time to ensure pulses are smoothed or mixed before being sent downstream of the SCM.

A.9.4 Amplitude pulse shaping using a SCM

Once a SCM is filled with a specific pattern of reconstituted reagent and the diversion rail bursts, Taylor dispersion is unavoidable in the channel. Typically, a SCM is used to send a train of reagent pulses of precise shape to a DZ (an antibody array, a SPR sensor, a cell culture chamber, etc.), located at a distance d downstream of a channel. Therefore, dispersion starts occurring inside the SCM as soon as the diversion rail bursts and the fluid in the SCM is set in motion towards the DZ. Following Taylor's classical analysis, the reagent disperses under Stokes flow in a long, shallow channel of rectangular cross section HW as prescribed by a simple 1D diffusion model with effective diffusion coefficient:

$$K = D \left(1 + \frac{\text{Pé}^2}{k} \right) \quad (\text{A.15})$$

where D is the reagent diffusion coefficient, $\text{Pé} = UH/D$ is the Péclet number, U is the mean flow velocity, H the channel height, and k a proportionality constant depending on the channel geometry. For a rectangular channel of aspect ratio H/W , k is found to be [80]

$$k = \frac{420}{17} \left(1 + 2.4 \frac{H}{W} + \left(\frac{H}{W} \right)^2 \right) \quad (\text{A.16})$$

wherein the specific case where the aspect ratio is 1 : 10, $k = 30.88$.

In a SCM, the time at which the diversion rail bursts can be viewed as the time at which TAD starts operating inside the SCM. We define it as $t = t_{burst}$. Whatever spatial reagent pattern $C_{SCM}(x, y, t_{burst})$ contained in the SCM at that precise moment will propagate and disperse in the detection channel, downstream of the SCM. When a delay chamber is used to laterally homogenize reagents, the initial distribution function becomes simply $C_{SCM}(x, t_{burst})$. The Green's function associated with 1D diffusion in an infinite medium is identical to Eq. A.12 with the TAD coefficient K replacing the diffusion constant D :

$$G_x(x, x', t, t') = \frac{e^{-\frac{(x-x')^2}{4K(t-t')}}}{\sqrt{4\pi K(t-t')}} \quad (\text{A.17})$$

The convolution of G_x with the initial concentration profile gives the pulse shape as it propagates downstream of a channel towards a detection zone. In the case where the concentration has previously been laterally homogenized using a delay chamber, we get:

$$C(x,t) = \langle C_{SCM} * G \rangle = \int_{-\infty}^{\infty} \int_{-\infty}^{\infty} C_{SCM}(x',t') \delta(t' - t_{burst}) G_{x,t}(x,x',t,t') dx' dt' \quad (\text{A.18})$$

Here, the input concentration profile C_{SCM} is the output of the Green's function for passive diffusion in the delay chamber.

In Fourier space, we observe that the channel is inherently dispersive and that dispersion of the initial concentration profile strongly increases with spatial frequency ν , such that higher spatial frequency quickly vanish, leaving only the fundamental spatial frequency remaining after sufficient time has elapsed:

$$\mathcal{F}\{C(x,t)\} = \mathcal{F}\{C_0(x)\} e^{-\nu^2 K t} \quad (\text{A.19})$$

where \mathcal{F} is the Fourier operator.

Nevertheless, as discussed in section A.9.5 a significant spatial information component can be kept in the pulse by minimizing Taylor dispersion inside the channel.

A.9.5 Minimizing TAD over a travelled distance d

No matter their initial separation distance Δx , two reagent pulses will eventually decay in a single Gaussian peak after sufficient time has elapsed. In TAD, dispersion is either dominated by pure diffusion (when $\text{Pé} \ll 1$) or by fluid advection (when $\text{Pé} \gg 1$). In either extreme cases of $\text{Pé} \rightarrow 0$ and $\text{Pé} \rightarrow \infty$, information content in the pulses will be completely lost once they reach the DZ at distance d . The optimal Pé to minimize TAD can be found using the autocorrelation function described in subsection A.9.3 above. The critical distance travelled by two pulses separated by a distance Δx over which they will lose a $2n\sigma$ spatial resolution can be found by adapting Eq. A.15 and is given

$$d_{crit} = U t_{crit} \quad (\text{A.20})$$

where

$$d_{crit} < \frac{U \Delta x^2}{8n^2 K} = \frac{\Delta x^2}{8Hn^2} \frac{\text{Pé}}{1 + \text{Pé}^2/k} \quad (\text{A.21})$$

No matter what the resolution requirement n is, this distance will be maximal when

$$\frac{\partial d_{crit}(\text{Pé})}{\partial \text{Pé}} = 0 \quad \Rightarrow \quad \text{Pé} = \sqrt{k} \quad (\text{A.22})$$

At this critical $Pé$, $d_{crit} = \Delta x^2 \sqrt{k}/16Hn^2$. Knowing the distance d of a detection zone from a SCM, it is therefore possible to calculate the optimal mean velocity to carry the SCM's reagents with minimal dispersion:

$$U_{opt} = \frac{\sqrt{kD}}{H} \quad (\text{A.23})$$

For a SCM with a $50 \times 500 \mu\text{m}^2$ cross section, we find that $Pé = 5.6$, and the optimal mean velocity and associated flow rates are respectively $U_{opt} = 56 \mu\text{m/s}$, and $Q_{opt} = 83 \text{ nL/s}$.

This simple result has very powerful implications for SCMs, but also in any type of transport problems where concentration peaks are eluted in a dispersive media (*e.g.* chromatography, capillary electrophoresis). In the context of microfluidics, these optimal flow conditions have been hinted at, although not specifically stated, in Bontoux *et al.* [303] The general result states that, when sending pulses in a dispersive channel over a fixed distance, there exists an optimal flow rate such that the samples are minimally dispersed over this distance, and the resulting effective dispersion coefficient is $K = 2D$.

A.9.6 Exploring the possibilities of reagent pulse shaping using SCM with a simple software

To predict the shape of pulses sent down from SCMs, we have written a code using MapleTM software to calculate the profile of a complex pulse specified by sets of printed dots at arbitrary spatial resolution. The software first computes the distribution of the reconstituted reagents $C(x, y, t)$ using the output of the SCM's Green function. When reconstitution time is short, each dot can also be directly modelled using a Dirac peak

$$C_{0,i}(x, y) = (m_{r,i}/H) \delta(x - x_i) \delta(y - y_i) \quad (\text{A.24})$$

with a mass of reagent

$$m_{r,i} \propto \int C_{0,i} dV \quad (\text{A.25})$$

The reagent distribution in the channel is then convoluted with the Green's function describing TAD to obtain $C(x, t)$ as in Eq. A.18. Results in Extended Data Figure 5 summarize the concentration profiles achieved at a specific DZ located at a distance d downstream of the diversion rail for various spotted dot distributions representing i) regular spotting with different pitch (Extended Data Fig. A.10b-c); ii) the effect on peak resolution of varying the DZ distance d (Extended Data Fig. A.10d); iii) minimizing overlap using two consecutive homogeneous reagents (Extended Data Fig. A.10e); iv) achieving fast oscillation when pulsing two reagents or complete mixing (Extended Data Fig. A.10f); v) to generate counter-gradients (Extended Data Fig. A.10g); or 6) to generate arbitrary pulse shapes with multiple reagents within the limits imposed by TAD. An outstanding match was

found between the results predicted by the software and experimental results presented in Figure A.4.

In all cases, making longer SCM will allow the possibility to arbitrarily increase spatial resolution between pulses; making them shallower also decreases Pé and the resulting dispersion. Thus, SCM are a versatile platform to generate complex reagent pulses within a simple passive microdevice.

APPENDIX B SAFFMAN–TAYLOR INSTABILITY

Assuming two fluids, denoted by the indices $i = 1, 2$, are embedded in a porous medium of constant isotropic permeability, k , and an initial unperturbed pressure field $p_{i,0}$ where $p_{1,0} = p_{2,0}$ at the fluid-fluid interface. Driving the fluid of viscosity μ_1 into the fluid of viscosity μ_2 , the pressure within the two fluids has to obey Darcy's law, i.e. $p \sim x$, and the pressure at the interface must be continuous in such a way that $p_1 = p_2 = p_\sigma$ at the interface. Thus, the scalar pressure field can be written as

$$p_{i,0} = p_\sigma + \frac{v\mu_i}{k}x \quad (\text{B.1})$$

where v is the flow velocity. For simplicity, let us assume an initial flat interface at $x = 0$ in the $x - y$ plane. A small perturbation of the interface's flatness may be represented by

$$x(y) = \varepsilon \exp(iqy + at) \quad (\text{B.2})$$

where $|\varepsilon| \ll 1$ and $q = 2\pi n/W$ is the wave vector associated with the width, W , of the cell, n is a positive integer, and a is the temporal amplification of the wave. The pressure field in both fluids may then be written as

$$p_i = p_{i,0} + p'_i(x) \exp(iqy + at) \quad (\text{B.3})$$

To obey Darcy's law, i.e. the Laplace equation $\nabla^2 p = 0$, the pressure fields must be harmonic and perturbations must decay at both ends of the domain. In other words, $p'_i(x)$ must vary as e^{qx} or e^{-qx} , and we can write $p'_i(x) = p'_i e^{s(i)qx}$ where $p'_{i=\{1,2\}}$ are constants to be determined and $s(i)$ is the sign function for which $s(1) = +1$ and $s(2) = -1$. From the incompressibility conditions

$$-\frac{k}{\mu_i} \frac{\partial p'_i}{\partial x} \Big|_{x=0} = a\varepsilon \quad (\text{B.4})$$

we obtain

$$p'_i = -s(i) \frac{a\varepsilon\mu_i}{qk} \quad (\text{B.5})$$

Finally, from the continuity condition, Eq. B.1 and B.3, we can write the temporal growth of the perturbations as

$$a = qv \left(\frac{\mu_2 - \mu_1}{\mu_1 + \mu_2} \right) \quad (\text{B.6})$$

Thus, if the driving fluid is less viscous than the driven fluid, i.e. $\mu_2 > \mu_1$, perturbation growth ensues. The current stability analysis only holds for fluids without surface tension. Adding surface

tension to the picture changes the growth rate significantly by introducing a pressure jump across the interface. The perturbation growth rate after including surface tension effects can be written as

$$a = \frac{qv(\mu_2 - \mu_1) - q^3\sigma\kappa}{\mu_1 + \mu_2} \quad (\text{B.7})$$

where σ is the surface tension between the two fluids, and κ is the curvature of the interface. For more details on how to obtain Eq. B.7, we refer to [101, 304].

APPENDIX C CONSERVATION OF MASS AND MOMENTUM FOR A CONTINUUM

Starting from the general continuity equation (Eq. 2.5), and assuming there are no sources or sinks in the volume element Ω , i.e. $s = 0$, mass conservation is expressed by replacing the intensive parameter by the fluid density ρ :

$$\boxed{\frac{\partial \rho}{\partial t} + \nabla \cdot (\rho \mathbf{u}) = 0} \quad (\text{C.1})$$

For incompressible fluids, the density is invariant and therefore

$$\nabla \cdot \mathbf{u} = 0 \quad (\text{C.2})$$

Momentum conservation is expressed by replacing φ with $\rho \mathbf{u}$, hence

$$\frac{\partial \rho \mathbf{u}}{\partial t} + \nabla \cdot (\rho \mathbf{u} \mathbf{u}) + \mathbf{s} = \mathbf{0} \quad (\text{C.3})$$

where $\mathbf{u} \mathbf{u}$ is a dyadic product and \mathbf{s} is a body force per volume unit exerted on Ω . From the product rule, we can rewrite the momentum conservation as

$$\mathbf{u} \frac{\partial \rho}{\partial t} + \rho \frac{\partial \mathbf{u}}{\partial t} + \mathbf{u} \mathbf{u} \cdot \nabla \rho + \rho \nabla \cdot \mathbf{u} \mathbf{u} + \mathbf{s} = \mathbf{0} \quad (\text{C.4})$$

and knowing the divergence of a dyadic is $\nabla \cdot (\mathbf{a} \mathbf{b}) = (\nabla \cdot \mathbf{a}) \mathbf{b} + \mathbf{a} \cdot \nabla \mathbf{b}$,

$$\mathbf{u} \frac{\partial \rho}{\partial t} + \rho \frac{\partial \mathbf{u}}{\partial t} + \mathbf{u} \mathbf{u} \cdot \nabla \rho + \rho (\nabla \cdot \mathbf{u}) \mathbf{u} + \rho \mathbf{u} \cdot \nabla \mathbf{u} + \mathbf{s} = \mathbf{0} \quad (\text{C.5})$$

equivalent to

$$\mathbf{u} \frac{\partial \rho}{\partial t} + \rho \frac{\partial \mathbf{u}}{\partial t} + (\mathbf{u} \cdot \nabla \rho + \rho \nabla \cdot \mathbf{u}) \mathbf{u} + \rho \mathbf{u} \cdot \nabla \mathbf{u} + \mathbf{s} = \mathbf{0} \quad (\text{C.6})$$

From the product rule and regrouping,

$$\mathbf{u} \left(\frac{\partial \rho}{\partial t} + \nabla \cdot (\rho \mathbf{u}) \right) + \rho \left(\frac{\partial \mathbf{u}}{\partial t} + \mathbf{u} \cdot \nabla \mathbf{u} \right) + \mathbf{s} = \mathbf{0} \quad (\text{C.7})$$

where the leftmost part is the conservation of mass as derived in Eq. C.1. Thus, the conservation of momentum can be written as

$$\rho \left(\frac{\partial \mathbf{u}}{\partial t} + \mathbf{u} \cdot \nabla \mathbf{u} \right) + \mathbf{s} = \mathbf{0} \quad (\text{C.8})$$

The body forces \mathbf{s} in a fluid can be split in two distinct parts, i.e. body forces and internal stresses such that

$$\rho \left(\frac{\partial \mathbf{u}}{\partial t} + \mathbf{u} \cdot \nabla \mathbf{u} \right) = \mathbf{f}_s + \mathbf{f}_b \quad (\text{C.9})$$

Body forces can be of several origins, such as gravitational, electro-magnetic, and surface tension to name a few. For simplicity, we group them all as $\mathbf{f}_b = \sum_i \mathbf{f}_i$. On the other hand, internal stresses can be expressed as the divergence of the Cauchy stress tensor:

$$\mathbf{f}_s = \nabla \cdot \boldsymbol{\sigma} = \nabla \cdot \begin{bmatrix} \sigma_{xx} & \sigma_{xy} & \sigma_{xz} \\ \sigma_{yx} & \sigma_{yy} & \sigma_{yz} \\ \sigma_{zx} & \sigma_{zy} & \sigma_{zz} \end{bmatrix} \quad (\text{C.10})$$

The Cauchy stress tensor diagonal components are normal stresses. They can be either tensions, if $\sigma_{ii} > 0$, or compressions, if $\sigma_{ii} < 0$. The other components are shear stresses. It is common to split the stress tensor to remove the internal stresses due to pressure gradients. Thus,

$$\boldsymbol{\sigma} = - \begin{bmatrix} p & 0 & 0 \\ 0 & p & 0 \\ 0 & 0 & p \end{bmatrix} + \begin{bmatrix} \sigma_{xx} + p & \sigma_{xy} & \sigma_{xz} \\ \sigma_{yx} & \sigma_{yy} + p & \sigma_{yz} \\ \sigma_{zx} & \sigma_{zy} & \sigma_{zz} + p \end{bmatrix} = -p\mathbf{I} + \boldsymbol{\tau} \quad (\text{C.11})$$

where \mathbf{I} is the second-order (3×3) identity tensor and $\boldsymbol{\tau}$ is known as the viscous stress tensor. Combining everything together so far, we obtain the equation of conservation of momentum for any fluids

$$\rho \left(\frac{\partial \mathbf{u}}{\partial t} + \mathbf{u} \cdot \nabla \mathbf{u} \right) = -\nabla p + \nabla \cdot \boldsymbol{\tau} + \sum_i \mathbf{f}_i \quad (\text{C.12})$$

also known as the Navier-Stokes equation. For Newtonian fluids, i.e. fluids with viscous stresses increasing linearly with respect to strain rate, the constraint tensor $\boldsymbol{\tau}$ can be written as

$$\boldsymbol{\tau} = 2\mu\mathbf{S} - \frac{2}{3}\mu(\nabla \cdot \mathbf{u})\mathbf{I} \quad (\text{C.13})$$

where μ is the dynamic viscosity of the fluid (Pa·s), and $\mathbf{S} = (\nabla \mathbf{u} + \nabla \mathbf{u}^\top)/2$ is the strain rate tensor. For incompressible fluids, $\nabla \cdot \mathbf{u}$ from the conservation of mass, and the constraint tensor reduces to $\boldsymbol{\tau} = 2\mu\mathbf{S} \equiv \mu\nabla^2 \mathbf{u}$. Thus, for incompressible isothermal Newtonian fluids, the Navier-Stokes equation becomes

$$\rho \left(\frac{\partial \mathbf{u}}{\partial t} + \mathbf{u} \cdot \nabla \mathbf{u} \right) = -\nabla p + \mu\nabla^2 \mathbf{u} + \sum_i \mathbf{f}_i \quad (\text{C.14})$$

APPENDIX D ENZMODSIMULATOR CODE VALIDATION

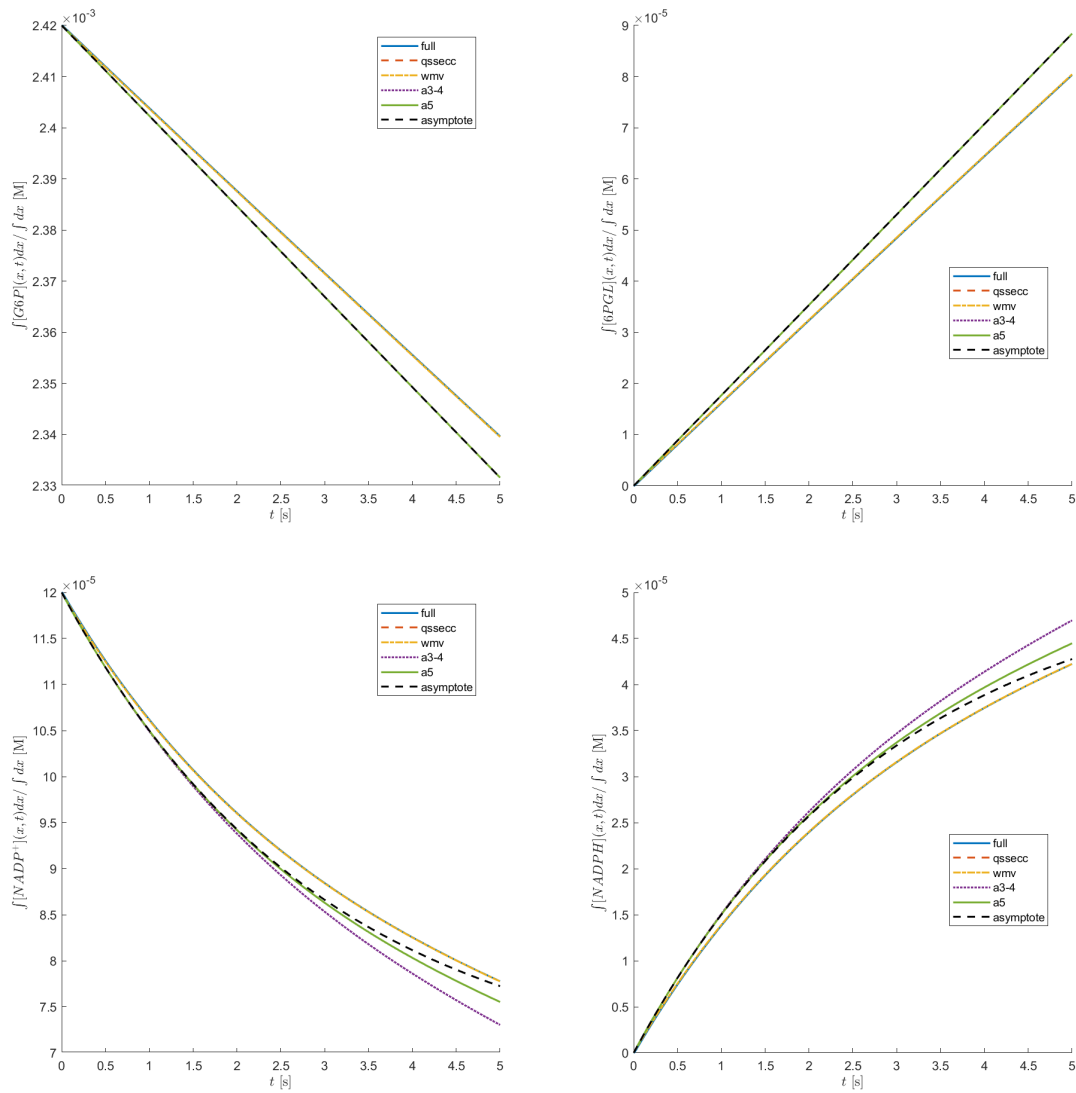


Figure D.1 Validation of the EMS code by comparing results to simplified models. It is expected that the asymptotic model only represents the full model for small times.

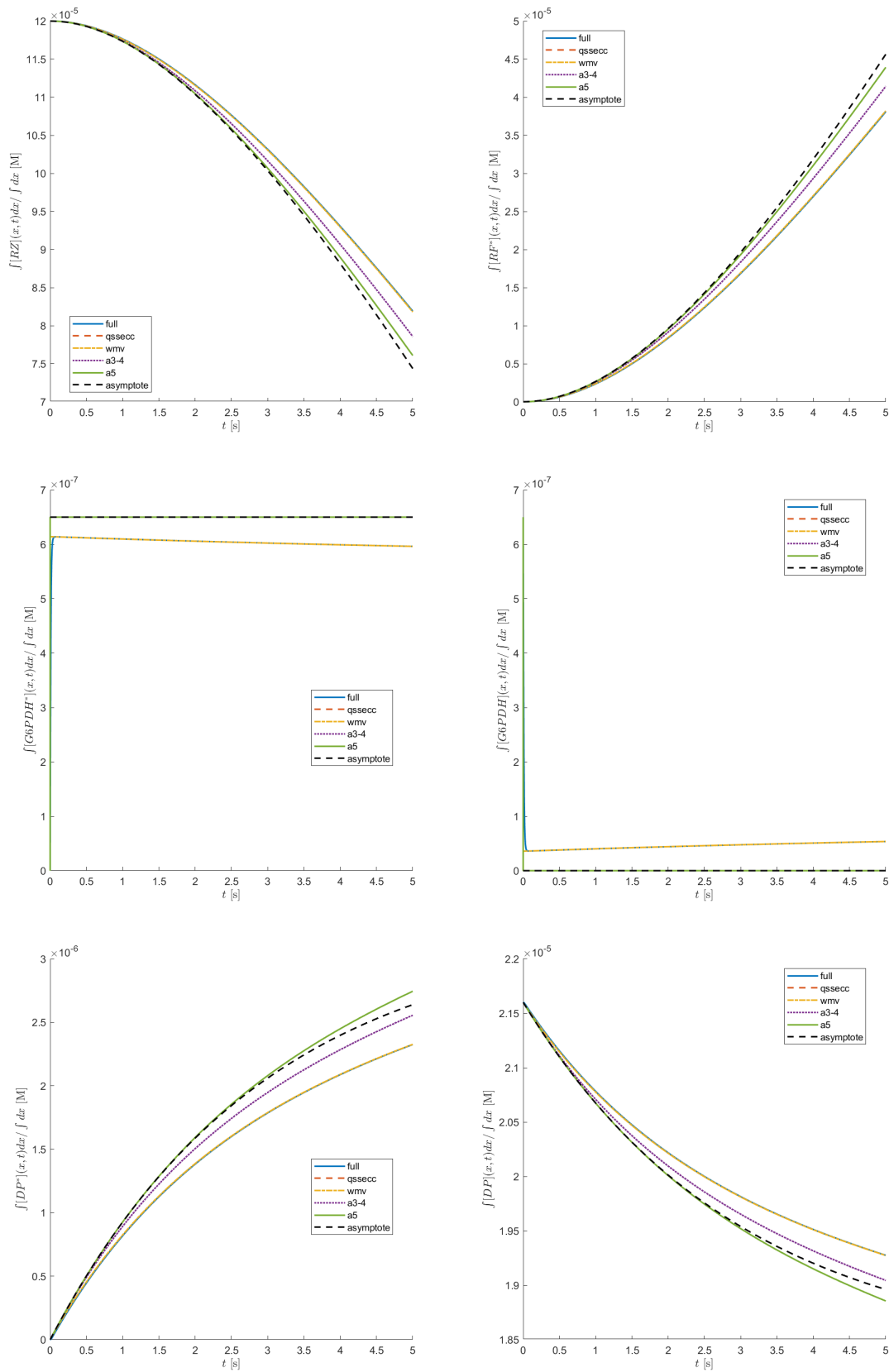


Figure D.1 Validation of the EMS code by comparing results to simplified models. It is expected that the asymptotic model only represents the full model for small times (continued)

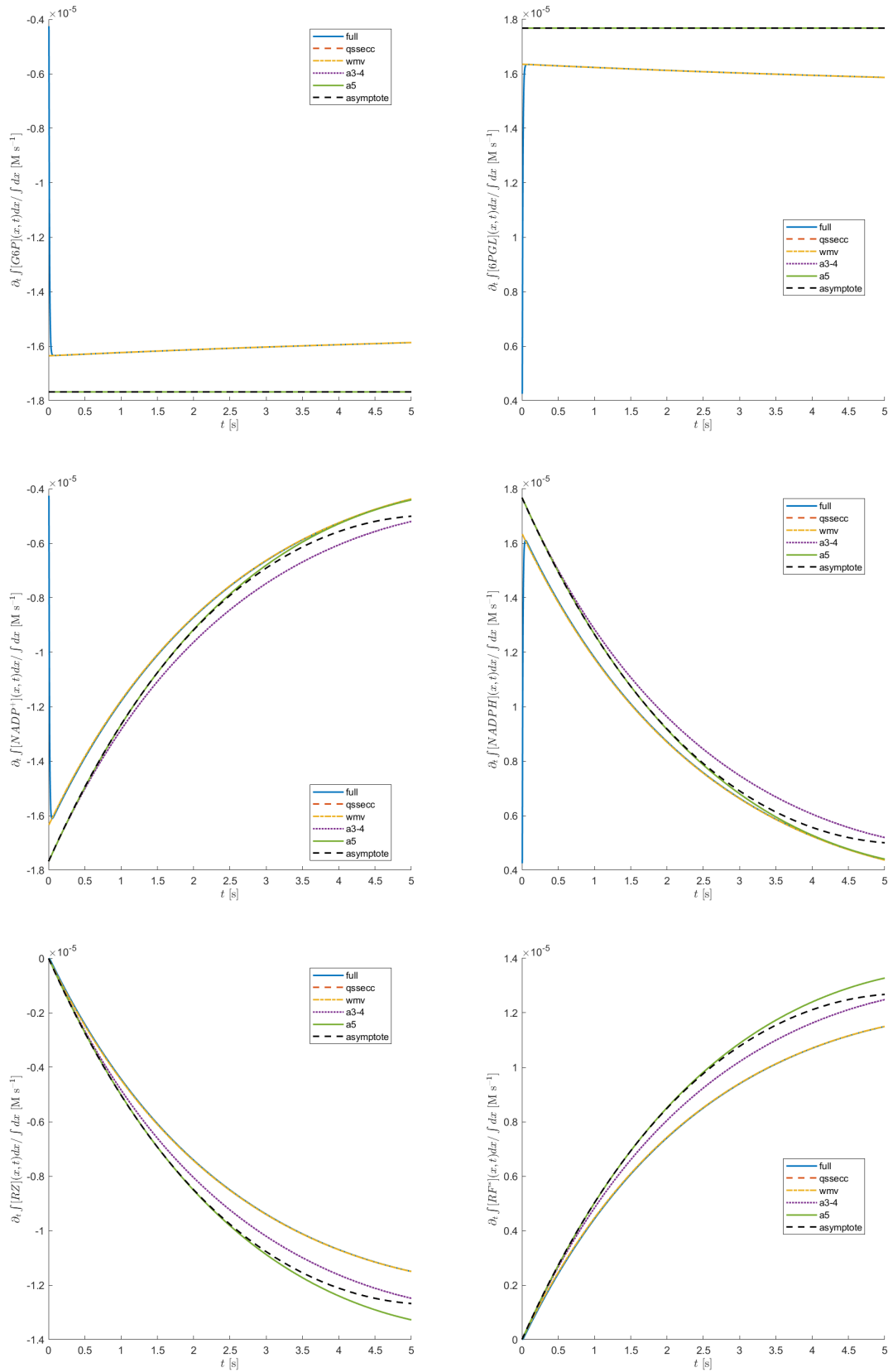


Figure D.1 Validation of the EMS code by comparing results to simplified models. It is expected that the asymptotic model only represents the full model for small times (continued)

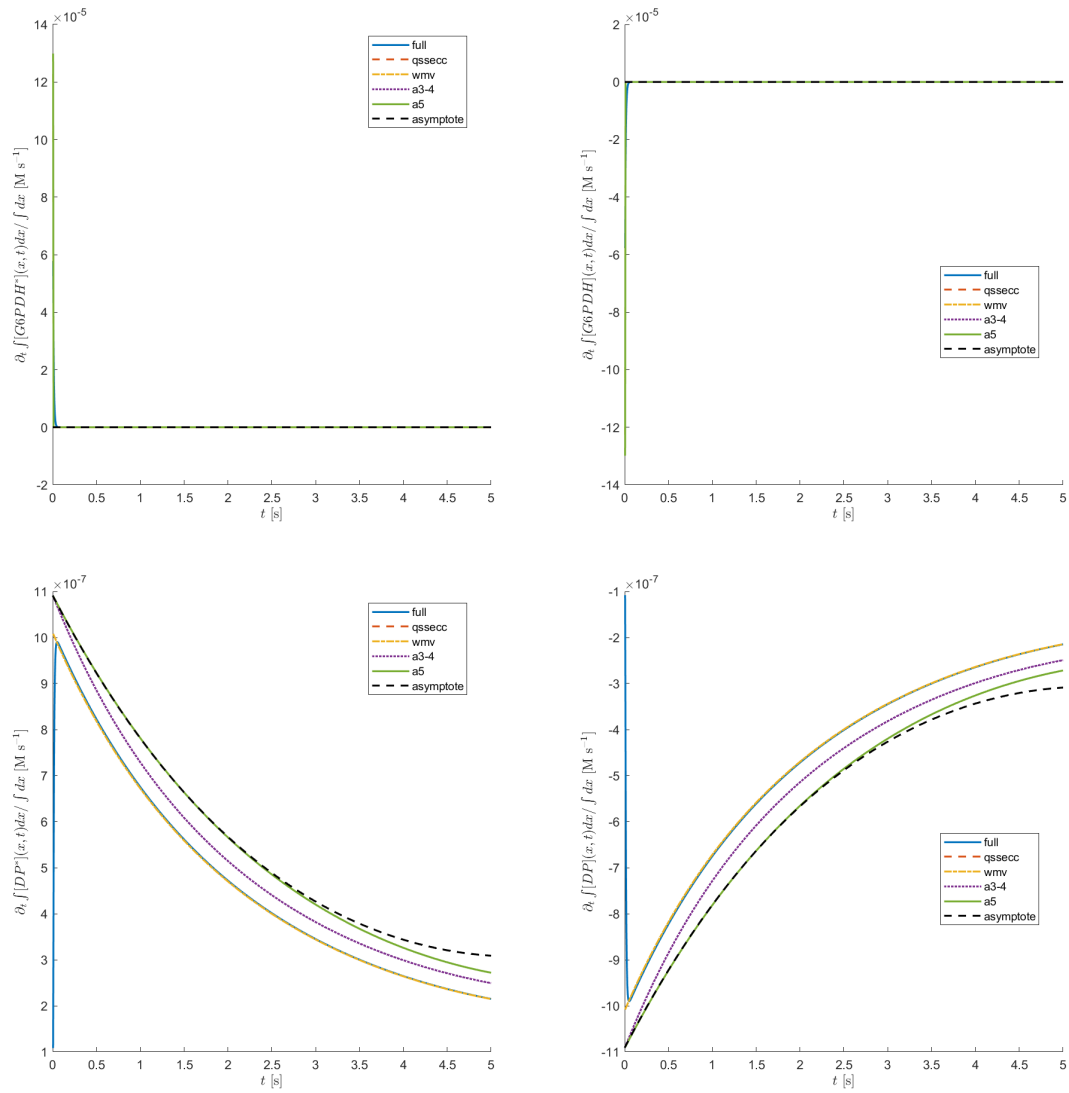


Figure D.1 Validation of the EMS code by comparing results to simplified models. It is expected that the asymptotic model only represents the full model for small times (continued)

APPENDIX E ENZMODSIMULATOR INPUT FILE EXAMPLE

```

# ----- #:0
# ----- Simulation Parameters ----- #:0
# ----- #:0
Domain length L [mm]: 13
Simulation time [s]: 600
Filling time (delay) [s]: 0
# ----- #:0
# ----- Model Options ----- #:0
# ----- #:0
Dimension: 1
Level of approximation: 0
Solve hydrogen equation: 0
# ----- #:0
# ----- Simulation Options ----- #:0
# ----- #:0
Writing precision (number of decimals): 16
Negative concentrations limiter: 0
Reaction limiter value: 0.001
Diffusion limiter value: 0.5
Manual time step [s]: 0
# ----- #:0
# ----- 1D Simulation Options ----- #:0
# ----- #:0
Number of elements: 1000
FDM scheme order in space: 2
Probe location x0 [mm]: 0.5
Probe location x1 [mm]: 3
Spot radius [um]: 75
Spot pitch [um]: 300
Number of figures to print: 21
# ----- #:0
# ----- Physical Constants ----- #:0

```

```

# ----- #:0
Diffusion constant D_G6P [um2.s-1]: 534
Diffusion constant D_6PGL [um2.s-1]: 534
Diffusion constant D_NADP+ [um2.s-1]: 420
Diffusion constant D_NADPH [um2.s-1]: 420
Diffusion constant D_RZ [um2.s-1]: 480
Diffusion constant D_RF* [um2.s-1]: 480
Diffusion constant D_G6PDH* [um2.s-1]: 74
Diffusion constant D_G6PDH [um2.s-1]: 74
Diffusion constant D_DP* [um2.s-1]: 74
Diffusion constant D_DP [um2.s-1]: 74
Diffusion constant D_H+ [um2.s-1]: 1000
Bimolecular kinetics constant k_on_1 [s-1.M-1]: 1e6
Bimolecular kinetics constant k_on_2 [s-1.M-1]: 1e6
Bimolecular kinetics constant k_off_1 [s-1]: 7
Bimolecular kinetics constant k_off_2 [s-1]: 350
Catalytic rate constant k_cat_1 [s-1]: 222.21
Catalytic rate constant k_cat_2 [s-1]: 3.73
Michaelis-Menten constant K_M_1 [M]: 52e-6
Michaelis-Menten constant K_M_2 [M]: 1500e-6
# ----- #:0
# ----- Initial Fields ----- #:0
# ----- #:0
Initial concentration C_G6P_0 [uM]: 43460
Initial concentration C_6PGL_0 [uM]: 0
Initial concentration C_NADP+_0 [uM]: 2173
Initial concentration C_NADPH_0 [uM]: 0
Initial concentration C_RZ_0 [uM]: 2173
Initial concentration C_RF*_0 [uM]: 0
Initial concentration C_G6PDH*_0 [uM]: 0
Initial concentration C_G6PDH_0 [uM]: 0.01875
Initial concentration C_DP*_0 [uM]: 0
Initial concentration C_DP_0 [uM]: 388
Initial concentration C_H+_0 [uM]: 0

```

**APPENDIX F MULTIPHASE LATTICE BOLTZMANN METHOD
IMPLEMENTATION (IN FRENCH) / IMPLÉMENTATION DE LA MÉTHODE DE
BOLTZMANN SUR RÉSEAU.**

F.1 Introduction

La méthode de Boltzmann sur réseau (LBM) se situe dans les méthodes dites mésoscopiques, étant issue fondamentalement de la physique statistique mésoscopique. Dans la LBM, on étudie le comportement de distributions de particules et non des quantités physiques macroscopiques comme en mécanique des fluides classique (e.g. équations de Navier-Stokes). Une avenue en pleine maturation de la LBM est celle des fluides multiphases.

Plusieurs approches de modélisation existent en LBM multiphase, soit l'approche de Rothman et Keller [117], l'approche de Shan et Chen [305], les modèles à énergie libre [306], champs moyens [307] et champs médians [308], pour ne nommer que ceux-ci. Une discussion plus approfondie relatives à certains modèles peut être trouvée dans *Huang et al.*, 2015 [309].

Les fluides multiphases ont de multiples applications, par exemple, dans le domaine de la miniaturisation de laboratoires sur puces (pompes capillaires, guides de phase, microfluidique sur papier, valves capillaires, etc.) Dans cette annexe, nous donnons un exemple d'implémentation de la LBM à plusieurs composants.

F.2 Théorie

Les fondements de la LBM résident dans la physique statistique, en particulier dans la théorie cinétique des gaz. Soit une distribution de particules $f \equiv f(\mathbf{x}, \mathbf{c}, t)$ donnée au temps t et en un point (\mathbf{x}, \mathbf{c}) de l'espace phase, où $\mathbf{x} \equiv (x, y, z)$ et $\mathbf{c} \equiv (c_x, c_y, c_z)$ avec 3 dimensions spatiales. On intègre $\mathbf{c}^n f$ dans l'espace des vitesses pour obtenir les différentes quantités Π_n représentant des variables physiques macroscopiques comme la densité $\rho \equiv \rho(\mathbf{x}, t)$, la vitesse $\mathbf{u} \equiv \mathbf{u}(\mathbf{x}, t)$ et la densité d'énergie totale $E \equiv E(\mathbf{x}, t)$:

$$\Pi_0 = \rho = \int_{\mathbf{c}} f d\mathbf{c} \quad (\text{F.1})$$

$$\Pi_1 = \rho \mathbf{u} = \int_{\mathbf{c}} \mathbf{c} f d\mathbf{c} \quad (\text{F.2})$$

$$\Pi_2 = \rho E = \int_{\mathbf{c}} \|\mathbf{c}\|^2 f d\mathbf{c} \quad (\text{F.3})$$

où $\|\cdot\|$ est la norme Euclidienne. Si on centre la vitesse \mathbf{u} par rapport au centre de la distribution locale de vitesse (on assume une distribution symétrique), on peut calculer la densité d'énergie interne $e \equiv e(\mathbf{x}, t)$:

$$\Pi_2 = \rho e = \int_{\mathbf{c}} \|\mathbf{U}\|^2 f d\mathbf{c} \quad (\text{F.4})$$

où $\mathbf{U} \equiv \mathbf{c} - \mathbf{u}$ est la vitesse relative locale. En intégrant dans l'espace de phase, on peut calculer les variables extensives associées aux quantités Π_n , e.g. la masse :

$$M = \int_{\mathbf{c}} \int_{\mathbf{x}} f d\mathbf{x} d\mathbf{c} \quad (\text{F.5})$$

F.2.1 Équation d'état

Selon la théorie cinétique des gaz, l'énergie cinétique totale d'une molécule d'un gaz parfait est donnée par

$$e = \frac{3}{2} k_B T \quad (\text{F.6})$$

où k_B est la constante de Boltzmann et T la température. Selon la loi des gaz parfait, la pression est donnée par

$$p = \rho k_B T \quad (\text{F.7})$$

d'où en combinant les équations F.6 et F.7 on obtient l'équation d'état

$$\rho e = \frac{3}{2} p \quad (\text{F.8})$$

F.2.2 Équation de transport de Boltzmann et LBM

Pour étudier le comportement de la distribution f dans le temps, on prend sa dérivée totale :

$$\frac{df}{dt} = \frac{\partial f}{\partial t} + \dot{\mathbf{x}} \cdot \nabla_{\mathbf{x}} f + \dot{\mathbf{c}} \cdot \nabla_{\mathbf{c}} f \quad (\text{F.9})$$

avec laquelle on obtient l'équation de transport de Boltzmann :

$$\frac{\partial f}{\partial t} + \mathbf{c} \cdot \nabla_{\mathbf{x}} f + \mathbf{g} \cdot \nabla_{\mathbf{c}} f = \Omega(f) \quad (\text{F.10})$$

où Ω est l'opérateur de collision et \mathbf{g} est l'accélération résultante d'une force externe appliquée sur le volume de gaz, e.g. l'accélération gravitationnelle. Le terme de collision peut être simplifié en

le substituant par l'opérateur de Bhatnagar-Gross-Krook (BGK), soit

$$\Omega = -\frac{f - f^{(e)}}{\tau} \quad (\text{F.11})$$

où $f^{(e)}$ est la distribution à l'équilibre, soit lorsque $t \rightarrow \infty$, et τ est un temps caractéristique de relaxation. Cette approximation, même si considérable, conserve la masse et respecte le théorème \mathcal{H} .

On obtient la distribution à l'équilibre en posant $\Omega(f) = 0$ et on trouve :

$$f^{(e)} = \rho \left(\frac{1}{2\pi k_B T} \right)^{\frac{3}{2}} e^{-\frac{\|\mathbf{c}-\mathbf{u}\|^2}{2k_B T}} \quad (\text{F.12})$$

On peut également obtenir cette distribution à partir du formalisme de l'ensemble canonique (voir par exemple S. Salinas, *Introduction to Statistical Physics*, setion 6.2 [310]).

En approximant la distribution à l'équilibre par un polynôme d'ordre 2 (méthode de Champman-Enskog), on obtient

$$f^{(e)} = \rho \left(\frac{1}{2\pi k_B T} \right)^{\frac{3}{2}} e^{-\frac{\|\mathbf{c}\|^2}{2k_B T}} \left(1 + \frac{(\mathbf{c} \cdot \mathbf{u})}{k_B T} + \frac{(\mathbf{c} \cdot \mathbf{u})^2}{k_B T} - \frac{\mathbf{u}^2}{k_B T} \right) + \mathcal{O}(\mathbf{u}^3) \quad (\text{F.13})$$

Finalement, en discrétisant le tout sur un réseau LBM, on obtient

$$f_i^{(e)} \approx \rho \left(1 + 3(\mathbf{c}_i \cdot \mathbf{u}) + \frac{9}{2}(\mathbf{c}_i \cdot \mathbf{u})^2 - \frac{3}{2}\mathbf{u}^2 \right) \quad (\text{F.14})$$

Pour simplifier la notation, on a assumé que la vitesse du réseau $c = \Delta x / \Delta t = 1$ comme dans S. Leclaire [311].

Pour un fluide à plusieurs phases, on doit ajouter une contribution multiphase ϕ et Φ qui dépendent respectivement de la densité initiale ρ^0 et du gradient de densité :

$$f_i^{(e)} \approx \rho \left(\phi(\rho^0) + 3(\mathbf{c}_i \cdot \mathbf{u}) + \frac{9}{2}(\mathbf{c}_i \cdot \mathbf{u})^2 - \frac{3}{2}\mathbf{u}^2 \right) + \Phi(\nabla \rho) \quad (\text{F.15})$$

F.3 Modélisation numérique

Pour ce travail, la méthode de Reis et Phillips [312], qui dérive de la méthode de Rothman et Keller [117], a été choisie en suivant principalement les travaux de S. Leclaire [311, 313–317].

Posons les grandes lignes du modèle. Pour chaque fluide non miscible k , on associe une fonction de distribution $f_i^k(\mathbf{x}, t)$ où \mathbf{x} est le vecteur position dans le réseau DnQm et t est le temps. Pour ce travail, on modélise deux fluides, soit $k = \{r, b\}$, sur un réseau D2Q9 ayant les vitesses $|\mathbf{c}|$ décrites à la Table F.1. La distribution de couleur combinée (*color-blind distribution*) est alors donnée par $f_i(\mathbf{x}, t) = f_i^r(\mathbf{x}, t) + f_i^b(\mathbf{x}, t)$. En considérant des conditions périodiques partout sur les frontières du domaine, le coeur de l'algorithme est :

1. collision BGK : $|f(\mathbf{x}, t_1)\rangle = \Omega^{(1)}(|f(\mathbf{x}, t_0)\rangle)$;
2. perturbation multiphase : $|f(\mathbf{x}, t_2)\rangle = \Omega^{(2)}(|f(\mathbf{x}, t_1)\rangle)$;
3. recoloriage : $|f^k(\mathbf{x}, t_3)\rangle = \Omega^{(3)}(|f^k(\mathbf{x}, t_2)\rangle)$, $\forall k$;
4. advection : $|f(\mathbf{x} + |\mathbf{c}|, t_0)\rangle = |f(\mathbf{x}, t_3)\rangle$,

où $\Omega^{(1)}$, $\Omega^{(2)}$ et $\Omega^{(3)}$ sont respectivement l'opérateur de collision BGK, l'opérateur de collision multiphase (perturbation) et l'opérateur de recoloriage. On peut ensuite calculer la pression dans le fluide k avec l'équation d'état, soit [317] :

$$p_k = \rho_k \frac{3(1 - \alpha_k)}{5} \quad (\text{F.16})$$

où α_k est un paramètre de stabilité d'interface entre 0 et 1 qui doit respecter

$$\frac{\rho_r^0}{\rho_b^0} = \frac{1 - \alpha_b}{1 - \alpha_r} \quad (\text{F.17})$$

où ρ_k^0 est la densité initiale du fluide k .

Table F.1 Vitesses du réseau D2Q9

i	\mathbf{c}_i
0	(+0, +0)
1	(+c, +0)
2	(+0, +c)
3	(-c, +0)
4	(+0, -c)
5	(+c, +c)
6	(-c, +c)
7	(-c, -c)
8	(+c, -c)

Table F.2 Poids pour le réseau D2Q9

D2Q9	$\{i : \mathbf{c}_i ^2 = 0\}$	$\{i : \mathbf{c}_i ^2 = 1\}$	$\{i : \mathbf{c}_i ^2 = 2\}$
W_i	4/9	1/9	1/36
ϕ_i	0	1/5	1/20
φ_i	1	-1/5	-1/20
ψ_i	-8/3	-1/6	1/12
ξ_i	0	1/2	1/8
B_i	-4/27	2/27	5/108

F.3.1 Collision BGK

L'opérateur de collision BGK se note :

$$\Omega^{(1)}(|f\rangle) = |f\rangle - \mathbf{M}^{-1} \mathbf{K} \mathbf{M}(|f\rangle - |f^{(e)}\rangle) \quad (\text{F.18})$$

avec la notation MRT standard [311]. Pour ce travail, nous avons implémenté un temps de relaxation unique, soit

$$\Omega^{(1)}(|f\rangle) = |f\rangle - \omega_{\text{eff}}(|f\rangle - |f^{(e)}\rangle) \quad (\text{F.19})$$

où ω_{eff} est le facteur de relaxation constant et la distribution à l'équilibre est donnée par (la notation des poids suit celle de S. Leclaire *et al.*, 2017 [311] et leur valeurs sont présentés à la Table F.2) :

$$|f^{(e)}\rangle = \bar{v} [\phi_i(\mathbf{u} \cdot \nabla \rho) + \xi_i(\mathbf{G} : |\mathbf{c}\rangle \otimes |\mathbf{c}\rangle)] + \rho \left[\phi_i + \varphi_i \bar{\alpha} + 3(|\mathbf{c}\rangle \cdot \mathbf{u}) + \frac{9}{2}(|\mathbf{c}\rangle \cdot \mathbf{u})^2 - \frac{3}{2}\mathbf{u}^2 \right] \quad (\text{F.20})$$

où le tenseur \mathbf{G} est défini par

$$\mathbf{G} = (\mathbf{u} \otimes \nabla \rho) + (\mathbf{u} \otimes \nabla \rho)^T \quad (\text{F.21})$$

$\bar{\alpha}$ est la moyenne géométrique par la densité du paramètre de stabilisation [311] :

$$\bar{\alpha} = \frac{\rho_r}{\rho_r + \rho_b} \alpha_r + \frac{\rho_b}{\rho_r + \rho_b} \alpha_b \quad (\text{F.22})$$

et \bar{v} est la moyenne harmonique par la densité de la viscosité

$$\frac{1}{\bar{v}} = \frac{\rho_r}{\rho_r + \rho_b} \frac{1}{v_r} + \frac{\rho_b}{\rho_r + \rho_b} \frac{1}{v_b} \quad (\text{F.23})$$

Il faut noter que d'autres méthodes [315] sont disponibles pour calculer \bar{v} , ce qui peut grandement affecter la stabilité de l'interface pour de grands ratios de viscosité et de densité. Le facteur de

relaxation est alors donné par

$$\omega_{\text{eff}} = \frac{2}{6\bar{v} + 1} \quad (\text{F.24})$$

F.3.2 Perturbation multiphase

La tension de surface se modélise par un opérateur de perturbation, soit

$$\Omega^{(2)}(|f\rangle) = |f\rangle - |f^{\text{pert}}\rangle \quad (\text{F.25})$$

où

$$|f^{\text{pert}}\rangle = A\mathbf{F} \left[W_i \frac{(\mathbf{F} \cdot |\mathbf{c}\rangle)^2}{\|\mathbf{F}\|^2} - B_i \right] \quad (\text{F.26})$$

Le gradient de la fonction de couleur \mathbf{F} est donnée par

$$\mathbf{F} = \nabla \left(\frac{\rho_r - \rho_b}{\rho} \right) \quad (\text{F.27})$$

et le paramètre A est défini à partir de la tension de surface σ et du facteur de relaxation comme suit :

$$A = \frac{9}{4} \omega_{\text{eff}} \sigma \quad (\text{F.28})$$

Toutefois, même si cet opérateur introduit l'effet de la tension de surface, il n'impose pas l'immiscibilité des fluides.

F.3.3 Recoloriage

Pour s'assurer que les fluides soient non miscibles, on introduit l'opérateur de recoloriage :

$$(\Omega^r)^{(3)}(|f^r\rangle) = \frac{\rho_r}{\rho} |f^r\rangle + \beta \frac{\rho_r \rho_b}{\rho^2} \cos(|\theta\rangle) |f^{(e)}|_{\mathbf{u}=\mathbf{0}}\rangle \quad (\text{F.29})$$

$$(\Omega^b)^{(3)}(|f^b\rangle) = \frac{\rho_r}{\rho} |f^b\rangle - \beta \frac{\rho_r \rho_b}{\rho^2} \cos(|\theta\rangle) |f^{(e)}|_{\mathbf{u}=\mathbf{0}}\rangle \quad (\text{F.30})$$

avec β un paramètre qui affecte l'épaisseur de l'interface, généralement entre 0.7 et 0.99 [317], et $|\theta\rangle$ l'angle entre le gradient de couleur \mathbf{F} et la vitesse du réseau $|\mathbf{c}\rangle$.

Le but de cet opérateur est de renvoyer du fluide r vers le fluide r et vice-versa pour le fluide b tout en conservant la masse des deux. Ainsi, on réduit l'épaisseur de l'interface diffuse.

F.4 Vérification

La méthode est implémentée en série (un seul processeur) en utilisant le langage C++. Deux cas sont utilisés pour la vérification du code. Dans un premier temps, on place deux sphères 2D de rayon $R_1 = L/8$ (Fig. F.1) dans une boîte carrée de surface $L \times L$ avec un maillage de taille h . En raison de la tension de surface, les deux sphères coalescent pour former une sphère de rayon $R_2 = \sqrt{2}R_1$. Dans un deuxième temps, on place une goutte carrée qui auto-coalesce comme présenté à la Fig. F.2. La définition de l'erreur est donnée comme

$$\text{Err} = \frac{|R_2 - R_2^{\text{num}}|}{R_2} \quad (\text{F.31})$$

Les résultats des simulations pour les deux gouttes et le carré sont présentés aux Fig. F.1 et F.2 et les erreurs sont présentées à la Tab. F.3 et aux Fig. F.3 et F.4 respectivement.

Table F.3 Erreur sur le rayon final de deux gouttes qui coalescent et de l'auto-coalescence d'un carré.

$1/h$	$\text{Err}_{\text{gouttes}}$	$\text{Err}_{\text{carré}}$
32	5.719×10^{-2}	5.239×10^{-2}
64	4.269×10^{-2}	2.470×10^{-2}
128	1.334×10^{-2}	1.085×10^{-2}
256	1.505×10^{-3}	3.929×10^{-3}

Figure F.1 Coalescence de deux gouttes avec la LBM (fonction de couleur). Les paramètres sont $\rho_r = \rho_b = 1$, $v_r = v_b = 1/6$, $\sigma = 0.1$ et $\beta = 0.99$.

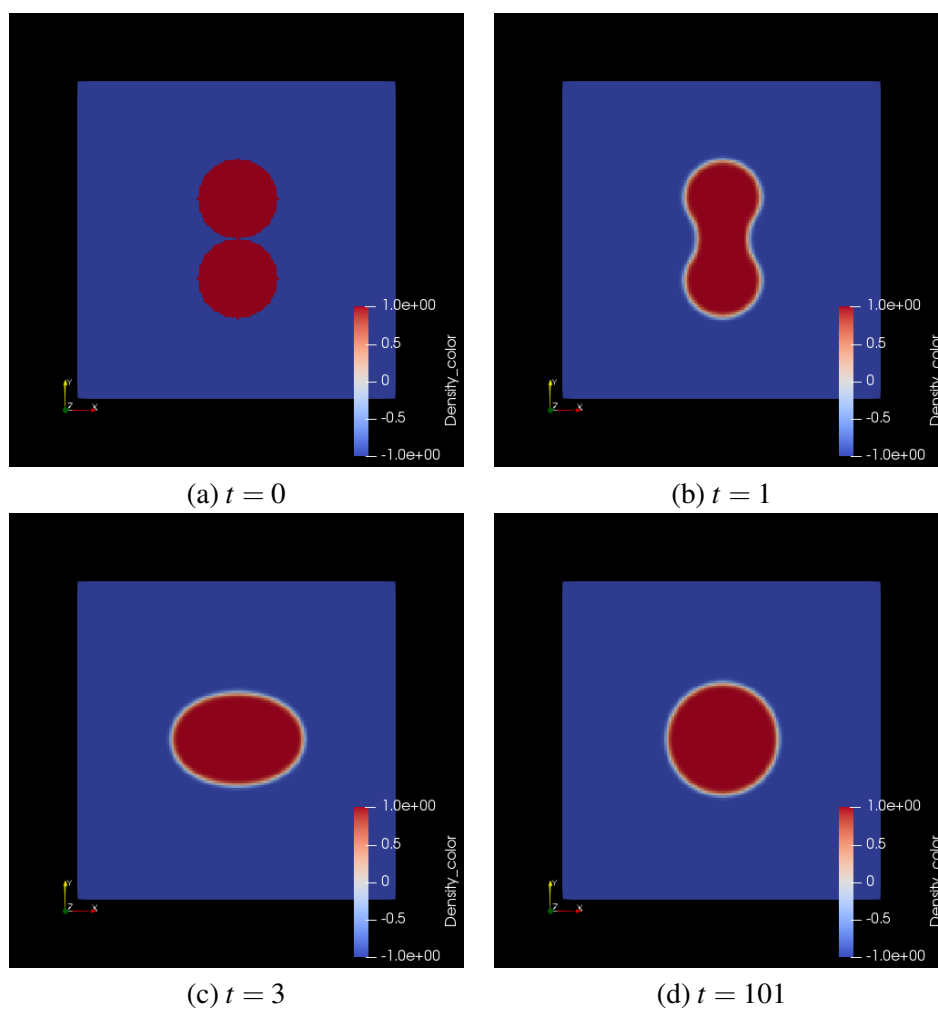
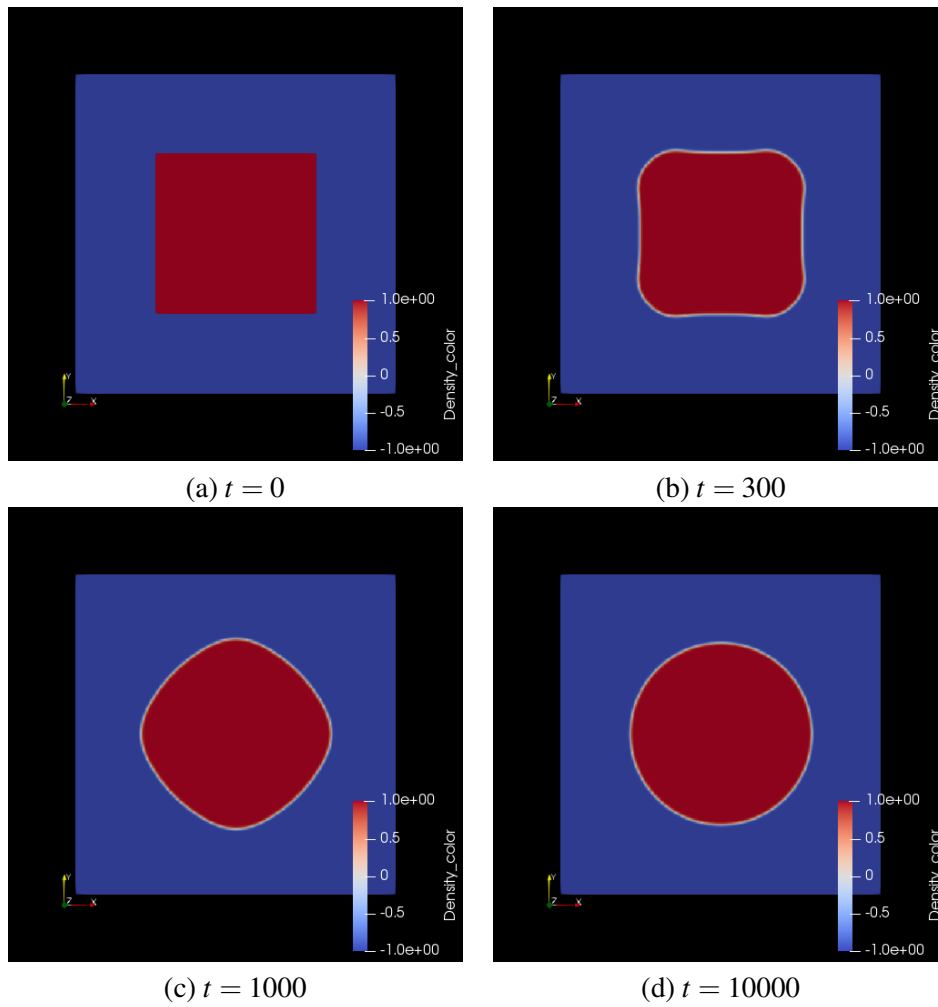


Figure F.2 Fonction de couleur d'un carré auto-coalescent. Les paramètres sont $\rho_r = \rho_b = 1$, $v_r = v_b = 1/6$, $\sigma = 0.1$ et $\beta = 0.99$.



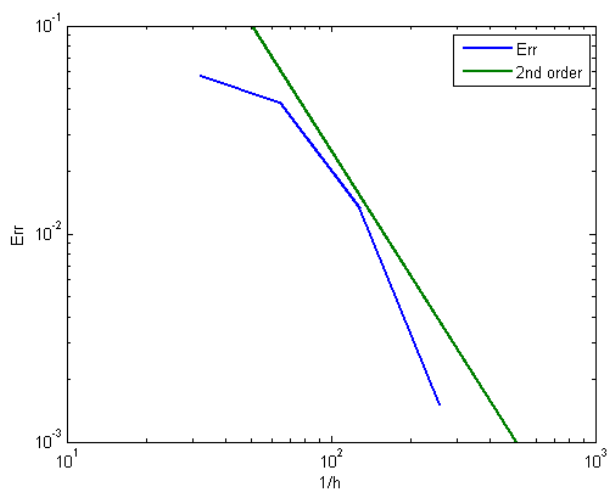


Figure F.3 Erreur en fonction de la taille du maillage pour la simulation de deux gouttes qui coalescent.

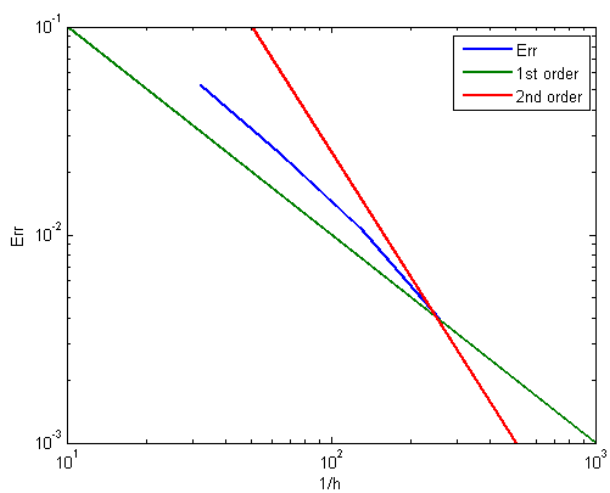


Figure F.4 Erreur en fonction de la taille du maillage pour la simulation de l'auto-coalescence d'un carré.

APPENDIX G HEURISTIC PROOF AND DECOUPLING OF MODELLING AND DISCRETIZATION ERRORS FOR CAPILLARY DYNAMIC SIMULATIONS WITH MOVING CONTACT LINES IN MICROFLUIDIC CHANNELS (IN FRENCH) / PREUVE HEURISTIQUE ET DÉCOUPLAGE DES ERREURS DE MODÉLISATION ET DE DISCRÉTISATION POUR DES SIMULATIONS DE DYNAMIQUE CAPILLAIRE AVEC LIGNE DE CONTACT EN MOUVEMENT DANS UN CANAL MICROFLUIDIQUE.

G.1 Modélisation multiphase en microfluidique

En raison d'une augmentation de l'intérêt pour les systèmes capillaires autonomes en microfluidique [197,318], il est important de développer des outils de modélisation capable de prédire avec précision le comportement des écoulements multiphases dans ces microstructures. Cependant, ceci n'est pas une tâche simple en raison d'effets multi-échelle intrinsèque à de tels écoulements. Pour cette étude, nous utiliserons la librairie OpenFOAM (Open Field Operation and Manipulation) qui utilise une formulation centrée aux cellules de la méthode des volume finis pour résoudre, principalement, des problèmes de transport. Plus de détails sur les équations à résoudre ainsi que les algorithmes utilisés suivront à la Section G.3. Le but de cette étude est de découpler les erreurs de modélisation et les erreurs de discrétisation pour des simulations de dynamique capillaire avec ligne de contact en mouvement dans un canal microfluidique.

G.2 Défi des lignes de contact en mouvement

Modéliser une interface en mouvement utilisant des méthodes Eulériennes, e.g. éléments-, volumes- et différences finies, requiert généralement l'utilisation d'interfaces diffuse dont l'épaisseur dépend linéairement en fonction du pas de grille [109]. De plus, les modèles continus de la mécanique des fluides, e.g. les équations de Navier-Stokes, ne représentent pas avec précision les phénomènes physiques intrinsèquement mésoscopique et microscopique tel le déplacement d'une ligne de contact sur un mur avec friction (condition de Dirichlet) [173]. Cela vient du fait que la pression, et donc la contrainte, au point de contact triphasique solide-liquide-gaz est singulière pour un écoulement de Stokes dans un coin avec une condition des Dirichlet sur l'une des deux (ou les deux) surfaces. Ceci est un résultat classique de la mécanique des fluides développé par Taylor pour deux conditions de Dirichlet et subséquemment Moffat avec une des deux surfaces possédant une condition de Neumann, ce qui est le cas avec une interface capillaire [190]. La pression en coordonnées polaires selon le développement de Taylor et Moffat est respectivement donnée par l'Éq. G.1 et G.2. Ce résultat est évidemment non physique lorsque $r \rightarrow \infty$, et il faut en tenir compte

lors de toute modélisation numérique de lignes de contact en mouvement utilisant une formulation continue de la mécanique des fluides.

$$p(r, \theta) - p_\infty = \frac{2\mu U}{r} \frac{\beta \sin \theta + \sin \beta \sin(\beta - \theta)}{\beta^2 - \sin^2 \beta} \quad (\text{G.1})$$

$$p(r, \theta) - p_\infty = \frac{2\mu U}{r} \frac{\theta \cos \theta \sin \beta - \beta \cos \beta \sin \theta}{\sin \beta \cos \beta - \beta} \quad (\text{G.2})$$

G.3 Méthodologie numérique (VOF)

Pour cette étude, nous utiliserons le modèle « Volume Of Fluid » (VOF). Dans ce modèle, un seul système d'équations de Navier-Stokes dans lequel on ajoute un terme de tension de surface dans l'équation de conservation de quantité de mouvement qui est calculé à partir du gradient du champ de phase α , où $\alpha = 0$ dénote l'air et $\alpha = 1$ dénote l'eau, dans le modèle CSF (Continuum Surface Force formulation) [65]. La viscosité et la densité de la mixture est définie spatialement par une simple pondération obtenue avec le champ de phase. Le champ de phase est advecté par une équation de transport de premier ordre auquel on ajoute un terme de compression pour mitiger la diffusion numérique de l'interface [249]. La discrétisation spatiale est une simple grille orthogonale structurée faite à l'aide de l'outil `blockMesh` d'OpenFOAM. Les simulations plus larges ($H/\Delta \geq 16$) sont lancées en parallèle sur 10 CPU sur un serveur « homebrewed » possédant 2 CPU Intel Xeon. La parallélisation est une division simple du domaine en 10 parties égales selon la longueur. L'algorithme PISO (Pressure-Implicit with Splitting of Operators) est utilisé pour le couplage pression-vitesse transitoire.

G.3.1 Équations constitutives du modèle VOF

On résout les équations de Navier-Stokes pour un écoulement incompressible composé d'un mélange de deux fluides Newtoniens non miscibles. La conservation de la masse et de la quantité de mouvement s'écrit:

$$\nabla \cdot \mathbf{u} = 0 \quad (\text{G.3})$$

$$\frac{\partial \rho \mathbf{u}}{\partial t} + \nabla \cdot (\rho \mathbf{u} \mathbf{u}) = -\nabla p + \mu \nabla^2 \mathbf{u} + \mathbf{F} \quad (\text{G.4})$$

où ρ est la densité, μ est la viscosité, \mathbf{u} est le champ vectoriel de vitesse, p est la pression, et \mathbf{F} et le terme de tension de surface. Dans la formulation VOF, on résout une seule équation de Navier-Stokes (Eq. G.4) avec

$$\rho = \alpha \rho_1 + (1 - \alpha) \rho_2 \quad (\text{G.5})$$

et

$$\mu = \alpha\mu_1 + (1 - \alpha)\mu_2 \quad (\text{G.6})$$

Le transport du champ de phase est effectué par

$$\frac{\partial \alpha}{\partial t} + \nabla \cdot (\alpha \mathbf{u}) - \nabla \cdot [\alpha(1 - \alpha)\mathbf{u}_r] = 0 \quad (\text{G.7})$$

avec

$$\mathbf{u}_r = \mathbf{n}_f \min \left[C_\gamma \frac{|\phi_f|}{|S_f|}, \max \frac{|\phi_f|}{|S_f|} \right] \quad (\text{G.8})$$

où ϕ_f , S_f et \mathbf{n}_f sont respectivement le flux de volume à travers la surface f , l'aire de la surface et le vecteur unitaire normal à cette surface, et $C_\gamma \in [0, 4]$ est une constante de compression. La tension de surface \mathbf{F}_γ est calculée en utilisant le modèle « Continuum Surface Force » (CSF) [65] :

$$\mathbf{F}_\gamma = \gamma \kappa (\nabla \alpha) \quad (\text{G.9})$$

où $\kappa = \nabla \cdot (\nabla \alpha / |\nabla \alpha|)$ est la courbure du champ de phase.

G.4 Test « benchmark » et dynamique capillaire

Pour être en mesure de découpler les erreurs de modélisation et les erreurs de discrétisation, nous devons premièrement définir une métrique. Considérons le test benchmark d'un canal rectangulaire 2D d'une longueur et d'une hauteur H . Les conditions frontières sont 1) angle de contact θ constant en paroi, 2) condition de Dirichlet $u = 0$ en paroi, et 3) pression nulle à l'entrée et à la sortie du canal. La solution analytique au déplacement du ménisque dans le canal est donnée par une balance de la pression de Laplace et la pression hydraulique, soit la loi d'Hagen-Poiseuille, l'équivalent hydrodynamique de la loi d'Ohm en électrodynamique. La solution à l'équation différentielle non linéaire obtenue par ce système est donnée par l'équation de Washburn [82]. Ici, on assume que les effets inerties sont nuls. C'est pourquoi la vitesse est singulière en $x = 0$, ce qui est évidemment non physique. Pour bien capturer la physique proche de $x = 0$, il faut inclure un terme inertiel à la balance de pression. Cela est donné par l'équation de Bosanquet [255]. Cependant, pour cette étude, on assume que ce terme additionnel est négligeable puisqu'on fera nos mesures loin de $x = 0$. Ces équations sont des résultats classiques de la mécanique des fluides et ont été validés en laboratoire à maintes reprises. Nous utiliserons l'équation de Washburn pour faire une étape de validation numérique [228] par proxy. L'équation de Washburn pour ce cas spécifique est donnée par

$$x = H \sqrt{\frac{t}{\tau}} \quad (\text{G.10})$$

et où la constante de temps de Washburn, τ , est donnée par

$$\tau = \frac{3\mu H}{\cos \theta} \quad (\text{G.11})$$

La métrique utilisée pour l'analyse sera la constante de temps tau de l'équation de Washburn. On commence notre analyse par une démonstration de la dépendance en maillage des simulations. À la Fig. G.2, on observe que plus le maillage est fin plus le liquide met de temps à remplir le canal (fraction de volume de 1). Cela se traduit en une augmentation de la constante de temps de Washburn (Fig. G.3). Cela est attendu puisque 1) l'erreur de discrétisation vient en effet réduire la résistance hydraulique du canal, et 2) l'erreur de modélisation augmente la contrainte au point triphasique de la ligne de contact. On observe deux zones de convergence logarithmique, soit une zone de superconvergence préasymptotique lorsque $H/\Delta < 4$, et une zone de convergence vers la solution singulière lorsque $H/\Delta > 8$. Notre hypothèse est que les erreurs de discrétisation dominent la première zone et les erreurs de modélisation dominent la seconde.

G.5 Analyse et méthodologie

La première étape de notre analyse consiste à vérifier l'indépendance des simulations selon la discrétisation en temps. Pour ces simulations, le pas de temps numérique est limité par la convection et donc le nombre de Courant [181]. On choisit une discrétisation spatiale $H/\Delta = 6$, un angle de contact $\theta = 60$ deg et on refait les simulations avec différents Co_{\max} . Comme montré à la Fig. G.4, on observe très peu de variation (moins de 0.5%) pour tout $\text{Co}_{\max} < 1$. On continue notre analyse avec $\text{Co}_{\max} = 0.2$.

Pour être en mesure de discerner les erreurs de modélisation et les erreurs de discrétisation spatiale, on doit mesurer la pression de Laplace du ménisque en mouvement. Comme la pression du ménisque est invariante dans l'espace et dans le temps, excepté proche de $t = 0$ où des effets transitoires sont présents pour la stabilisation de l'interface, on peut calculer la pression au ménisque, p_m , en

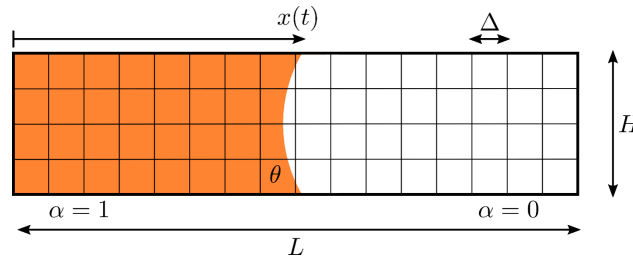


Figure G.1 Schéma

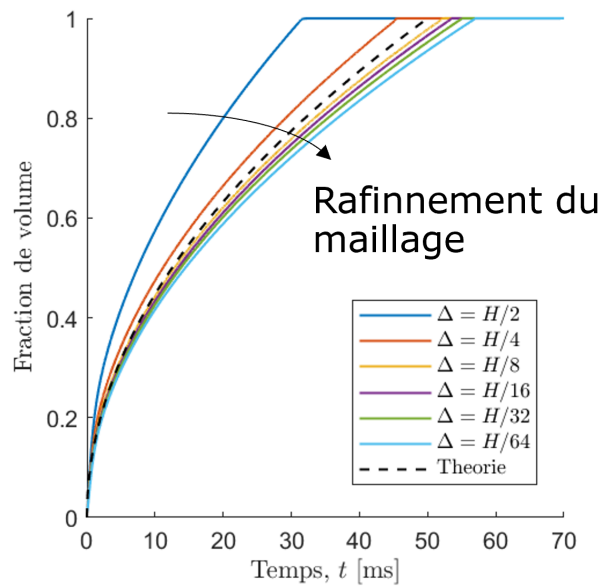


Figure G.2 Fraction de volume dépendante en fonction du maillage.

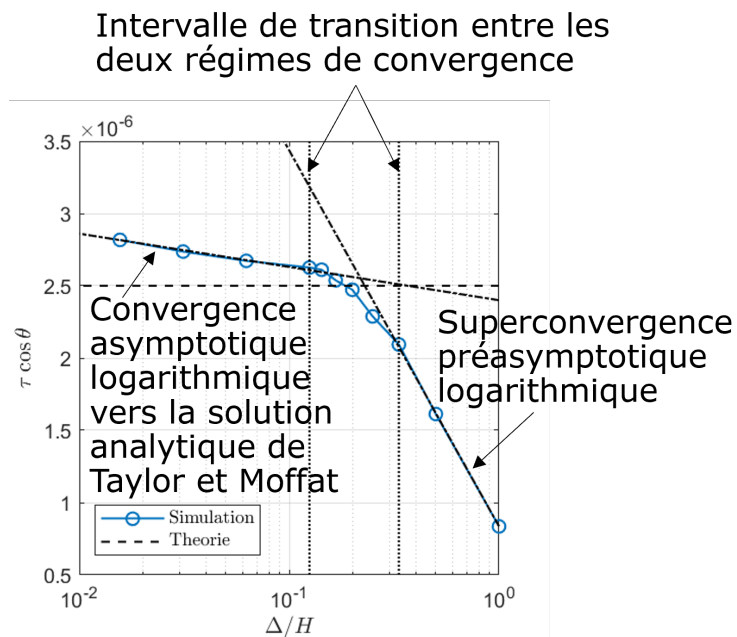


Figure G.3 Augmentation de la constante de temps de Washburn en fonction du maillage. On dénote deux régimes logarithmiques: une superconvergence préasymptotique, ainsi qu'une convergence asymptotique divergente.

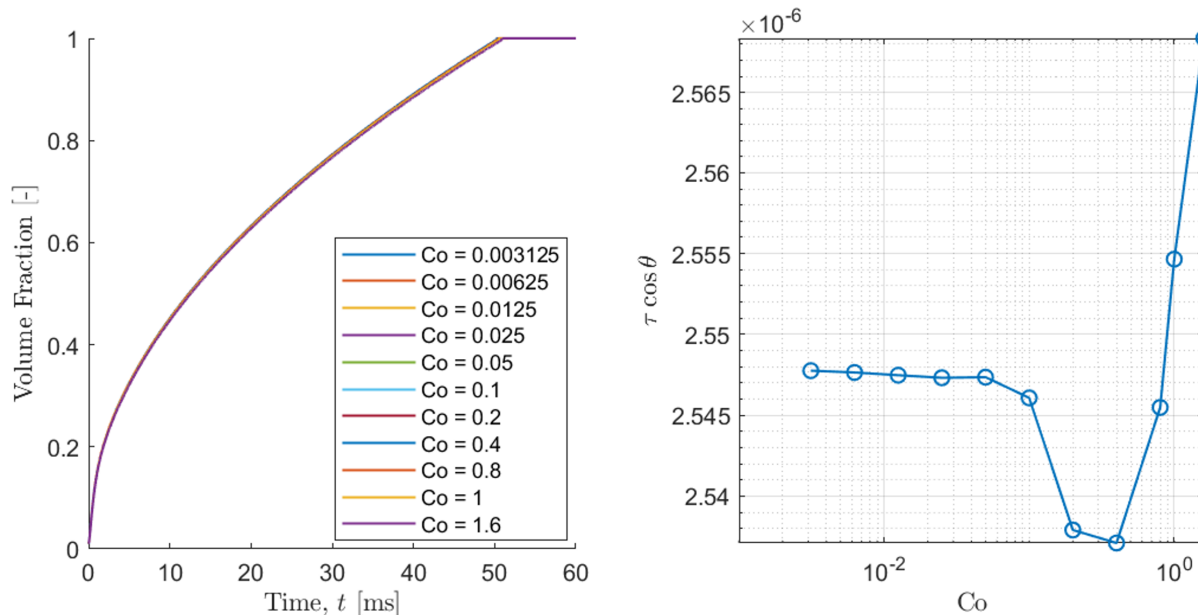


Figure G.4 Quasi-invariance des résultats en fonction de la discrétisation en temps limitée par le nombre de Courant.

calculant le minimum de la pression en un point fixe, i.e. le moment où le ménisque passe par ce point. On choisit le point $(x, y) = (H, L)/2$ où on vient calculer la pression pour tous les pas de temps Δt déterminés par Co_{\max} .

On mesure d'importantes fluctuations de la pression (Fig. G.5). Ces fluctuations de la pression sont liées à l'augmentation des courants parasites plus Δ est petit [199]. Cela expliquerait pourquoi les fluctuations semblent augmenter avec le raffinement du maillage. Cependant, une étude plus approfondie serait nécessaire pour bien élucider cet artefact numérique. On compare les pressions mesurées à la pression de Laplace théorique ($p_{th} = 1200$ Pa).

G.5.1 Mesure de la pression moyennée (méthode I)

Pour obtenir une valeur plus exacte de la pression, on fait un moyennage temporel de la pression. On cherche alors un intervalle δt approprié qui diminue suffisamment les fluctuations pour avoir un profil de pression plus lisse, tel qu'illustré à la Fig. G.6.

On fait le moyennage avec différents δt , et on présente quelque exemple. Pour $\delta t = 1.2207 \times 10^{-5}$ s les fluctuations sont encore importantes de manière générale. Pour $\delta t = 4.8828 \times 10^{-5}$ s les fluctuations sont importantes dans certaines régions, mais commencent à diminuer dans certaines zones proches de $t = 25$ ms. Pour $\delta t = 1.9531 \times 10^{-4}$ s le profil de pression est suffisamment lisse (Fig. G.7).

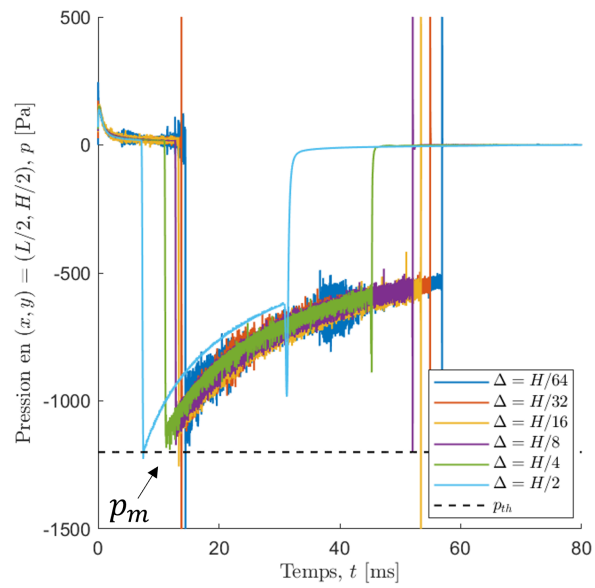


Figure G.5 Mesure de la pression pour différents maillages en un point fixe dans l'espace.

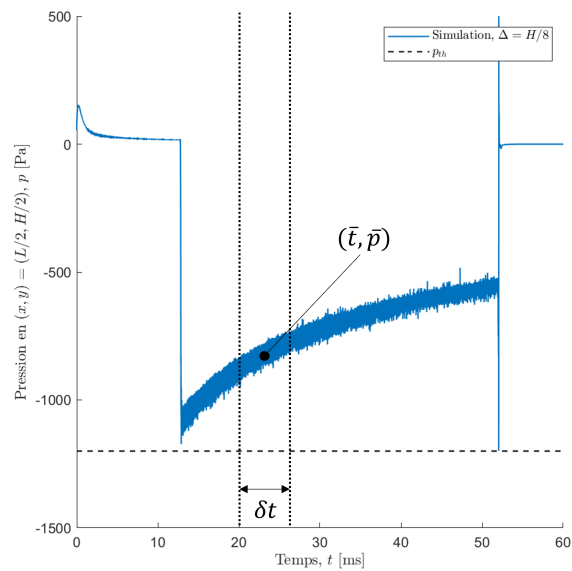


Figure G.6 Schéma du choix d'un intervalle δt pour calculer le temps moyen et la pression moyenne (\bar{t}, \bar{p}) .

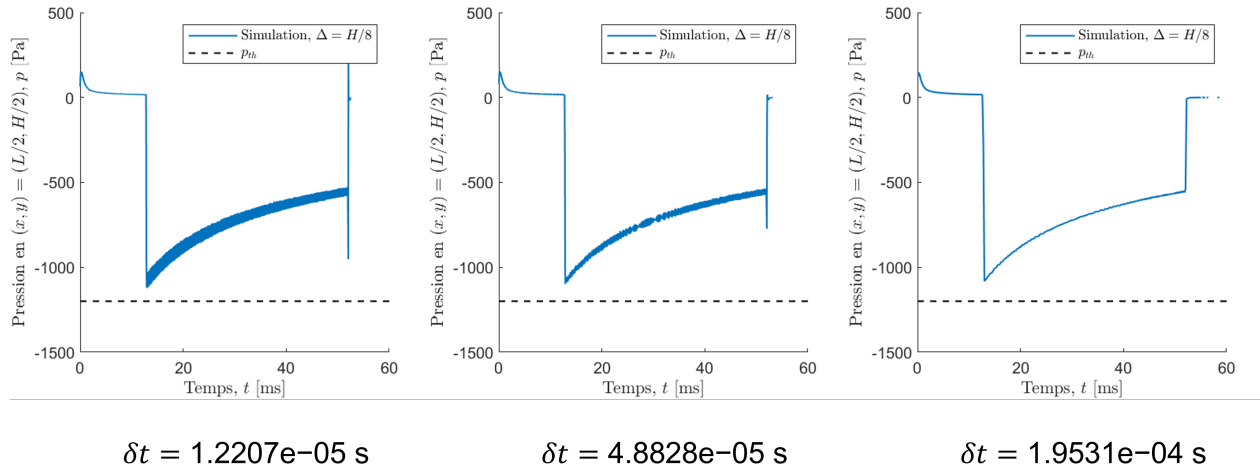


Figure G.7 Profil de pression moyenné sur différents intervalles temporels.

Pour faire un meilleur choix de δt , on trace le graphique de la pression de Laplace numérique p_m en fonction de l'intervalle de moyennage temporel δt (Fig. G.8). On observe que pour de petites et grandes valeurs de δt , p_m varie significativement par rapport à la valeur théorique. Cela est attendu puisque pour δt petit, les fluctuations sont encore grandes, et pour δt grand, la valeur de p_m est diluée par le plateau de pression $p = 0$ avant le passage du ménisque.

G.5.2 Mesure de la pression moyennée (méthode II)

Pour vérifier que l'on ne commet pas un grande erreur sur la mesure de p_m en raison du plateau de pression $p = 0$ avant le passage du ménisque au point $(x, y) = (H, L)/2$, on refait le moyennage avec une seconde méthode. Cette fois-ci, on définit à quel moment le ménisque passe par la sonde de pression et on calcule le premier moyennage à partir de ce point (Fig. G.9). De cette manière, on ne vient pas diminuer la valeur de p_m avec les valeurs voisines.

Une fois de plus, on fait le moyennage avec différents δt , et quelque exemples sont présentés à la Fig. G.10. Les conclusions sont identiques à la méthode précédente. Cela est attendu puisque, en dehors d'une zone de changement abrupt de pression, la pression moyennée devrait être similaire peu importe le point de référence du moyennage.

Comme vu précédemment, on présente la pression de Laplace numérique p_m en fonction de l'intervalle de moyennage temporel δt . On observe que les valeurs fluctuent beaucoup moins qu'à la Fig. G.11, ce qui était le but de la seconde méthode. On doit maintenant choisir un δt pour continuer notre analyse. Ici, on choisit $\delta t = 1.9531 \times 10^{-4}$ s.

La Fig. G.12 démontre que la pression de Laplace numérique p_m ne varie pas significativement

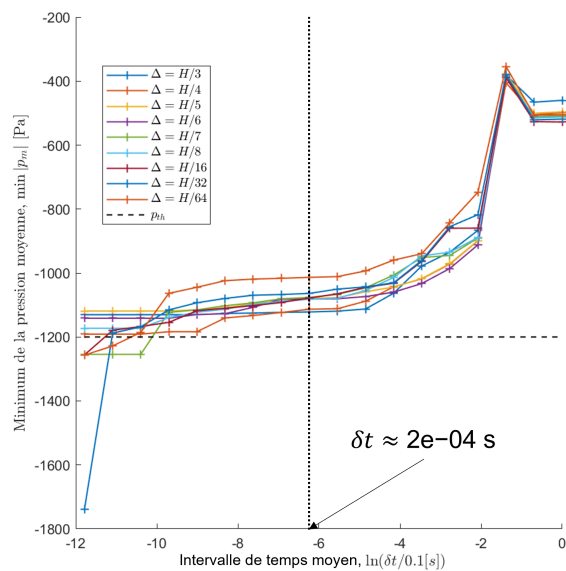


Figure G.8 Pression au ménisque en fonction du moyennage temporel pour différents maillages.

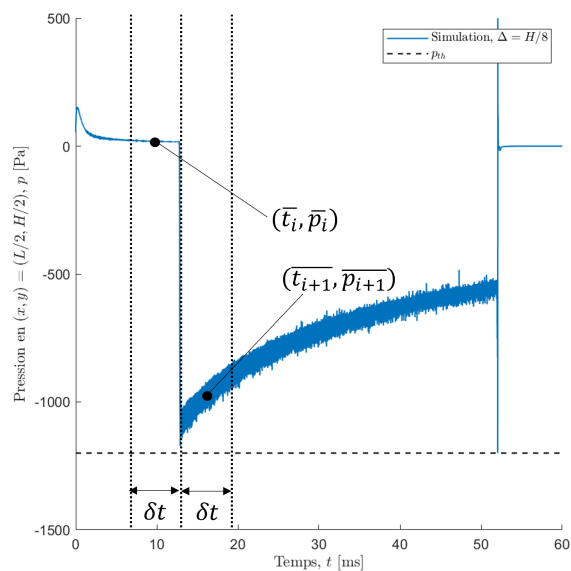


Figure G.9 Schéma du choix d'un intervalle δt centré sur p_m pour calculer le temps moyen et la pression moyenne (\bar{t}, \bar{p}) .

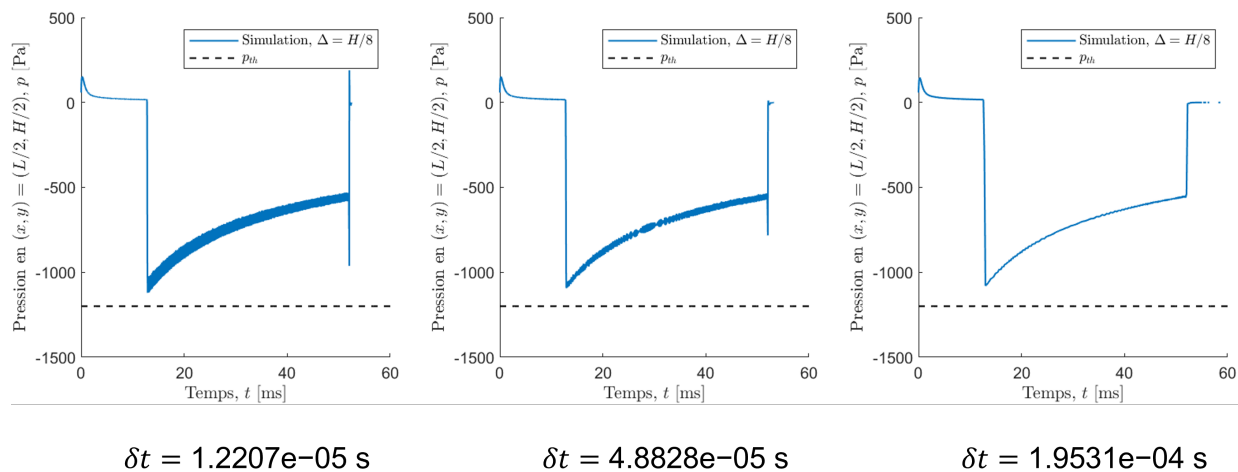


Figure G.10 Profil de pression moyenné sur différents intervalles temporels centrés sur p_m .

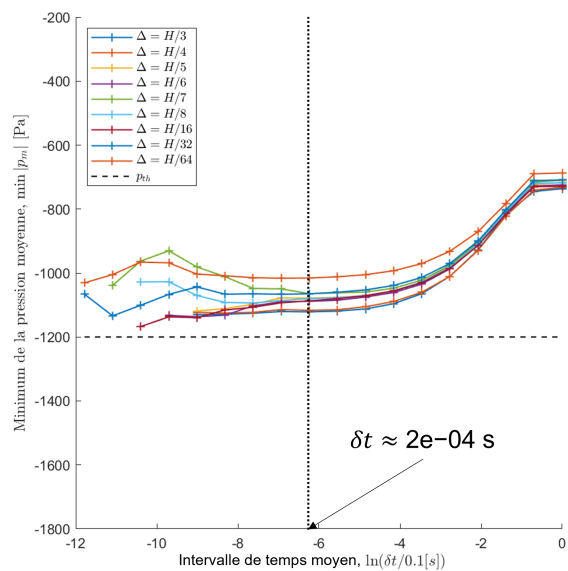


Figure G.11 Pression au ménisque en fonction du moyennage temporel avec la méthode centrée sur p_m pour différents maillages.

en fonction du type de méthode utilisée pour le moyennage temporel de la pression avec $\delta t = 1.9531 \times 10^{-4}$ s. Cependant, cela peut servir de base pour argumenter d'une erreur sur la mesure de quelques pourcents en fonction de la méthode. Soit, environs 2,5 % dépendant du maillage utilisé.

Pour continuer notre analyse du découplage des erreurs de modélisation et des erreurs de discrétisation, on doit mesurer la vitesse en entrée du canal. Pour ce faire, on mesure le débit et on divise celui-ci par la surface de l'entrée d'eau. Le résultat en fonction du maillage est comparé à la théorie donnée par l'équation de Washburn à cette figure.

Pour calculer les erreurs sur la résistance hydraulique, on substitue la pression de Laplace mesurée dans la loi de Hagen-Poiseuille. Connaissant le débit numérique, on calcule la résistance hydraulique numérique et on la compare à la résistance hydraulique théorique donnée pour des plaques parallèles [68]. L'erreur entre la résistance hydraulique numérique et théorique est moins de 2%, ce qui est amplement dans la marge de l'erreur commise sur la mesure de la pression (Fig. G.14). On observe également une convergence d'ordre 1.5 sur la résistance hydraulique. Comme la mesure de la résistance hydraulique dépend de la mesure de la vitesse, On s'attendrait à un ordre de convergence de deux avec la méthode des volumes finis, cependant l'ordre est peut-être réduit en raison de la formulation CSF pour le calcul de la pression ou autres parties du code. Une autre hypothèse est que la vitesse calculée à la frontière converge différemment puisqu'elle est liée à la condition frontière $p = 0$. En effet, les valeurs en frontières peuvent converger différemment dépendant des méthodes utilisées. Une étude plus approfondie de cette convergence 1.5 devrait être faite pour être plus rigoureux, mais cela n'est pas nécessaire pour les objectifs de ce travail.

G.6 Resultats

Finalement, pour combiner tous les morceaux du puzzle, on doit redériver l'équation de Washburn avec les variables utilisées pour cette étude. Soit, la résistance hydraulique et la pression de Laplace. La constante de temps de Washburn exprimée en fonction de la résistance hydraulique et de la pression de Laplace s'exprime comme

$$\tau^* = \frac{WH^3 R_{\text{hyd},L/2}}{\Delta p L} \quad (\text{G.12})$$

Pour calculer l'impact de l'erreur de modélisation sur tau, on substitue Δp par p_m et $R_{\text{hyd},L/2}$ par $R_{\text{hyd},\text{th}}$. D'autre part, pour calculer l'impact de l'erreur de discrétisation sur tau, on substitue Δp par p_{th} et $R_{\text{hyd},L/2}$ par R_{num} .

Pour terminer, on compare les résultats sur à la Fig. G.15. On observe bien deux zones de con-

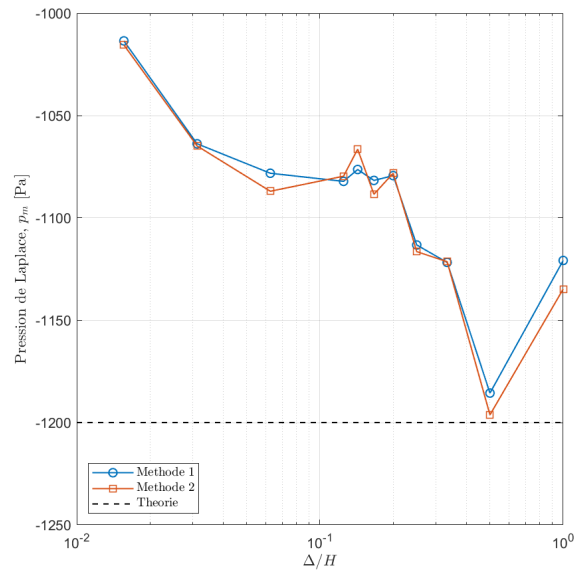


Figure G.12 Pression de Laplace calculée avec les deux méthodes et comparaison avec la valeur théorique.

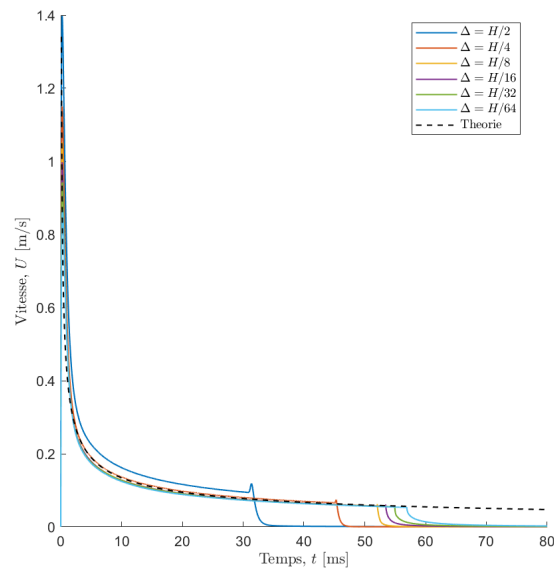


Figure G.13 Vitesse moyennée à l'entrée du canal microfluidique.

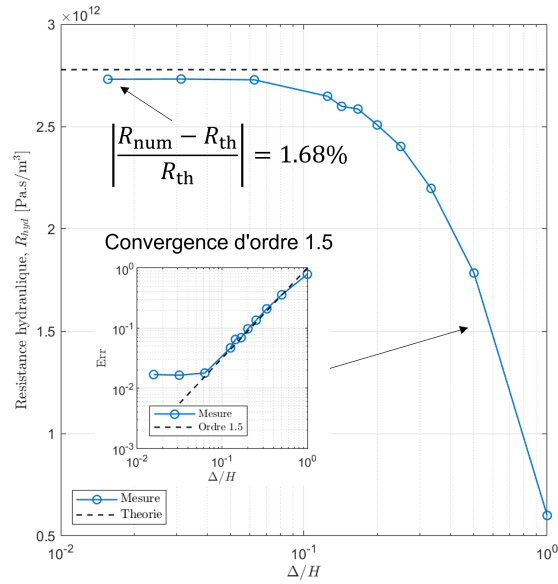


Figure G.14 Résistance hydraulique en fonction du maillage comparée à la valeur théorique.

vergence, soit 1) une zone contrôlée par les erreurs sur la pression de Laplace, i.e. les erreurs de modélisation en raison de la pression singulière donnée par l'analyse de Taylor et Moffatt, et 2) une zone contrôlée par les erreurs sur la résistance hydraulique, i.e. les erreurs de discrétisation sur le champ de vitesse. Initialement, les erreurs de discrétisation dominent et deviennent négligeables par rapport aux erreurs de modélisation pour $H/\Delta > 8$. Pour $H/\Delta > 4$ et $H/\Delta < 8$, les erreurs de discrétisation et de modélisation sont du même ordre. Cela est important à savoir puisqu'en général, pour la simulation de dispositifs microfluidique capillaire, nous sommes dans cet intervalle de résolution de maillage.

Pour comparer la constante de Washburn obtenue théoriquement par les valeurs calculés on substitue Δp par p_m et $R_{\text{hyd},L/2}$ par R_{num} dans l'Éq. G.12. On observe que l'on est bien dans un intervalle d'environ 5% avec la valeur simulée, ce qui concorde bien avec la résolution approximée de la méthode de calcul. En théorie, si les méthodes de calcul étaient parfaitement exactes et que seules les erreurs sur la pression et la résistance hydraulique sont significatives, on devrait voir la courbe $R_{\text{hyd}} + p_m$ parfaitement épouser les résultats de simulation.

G.7 Conclusion

Dans cette étude, nous avons découplé les erreurs de modélisation et les erreurs de discrétisation pour des simulations de dynamique capillaire avec ligne de contact en mouvement dans un canal microfluidique. Pour $H/\Delta > 8$, les erreurs de modélisation dominent, et pour $H/\Delta < 4$, les erreurs

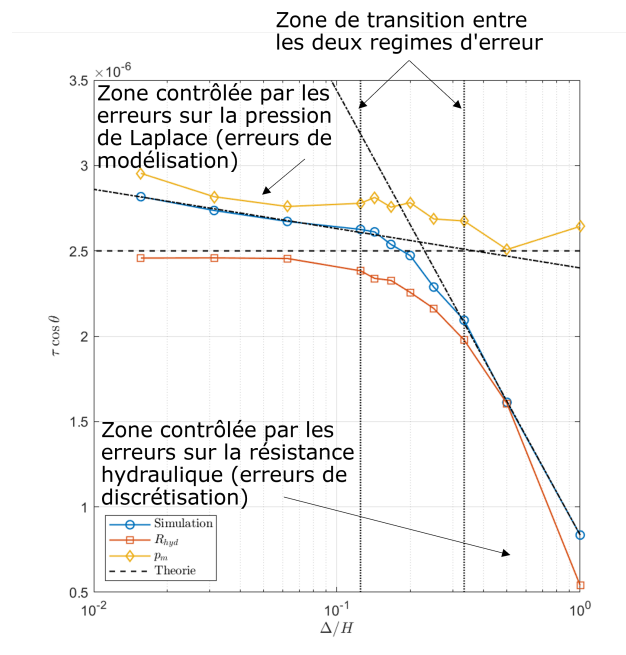


Figure G.15 Constante de temps de Washburn simulée comparée aux erreurs de discrétisation et de modélisation (résistance hydraulique et pression de Laplace).

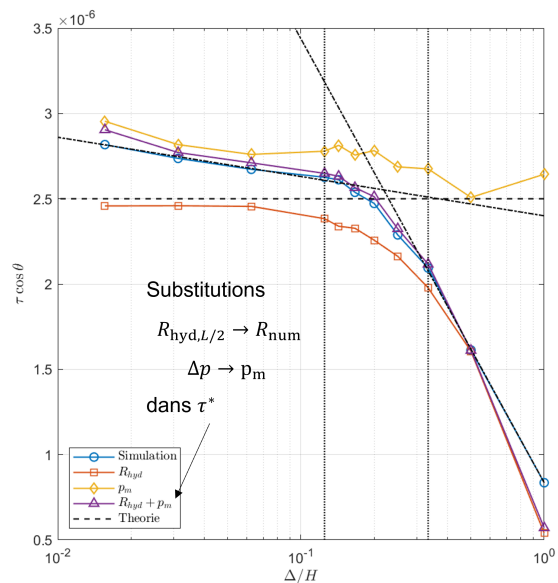
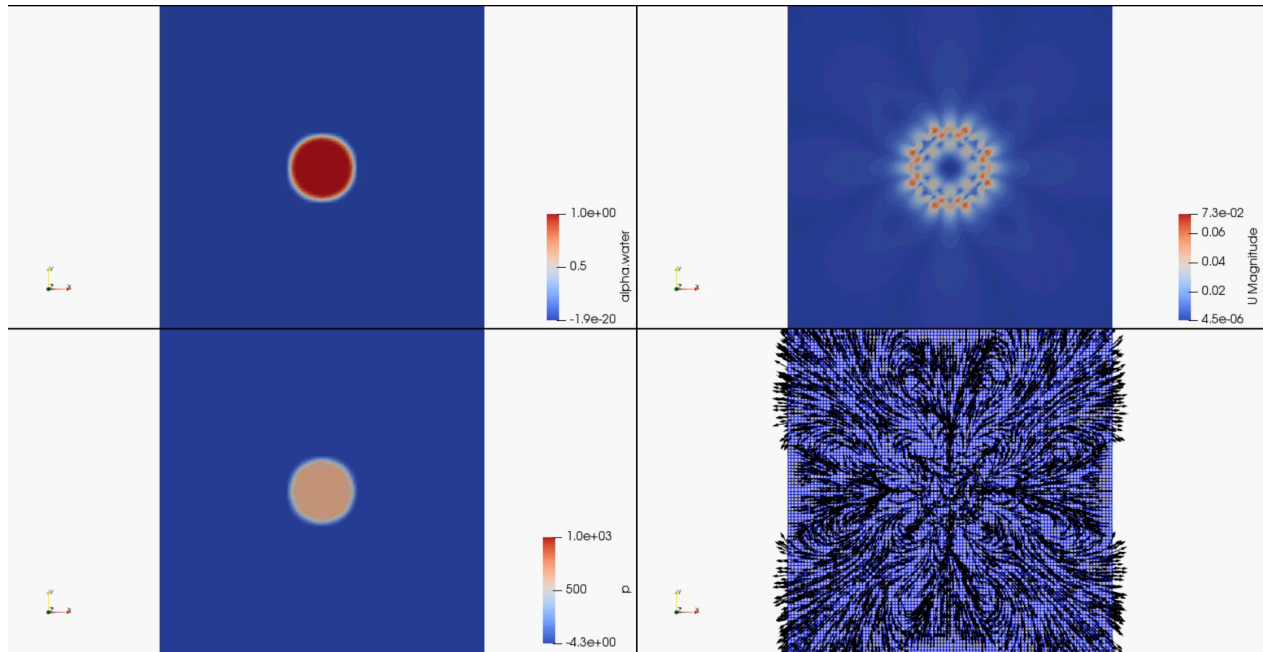


Figure G.16 Substitution des valeurs calculés dans l'équation de Washburn et comparaison entre la constante de Washburn calculée et simulée.

de discrétisation dominant. Entre ces deux intervalles, les erreurs sont environ du même ordre de grandeur. Pour faire une étude plus rigoureuse, une analyse statistique des fluctuations de la pression et établir une métrique plus précise pour en faire le moyennage temporel pourrait être fait. Par exemple, on pourrait faire une analyse de Fourier des fluctuations et imposer un filtre fréquentiel adéquat en fonction des différentes fréquences mesurées. Cette méthode est gardée pour des travaux futurs.

**APPENDIX H PARAMETRIC ANALYSIS OF SPURIOUS CURRENTS IN OPENFOAM
(VOF-FVM WITH COMPRESSIVE CSF)**



Video H.1 Spurious currents for a droplet of water. (Flash Player required)

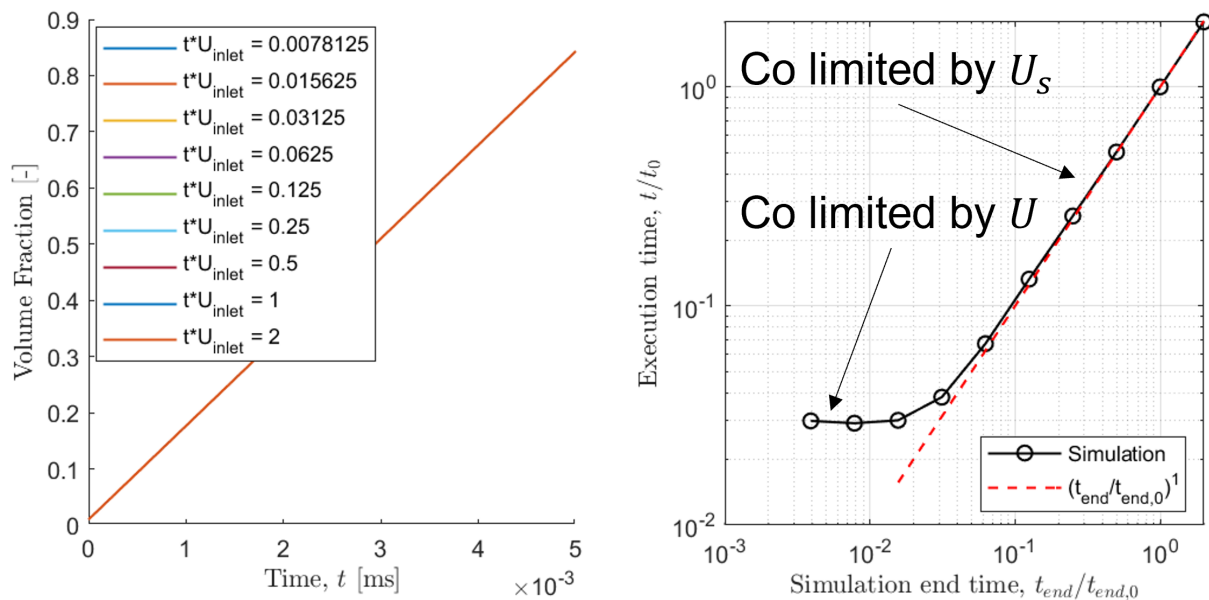


Figure H.2 Execution time with respect to the physical simulation time t_{end} . The spurious velocities U_s are constant with respect to U . If $U < U_s$, the execution time t_{sim} is proportional to t_{end} .

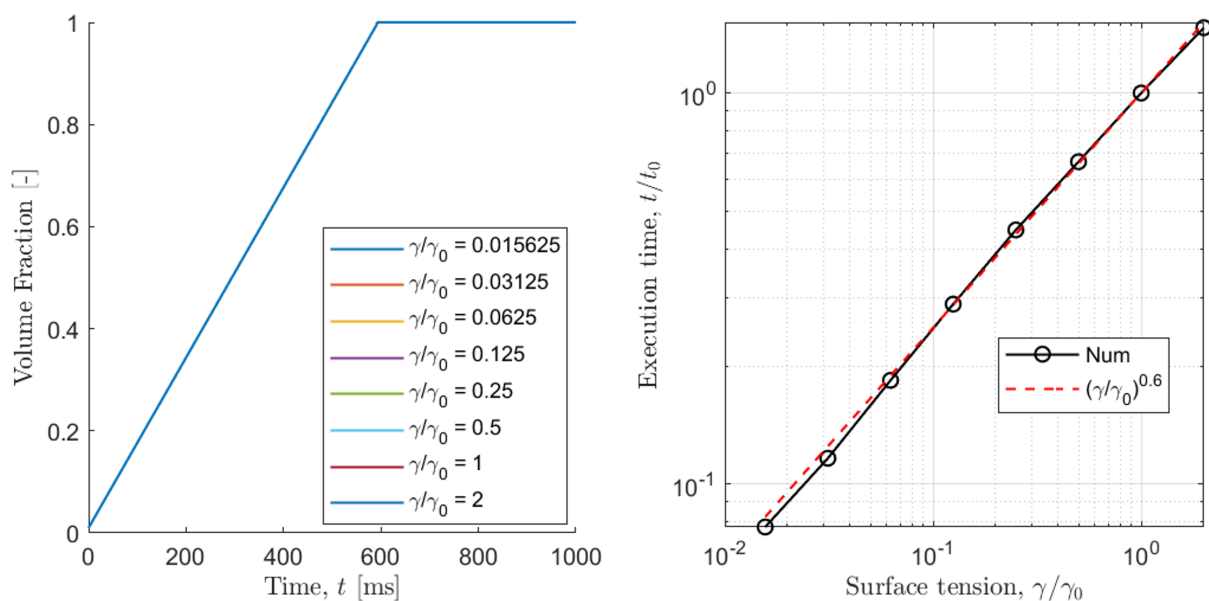


Figure H.3 Execution time with respect to surface tension γ with $\gamma_0 = 0.072 \text{ N m}^{-1}$. Spurious currents are proportional to surface tension: $t_{\text{sim}} \sim \gamma^{0.6}$.

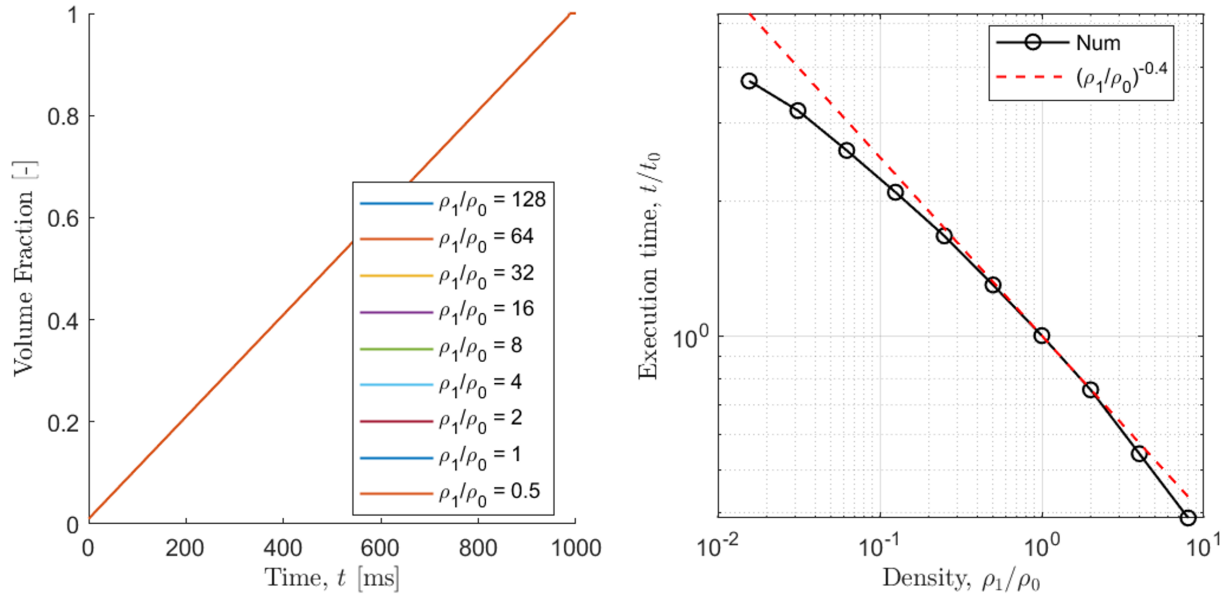


Figure H.4 Execution time with respect to density ρ with $\rho_0 = 1000 \text{ kg m}^{-3}$. Spurious currents are inversely proportional to density: $t_{\text{sim}} \sim \rho^{-0.4}$.

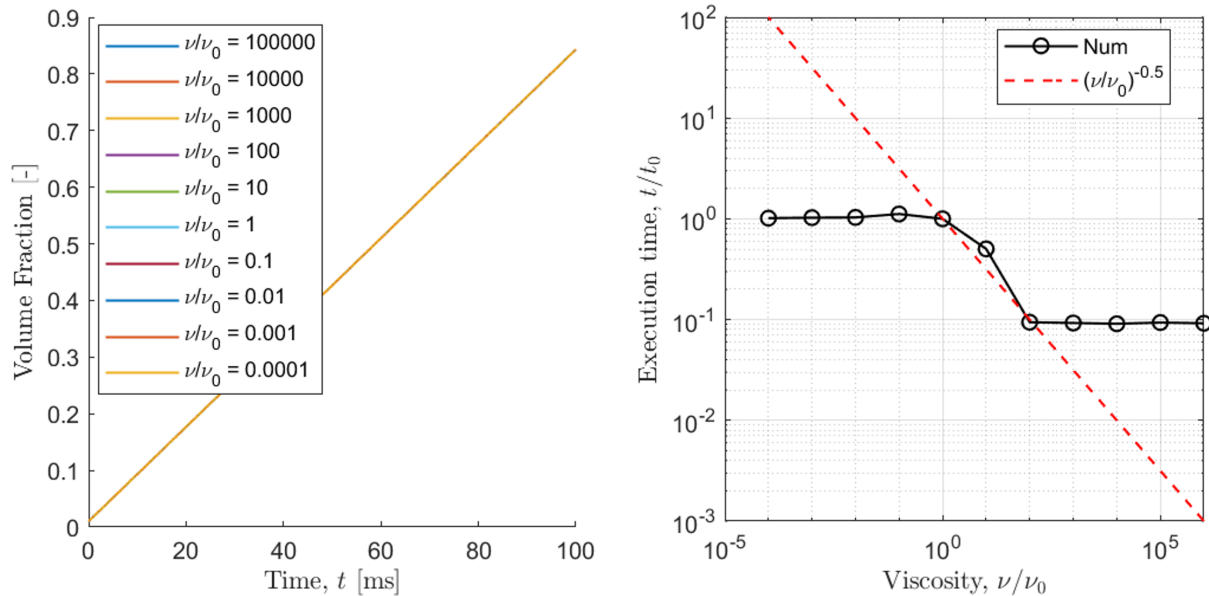


Figure H.5 Execution time with respect to viscosity $\nu = \mu/\rho$ with $\mu_0 = 0.001 \text{ Pa} \cdot \text{s}$. Spurious currents are inversely proportional to viscosity within 2 orders of magnitude of μ_0 : $t_{\text{sim}} \sim \nu^{-0.5}$.